FACULTY OF MATHEMATICS AND PHYSICS
Charles University

DOCTORAL THESIS

RNDr. Marcel Lamač

Relativistic Optics: The Frontier of Ultrashort X-ray Pulse Generation

Department of Chemical Physics and Optics

Prague 2024

I declare that I carried out this doctoral thesis independently and only with the cited sources, literature, and other professional sources. It has not been used to obtain another or the same degree.

I understand that my work relates to the rights and obligations under Act No. 121/2000 Sb., the Copyright Act, as amended, in particular, the fact that the Charles University has the right to conclude a license agreement on the use of this work as a school work under Section 60 subsection 1 of the Copyright Act.

In . . . . date . . . .
Author's signature

Title: Relativistic Optics: The Frontier of Ultrashort X-ray Pulse Generation

Author: RNDr. Marcel Lamač

Department: Department of Chemical Physics and Optics

Supervisor: Ing. Jaroslav Nejdl, Ph.D., ELI Beamlines, The Extreme Light Infrastructure ERIC

Abstract: In his 1905 work on the theory of special relativity, A. Einstein predicted that a radiation pulse reflected from a counter-propagating relativistic mirror undergoes blueshift and length contraction due to the relativistic Doppler effect. Nowadays, high-powered laser systems enable the creation of such relativistic mirrors through nonlinear processes that occur when a relativistically intense laser pulse interacts with plasma. The proliferation of high-powered laser systems in the past years motivates us to explore a new kind of nonlinear optics, which emerge due to laser-induced nonlinear oscillations of charged particles, the velocity of which can get close to the speed of light. The insights into what is now called relativistic optics have a transformative potential to advance particle acceleration, coherent X-ray pulse generation, laboratory astrophysics, ultrafast X-ray spectroscopy, medical imaging or radiotherapy, and many other applications. This doctoral thesis serves as a brief introduction to the field of relativistic optics, as well as a summary of the research conducted by the author in this field.

> *And here, poor fool! With all my lore,*
> *I stand no wiser than before.*
>
> – Goethe's Faust (1800)

Contents

Contents

1

Introduction

In the opening chapter, we introduce a very coarse review of historical milestones and some of the most important achievements in high-power laser technology and applications. Then, we define and put our research objectives in the context of these advancements. Finally, we outline how the structure of this doctoral thesis is organized.

1.1   Historical overview and motivation

Relativistic optics can be defined as a regime of light-matter interaction where relativistic effects become non-negligible [Mourou et al., 2006]. This occurs when the velocity of the lightest component of matter, the electron, approaches the speed of light. To study such a regime, we require large amplitude electromagnetic waves. Therefore, the journey towards relativistic optics was intimately tied to the development of intense electromagnetic radiation, which began with the first demonstration of the *laser*[1], which stands for light amplification by stimulated emission of radiation. The laser produces a coherent state of visible light, where all waves are of the same wavelength and entirely in phase. This was achieved using a solid-state synthetic ruby crystal [Maiman, 1960][2].

This achievement was rapidly followed by the introduction of *Q-switching* [McClung and Hellwarth, 1962] and *mode-locking* [Hargrove et al., 1964; Mocker and Collins, 1965], two techniques that led to the generation of ultrashort laser pulses. Q-switching requires a variable attenuator inside the optical resonator. For a gain medium with population inversion, a decrease of attenuation rapidly generates a burst of electromagnetic energy, a laser *pulse* [McClung and Hellwarth, 1962]. In mode-locking [Hargrove et al., 1964; Mocker and Collins, 1965], an active or passive modulator modulates the transmission of the laser at some frequency. If the modulation frequency equals frequency spacing of the oscillator modes, these modes[3] become locked in phase, and an ultrashort laser pulse is produced. Following these developments, large-amplitude laser pulses stimulated rapid exploration

---

[1] For a review and historical overview of laser physics, we recommend [Saleh and Teich, 1991].

[2] The realization of a laser was preceded by the *maser* [Gordon et al., 1955], which is based on the same principle of stimulated emission of radiation, but operates in the microwave spectral range.

[3] Within the spectral bandwidth of the gain medium.

of nonlinear optics in the 1960s [Franken et al., 1961; Bass et al., 1962; Armstrong et al., 1962; Maker et al., 1964; Woodbury and Ng, 1962; Chiao et al., 1964b; Chiao et al., 1964a; Kaiser and Garrett, 1961; Voronov and Delone, 1966], such as generation of harmonics of the fundamental optical frequency [Franken et al., 1961].

These discoveries laid the groundwork for further advancements in laser technology and applications. Throughout the 1970s and 1980s, the push towards increasingly shorter laser pulses continued with the development of dye lasers and solid-state crystals. Today, amplifying media provide gain bandwidths that produce laser pulses as short as a few femtoseconds ($1\,\text{fs} = 10^{-15}\,\text{s}$) [Mocker and Collins, 1965], with the primary representative being a solid-state crystal of sapphire (Al_2O_3) doped with titanium ions (Ti^{3+}), referred to as *Ti:sapphire laser system*, which operates in the infrared range with a central wavelength of $\lambda = 0.8\,\mu\text{m}$. Ti:Sa laser systems typically produce laser pulses with a duration of ≈ 30 fs. In the 1990s, passive mode-locking saturable absorbers were refined [Shank et al., 1982], and the introduction of Kerr-lens mode-locking represented a significant breakthrough. Now, femtosecond laser pulses could have been produced without an additional saturable absorber in the resonant optical cavity [Spence et al., 1991].

Despite these advances, generating powerful femtosecond pulses proved challenging without inducing ionization damage to the amplifying medium. The damage threshold of amplifying media was overcome with the advent of chirped pulse amplification (CPA) in the 1980s [Strickland and Mourou, 1985], a technique that has since become foundational for high-power laser systems and was awarded the Nobel Prize in Physics 2018. CPA works around the damage threshold by stretching a short pulse in time to reduce its peak power before amplification and then compressing it back to its original duration after amplification. This enabled the amplification of laser pulses to unprecedented energies without damaging the amplifying medium [Strickland and Mourou, 1985; Maine and Mourou, 1988]. The introduction of optical chirped pulse amplification (OPCPA) [Dubietis et al., 1992], which combines CPA with optical parametric amplifiers [Giordmaine and Miller, 1965; Baumgartner and Byer, 1979], offered additional bandwidth increase and pushed the pulse durations below 10 fs. Currently, the state-of-the-art technique for ultrashort pulse generation is the nonlinear self-phase modulation in hollow-core fibers [Nisoli et al., 1996], which can produce few fs laser pulses, with a recent record of peak powers over 1 terawatt (TW) [Ouillé et al., 2020; Nagy et al., 2020]. This rapid development of laser technology led to the proliferation of high-power lasers worldwide[4].

Today, laser systems exceed the petawatt (PW) peak power threshold [Perry et al., 1999; Haefner et al., 2017; Zeng et al., 2017; Danson et al., 2019], with a current record of 10 PW peak power [Tanaka et al., 2020; Radier et al., 2022]. Global efforts towards making lasers even more powerful are continuing, with plans already in place to reach the 100 PW peak power in the future [Li et al., 2021]. Focusing a petawatt laser pulse into a diffraction-limited focal spot with a diameter of $\approx \lambda \approx 1\,\mu\text{m}$, we obtain focused intensity of $\approx 10^{23}\,\text{W/cm}^2$, which corresponds to the current experimental record of focused intensity [Yoon et al., 2021]. This is five orders of magnitude above what is known as the *threshold of relativistic optics*, an intensity threshold of $\approx 10^{18}\,\text{W/cm}^2$ [Mourou et al., 2006], beyond which electrons attain relativistic velocities. Indeed, relativistic laser-plasma interactions already become significant at the TW level [Bahk et al., 2004; Lazzarini et al., 2024] and have been studied since the advent of CPA [Gibbon, 2005]. Yet, pushing below the *femtosecond barrier* at the petawatt level proves a challenge using conventional technology of large-aperture solid-state optics.

A way towards the attosecond regime opened by pushing the nonlinear laser-matter interaction closer to the ionization threshold, where nonlinear polarization of atoms becomes

---

[4]For an up-to-date overview of petawatt laser systems worldwide, see [Danson et al., 2019].

dominant. Ionized noble gases enabled the generation of high harmonics of the fundamental laser frequency [Ferray et al., 1988], the presence of which dramatically increases the available bandwidth, with a current world record for the shortest pulse of coherent radiation being 43 as[5] [Gaumnitz et al., 2017]. This technique was awarded the Nobel Prize in Physics 2023 because it opened the way towards the study of attosecond physics[6], where the dynamic of individual electrons in atomic systems is studied. For example, the oscillation period of a hydrogen electron oscillating between the $1s$ and $2p$ energy levels is approximately 400 as. Yet, limitations remain. High-harmonic generation in gases requires laser intensities at or below the ionization threshold of the gas medium, which is approximately $\approx 10^{15} \, \mathrm{W/cm^2}$. Therefore, employing nonlinear effects for even shorter pulse generation requires laser interaction with the final frontier of the states of matter – plasma, an electrically quasineutral medium composed of light negatively-charged electrons and heavy positively-charged ionized atoms.

Today, nonlinear interactions in plasma continue to open the way toward even shorter and brighter radiation sources. In plasma, the nonlinear interaction occurs due to a fundamental limit on the oscillation velocity of electrons – the speed of light [Mourou et al., 2006]. The oscillation velocity of electrons must be smaller than this limit, leading to laser-driven nonlinear relativistic oscillations. The field of high-intensity laser physics is currently bursting with activity, with many different research directions leveraging the relativistic nonlinearity. Currently, the main research activities can be narrowed down to compact particle acceleration and generation of coherent and incoherent high-frequency[7] electromagnetic, both of which have numerous applications in medicine, industry, and fundamental science [Gibbon, 2005; Mourou et al., 2006; Corde et al., 2013; Albert and Thomas, 2016; Attwood and Sakdinawat, 2017; Rivas et al., 2017; Faure et al., 2019; Tanaka et al., 2020; Toth et al., 2020; Chaulagain et al., 2022].

1.2 Goals of the thesis and author's contributions

The goals of this doctoral thesis can be defined in two parts:

1. Produce a compendium of theory and literature relevant to the author's results and the field of relativistic optics.

2. Present the author's results and contributions in the field of relativistic optics, mainly in the form of peer-reviewed publications.

This doctoral thesis has been supervised by Jaroslav Nejdl, with additional guidance provided by Sergei Bulanov and Uddhab Chaulagain. The postgraduate studies occurred at the Faculty of Mathematics and Physics, Charles University, and the ELI Beamlines Facility, Extreme Light Infrastructure ERIC. The research projects I have worked on are extensively documented in publications by me and my co-authors. I have authored or co-authored 19 publications, including 7 in peer-reviewed journals, 1 pre-print, and 11 in conference proceedings. The central part of this doctoral thesis is based on the following four selected publications:

---

[5] $1 \, \mathrm{as} = 10^{-18}$ s. An attosecond is to a second as a second is to about 31.78 billion years. To give a sense of a scale, this is more than two times the current estimate for the age of our universe, which is approximately 13.78 billion years.

[6] For an overview of attosecond physics, see [Krausz and Ivanov, 2009].

[7] X-rays, extreme ultraviolet radiation, broadband attosecond pulses.

I. M. Lamač, K. Mima, J. Nejdl, U. Chaulagain, and S. V. Bulanov (2023). Anomalous relativistic emission from self-modulated plasma mirrors. *Physical Review Letters*, **131**(20), 205001

II. M. Lamač, P. Valenta, J. Nejdl, U. Chaulagain, T. M. Jeong and S. V. Bulanov (2024). Bright coherent attosecond X-ray pulses from beam-driven relativistic mirrors. *arXiv*, preprint arXiv:2403.03277. (submitted)

III. M. Lamač, U. Chaulagain, L. Jurkovičová, J. Nejdl, and S. V. Bulanov (2021). Two-color nonlinear resonances in betatron oscillations of laser-accelerated relativistic electrons. *Physical Review Research*, **3**(3), 033088.

IV. M. Lamač, U. Chaulagain, J. Nejdl and S. V. Bulanov (2023). Generation of intense magnetic wakes by relativistic laser pulses in plasma. *Scientific Reports*, **13**(1), 1701.

The results obtained have also been presented at several international conferences and workshops. The most important oral and poster contributions related to Refs. I. – IV. are mentioned in Chapter 3.

1.3   Outline of the thesis

The remainder of this doctoral thesis is organized as follows:

Chapter 2 fulfills the first goal of this doctoral thesis. It presents an overview of the theory of relativistic optics, where we discuss various topics relevant to the author's main research activities and results. Our approach is pedagogical and concise, intending to produce a compendium of theory that builds up the key concepts and provides a literature overview. Crucially, we do not aim for an exhaustive description of all consequences and applications. A significant body of literature is provided in each section to give the reader more details, contextual information, and references.

Chapter 3 fulfills the second goal of this doctoral thesis. It presents a brief commentary on the author's primary results, which are presented in the form of four selected publications in Appendix B. We also discuss the author's role and contributions.

Chapter 4 summarizes this doctoral thesis's content, highlights the author's key findings, and indicates potential avenues for future research.

Appendix A includes a comprehensive list of the author's publications up to the submission date of this doctoral thesis, encompassing those in peer-reviewed journals and conference proceedings, as well as pre-prints.

Appendix B features the four selected publications, Refs. I. – IV., reproduced in full with permission.

2

Theory of relativistic optics

This chapter serves as a theoretical primer for relativistic optics and the author's original results within the field. We begin by defining the relativistic regime of laser-matter interaction and outline basic equations and key parameters. Further, we show that the relevant physics naturally splits into two cases, and therefore, we provide each with its section. In the first case, denoted as relativistically underdense, the laser can propagate within the interacting medium. Here, we present key concepts related to the author's research, such as plasma wakefield acceleration, betatron X-ray generation, realization of relativistic mirrors, and generation of magnetic fields relevant to laboratory astrophysics. In the second case, the medium is relativistically overdense, and the laser is reflected upon interaction. The key concepts presented are high-harmonic generation and laser intensity amplification, both of which can arise from a relativistic oscillating mirror induced by the incident intense laser.

2.1   Interaction of electromagnetic field with matter

The microscopic Maxwell's equations give the evolution of classical electromagnetic field [Maxwell, 1865; Born and Wolf, 1959; Jackson, 1962; Zangwill, 2013]

$$\nabla \cdot \mathbf{E} = \frac{\rho}{\varepsilon_0}, \tag{1}$$

$$\nabla \cdot \mathbf{B} = 0, \tag{2}$$

$$\nabla \times \mathbf{E} = -\frac{\partial \mathbf{B}}{\partial t}, \tag{3}$$

$$\nabla \times \mathbf{B} = \mu_0 \mathbf{j} + \mu_0 \varepsilon_0 \frac{\partial \mathbf{E}}{\partial t}, \tag{4}$$

where ρ and $\mathbf{j}$ are the electric charge and current densities, which act as the sources of electromagnetic field, $\mathbf{E}$ is the electric field, and $\mathbf{B}$ is the magnetic field, ε_0 is the vacuum permittivity, and μ_0 is the vacuum permeability. By combining Maxwell's equations, we may find that electromagnetic fields satisfy the wave equation, with phase velocity given by the speed of light in vacuum c, i.e., without charges and currents, which is defined as $\mu_0 \epsilon_0 c^2 = 1$.

Due to the linearity of Maxwell's equations, any electromagnetic field can be described as a superposition of propagating electromagnetic waves [Born and Wolf, 1959; Jackson, 1962; Zangwill, 2013].

Taking the curl of Ampere's law (4), with the use of Gauss' law (1), we obtain the continuity equation

$$\frac{\partial \rho}{\partial t} + \nabla \cdot \mathbf{j} = 0, \tag{5}$$

which is a microscopic formulation of charge conservation. In macroscopic terms, the total charge is always conserved, and any change in total charge in a given volume is always equal to the net current going through the boundary of that volume.

An equivalent formulation of the Maxwell's equations can be given in terms of the electromagnetic potentials, which are defined to satisfy

$$\mathbf{E} = -\frac{\partial \mathbf{A}}{\partial t} - \nabla \phi, \tag{6}$$

$$\mathbf{B} = \nabla \times \mathbf{A}, \tag{7}$$

where $\mathbf{A}$ is the magnetic vector potential and ϕ is the electric scalar potential. The electromagnetic potentials are not unique. The electromagnetic fields are invariant to the following gauge transformation: $\mathbf{A} = \mathbf{A}' + \nabla f$ and $\phi = \phi' - \frac{\partial f}{\partial t}$, where f is any differentiable scalar function. As we will illustrate in this chapter, the fact that the scalar function f can be chosen arbitrarily often allows us to simplify our calculations significantly.

The change of electromagnetic fields due to charge and current distributions is described by Maxwell equations (1) – (4). In turn, the charge distribution must react to changes in electromagnetic fields. The change in momentum $\mathbf{p}$ of a particle with mass m and charge q is given by the Lorentz force, written as

$$\frac{\mathrm{d}\mathbf{p}}{\mathrm{d}t} = q\left(\mathbf{E} + \mathbf{v} \times \mathbf{B}\right), \tag{8}$$

where $\mathbf{v}$ is the particle velocity. Multiplying Eq. (8) by $\mathbf{v}$, we get the power acting on the charged particle

$$\frac{\mathrm{d}\left(\gamma m c^2\right)}{\mathrm{d}t} = q\mathbf{v} \cdot \mathbf{E}, \tag{9}$$

where $\gamma = 1/\sqrt{1 - (\mathbf{v}/c)^2}$ is the Lorentz factor of the charged particle.

To understand the onset of relativistic effects in light-matter interaction, let us first focus on the lightest component of matter, the electron. The electron has $q = -e$ and $m = m_e$, where e is the elementary charge and m_e is the electron mass. The following exposition is an adaptation from [Gibbon, 2005], where additional information can be found. Using $\mathbf{v} \times (\nabla \times \mathbf{A}) = \nabla(\mathbf{v} \cdot \mathbf{A}) - (\mathbf{v} \cdot \nabla)\mathbf{A}$, where we note that the gradient only acts on the field since coordinates and particle velocity are independent variables, Eqs. (8) – (9) can be rewritten in terms of the electromagnetic potentials as

$$\frac{\mathrm{d}}{\mathrm{d}t}\left(\mathbf{p} - e\mathbf{A}\right) = e\nabla\left(\phi - \mathbf{v} \cdot \mathbf{A}\right), \tag{10}$$

$$\frac{\mathrm{d}}{\mathrm{d}t}\left(\gamma - 1\right)m_e c^2 = e\mathbf{v} \cdot \left(\nabla\phi + \frac{\partial \mathbf{A}}{\partial t}\right). \tag{11}$$

Let us now consider that the electron interacts with an electromagnetic plane wave with

elliptical polarization propagating in the x-direction in vacuum ($\phi = 0$); the vector potential is then given as

$$\mathbf{A} = A_0 \left(0, \delta \cos \varphi, \sqrt{1 - \delta^2} \sin \varphi \right), \tag{12}$$

where $\varphi = \omega t - kx$ is the phase of the wave, ω is the angular frequency, k is the wave number, A_0 is the amplitude of the vector potential and δ is the polarization parameter, where $\delta \in \{\pm 1, 0\}$ for a linear polarization and $\delta = \pm 1/\sqrt{2}$ for right-handed and left-handed circular polarization, respectively. To further simplify the analysis, we introduce the following normalizations,

$$\mathbf{a} = \frac{e\mathbf{A}}{m_e c}, \quad \mathbf{p} \to \frac{\mathbf{p}}{m_e c}, \quad \phi \to \frac{e\phi}{m_e c^2}, \quad \boldsymbol{\beta} = \frac{\mathbf{v}}{c}, \quad t \to \omega t, \quad x \to kx, \tag{13}$$

which is equivalent to a system of normalized units where $\omega = k = c = e = m_e = 1$. Eqs. (10) – (11) can be then written in normalized units as

$$\frac{\mathrm{d}\left(\mathbf{p}_\perp - \mathbf{a}\right)}{\mathrm{d}t} = 0, \tag{14}$$

$$\frac{\mathrm{d}\left(p_x - \gamma\right)}{\mathrm{d}t} = -\boldsymbol{\beta} \cdot \left(\frac{\partial \mathbf{a}}{\partial t} + \frac{\partial \mathbf{a}}{\partial x}\right) = 0, \tag{15}$$

where the second equation is identically zero since the electromagnetic wave given by Eq. (12) depends only on the phase, $\varphi = t - x$, and therefore $\partial_t \mathbf{a} = -\partial_x \mathbf{a}$. Integrating Eqs. (14) – (15), we get two constants of motion, a longitudinal constant $\gamma - p_x = \alpha$ and a transverse constant $\mathbf{p}_\perp - \mathbf{a} = \boldsymbol{\kappa}$, which are given by the initial conditions. Using the energy-momentum relation $\gamma^2 = 1 + |\mathbf{p}|^2$, we can write the momentum components as

$$\mathbf{p}_\perp = \mathbf{a} + \boldsymbol{\kappa}, \tag{16}$$

$$p_x = \frac{1 + |\mathbf{p}_\perp|^2 - \alpha^2}{2\alpha}, \tag{17}$$

which is a general Lorentz-covariant (choice of constants is frame-dependent) solution for the motion of free electrons in an electromagnetic wave. Taking the time derivative of the phase[1] corresponding to the longitudinal position of the particle, we get the following relationship between the phase φ and the longitudinal constant of motion α [Gibbon, 2005],

$$\frac{\mathrm{d}\varphi}{\mathrm{d}t} = \frac{\partial \varphi}{\partial t} + \frac{p_x}{\gamma} \frac{\partial \varphi}{\partial x} = 1 - \frac{p_x}{\gamma} = \frac{\alpha}{\gamma}. \tag{18}$$

Thus, $\gamma = p_x + \alpha$. We also have

$$\mathbf{p} = \gamma \frac{\mathrm{d}\mathbf{r}}{\mathrm{d}t} = \gamma \frac{\mathrm{d}\varphi}{\mathrm{d}t} \frac{\mathrm{d}\mathbf{r}}{\mathrm{d}\varphi} = \alpha \frac{\mathrm{d}\mathbf{r}}{\mathrm{d}\varphi}. \tag{19}$$

Let us now consider the special case of an electron initially at rest, then we have

---

[1]We use the chain rule, $\dot{\varphi}(x(t), t) = \partial_t \varphi + v_x \partial_x \varphi = \partial_t \varphi + (p_x/\gamma)\partial_x \varphi$.

$\boldsymbol{\kappa} = \mathbf{p}_{\perp 0} = \mathbf{0}$, $\alpha = \gamma_0 - p_{x0} = 1$, and Eqs. (16) – (17) become

$$\mathbf{p}_\perp = \mathbf{a}, \tag{20}$$

$$p_x = \frac{|\mathbf{a}|^2}{2}. \tag{21}$$

Eqs. (20) – (21) show that magnitude of normalized vector potential $|\mathbf{a}| = e|\mathbf{A}|/(m_e c)$ serves as a key parameter which identifies non-relativistic and relativistic regime of interaction. For $|\mathbf{a}| \ll 1$, the electrons oscillate purely in the polarization direction of the electric field vector, and their momentum is non-relativistic, $|\mathbf{p}_\perp| = |\mathbf{a}| \ll 1$. For $|\mathbf{a}| \geqslant 1$, the oscillations become relativistic, e.g., for $|\mathbf{a}| = 1$ we have $|\mathbf{p}_\perp| = m_e c$ and the electron velocity approaches the speed of light in vacuum, $|\mathbf{v}_\perp|/c = 1/\sqrt{2} \approx 71\%$. The nonlinear longitudinal oscillations also become dominant for $|\mathbf{a}| \gg 1$, and the electron has significant longitudinal momentum.

For an electromagnetic wave propagating in vacuum, the critical parameter becomes the peak amplitude of the normalized vector potential, $a_0 = eA_0/(m_e c)$, where $A_0 = E_0/\omega$ is the peak amplitude of the vector potential, E_0 is the peak amplitude of the oscillating electric field and ω is the angular frequency of the wave. It is helpful to express this parameter in terms of the radiation intensity I_0 and wavelength λ_0[2]:

$$a_0 = \frac{eE_0}{m_e \omega_0 c} = 0.85 \left(I_0 \left[10^{18} \, \frac{\mathrm{W}}{\mathrm{cm}^2} \right] \lambda_0^2 \, [\mu\mathrm{m}] \right)^{1/2}. \tag{22}$$

Table 1 presents the intensity required to reach $a_0 = 1$ for typical coherent light sources. Eq. (22) makes it clear that longer wavelength sources are preferred for the study of relativistic interactions since the required intensity is orders of magnitude smaller in comparison to short wavelength radiation sources, such as the high harmonics from noble gases or free electron laser, as presented in the table.

Laser system	λ_0	$I_0 \left[10^{18} \, \mathrm{W/cm}^2 \right]$
Nd:Glass	1 μm	1.4
Ti:Sapphire	800 nm	2.2
KrF	248 nm	23
59th harmonic of Ti:Sa from neon gas	13.5 nm	10^4
Free electron laser	0.1 nm	1.5×10^8

Table 1: Intensity required to enter regime of relativistic optics ($a_0 = 1$) for various laser systems.

The global proliferation of Ti:Sapphire high-powered laser systems establishes them as the premier instruments in relativistic optics [Perry et al., 1999; Mourou et al., 2006; Danson et al., 2019; Tanaka et al., 2020; Li et al., 2021; Radier et al., 2022]. Therefore, in the following sections, we consider that the laser operates within the wavelength range $\lambda_0 = 0.8 - 1$ μm unless stated otherwise. The intensity corresponding to $I_{rel} \approx 10^{18}$ W/cm^2 is therefore often referred to as the threshold of relativistic optics [Mourou et al., 2006]. To create a reference point, let us consider an electron bound to an atom at a distance of Bohr radius, $r_a = \hbar^2/(m_e e^2) = 53$ pm, where $\hbar$ is the reduced Planck constant. The electric field

---

[2]We consider the linear polarization.
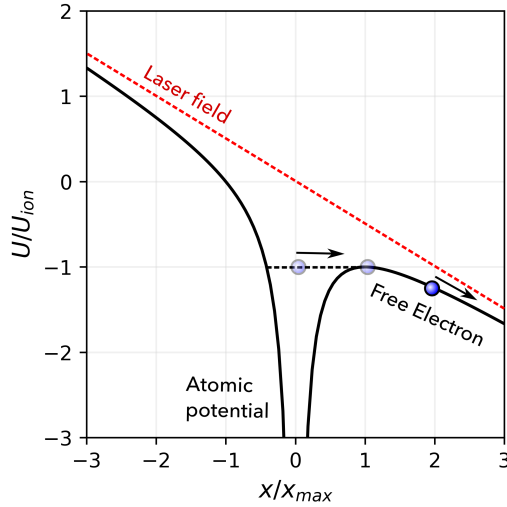
Figure 1: The Coulombic potential in the presence of a laser field with intensity given by Eq. (27).

acting on the bound electron is then [Gibbon, 2005]

$$E_a = \frac{e}{4\pi\epsilon_0} \frac{1}{r_a^2} \approx 5.1 \times 10^9 \ \frac{\text{V}}{\text{m}}, \tag{23}$$

which corresponds to *atomic intensity* of

$$I_a = \frac{\epsilon_0 c E_a^2}{2} \approx 3.5 \times 10^{16} \ \frac{\text{W}}{\text{cm}^2}. \tag{24}$$

Since $I_{rel} \gg I_a$, we have good reasons to believe that any target of a relativistic laser pulse becomes ionized swiftly, and the radiation interacts with ionized matter – plasma. In the next section, we briefly describe this ionization process and show that the ionization intensity threshold can be even much smaller than the atomic estimate given by Eq. (24).

2.1.1 Interaction with a single atom

Let us consider an electron bound in the Coulombic potential interacting with a low-frequency incident laser, such as the relativistically interesting Ti:Sapphire laser system mentioned before. Specifically, we assume that the laser photon energy is much smaller than the electron's binding energy. Then, we may approximate such a laser with a constant electric field with strength E_0[3] [Bethe and Salpeter, 1957]

$$U(x) = -\frac{Ze^2}{4\pi\epsilon_0} \frac{1}{|x|} - eE_0 x. \tag{25}$$

Local maximum can be found at $x_{\max} = \sqrt{Ze/(4\pi\epsilon_0 E_0)}$. If the potential energy at the local maximum equals the ionization energy, $U(x_{\max}) = U_{ion}$, the Coulombic barrier is suppressed,

---

[3]This is reasonable since $\lambda_0 \gg r_a$. Therefore, we have $E_0 \cos(\omega t - kx) \approx E_0$ for $x \ll \lambda_0$ and times much smaller than the laser period, $t \ll c/\lambda_0$.

and the electron will escape into the vacuum, as shown, in Fig. 1. The critical electric field required to free the electron is given from this condition as

$$E_c = \frac{\pi \epsilon_0 U_{ion}^2}{Ze^3}, \tag{26}$$

giving us the *threshold intensity* required to release electrons from ions with charge number Z, assuming linear polarization, as

$$I_{th} = \frac{\epsilon_0 c E_c^2}{2} \approx 4 \times 10^9 \frac{U_{ion}^4[\text{eV}]}{Z^2} \frac{\text{W}}{\text{cm}^2}. \tag{27}$$

For ground state hydrogen ($Z = 1$), the ionization energy is given using the fine-structure constant $\alpha = e^2/(4\pi\epsilon_0 \hbar c) \approx 1/137$ as $U_{ion} = \alpha/(4\pi r_a) = 1\,\text{Ry} = 13.6\,\text{eV}$, and the critical electric field is $E_c \approx E_a/16$, which gives $I_{th} \approx 1.4 \times 10^{14}\,\text{W/cm}^2$. Eq. (27) describes the threshold intensity required for *barrier suppression ionization*, which holds remarkably well for many electron atoms interacting with intense short laser pulses. Other ionization processes relevant at lower intensities, such as multiphoton or tunneling ionization [Keldysh, 1965; Perelomov et al., 1966], can bring the appearance threshold even below that of Eq. (27). Thus, our focus is reduced to the interaction of electromagnetic fields with electrons and ions in the following sections.

2.1.2 Interaction with a single electron

Now, we understand that relativistic lasers immediately ionize their target. So, we gain additional motivation to study the interaction of electromagnetic waves with electrons in more detail (See also [Landau and Lifshitz, 1962; Gibbon, 2005] and references therein for more information). Let us, therefore, return to Eqs. (20) – (21), where we consider the interaction of a free electron with an elliptically-polarized electromagnetic wave in the laboratory reference frame.

Laboratory frame

Using the definition of laser field given by Eq. (12), we can write Eqs. (20) – (21) explicitly in terms of the wave phase φ:

$$p_x = \frac{a_0^2}{4} \left[1 + \left(2\delta^2 - 1 \right) \cos 2\varphi \right], \tag{28}$$

$$p_y = a_0 \delta \cos \varphi, \tag{29}$$

$$p_z = a_0 \sqrt{1 - \delta^2} \sin \varphi. \tag{30}$$

Averaging the momentum components in time over the wave period, we find that the electrons drift along the x-direction for any polarization, with drift momentum $\bar{p}_x = \frac{1}{2\pi} \int_0^{2\pi} p_x \mathrm{d}\varphi = a_0^2/4$, where the overscore denotes averaging over the wave period. We know from Eq. (18) that $\gamma(t) = \alpha + p_x(t)$. For a free electron in vacuum initially at rest, $\alpha = 1$, we may average its Lorentz factor to obtain

$$\bar{\gamma} = 1 + \bar{p}_x = 1 + \frac{a_0^2}{4}. \tag{31}$$
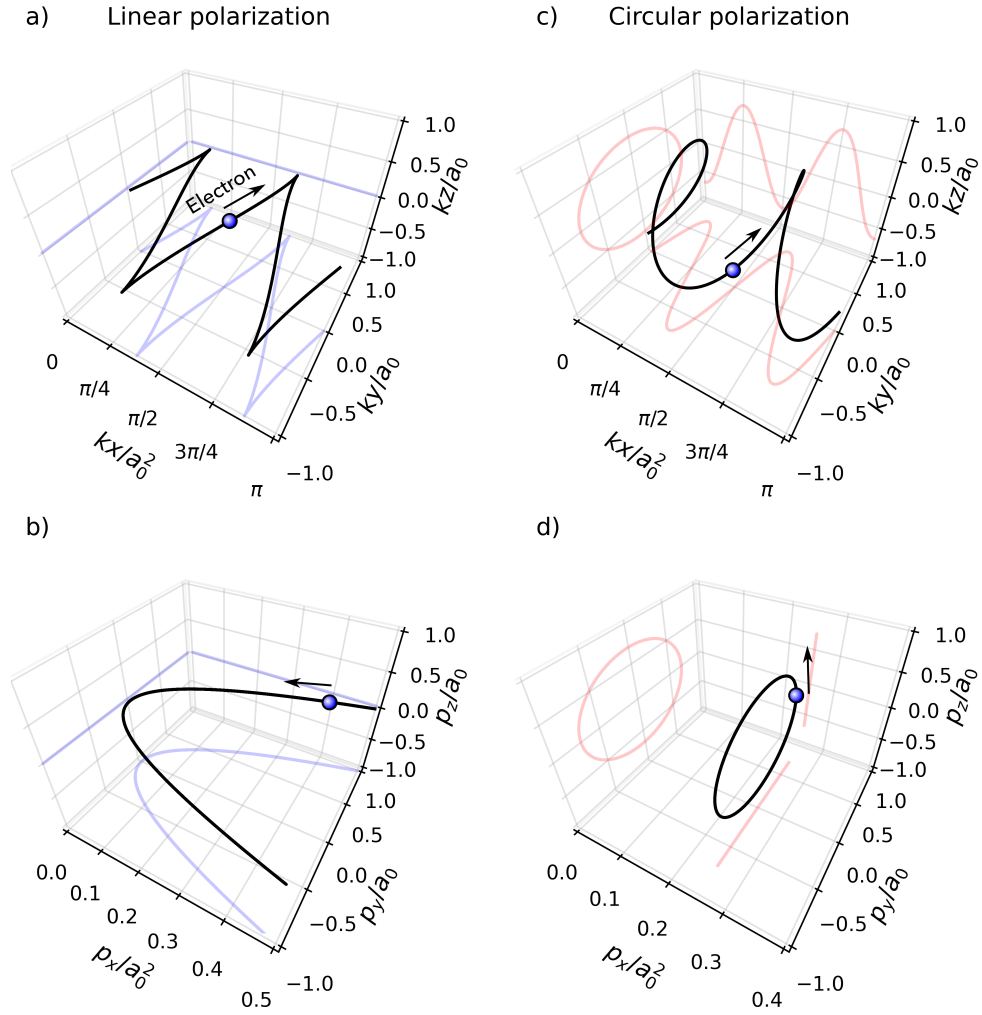
Figure 2: Trajectory of an electron (which was initially at rest) in the field of an electromagnetic wave with linear (a) and circular (c) polarization. Trajectory of the electron in the momentum space for linear (b) and circular (d) polarization.

We note that Eq. (31) is exact for circular polarization, i.e. without averaging, $\gamma_{CP,free} = 1 + (a_0/2)^2$. We can also express the electron drift velocity,

$$\beta_d = \bar{\beta}_x = \frac{\bar{p}_x}{\bar{\gamma}} = \frac{a_0^2}{4 + a_0^2}. \tag{32}$$

The electron orbits can be obtained using Eq. (19) for arbitrary polarization δ by direct integration of Eqs. (28) – (30) over phase as (retrieving the dimensional electron coordinates

as $\omega t \rightarrow t$ and $kx \rightarrow x$)

$$kx = \frac{a_0^2}{4}\left[\varphi + \left(\delta^2 - \frac{1}{2}\right)\sin 2\varphi\right], \tag{33}$$

$$ky = a_0\delta\sin\varphi, \tag{34}$$

$$kz = -a_0\sqrt{1-\delta^2}\cos\varphi. \tag{35}$$

The electron trajectories, described by the set of variables $\{kx/a_0^2, ky/a_0, kz/a_0\}$, are self-similar, as shown in Fig. 2. We see that in the longitudinal x-direction, the electron drifts with velocity β_d. Additionally, for $\delta \neq \pm 1/\sqrt{2}$, the electron trajectory exhibits longitudinal oscillations with periodicity of twice the fundamental wave frequency. For circular polarization ($\delta = \pm 1/\sqrt{2}$), the longitudinal oscillations disappear, and the electron drifts with velocity β_d since the longitudinal momentum is constant $p_x = a_0^2/4$. The electromagnetic wave also imparts angular momentum to the electron. Using the trajectory and momentum components obtained above, we can calculate the component of electron angular momentum along the drift direction as

$$L_x = (\mathbf{r} \times \mathbf{p})_x = \frac{a_0^2}{k}\delta\sqrt{1-\delta^2}. \tag{36}$$

Note that for linear polarization ($\delta \in \{0, \pm 1\}$), the electron gains no angular momentum in the x-direction. Conversely, the angular momentum is maximized for circular polarization ($\delta = \pm 1/\sqrt{2}$). Furthermore, we note that apart from acceleration, the nonlinear dependence of longitudinal momentum on field strength, given by Eq. (17), tells us that the laser field can also serve as a spectrometer of laser-accelerated electrons. To show this, we again consider the longitudinal constant of motion for electrons initially at rest with Eq. (17), i.e., $p_x = \gamma - 1 = p_\perp^2/2$. Therefore, the maximum angle at which the electrons can be emitted from the laser focus must be given simply by the maximum ratio of the transverse and longitudinal momentum components,

$$\tan\theta = \frac{p_\perp}{p_x} = \sqrt{\frac{2}{\gamma - 1}} = \frac{\sqrt{8}}{a_0}, \tag{37}$$

where the last equality is valid exactly for circular polarization, corresponding to the pitch angle of the helical trajectory shown in Fig. 2c, and on average for the trajectory due to linear polarization shown in Fig. 2a, where it corresponds to the ratio of transverse momentum amplitude to the averaged longitudinal momentum. Eq. (37) shows that the electron angular distribution is related to the electron energy spectrum, which can be utilized for simple spectrometry of laser-accelerated electrons [Moore et al., 1995; Meyerhofer, 1997; Malka et al., 1997].

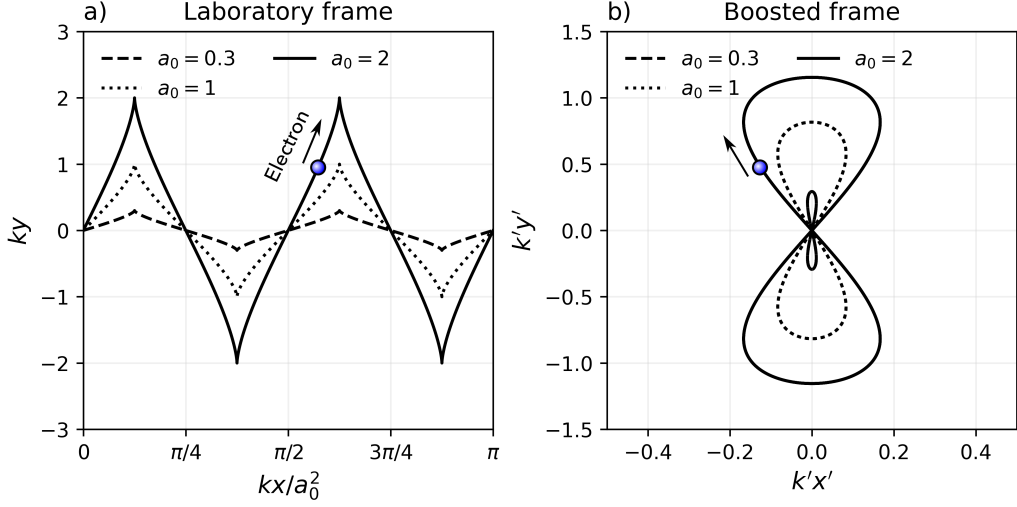**Boosted frame**

To further analyze the laser-driven electron orbits, we perform a Lorentz transformation into the drift reference frame moving with velocity given β_d by Eq. (32). Here, the transformed momentum components are given as follows

$$p'_x = \gamma_d(p_x - \beta_d\gamma_e) = p_x - p_d, \tag{38}$$

$$p'_y = p_y, \tag{39}$$

$$p'_z = p_z, \tag{40}$$

Figure 3: Electron trajectories in the field of an electromagnetic wave with linear polarization in the laboratory frame (a) where the electron is initially at rest and in the boosted frame (b) moving with drift velocity (32).

where we have used the first constant of motion, $\gamma_e - p_x = 1$. Since the phase is Lorentz-invariant, $\varphi' = \omega't' - k'x' = \omega t - kx = \varphi$, the momentum components can be directly written in the boosted frame as

$$p'_x = \frac{a_0^2}{4}\left(2\delta^2 - 1\right)\cos 2\varphi', \tag{41}$$

$$p'_y = a_0\delta\cos\varphi', \tag{42}$$

$$p'_z = a_0\sqrt{1 - \delta^2}\sin\varphi'. \tag{43}$$

The averaged momentum in the boosted frame is zero, $\bar{p}'_x = 0$. Therefore we can obtain the longitudinal constant of motion α' by averaging over Eq. (17) in the boosted frame, $\alpha' = \sqrt{1 + |\bar{\mathbf{a}}|^2} = \sqrt{1 + (a_0^2/2)} = \bar{\gamma}'$. Therefore, the longitudinal constant equals the electron *quiver energy* in the boosted frame, $\alpha' = \bar{\gamma}'$. Note that this Lorentz factor is exact for circular polarization, $\bar{\gamma}' = \gamma'$, since no longitudinal oscillations are present. After integrating Eqs. (41) – (43), we get

$$k'x' = \frac{a_0^2}{4\bar{\gamma}'}\left(\delta^2 - \frac{1}{2}\right)\sin 2\varphi', \tag{44}$$

$$k'y' = \frac{a_0}{\bar{\gamma}'}\delta\sin\varphi', \tag{45}$$

$$k'z' = -\frac{a_0}{\bar{\gamma}'}\sqrt{1 - \delta^2}\cos\varphi', \tag{46}$$

the frequency and wave number in the boosted frame are given as $\omega' = ck' = \omega/\gamma'$, where ω is the angular frequency in the laboratory frame.

Let us focus on linear polarization ($\delta = 1$). The electron orbit in the boosted frame can

15

be written in the following implicit form

$$16(k'x')^2 = (k'y')^2 \left[\left(\frac{a_0}{\bar{\gamma}'} \right)^2 - (k'y')^2 \right], \tag{47}$$

which is the famous *lemniscate of Gerono*, also known as *figure-eight curve*, which is a special case of a *Lissajous curve*. The lemniscate is drawn in Fig. 3b, where the second harmonic content of the longitudinal oscillations is visualized.

The Maxwell equations also state that an oscillating relativistic electron must generate its electromagnetic field. As we will show in the next section, the radiation of periodically oscillating electrons is composed of harmonics of the fundamental oscillating frequency.

2.2   Radiation from relativistic electrons

To describe radiation emitted from relativistic electrons, we begin by rewriting Eqs. (1) and (4) in terms of the potentials given by Eqs. (6)–(7), which yields[4] [Jackson, 1962; Born and Wolf, 1959; Zangwill, 2013]

$$\nabla \cdot \left(\nabla \phi + \frac{\partial \mathbf{A}}{\partial t} \right) = -\frac{\rho}{\varepsilon_0}, \tag{48}$$

$$\left(\Delta \mathbf{A} - \frac{1}{c^2} \frac{\partial^2 \mathbf{A}}{\partial t^2} \right) - \nabla \left(\nabla \cdot \mathbf{A} + \frac{1}{c^2} \frac{\partial \phi}{\partial t} \right) = -\mu_0 \mathbf{j}. \tag{49}$$

Let us now apply the *Lorenz gauge*, which amounts to the requirement that $\nabla \cdot \mathbf{A} + \partial_t \phi / c^2 = 0$. This is equivalent to a choice of a scalar function f, within a gauge transformation, which satisfies $\Delta f - \partial_t^2 f / c^2 = -\nabla \cdot \mathbf{A}' - \partial_t \phi' / c^2$, where $\mathbf{A}'$ and ϕ' are the potentials prior to the gauge transformation. Using the Lorenz gauge, the potential formulation of Maxwell equations reduces to inhomogeneous wave equations

$$\Delta \phi - \frac{1}{c^2} \frac{\partial^2 \phi}{\partial t^2} = -\frac{\rho}{\varepsilon_0}, \tag{50}$$

$$\Delta \mathbf{A} - \frac{1}{c^2} \frac{\partial^2 \mathbf{A}}{\partial t^2} = -\mu_0 \mathbf{j}, \tag{51}$$

and the particular solutions are obtained by a convolution of the source terms on the right-hand side with the *fundamental solution for the wave equation*, $F(\mathbf{r}, t) = \delta(t - |\mathbf{r}|/c)/(4\pi|\mathbf{r}|)$ [Riley et al., 2006]. Performing the convolution in time and space, we get

$$\phi(\mathbf{r}, t) = \frac{1}{4\pi\epsilon_0} \int \frac{\rho(\mathbf{r}', t - R/c)}{R} \mathrm{d}^3 \mathbf{r}', \tag{52}$$

$$\mathbf{A}(\mathbf{r}, t) = \frac{\mu_0}{4\pi} \int \frac{\mathbf{j}(\mathbf{r}', t - R/c)}{R} \mathrm{d}^3 \mathbf{r}', \tag{53}$$

where $R = |\mathbf{R}| = |\mathbf{r} - \mathbf{r}'|$ is the distance from the position of the charge distribution $\mathbf{r}'$ to the field observation point $\mathbf{r}$, where the potentials are evaluated. We see that the charge and current distributions are now evaluated in terms of the *retarded time*, $t - R/c$, which corresponds to the emission time of radiation originating at position $\mathbf{r}'$ and arriving at

---

[4]Using the definition of potentials given by Eqs. (6)–(7), and the vector identities $\nabla \cdot (\nabla \times \mathbf{A}) = 0$ and $\nabla \times (\nabla \phi) = 0$, it is easy to verify that the remaining two Maxwell equations are satisfied identically.
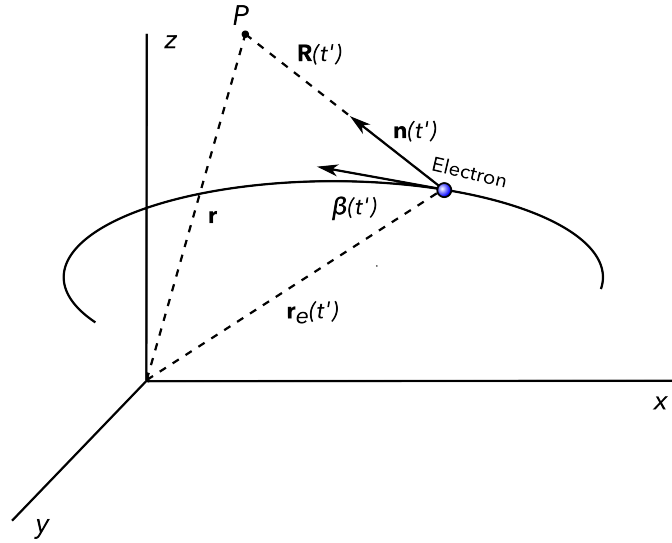
Figure 4: Trajectory of an electron and illustration of the vectors defining the Lienard-Wiechert potentials (54) – (55) and the corresponding electromagnetic field (56) – (57).

position $\mathbf{r}$ at time t. This is clear from the fact that the time radiation takes to propagate between $\mathbf{r}'$ and $\mathbf{r}$ is simply R/c.

We may also add the solution to the homogeneous wave equation, which is determined by initial conditions. For example, the homogeneous solution must represent the fields responsible for the motion of the charge distribution, which in turn produces current and electromagnetic field described by the solutions (50) – (51), which radiates away in the direction of increasing distance R. The real electric and magnetic fields can then be obtained by differentiation according to the definition (6) – (7).

Electromagnetic field due to a single particle with charge q propagating with arbitrary trajectory $\mathbf{r}_e(t)$ can be obtained by integrating Eqs. (52) – (53) with the charge and current distribution given as $\rho(\mathbf{r}, t) = q\delta[\mathbf{r} - \mathbf{r}_e(t)]$ and $\mathbf{j}(\mathbf{r}, t) = qc\boldsymbol{\beta}\delta[\mathbf{r} - \mathbf{r}_e(t)]$, where $\delta(x)$ is the Dirac delta function. Integrating over the delta function yields the *Lienard-Wiechert potentials* (we retrieve the SI units, see, e.g., [Jackson, 1962; Lamač, 2023] for integration details[5].)

$$\phi(\mathbf{r}, t) = \frac{q}{4\pi\epsilon_0}\left[\frac{1}{(1 - \boldsymbol{\beta}\cdot\mathbf{n})R}\right]_{ret.} \tag{54}$$

$$\mathbf{A}(\mathbf{r}, t) = \frac{q}{4\pi\epsilon_0}\left[\frac{\boldsymbol{\beta}}{(1 - \boldsymbol{\beta}\cdot\mathbf{n})R}\right]_{ret.}, \tag{55}$$

where $R = |\mathbf{R}(t)| = |\mathbf{r} - \mathbf{r}_e(t)|$ is the distance vector between the field observation point P situated at $\mathbf{r}$ and the position of the charged particle at $\mathbf{r}_e(t)$ at time t, $\mathbf{n} = \mathbf{R}/R$ is the direction pointing from the particle towards the observation point P. The square brackets $[\cdot]_{ret.}$ indicate that all quantities inside the bracket are evaluated at the retarded time $t' = t - |\mathbf{r} - \mathbf{r}_e(t')|/c$. We reiterate that the retarded time has the following interpretation: it

---

[5]The only challenging part about the integration is correct change of variables. It is useful to note the following identity, $\int f(t')\delta[t - g(t')]dt' = \int f[t'(g)]\delta(t - g)(dt'/dg)dg = \int(f[t'(g)]/\dot{g}[t'(g)])\delta(t - g)dg = f[t'(t)]/\dot{g}[t'(t)]$

is the time at which radiation observed at position $\mathbf{r}$ and *observer time* t begins to propagate towards observation point P from the position of the particle $\mathbf{r}_e(t')$ at retarded time t' (see Fig. 4). Once again, the time taken by light to propagate between $\mathbf{r}$ and $\mathbf{r}_e(t')$ is simply $|\mathbf{r} - \mathbf{r}_e(t')|/c$. Therefore, subtracting it from the observer time t gives us the time of radiation emission, the retarded time $t' = t - R(t')/c$.

The electromagnetic field can be obtained from Lienard-Wiechert potentials using the defining relations given by Eqs. (6) – (7) as

$$\mathbf{E}(\mathbf{r},t) = \mathbf{E}_{near} + \mathbf{E}_{far} = \frac{q}{4\pi\epsilon_0}\left[\frac{\mathbf{n}-\boldsymbol{\beta}}{\gamma^2\kappa^3R^2}\right]_{ret.} + \frac{q}{4\pi\epsilon_0 c}\left[\frac{\mathbf{n}}{\kappa^3 R}\times[(\mathbf{n}-\boldsymbol{\beta})\times\dot{\boldsymbol{\beta}}]\right]_{ret.}, \quad (56)$$

$$\mathbf{B}(\mathbf{r},t) = \frac{\mathbf{n}(t')\times\mathbf{E}(\mathbf{r},t)}{c}, \tag{57}$$

where $\kappa = \frac{\mathrm{d}t}{\mathrm{d}t'} = \frac{\mathrm{d}}{\mathrm{d}t'}\left[t' + |\mathbf{r} - \mathbf{r}_e(t')|/c\right] = 1 - \mathbf{R}\cdot\boldsymbol{\beta}/R = 1 - \mathbf{n}\cdot\boldsymbol{\beta} = 1 - \beta\cos\theta$ is the derivative of observer time t with respect to retarded time t' and θ is the angle between $\boldsymbol{\beta}$ and $\mathbf{n}$. We note that for observers close to the axis of ultra-relativistic motion, it can be approximated as $\kappa \approx \left[1 + (\gamma\theta)^2\right]/(2\gamma^2)$. The electromagnetic field is split into two parts: the *near-field*, which is due to velocity $\boldsymbol{\beta}$, and the *far-field*, which depends on acceleration $\dot{\boldsymbol{\beta}}$. The near-field is static and drops off with distance as $1/R^2$, whereas the far field is responsible for the radiation since it drops off with distance as $\sim 1/R$. Therefore, the far-field term will dominate the near-field term far from the charged particle. Note that for a static charge ($\boldsymbol{\beta} = \dot{\boldsymbol{\beta}} = 0$), we recover Coulomb's law. To give another example, an electron that is in uniform motion along the x axis ($\dot{\boldsymbol{\beta}} = 0$) has the following electric near-field

$$\mathbf{E}_{near}(\mathbf{r},t) = \frac{q}{4\pi\epsilon_0}\frac{\mathbf{R}}{\gamma^2\left[(z^2+y^2)/\gamma^2 + (x-vt)^2\right]^{3/2}}, \tag{58}$$

where $\mathbf{R} = (x-vt, y, z)$. The magnetic near field follows as $\mathbf{B}_{near} = (\mathbf{v}\times\mathbf{E}_{near})/c^2$. Eq. (58) is the relativistic version of Coulomb's law. It shows that the on-axis ($z = y = 0$) near field drops off with velocity as $E_x \sim 1/(R\gamma)^2$, while in the transverse plane ($x = vt$), within a narrow cone of angular width $\theta \sim 1/\gamma$, the field grows as $E_{y,z} \sim \gamma/R^2$. This is schematically illustrated in Fig. 5. In the ultra-relativistic limit $\beta \to 1$, the field lines assume an infinitely thin "pancake" shape, and the electromagnetic field is purely transversal to the direction of motion.

Since we are primarily interested in radiation emitted by relativistic particles, we adopt the far-field approximation $R \gg 1$. For a single electron, this allows us to estimate the electric field as $\mathbf{E} \approx \mathbf{E}_{far}$. Then, the general solution given by Eq. (53) can also be simplified. Choosing the origin anywhere near the current distribution, the distance between the far away observation position $\mathbf{r}$ and the position within the radiating charge distribution $\mathbf{r}'$ can be approximated as $R = |\mathbf{r} - \mathbf{r}'| \approx r - \mathbf{r}'\cdot\mathbf{n}$, where $r = |\mathbf{r}| \gg \mathbf{r}'$. Substituting into Eq. (53), we get

$$\mathbf{A}(\mathbf{r},t) = \frac{\mu_0}{4\pi r}\int\mathbf{j}\left(\mathbf{r}', t - \frac{r - \mathbf{r}'\cdot\mathbf{n}}{c}\right)\mathrm{d}^3\mathbf{r}', \tag{59}$$

where we have approximated the denominator as $R \approx r$. However, such approximation is not generally possible in the retarded time $t' \approx t - r/c - \mathbf{r}'\cdot\mathbf{n}/c$, since we do not know how fast the current changes during the time $\mathbf{r}'\cdot\mathbf{n}/c$.
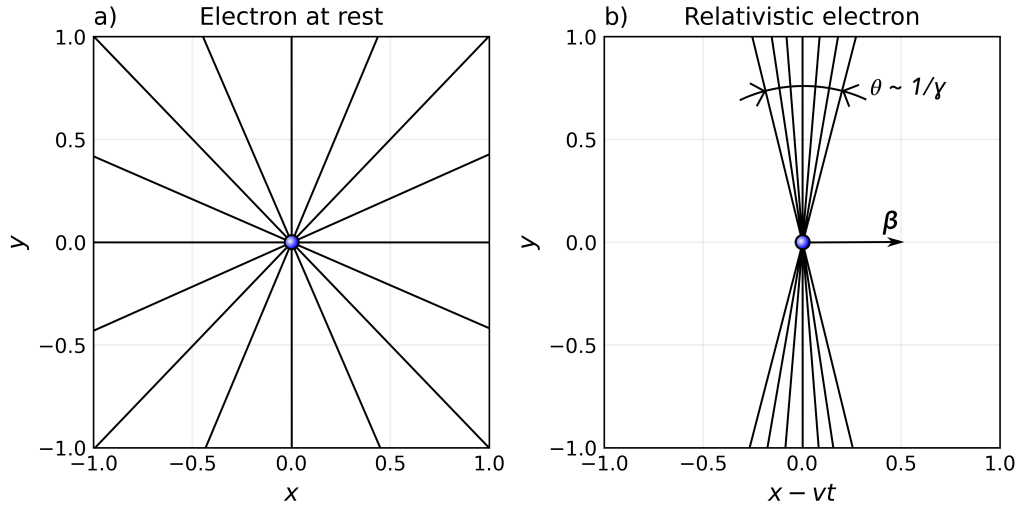
Figure 5: Electric field lines induced by a charged particle at rest (a) and in uniform motion (b), given by Eq. (58).

2.2.1 Angular distribution of radiation power and energy spectrum

The energy flux $\mathbf{S}$, also known as the Poynting vector, can be readily calculated at the observation point P using Eq. (59) as [Landau and Lifshitz, 1962; Jackson, 1962]

$$\mathbf{S}(\mathbf{r}, t) = \frac{1}{\mu_0} \left(\mathbf{E} \times \mathbf{B}\right) = c\epsilon_0 |\mathbf{E}|^2 \mathbf{n} = \frac{c}{\mu_0} |\mathbf{B}|^2 \mathbf{n}, \tag{60}$$

where we have used $c\mathbf{B} = \mathbf{n} \times \mathbf{E}$. Thanks to this transversality of radiation fields, the energy flux can also be written as $\mathbf{S} = c\mathcal{E}\mathbf{n}$, where $\mathcal{E} = (\epsilon_0 |\mathbf{E}|^2 + |\mathbf{B}|^2/\mu_0)/2$ is the energy density of the electromagnetic field. The fields can be readily calculated from the far-field vector potential (59) as [Landau and Lifshitz, 1962]

$$\mathbf{B}(\mathbf{r}, t) = \frac{1}{c} \left(\dot{\mathbf{A}} \times \mathbf{n}\right), \tag{61}$$

$$\mathbf{E}(\mathbf{r}, t) = \left(\dot{\mathbf{A}} \times \mathbf{n}\right) \times \mathbf{n}, \tag{62}$$

where all the quantities are evaluated in terms of the retarded time $t' = t - R(t')/c$ and $\dot{\mathbf{A}}$ is the derivative of vector potential with respect to the retarded time. The power per unit area radiated in the direction of $\mathbf{n}$ is simply the projection $\mathbf{S} \cdot \mathbf{n}$. The area can also be written in terms of the solid angle, using $\mathrm{d}A = R^2 \mathrm{d}\Omega$. The radiated power per unit solid angle can be, therefore, calculated using the following equal expressions

$$\frac{\mathrm{d}^2 W}{\mathrm{d}\Omega \mathrm{d}t} = R^2 \left(\mathbf{S} \cdot \mathbf{n}\right) = c\epsilon_0 |\mathbf{E} \cdot \mathbf{R}|^2 = c\epsilon_0 |\mathbf{E}|^2 R^2 = \frac{c}{\mu_0} |\mathbf{B}|^2 R^2 = c\epsilon_0 |\mathbf{n} \times \dot{\mathbf{A}}|^2 R^2. \tag{63}$$

For the far field of a single charged particle, given by Eq. (56), we can perform a non-trivial integration over the solid angle to obtain the *generalized Larmor formula*, which describes

19

the instantaneous power radiated by a relativistic charged particle

$$\frac{\mathrm{d}W}{\mathrm{d}t} = \frac{q^2}{6\pi\epsilon_0 c}\gamma^6\left(\dot{\boldsymbol{\beta}}^2 - |\boldsymbol{\beta}\times\dot{\boldsymbol{\beta}}|^2\right) = \frac{q^2}{6\pi\epsilon_0 c}\gamma^6\dot{\beta}^2\left(1 - \beta^2\sin^2\theta\right), \tag{64}$$

where θ is the angle between $\boldsymbol{\beta}$ and $\dot{\boldsymbol{\beta}}$.

Before we return to the general discussion, we will now discuss some consequences of Eq. (64), which illustrate some properties of radiation emitted by relativistic particles. When velocity is parallel to acceleration, we have $P \sim \gamma^6\dot{\beta}^2$, while for the perpendicular case $P \sim \gamma^6(1-\beta^2)\dot{\beta}^2 = \gamma^4\dot{\beta}^2$. This could lead us to conclude that longitudinal acceleration yields greater radiated power than transverse acceleration, but that conclusion is wrong. To see that, let us consider the case of a charged particle traveling along a straight line while accelerated by a parallel constant force F. Then we have $\boldsymbol{\beta}\times\dot{\boldsymbol{\beta}} = 0$ and the radiated power can be written as $P \sim \dot{p}^2 = F^2$, where we have used (in normalized units) $\dot{p} = \dot{\gamma}\beta + \gamma\dot{\beta} = \gamma^3\dot{\beta}\beta^2 + \gamma^3(1-\beta^2)\dot{\beta} = \gamma^3\dot{\beta}$. Therefore, the radiation is proportional to the square of the accelerating force acting on the particle, $P \sim \dot{p}^2 = F^2$.

Now, let us focus on the perpendicular case where the velocity and acceleration are orthogonal. Here we have $|\boldsymbol{\beta}\times\dot{\boldsymbol{\beta}}|^2 = \beta^2\dot{\beta}^2$, and so in terms of momentum using the above formula (with $\dot{\gamma} = 0$ valid for perpendicular acceleration) we have $\dot{p} = \gamma\dot{\beta}$, and therefore $P \sim \gamma^2\dot{p}^2 = \gamma^2 F^2$. At last, we come to the opposite conclusion – radiated power is increased by a factor γ^2 in the case of transverse acceleration, assuming the accelerating force is equal in magnitude in both cases. This is sometimes referred to as the concept of *longitudinal and transverse inertia*, which can be summarized as follows: compared to perpendicular acceleration, the inertia of a charged particle is effectively increased by a factor of γ^2 for any force acting parallel to its direction of motion, which can be written as

$$\dot{p}_\parallel = m_e c\gamma^3\dot{\beta}_\parallel \tag{65}$$

$$\dot{p}_\perp = m_e c\gamma\dot{\beta}_\perp. \tag{66}$$

We now return to the general discussion of Eqs. (59) – (63). To understand the spatial or angular distribution of the radiation energy spectrum, we use the linearity of Maxwell's equations to decompose the vector potential (59) into a sum of monochromatic waves, $\mathbf{A}(\mathbf{r},t) = \int\mathbf{A}_\omega(\mathbf{r},t)d\omega$, where $\mathbf{A}_\omega(\mathbf{r},t) = \mathbf{A}(\mathbf{r},\omega)e^{-i\omega t}$. The spatial component of the monochromatic waves, $\mathbf{A}(\mathbf{r},\omega)$, is related to the temporal profile of the total field, $\mathbf{A}(\mathbf{r},t)$, through the Fourier transform as

$$\mathbf{A}(\mathbf{r},\omega) = \int\mathbf{A}(\mathbf{r},t)e^{i\omega t}\mathrm{d}t, \tag{67}$$

$$\mathbf{A}(\mathbf{r},t) = \int\mathbf{A}(\mathbf{r},\omega)e^{-i\omega t}\frac{\mathrm{d}\omega}{2\pi}. \tag{68}$$

If we also express the current $\mathbf{j}(\mathbf{r}',t')$ in Eq. (59) in terms of its spectral Fourier transform, the spatial component of the monochromatic waves (67) can be expressed as

$$\mathbf{A}(\mathbf{r},\omega) = \frac{\mu_0}{4\pi}\frac{e^{ikr}}{r}\int\mathbf{j}(\mathbf{r}',\omega)e^{-i\mathbf{k}\cdot\mathbf{r}'}\mathrm{d}^3\mathbf{r}' = \frac{\mu_0}{4\pi}\frac{e^{ikr}}{r}\mathbf{j}(\mathbf{k},\omega), \tag{69}$$

where $\mathbf{k} = k\mathbf{n}$ is the wave vector with magnitude $k = \omega/c$ and

$$\mathbf{j}(\mathbf{k}, \omega) = \int\int \mathbf{j}(\mathbf{r}, t)e^{i(\omega t - \mathbf{k}\cdot\mathbf{r})}\mathrm{d}^3\mathbf{r}\,\mathrm{d}t, \tag{70}$$

is the spacetime Fourier transform of the current distribution [Attwood and Sakdinawat, 2017]. We see that monochromatic waves have the form of outgoing spherical waves, with amplitudes[6] fully determined by the spacetime Fourier transform (70). The Fourier components of the electromagnetic field can be then obtained from Eqs. (61)–(62) as

$$\mathbf{B}(\mathbf{r}, \omega) = \frac{i\mu_0\omega}{4\pi c^2}\frac{e^{ikr}}{r}\mathbf{n}\times\mathbf{j}(\mathbf{k}, \omega), \tag{71}$$

$$\mathbf{E}(\mathbf{r}, \omega) = \frac{\mu_0\omega}{i4\pi c}\frac{e^{ikr}}{r}\mathbf{n}\times\left[\mathbf{n}\times\mathbf{j}(\mathbf{k}, \omega)\right], \tag{72}$$

To obtain the correct expression for the angular distribution of the radiation energy spectrum, we note that the total energy obtained by summing up over either spectral or temporal resolution must be the same, which can be formally proven using Plancherel's theorem $(\star)$ [Riley et al., 2006] as

$$\frac{\mathrm{d}W}{\mathrm{d}\Omega} = \int_{-\infty}^{\infty}\frac{\mathrm{d}^2W}{\mathrm{d}\Omega\mathrm{d}t}\mathrm{d}t = c\epsilon_0\int_{-\infty}^{\infty}r^2|\mathbf{E}(\mathbf{r}, t)|^2\mathrm{d}t \overset{\star}{=} \frac{c\epsilon_0}{2\pi}\int_{-\infty}^{\infty}r^2|\mathbf{E}(\mathbf{r}, \omega)|^2\mathrm{d}\omega \tag{73}$$

$$= \frac{c\epsilon_0}{\pi}\int_0^{\infty}r^2|\mathbf{E}(\mathbf{r}, \omega)|^2\mathrm{d}\omega \overset{\triangle}{=} \int_0^{\infty}\frac{\mathrm{d}^2W}{\mathrm{d}\Omega\mathrm{d}\omega}\mathrm{d}\omega. \tag{74}$$

From Eq. (67) it is clear that for a real signal $\mathbf{A}(t)$, the spectrum conjugate equals its negative part, $\mathbf{A}(-\omega) = \mathbf{A}^*(\omega)$, and therefore we can define the distribution of radiation spectrum, $\mathrm{d}^2W/\mathrm{d}\Omega\mathrm{d}\omega$, such that the negative components are omitted and the positive frequency components are multiplied by a factor of 2, which was done in the last step $(\triangle)$. Therefore, the angular distribution of the radiation energy spectrum can be generally written in terms of the following *radiation integral* [Landau and Lifshitz, 1962; Jackson, 1962]

$$\frac{\mathrm{d}^2W}{\mathrm{d}\Omega\mathrm{d}\omega} = \frac{c\epsilon_0}{\pi}r^2|\mathbf{E}(\mathbf{r}, \omega)|^2 = \frac{\omega^2}{16\pi^3\epsilon_0 c^3}\left|\int_{\infty}^{\infty}\mathbf{n}\times\left[\mathbf{n}\times\mathbf{j}(\mathbf{r}, t)\right]e^{i(\omega t - \mathbf{k}\cdot\mathbf{r})}\mathrm{d}^3\mathbf{r}\,\mathrm{d}t\right|^2 \tag{75}$$

$$= \frac{\omega^2}{16\pi^3\epsilon_0 c^3}\left|\mathbf{n}\times\left[\mathbf{n}\times\mathbf{j}(\mathbf{k}, \omega)\right]\right|^2. \tag{76}$$

We now have two recipes for obtaining the angular distribution of the radiation energy spectrum. Either, we can calculate the spacetime Fourier transform of the current distribution[7] (76), or we can directly evaluate the integral (75). Finally, it is important to remember these results are valid only for observation points far from the motion of the source $|\mathbf{r} - \mathbf{r}'| \gg 1$.

---

[6]Note that it is the spacetime Fourier transform of the current $\mathbf{j}(\mathbf{k},\omega)$ which determines the angular distribution of radiation since it depends on $\mathbf{k}$.

[7]It is useful to remind ourselves that evaluation of $\mathbf{j}(\mathbf{k}, \omega)$ gives us information about both: a) the spatial profile of the monochromatic waves composing the electric field according to Eq. (72) and b) the angular distribution of the energy spectrum according to Eq. (76).

Radiation from a single and many electrons

Let us now consider the case of a single charged particle; the spectrum distribution can be written in terms of the Fourier transform of the previously obtained electric far field Eq. (56), as[8]

$$
\frac{\mathrm{d}^2 W}{\mathrm{d}\Omega \mathrm{d}\omega} = \frac{c\epsilon_0}{\pi} |\mathcal{F}\left[r\mathbf{E}_{far}\right]|^2 = \frac{q^2}{16\pi^3\epsilon_0 c} \left| \int_\infty^\infty \frac{\mathbf{n} \times \left[(\mathbf{n} - \boldsymbol{\beta}) \times \dot{\boldsymbol{\beta}}\right]}{(1 - \boldsymbol{\beta} \cdot \mathbf{n})^2} e^{i\omega\left(t - \frac{\mathbf{n} \cdot \mathbf{r}_e(t)}{c}\right)} \mathrm{d}t \right|^2, \quad (77)
$$

where the integrand is now evaluated, before integration, in terms of the observer time t. Let us discern some general features of Eq. (77). First, the denominator shows that the radiation energy is concentrated primarily in the direction of motion, increasingly so for more relativistic motion ($\boldsymbol{\beta} \cdot \mathbf{n} \to 1$). Second, radiation vanishes for zero acceleration ($\dot{\boldsymbol{\beta}} = 0$). Third, the numerator shows that radiated energy emitted along the direction of relativistic motion is maximized for transverse acceleration ($[\mathbf{n} - \boldsymbol{\beta}] \times \dot{\boldsymbol{\beta}} = 0$ for $\mathbf{n} \parallel \boldsymbol{\beta} \parallel \dot{\boldsymbol{\beta}}$), following the discussion below Eq. (64). Finally, suppose that the electron performs harmonic oscillations along its trajectory, due to some transverse oscillating force with frequency ω_0. In that case, we can use the method of stationary phase to approximate the radiation frequency corresponding to the strongest emission, as $\omega \sim \gamma^2 \omega_0$. The electromagnetic field that oscillates the charged particle undergoes a double Doppler upshift.

Another simplification of Eq. (77) occurs if we note that

$$
\frac{\mathbf{n} \times \left[(\mathbf{n} - \boldsymbol{\beta}) \times \dot{\boldsymbol{\beta}}\right]}{\kappa^2} = \frac{\mathrm{d}}{\mathrm{d}t} \left[\frac{\mathbf{n} \times (\mathbf{n} \times \boldsymbol{\beta})}{\kappa} \right]. \quad (78)
$$

Per partes integration then gives an expression more malleable for analytical evaluation, which is also equivalent to Eq (75), with the current given by a single charged particle, $\mathbf{j}(\mathbf{r}, t) = q\boldsymbol{\beta}(t)\delta(\mathbf{r} - \mathbf{r}_e(t))$,

$$
\frac{\mathrm{d}^2 W}{\mathrm{d}\Omega \mathrm{d}\omega} = \frac{q^2 \omega^2}{16\pi^3\epsilon_0 c} \left| \int_\infty^\infty \mathbf{n} \times (\mathbf{n} \times \boldsymbol{\beta}) \, e^{i\omega\left(t - \frac{\mathbf{n} \cdot \mathbf{r}_e(t)}{c}\right)} \mathrm{d}t \right|^2. \quad (79)
$$

Note that the vectorial direction of the integrand decides the polarization of emitted radiation, per Eq. (72). The radiation distribution for a particular polarization can be, therefore, obtained by calculating the scalar product of the integrand with a unit polarization vector of interest before taking the absolute square value.

Noticing that $\mathrm{d}\mathbf{r}_e(t)/\mathrm{d}t = c\boldsymbol{\beta}(t)$, Eq. (79) can also be written as an integral taken along the trajectory of a particle, as

$$
\frac{\mathrm{d}^2 W}{\mathrm{d}\Omega \mathrm{d}\omega} = \frac{q^2 \omega^2}{16\pi^3\epsilon_0 c} \left| \mathbf{n} \times \mathbf{n} \times \int_{\mathbf{r}_a}^{\mathbf{r}_b} \mathrm{d}\mathbf{r}_e e^{i\omega\left(t - \frac{\mathbf{n} \cdot \mathbf{r}_e}{c}\right)} \right|^2. \quad (80)
$$

Eq. (80) illustrates that each position along the trajectory of a radiating particle is weighted by a spherical wave[9] emitted at the retarded time $t' \approx t - r - \mathbf{n} \cdot \mathbf{r}_e(t')/c$, corresponding to a

---

[8]For numerical evaluation, instead of direct numerical integration, it is often computationally much faster to calculate fast Fourier transform (FFT) of the integrand (without the exponential term) of Eq. (77). The integrand must be first evaluated in terms of the retarded time $t' = t - |r - r_e(t')|/c$ before the transform.

[9]This point is a bit hidden in Eq. (80), but the instantaneous waves are indeed spherical. This is clear when we look back at Eq. (72). The same exercise as with Eq. (79) can be performed to show that it can also be written in terms of an integral along the trajectory of a radiating charged particle.
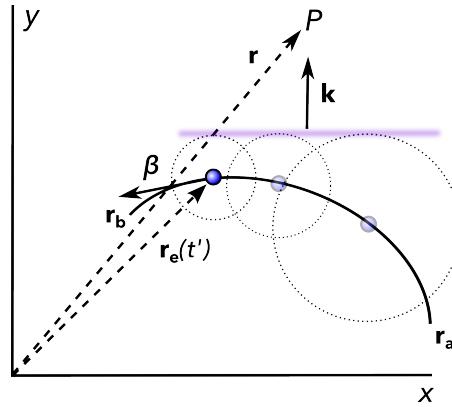
Figure 6: A schematic illustrating interpretation of Eq. (80).

given position $\mathbf{r}_e(t')$. The apparent wavefronts[10] formed by the individual spherical waves then form the radiation signal seen by the observer positioned at $\mathbf{r}$ at time t, as shown in Fig. 6.

Eq. (79) can be easily generalized to many charged particles by summing the far field contributions from individual charges, which turns out to be equal to the following substitution in the integrand of Eq. (79) [Jackson, 1962]:

$$q\boldsymbol{\beta} e^{-i(\omega/c)\mathbf{n}\cdot\mathbf{r}_e(t)} \rightarrow \sum_{i=1}^{N} q_i \boldsymbol{\beta}_i e^{-i(\omega/c)\mathbf{n}\cdot\mathbf{r}_i(t)}. \tag{81}$$

Similarly, radiation due to the motion of a continuous charge distribution, described by current density $\mathbf{j}(\mathbf{r},t)$, can be obtained with the substitution

$$q\boldsymbol{\beta} e^{-i(\omega/c)\mathbf{n}\cdot\mathbf{r}_e(t)} \rightarrow \frac{1}{c}\int \mathrm{d}^3\mathbf{r}\, \mathbf{j}(\mathbf{r},t)e^{-i\mathbf{k}\cdot\mathbf{r}}, \tag{82}$$

which once again yields the general result given by Eq. (75).

Periodic radiation and frequency harmonics

Yet, another simplification occurs when we consider the periodic motion of radiating charges. Then, periodic electric fields are produced, which can be written as

$$\mathbf{E}(\mathbf{r},t) = \sum_{n=-\infty}^{\infty} \mathbf{E}_n(\mathbf{r}, t - nT) = \int \mathbf{E}_n(\mathbf{r},t') \sum_{n=-\infty}^{\infty} \delta(t - nT - t')\mathrm{d}t', \tag{83}$$

where $\mathbf{E}_n(\mathbf{r},t)$ is the radiation field that describes the electric field within a single period, i.e., it is non-zero only for $t \in (0,T)$, where $T = 2\pi/\omega_0$ is the period of the signal. The second equality highlights that a periodic signal equals the convolution of a single period signal with a Dirac comb [Riley et al., 2006; Jackson, 1962]. According to the convolution theorem, the Fourier transform of a convolution of two functions is equal to the product of their Fourier

---

[10]Superposition of individual outgoing spherical waves, summed up over all frequencies.

transforms [Riley et al., 2006], which gives the spectrum of the electric field

$$\mathbf{E}(\mathbf{r}, \omega) = \mathbf{E}_n(\mathbf{r}, \omega) \int \sum_{n=-\infty}^{\infty} \delta(t - nT) e^{-i\omega t} \mathrm{d}t \tag{84}$$

$$= \mathbf{E}_n(\mathbf{r}, \omega) \sum_{n=-\infty}^{\infty} e^{-i\omega nT} \overset{\star}{=} \omega_0 \sum_{n=-\infty}^{\infty} \mathbf{E}_n(\mathbf{r}, \omega) \delta(\omega - n\omega_0), \tag{85}$$

where we have used the Poisson summation formula $(\star)$ [Riley et al., 2006], which states that the Fourier transform of a Dirac comb of period T is equal to a Dirac comb with period $\omega_0 = 2\pi/T$ (up to a factor of ω_0). Eq. (85) makes it clear that the spectrum of a periodic signal is spaced at integer frequencies, $\omega_n = n\omega_n$, which are called *harmonics* of the fundamental frequency. The amplitudes of the harmonics, $E_n(\mathbf{r}, \omega_n)$, are given by the Fourier transform of the single period signal evaluated at $\omega = n\omega_0$, given as

$$\mathbf{E}_n(\mathbf{r}, \omega_n) = \frac{\mu_0 n\omega_0}{i4\pi c} \frac{e^{ink_0 r}}{r} \int_0^{2\pi/\omega_0} \mathbf{n} \times (\mathbf{n} \times \mathbf{j}(\mathbf{r}, t)) \, e^{in\omega_0\left(t - \frac{\mathbf{n} \cdot \mathbf{r}}{c}\right)} \mathrm{d}^3\mathbf{r} \, \mathrm{d}t. \tag{86}$$

To convert the angular distribution of spectral energy to the angular distribution of power radiated per harmonic, we multiply Eq. (75) by the repetition rate $\nu = \omega_0/2\pi$ and by the fundamental frequency ω_0 to obtain [Jackson, 1962]

$$\frac{\mathrm{d}P_n}{\mathrm{d}\Omega} = \frac{n^2\omega_0^4}{32\pi^4\epsilon_0 c^3} \left| \int_0^{2\pi/\omega_0} \mathbf{n} \times (\mathbf{n} \times \mathbf{j}(\mathbf{r}, t)) \, e^{in\omega_0\left(t - \frac{\mathbf{n} \cdot \mathbf{r}}{c}\right)} \mathrm{d}^3\mathbf{r} \, \mathrm{d}t \right|^2. \tag{87}$$

An infinite periodic signal spectrum is given by a Dirac comb with periodicity ω_0. In much simpler terms, the previous discussion reduces to the understanding that any reasonable periodic function can be represented by its Fourier series. However, in reality, periodic signals have a temporally finite envelope. In such a case, the harmonics have a finite bandwidth. Let us assume that the signal is emitted for a duration of T. Then, the spectral lineshape of the individual harmonics can be obtained as

$$|\mathbf{E}_n(\mathbf{r}, \omega)|^2 = \left| \mathbf{E}_n(\mathbf{r}, \omega_n) \int_0^T e^{i\omega_n t} \mathrm{d}t \right|^2 = |\mathbf{E}_n(\mathbf{r}, \omega_n)|^2 T^2 \mathrm{sinc}^2 \left(\frac{(\omega - \omega_n)T}{2} \right), \tag{88}$$

where $\mathbf{E}_n(\mathbf{r}, \omega_n)$ is the electric field amplitude of the n-th harmonic given by Eq. (86) and $\mathrm{sinc}(x) = \sin(x)/x$ is the cardinal sine function. If we assume that the train of pulses is emitted for a duration of $T = 2\pi N/\omega_0$, where N is the number of periods of the signal, the full-width-at-half-maximum (FWHM) spectral bandwidth can be written as [Attwood and Sakdinawat, 2017]

$$\frac{\Delta\omega}{\omega_n} = \frac{1}{nN}. \tag{89}$$

Compared to the bandwidth of the fundamental frequency, $\Delta\omega = \omega_0/N$, the bandwidth of higher harmonics is further reduced with increasing harmonic order by a factor of $1/n$.

2.2.2 Relativistic aberration and searchlight effect

Let us now discuss a general property of radiation emitted by relativistic charged particles known as *relativistic beaming* or *relativistic aberration*. We consider a particle with normalized

velocity $\boldsymbol{\beta}_p'$ in the boosted frame R, which moves with normalized velocity β in the positive x direction with respect to the laboratory frame L. Then, the velocity components of the moving particle are given in the laboratory frame by the inverse Lorentz transform of four-velocity, as [Einstein, 1905; Jackson, 1962; Landau and Lifshitz, 1962; Attwood and Sakdinawat, 2017]

$$\beta_{x,p} = \frac{\beta_{x,p}' + \beta}{1 + \beta\beta_{x,p}'}, \tag{90}$$

$$\beta_{\perp,p} = \frac{\beta_{\perp,p}'}{\gamma(1 + \beta\beta_{x,p}')}, \tag{91}$$

where the velocity components are given as $\beta_{x,p}' = \beta_p'\cos\theta'$ and $\beta_{\perp,p}' = \beta_p'\sin\theta'$, in the coordinate system of the boosted frame R, where θ' is the altitude angle at which the particle propagates with respect to the x' axis. The angle under which the particle is seen to propagate in the L frame is then given as

$$\tan\theta = \frac{\beta_{\perp,p}}{\beta_{x,p}} = \frac{\beta_{\perp,p}'}{\gamma(\beta_{x,p}' + \beta)} = \frac{\beta_p'\sin\theta'}{\gamma(\beta_p'\cos\theta' + \beta)} \stackrel{(\beta_p'=1)}{=} \frac{\sin\theta'}{\gamma(\cos\theta' + \beta)}, \tag{92}$$

where for the last equality, we have assumed that the particle is, in fact, a photon, which travels at luminal velocity $\beta_p' = 1$ in all reference frames. Let us consider that the radiation is emitted along the y or z axis in the R frame. Then. $\sin\theta' = 1$ and $\cos\theta' = 0$, and the relativistic case ($\beta \approx 1$) then becomes

$$\tan\theta = \frac{1}{\gamma\beta} \approx \frac{1}{\gamma}. \tag{93}$$

Therefore, even radiation emitted in the perpendicular directions in the R frame is observed to be collimated along x in the L frame within a radiation cone with an opening angle of $\theta \approx 1/\gamma$, as illustrated in Fig. 7. This is a consequence of relativistic aberration, known as the *searchlight* or *headlight effect*.

An effective strategy to solve problems involving the motion of relativistic charges is to calculate the radiation distribution (77) in the boosted frame of the particle (R), $\mathrm{d}W'/\mathrm{d}\Omega'\mathrm{d}\omega'$, and then transform it back to the laboratory frame of reference (L), $\mathrm{d}W/\mathrm{d}\Omega\mathrm{d}\omega$. We now present the general procedure. The energy radiated at an angle θ' in the R frame is given by inverse Lorentz transformation in the L frame as $\mathrm{d}W = \gamma(1 + \beta\cos\theta')\mathrm{d}W'$. Frequency transforms in the same way, $\omega = \gamma(1 + \beta\cos\theta')\omega'$. Lastly, we are missing the transformation for the solid angle differential, $\mathrm{d}\Omega = \mathrm{d}\cos\theta\mathrm{d}\phi$. It now seems useful to express Eq. (93) in terms of cosines, which is given by (90) for a photon, which propagates in the R frame with speed $|\boldsymbol{\beta}_p'| = 1$, as

$$\cos\theta = \beta_{x,p} = \frac{\cos\theta' + \beta}{1 + \beta\cos\theta'}. \tag{94}$$

Using Eq. (94), we can find that the solid angle transforms as $\mathrm{d}\Omega = \mathrm{d}\Omega'/\left[\gamma(1 + \beta\cos\theta')\right]^2$. Combining all of the previous components with the identity $\gamma(1 - \beta\cos\theta) = 1/\left[\gamma(1 + \beta\cos\theta')\right]$, which can be easily verified using Eq. (94), we obtain that the angular distribution of radiation transforms as[11]

$$\frac{\mathrm{d}W}{\mathrm{d}\Omega} = \frac{1}{\gamma^3(1 - \beta\cos\theta)^3}\frac{\mathrm{d}W'}{\mathrm{d}\Omega'}. \tag{95}$$

---

[11]See [Jackson, 1962] or [Attwood and Sakdinawat, 2017] and references therein for more details on Lorentz transformations of radiation energy distributions.

Further, we can differentiate with respect to the frequency to obtain the angular distribution of energy spectrum,

$$\frac{\mathrm{d}W}{\mathrm{d}\Omega\mathrm{d}\omega} = \frac{1}{\gamma^2(1-\beta\cos\theta)^2}\frac{\mathrm{d}W'}{\mathrm{d}\Omega'\mathrm{d}\omega'}. \tag{96}$$

Finally, we need to transform the angular distribution of power. In that case, we need to find the relationship between the observer time interval in the L frame and retarded time interval in the R frame, which is the time that parametrizes particle trajectories in the R frame, e.g., Eqs. (44) – (46). The time intervals between the two frames are related as $\mathrm{d}t = \gamma\mathrm{d}t'$. However, this equation relates only to observer time intervals in the two frames. To obtain the relation between the observer time in L frame and the retarded time in R frame, we simply use the derivative of the observer time with respect to retarded time used in the previous section, $\kappa = \mathrm{d}t_{obs}/\mathrm{d}t_{ret} = 1 - \mathbf{n}\cdot\boldsymbol{\beta} = 1 - \beta\cos\theta$. The relationship between the observer time in the L frame and retarded time in the R frame is then $\mathrm{d}t_{obs} = \gamma(1-\beta\cos\theta)\mathrm{d}t'_{ret}$ and the angular power distribution therefore transforms as

$$\frac{\mathrm{d}W}{\mathrm{d}\Omega\mathrm{d}t} = \frac{1}{\gamma^4(1-\beta\cos\theta)^4}\frac{\mathrm{d}W'}{\mathrm{d}\Omega'\mathrm{d}t'}. \tag{97}$$

Note that the power scales on-axis ($\cos\theta = 1$) for ultra-relativistic boosts as $1/[\gamma^4(1-\beta)^4] \approx (2\gamma)^4$, since $1 - \beta \approx 1/(2\gamma^2)$. Additionally, it is useful to note that the relationship between observer and retarded time can be approximated for ultra-relativistic particles close to their propagation axis, as $\kappa = 1 - \beta\cos\theta \approx [1 + (\gamma\theta)^2]/2\gamma^2$.

We are now equipped with various tools and techniques required to calculate radiation emitted from charged particles in motion, for example, the laser-driven nonlinear orbits of relativistic electrons given by Eqs. (33) – (35).
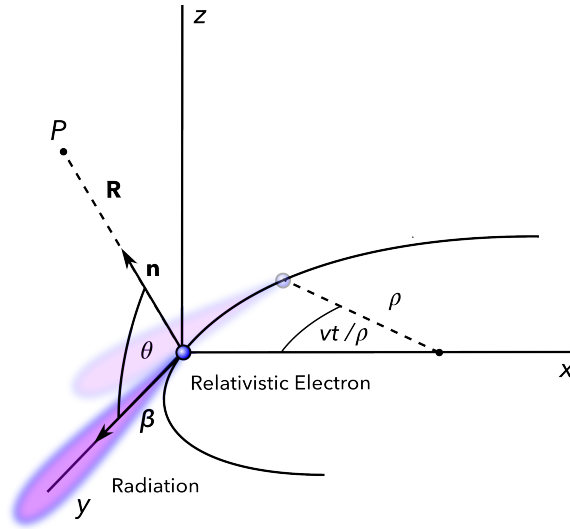
2.2.3 Instantaneous circular motion

We now consider the case of radiation emitted by an electron performing instantaneously circular motion. This is quite a useful problem to solve since any reasonable trajectory $\mathbf{r}_e(t)$ can be locally approximated by a circle with radius corresponding to the local radius of curvature, which can be calculated as $\rho(t) = |1 + \mathbf{r}'_e(t)|^{3/2}/|\mathbf{r}''_e(t)|$. As we've noted within our discussion of the radiation integral (77), radiation from a relativistic electron is observed only in short bursts since it is collimated along the direction of motion. This often makes radiation from instantaneous circular motion an excellent local (measured at some observation point P) approximation to radiation emitted from a much more complicated trajectory at relativistic velocities since most of the radiation detected by the observer comes from a tiny part of the trajectory. Here, we only cite the results of the derivation, which can be found in [Jackson, 1962; Landau and Lifshitz, 1962], with emission geometry shown in Fig. 7,

$$\frac{\mathrm{d}^2W}{\mathrm{d}\Omega\mathrm{d}\omega} = \frac{q^2\gamma^2}{16\pi^3\epsilon_0 c^3}\left(\frac{\omega}{\omega_c}\right)^2\left[1 + (\gamma\theta)^2\right]^2\left[K_{2/3}^2(\xi) + \frac{(\gamma\theta)^2}{1+(\gamma\theta)^2}K_{1/3}^2(\xi)\right], \tag{98}$$

where $K_n(x)$ is the modified Bessel function of the second kind [Gradshteyn and Ryzhik, 1965],

$$\omega_c = \frac{3}{2}\frac{c}{\rho}\gamma^3 \tag{99}$$

Figure 7: Illustration of the geometry of radiation emission from the instantaneous circular motion of a relativistic charged particle, which is given analytically by Eq. (98) and shown in Fig. 8.

is the critical frequency, where ρ is the radius of curvature, and the argument is given as

$$\xi = \frac{\omega}{\omega_c} \frac{\left[1 + (\gamma\theta)^2\right]^{3/2}}{2}. \tag{100}$$

The first term in the second square brackets of Eq. (98) corresponds to radiation polarized in the orbital plane, while the second term corresponds to radiation polarized perpendicular to that plane. These two components are visualized in Fig. 8. To obtain the angular distribution of radiation energy analytically, we can integrate over the frequency to obtain

$$\frac{\mathrm{d}W}{\mathrm{d}\Omega} = \int_0^\infty \frac{\mathrm{d}^2 W}{\mathrm{d}\Omega\mathrm{d}\omega}\mathrm{d}\omega = \frac{7q^2}{64\pi\epsilon_0} \frac{\gamma^5}{\rho} \frac{1}{(1 + (\gamma\theta)^2)^{5/2}} \left[1 + \frac{5}{7}\frac{(\gamma\theta)^2}{1 + (\gamma\theta)^2}\right], \tag{101}$$

where the first and second terms in the square brackets again correspond to orbit parallel and perpendicular polarization. A curious observation follows: if we individually integrate the two polarization terms in Eq. (101), we will find that the ratio of energy in the two polarizations is exactly $W_\parallel/W_\perp = 7$. The total radiation energy emitted per a single turn is explicitly

$$W = (2\pi)\int_{-\infty}^\infty \frac{\mathrm{d}W}{\mathrm{d}\Omega}\mathrm{d}(\gamma\theta) = W_\parallel + W_\perp = 2\pi\frac{7q^2}{64\pi\epsilon_0}\frac{\gamma^4}{\rho}\left[\frac{4}{3} + \frac{4}{21}\right] = \frac{q^2}{3\epsilon_0}\frac{\gamma^4}{\rho}. \tag{102}$$

A fundamental property of radiation emitted by relativistic electrons is confirmed explicitly with Eq. (101) – most of the radiation is emitted along the trajectory within a cone that has an opening angle $\theta \sim 1/\gamma$, as shown in Fig. 8. Therefore, as noted previously, radiation from relativistic particles is highly collimated along the particle trajectory. This is known as the *searchlight effect* or *headlight effect* because the angular distribution of radiation looks similar to the headlights of a car, as illustrated in Fig. 7. This also has significant consequences for the temporal properties of observed radiation since it can be registered only when the particle's velocity points toward the observer over an angle of $\theta \sim 1/\gamma$.
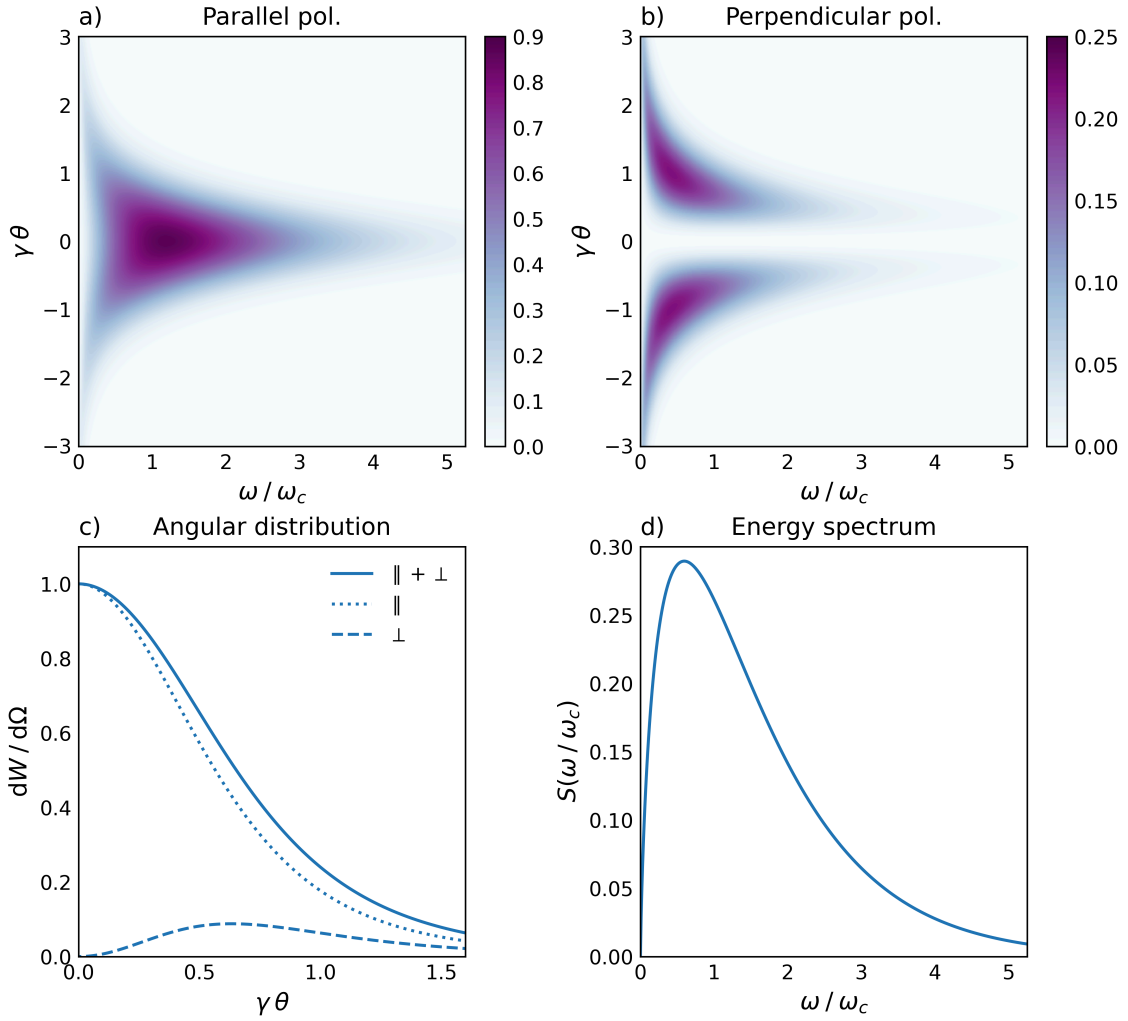
Figure 8: Distribution of radiation energy (98) for (a) polarization parallel to the orbital plane, and (b) polarization perpendicular to this plane. (c) Normalized angular distribution of radiation energy, given by Eq. (101). (d) Normalized radiation energy spectrum, given by Eq. (105).

Looking at geometry of Fig. 7, if the angle described by the particle along its trajectory in retarded time is equal to $\phi = vt'/\rho$, the particle will illuminate the observer within a single turn only for a short time interval of $\Delta t' \sim \rho/(c\gamma)$, since the angular width of the beam is of the order $1/\gamma$. However, the observer sees its own time interval $\Delta t \sim (\mathrm{d}t/\mathrm{d}t')\Delta t' = \kappa\Delta t' \approx \Delta t'/\gamma^2$. Therefore, the radiation pulse duration registered by the observer is given as

$$\Delta t \approx \frac{\rho}{\gamma^3 c} = \frac{1}{\omega_c}, \tag{103}$$

This agrees with the general properties of Fourier transform pairs since the energy spectrum extends up to the critical energy ω_c, which we will now show in detail. Integrating Eq. (98)

over the solid angle, we obtain the energy spectrum of the emitted radiation

$$\frac{\mathrm{d}W}{\mathrm{d}\omega} = \int_0^{4\pi} \frac{\mathrm{d}^2 W}{\mathrm{d}\Omega \mathrm{d}\omega} \mathrm{d}\Omega = \frac{2q^2\gamma}{9\epsilon_0 c} S\left(\frac{\omega}{\omega_c}\right), \tag{104}$$

where $S(x)$ is the normalized energy spectrum, given as

$$S(x) = \frac{9\sqrt{3}}{8\pi} x \int_x^{\infty} K_{5/3}(\eta) \mathrm{d}\eta. \tag{105}$$

The normalized spectrum satisfies $\int_0^{\infty} S(x)\mathrm{d}x = 1$. Also, note that $\int_0^1 S(x)\mathrm{d}x = 1/2$, which means that half of the total energy is emitted above the critical frequency ($x > 1$), and half below ($x < 1$). The radiation emitted by a relativistic charged particle in instantaneous circular motion is known as *synchrotron radiation*[12] because it was first observed as visible light emitted from a 70 MeV electron synchrotron by [Elder et al., 1947].

2.2.4 Periodic circular motion

Let us assume that the motion along the circle with radius ρ is not instantaneous but periodic. According to Eq. (84), the observer, in this case, sees radiation bursts described by the formulas presented in the previous section, with periodicity $T_0 = 2\pi\rho/v$, as shown in Fig. 9. Since the signal is periodic, it can be decomposed into Fourier series, which is given in terms of harmonics of the fundamental frequency $\omega_0 = \beta c/\rho$. To obtain the spectral intensity of the individual harmonics, we merely evaluate the energy distribution given by Eq. (98) for $\omega = \omega_n = n\omega_0$ and then multiply with the repetition rate $\nu = v/2\pi\rho \approx c/2\pi\rho$ and harmonic frequency $\omega_0 \approx c/\rho$ to convert energy radiated per unit frequency per solid angle into power radiated per harmonic per solid angle, which gives

$$\frac{\mathrm{d}P_n}{\mathrm{d}\Omega} = \frac{c^2}{2\pi\rho^2} \frac{\mathrm{d}^2 W}{\mathrm{d}\Omega \mathrm{d}\omega}\bigg|_{\omega=\omega_n}. \tag{106}$$

These results can be directly applied to the circularly polarized laser-driven electron orbits in the boosted drift frame given by Eqs. (44) – (46), where no longitudinal motion is present. This corresponds to synchrotron radiation from an electron circulating with velocity $a_0/(\sqrt{2}\gamma')$ at a radius $\rho = a_0/(\sqrt{2}k'\gamma')$, as shown in Fig. 10.

For any periodic motion of a relativistic electron which generates current $\mathbf{j}(\mathbf{r},t) = -e\boldsymbol{\beta}(t)\delta[\mathbf{r} - \mathbf{r}_e(t)]$, Eq. (107) gives

$$\frac{\mathrm{d}P_n}{\mathrm{d}\Omega} = \frac{q^2 c}{4\pi\epsilon_0} \frac{n^2 \omega_0^4}{(2\pi c)^3} \left| \int_0^{2\pi/\omega_0} \boldsymbol{\beta} \times \mathbf{n}\, e^{in\omega_0\left(t - \frac{\mathbf{n}\cdot\mathbf{r}_e(t)}{c}\right)} \mathrm{d}t \right|^2, \tag{107}$$

which can also be written in terms of a closed-loop integral over the trajectory

$$\frac{\mathrm{d}P_n}{\mathrm{d}\Omega} = \frac{q^2}{4\pi\epsilon_0 c} \frac{n^2 \omega_0^4}{(2\pi c)^3} \left| \oint (\mathrm{d}\mathbf{r}_e \times \mathbf{n})\, e^{in\omega_0\left(t - \frac{\mathbf{n}\cdot\mathbf{r}_e}{c}\right)} \right|^2. \tag{108}$$

The angular distribution of power per harmonic emitted by a relativistic electron conducting circular relativistic motion can be readily calculated using Eq. (108) as [Jackson,

---

[12]See [Attwood and Sakdinawat, 2017] and references therein for more details, historical overview, and applications of synchrotron radiation sources and free electron lasers.
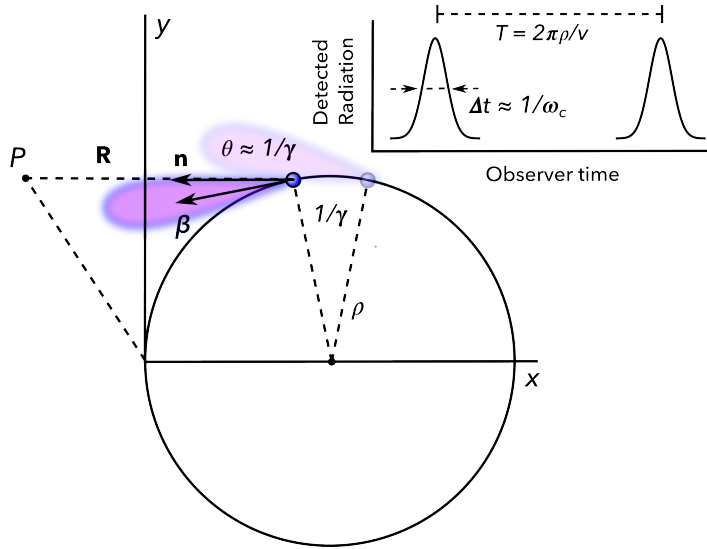
Figure 9: Schematic illustrating radiation emitted due to periodic circular motion of a relativistic charged particle. The observer is placed at point P in the orbital plane.

1962]

$$\frac{\mathrm{d}P_n}{\mathrm{d}\Omega} = \frac{q^2 c}{4\pi\epsilon_0} \frac{\rho^2 n^2 \omega_0^4}{2\pi c^3} \left[\frac{\cos^2\theta}{\beta^2 \sin^2\theta} J_n^2 \left(n\beta\sin\theta\right) + J_n'^2 \left(n\beta\sin\theta\right) \right], \tag{109}$$

where $J_n(x)$ is the Bessel function of the first kind and $J_n'(x)$ is its derivative [Gradshteyn and Ryzhik, 1965]. Here, the angle θ denotes the polar angle with respect to the orbital $y-z$ plane ($\theta \in [0, \pi]$) shown in Fig. 10a, i.e. the observation vector **n** is perpendicular to the orbital plane for $\theta = 0$, whereas in the radiation distribution for instantaneous circular motion (98) it denoted the altitude angle from the orbital plane ($\theta \in [-\pi/2, \pi/2]$), where for $\theta = 0$ the observation vector **n** rested within the orbital plane. This variable change will be useful when we discuss the laser-driven orbits, where the polar angle θ will be the angle between the observation vector **n** and the laser wave vector **k**. The first term in the square brackets ($\sim J_n^2$) corresponds to radiation polarized in the y direction, while the second term ($\sim J_n'^2$) corresponds to radiation polarized in the z direction. If the orbit is not circular but instead consists only of oscillations along the y or z (see Fig. 11a,c), the second term is equal to zero, and the radiation is polarized along the axis of oscillations. Note that polarization along the x axis is also naturally present in the radiation near field, but this is neglected within the far field approximation, and therefore Eq. (109) does not describe it.

It can be shown using the Nicholson's formula for Bessel functions [Jackson, 1962; Gradshteyn and Ryzhik, 1965] that Eq. (109) yields Eq. (106), with angular distribution given by Eq. (98), in the ultra-relativistic limit $\gamma \gg 1$. Note that while the electron orbits are harmonic with ω_0 (or ω_0' and $2\omega_0'$ in the case of electron orbits driven by laser with linear polarization in the boosted frame), the radiation is composed of all harmonics of ω_0, which is due to the causal relationship between radiation emission and propagation expressed by the retarded time, which modifies the phase factor in Eq. (77) with the term $\mathbf{n} \cdot \mathbf{r}_e(t)/c$. Without this, the observed radiation would contain only spectral components related to the frequencies present in the orbital motion. The angular distribution of power per harmonic from laser-driven orbits in the boosted drift frame (R frame shown in Fig. 10a) can be then

obtained by the following substitutions in Eq. (109), which is valid for the circular motion in the R frame, $\rho = a_0/(\sqrt{2}k'\gamma')$, $\beta = a_0/\gamma'$, $\theta \rightarrow \theta' = a_0/(\sqrt{2}k)$, where $\gamma' = \sqrt{1 + a_0^2/2}$. For linear polarization, the procedure is not as subtle, as it also includes the second harmonic longitudinal oscillations[13].

2.2.5 Boosted periodic circular motion

In the context of laser-driven relativistic orbits described in Sec. 2.1, we are ultimately interested in the angular distribution of radiation in the laboratory frame, where the electrons do not only perform oscillatory motion but also drift in the longitudinal direction (L frame, shown in Fig. 10b), either due to the laser field or due to their initial velocity. The power distribution of harmonics transforms according to Eq. (97) as

$$\frac{\mathrm{d}P_n}{\mathrm{d}\Omega} = \frac{1}{\gamma^4(1 - \beta\cos\theta)^4}\frac{\mathrm{d}P'_n}{\mathrm{d}\Omega'}, \tag{110}$$

where $\mathrm{d}P'_n/\mathrm{d}\Omega'$ is given by Eq. (109) and all the dashed variables (ω', θ') inside $\mathrm{d}P'_n/\mathrm{d}\Omega'$ are expressed in terms of the L frame non-dashed variables (ω, θ), as given by the inverse Lorentz transform. For example, the sine of angles in Eq. (109) is expressed according to the formulas on relativistic aberration, as $\sin\theta' = (\sin\theta/\gamma)/(1 - \beta\cos\theta)$. The harmonic frequencies are given in the L frame as

$$\omega_n = \frac{n\omega'_0}{\gamma(1 - \beta\cos\theta)}. \tag{111}$$

Nonlinear Thomson scattering

For electron orbits driven by circular polarization, we consider the R frame to propagate with drift velocity $\beta_d = a_0^2/(4 + a_0^2)$ and Lorentz factor $\gamma_d = 1/\sqrt{1 - \beta_d^2} = (1 + (a_0/2)^2)/\sqrt{1 + a_0^2/2}$. The frequency of the laser in the R frame is given as $\omega'_0 = \omega_0/\gamma'$, where $\gamma' = \sqrt{1 + a_0^2/2}$. Plugging into Eq. (110), we get the power distribution of harmonics as

$$\frac{\mathrm{d}P_n}{\mathrm{d}\Omega} = \frac{\left(1 + \frac{a_0^2}{2}\right)^2}{\left[1 + \frac{a_0^2}{4}(1 - \cos\theta)\right]^4}\frac{\mathrm{d}P'_n}{\mathrm{d}\Omega'}, \tag{112}$$

and for the harmonics, we have

$$\omega_n = \frac{n\omega_0}{1 + \frac{a_0^2}{4}(1 - \cos\theta)}. \tag{113}$$

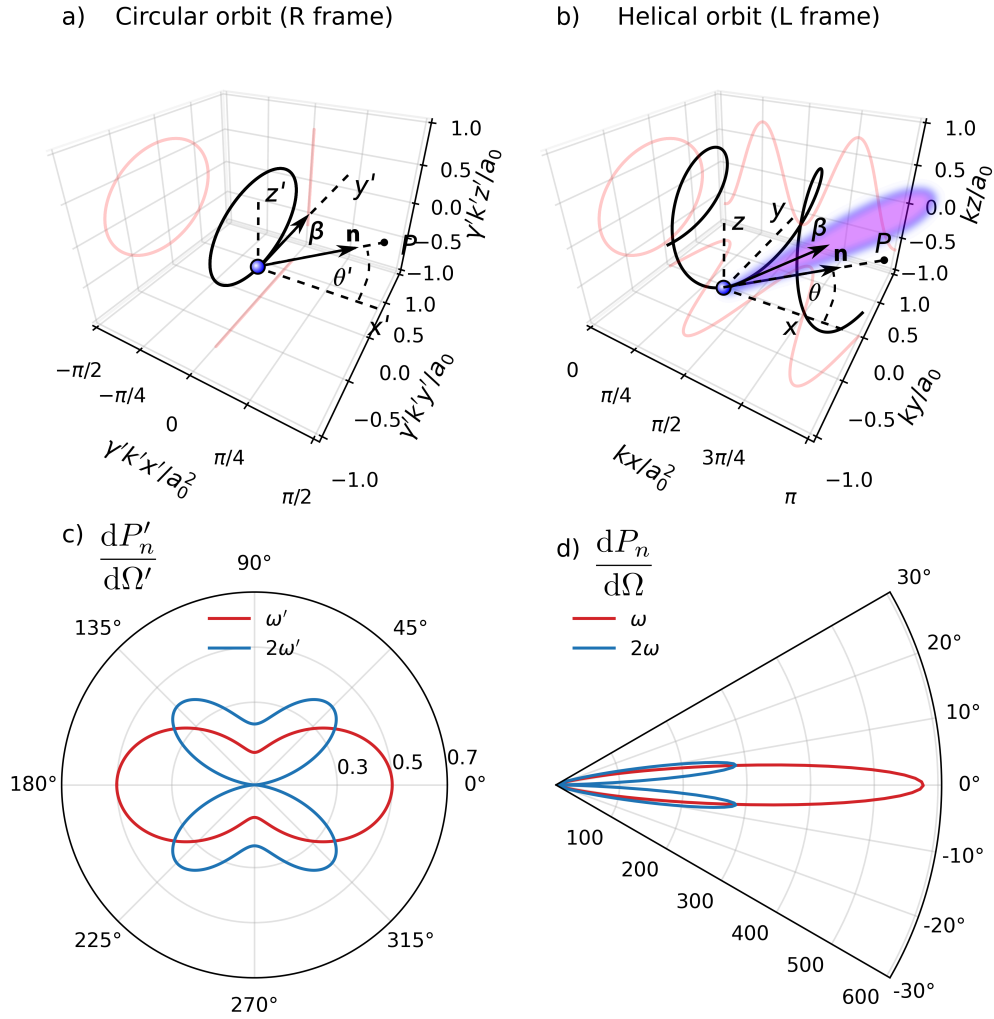The angular distribution of total radiated power is then simply the sum of all the harmonics

$$\frac{\mathrm{d}P}{\mathrm{d}\Omega} = \sum_{n=1}^{\infty}\frac{\mathrm{d}P_n}{\mathrm{d}\Omega}. \tag{114}$$

Radiation generated by the interaction of the free electron with laser field of relativistic intensity, described by Eq. (114), is said to be a result of *nonlinear Thomson scattering*

---

[13]We guide the reader to the seminal work on nonlinear Thomson scattering – [Sarachik and Schappert, 1970], where scattering due to circular or linear polarization is calculated, in both the laboratory (L) and the boosted (R) frame.

a)   Circular orbit (R frame)   b)   Helical orbit (L frame)

c) $\dfrac{\mathrm{d}P'_n}{\mathrm{d}\Omega'}$ d) $\dfrac{\mathrm{d}P_n}{\mathrm{d}\Omega}$

Figure 10: (a) Circular orbits of electrons driven by circularly polarized laser with $a_0 = 8$ in the boosted (R) frame, which propagates with the drift velocity $\beta_d = a_0^2/(4 + a_0^2)$ along the x direction with respect to the laboratory (L) frame. R frame trajectories are given by Eqs. (44)–(46). (b) Helical orbits of electrons driven by circularly polarized laser in the L frame, given by Eqs. (33)–(35). Angular distribution of power, calculated for the first two harmonics in the R frame (c) using Eq. (109), and L frame (d) given by Eq. (110). The R frame moves with respect to the L frame with the Lorentz factor $\gamma = 1/\sqrt{1 - \beta_d^2} \approx 3$, which corresponds to the opening angle $\theta = 1/\gamma \approx 20°$, in accordance with the radiation cone shown in (d).

[Sarachik and Schappert, 1970]. Electrons initially at rest scatter fundamental laser frequency ω_0 into harmonics given by Eq. (111), which are *intensity red-shifted* off-axis, i.e. for $\theta \neq 0$. For $a_0 \ll 1$, the total power of the harmonics has the following leading term, $P_n \approx I_0 \sigma_T a_0^{2n}$[14], where $I_0 = \epsilon_0 c E_0^2/2$ is the incident laser intensity and $\sigma_T = (8\pi/3)r_e$ is the *Thomson scattering cross section*, where r_e is the classical electron radius.

---

[14]See [Sarachik and Schappert, 1970] for more precise prefactors.
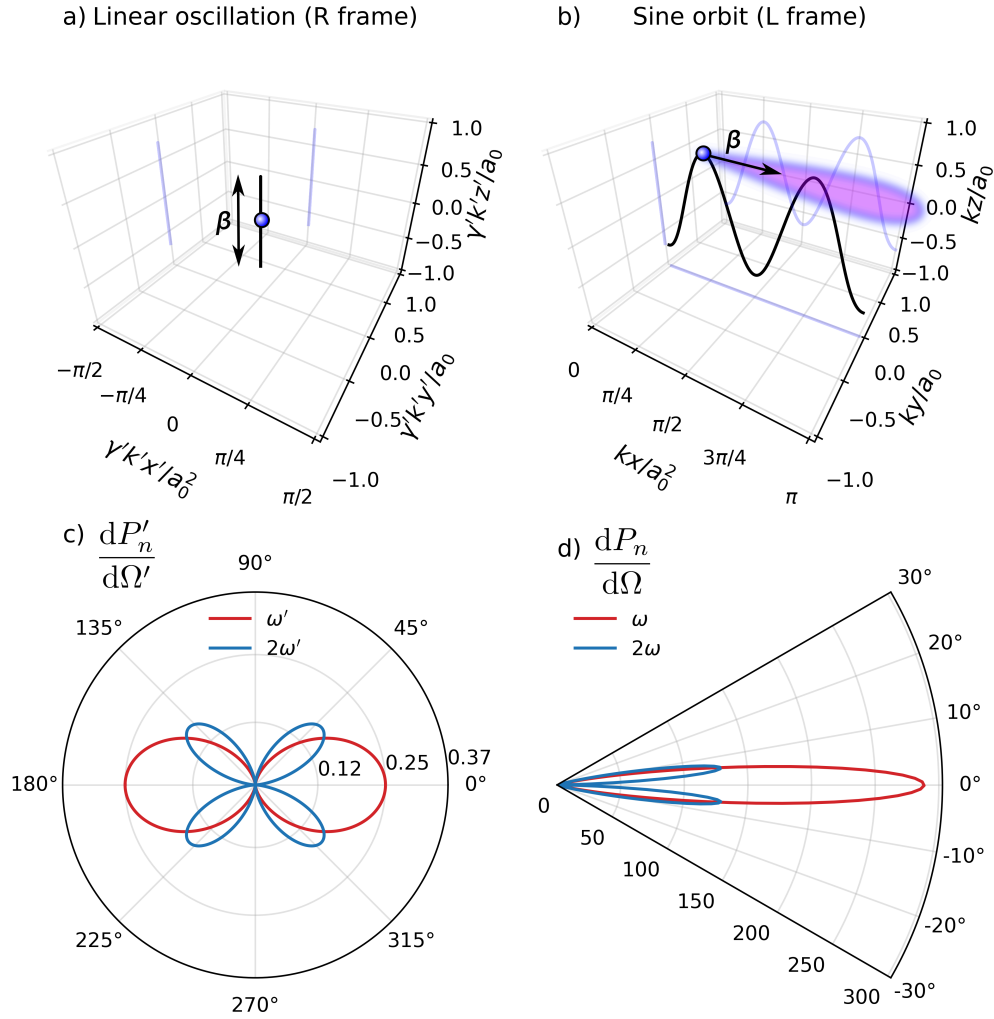
Figure 11: Linear oscillatory orbits in the R frame (a) with corresponding power distribution (c). Sine trajectory in the L frame (b) and corresponding power distribution (d). R frame moves with respect to L frame with $\gamma = 3$.

Nonlinear inverse Thomson scattering

Suppose the electrons are initially not at rest but propagate with some relativistic velocity β towards a head-on collision with the incident laser. In that case, the laser frequency is boosted in the R frame, as $\omega'_0 = \gamma\omega_0(1+\beta) \approx 2\gamma\omega_0$. Transforming back into the L frame, we find the harmonics given by Eq. (111) enhanced by a factor of $\sqrt{(1+\beta)/(1-\beta)} \approx 4\gamma^2$, i.e.

$$\omega_n \approx \frac{4\gamma^2 n\omega_0}{1 + \frac{a_0^2}{4}(1-\cos\theta)}. \tag{115}$$

With the upshift factor included in the harmonics, Eq. (114) describes what is known as *nonlinear inverse Thomson scattering*. This is illustrated in Fig. 11, which shows an electron

propagating with $\gamma = 3$ along the x axis in the L frame. If the electron performs linear harmonic oscillations in the R frame[15], the power distribution and frequency harmonics become boosted according to Eqs. (110)–(111), where the R frame laser frequency is given according to Lorentz transform, i.e., relativistic Doppler effect, as $\omega_0' = \gamma(1 + \beta)\omega_0$.

Nonlinear inverse Compton scattering

Yet, the zoo of laser scattering processes grows even more complex. If, in the R frame, the laser photon energy approaches the electron energy, $\hbar\omega_0' \approx \gamma' m_e c^2$, the process is called *inverse Compton scattering*. In this case, the conservation of energy and momentum leads to non-negligible electron recoil, which changes the energy of scattered radiation. The angular distribution of radiation can be calculated in the framework of quantum electrodynamics [Di Piazza et al., 2012], a detailed discussion of which is beyond the intended scope of this thesis, and patience of the kind reader[16]. In addition, it is sufficient for quantum effects to arise already if the local laser energy approaches the electron energy in the R frame, $n\hbar\omega_0' \approx \gamma' m_e c^2$, such process is then called *nonlinear inverse Compton scattering*. For the sake of completeness, we at least cite the result for the on-axis harmonics emitted due to this process [Meyerhofer, 1997]

$$\omega_n = \frac{4\gamma^2 n\omega_0}{1 + 4\gamma^2 n\frac{\hbar\omega_0}{m_e c^2} + a_0^2}. \tag{116}$$

The second term in the denominator enforces is due to the conservation of energy and momentum and can be obtained classically from relativistic kinematics. However, the third term is purely quantum due to a so-called electron *mass shift*.

In summary, we have discussed that relativistically intense lasers ionize matter and force electrons to execute harmonic oscillations, the velocity of which can approach the speed of light. We have shown that the motion of relativistic electrons always leads to a frequency shift of emitted radiation compared to the oscillation frequency. Radiation sources based on laser scattering from relativistic electron beams are known as inverse Compton scattering (ICS) sources [Ta Phuoc et al., 2012; Corde et al., 2013], and currently enjoy the focus of active research due to their immense potential for applications [Albert and Thomas, 2016; Chaulagain et al., 2022]. The following sections discuss relativistic laser interaction with a medium composed of many free electrons – plasma. As we will see, many of the radiation features discussed until now will also apply to the collective motion of electrons within the plasma.

2.3   Interaction of electromagnetic field with plasma

The interaction of plasma with electromagnetic fields is described by the coupled set of the following partial differential equations: microscopic Maxwell's equations (1)–(4), continuity equation (5) and the momentum equation for both electrons and ions (10). We adopt the Eulerian (fluid) description of plasma. In the Eulerian specification, we describe properties of

---

[15]This is true for counter-propagating laser with circular polarization, or linear polarization and $a_0 \ll 1$, at which point we can neglect the longitudinal $2\omega_0$ oscillations. We refer to [Sarachik and Schappert, 1970] for a general treatment, which includes the $2\omega_0$ longitudinal component. The most important consequence of the general treatment for linear polarization is that odd harmonics are non-zero on-axis. In contrast, the even harmonics are non-zero only off-axis.

[16]For recent summary and direction of quantum electrodynamics in the context of high-intensity lasers, we refer to [Di Piazza et al., 2012; Blackburn, 2020].

plasma, such as momentum $\mathbf{p}$, at every position in space and time, denoted by coordinates x and t, respectively. This allows us to rewrite the Lagrangian derivative in terms of the Eulerian coordinates as $(d_t)_{Lagr.} = (\partial_t + \mathbf{v} \cdot \nabla)_{Euler}$. The closed set of equations can be written out in Lorenz gauge as [Farina and Bulanov, 2001; Bulanov et al., 2013; Bulanov, 2021]

$$\Delta \mathbf{a} - \frac{\partial^2 \mathbf{a}}{\partial t^2} = n_e \boldsymbol{\beta}_e - Z n_i \boldsymbol{\beta}_i, \tag{117}$$

$$\Delta \phi - \frac{\partial^2 \phi}{\partial t^2} = n_e - Z n_i, \tag{118}$$

$$\frac{\partial n_\alpha}{\partial t} + \nabla \cdot (n_\alpha \boldsymbol{\beta}_\alpha) = 0, \tag{119}$$

$$\frac{\partial}{\partial t} (\mathbf{p}_\alpha + q_\alpha \mathbf{a}) = -\nabla (\rho_\alpha \phi + \gamma_\alpha) + \boldsymbol{\beta}_\alpha \times \nabla \times (\mathbf{p}_\alpha + q_\alpha \mathbf{a}). \tag{120}$$

The electron and ion variables are denoted by subscripts e and i, and $\alpha \in \{e, i\}$. In the momentum equation (120), we have used the identity $\mathbf{v} \times (\nabla \times \mathbf{p}) = \gamma^{-1} \nabla |\mathbf{p}|^2 - (\mathbf{v} \cdot \nabla) \mathbf{p}$. We have introduced the following normalizations to obtain dimensionless quantities

$$\mathbf{a} = \frac{e\mathbf{A}}{m_e c}, \quad \mathbf{p}_\alpha \to \frac{\mathbf{p}_\alpha}{m_\alpha c}, \quad \phi \to \frac{e\phi}{m_e c^2}, \quad \boldsymbol{\beta}_\alpha = \frac{\mathbf{v}_\alpha}{c}, \quad t \to \omega_{pe} t, \quad x \to \frac{c}{\omega_{pe}} x, \quad n_\alpha \to \frac{n_\alpha}{n_0}, \tag{121}$$

where $\omega_{pe} = \sqrt{e^2 n_0 / m_e \epsilon_0}$ is the linear plasma frequency and n_0 is the homogeneous density of the fluid components, which are initially at equilibrium. The number density of plasma electrons n_α is normalized by n_0. In these units, the Lorentz factor for both fluids is given as $\gamma_\alpha = \sqrt{1 + |\mathbf{p}_\alpha|^2}$. We have also introduced the normalized charge-to-mass ratio $\rho_\alpha = -(q_\alpha/e)(m_e/m_\alpha)$, where q_α and m_α are the particle charge and rest mass of the fluid component α. Specifically, for the electrons ($\alpha = e$) we have $q_\alpha = -e$ and $m_\alpha = m_e$, and for the ions ($\alpha = i$) we have $q_\alpha = Ze$ and $m_\alpha = m_i$, where Z is the ion charge number.

2.3.1 Ultrashort laser pulses and static ion approximation

In the following sections, we will be primarily interested in the interaction of plasma with electromagnetic laser pulses on the femtosecond (fs) timescale; that is, we will study the immediate effects that occur close to an ultrashort electromagnetic pulse propagating in plasma. In this case, the ion contribution can be neglected, which is known as *static ion approximation*, where we consider $\boldsymbol{\beta}_i \approx 0$ and $n_i \approx 1$. It is simple to verify that the electrons are the main contribution to the current affecting the electromagnetic field at this timescale. Lightest (in terms of ion mass m_i) plasma can be created by ionizing hydrogen, yielding protons as the ions, which carry the significantly larger mass of $m_p \approx 1837 m_e$. For any heavier stable element, the ratio of ion mass A to ion charge number Z will be at least twice as large.

Eqs. (117) – (120) describe the interaction of the electromagnetic field with *cold collisionless plasma* [Chen et al., 1984], where we consider only microscopic interaction between electrons, ions, and fields. At the timescale of ions $\tau \sim 1/\omega_{pi}$, which is typically of the order of picoseconds (ps)[17], the description of plasma dynamics should include the ion motion, but potentially also pressure and temperature effects due to Coulombic collisions. These are typically described by a more general *kinetic theory of plasma* [Chen et al., 1984; Arber

---

[17]This depends primarily on the amplitude of the laser. A sufficiently strong laser can induce ion motion on a faster timescale.

et al., 2015], which is based on particle distribution functions, the evolution of which is typically solved for numerically [18]. Coulomb collisions between individual electrons or electrons and ions can be indeed neglected for relativistic laser-plasma interaction since collisional cross-section follows $\sigma \sim 1/v^4$, where v is the relative velocity of two electrons [Chen et al., 1984]. At relativistic velocities, electrons are more "slippery", and such collisions become increasingly negligible, making the evolution of the macroscopic electromagnetic field the primary mechanism behind the motion of relativistic electrons.

For simplicity, we now assume ions with $Z = 1$. As stated above, within the static ion approximation, we solve only for the dynamical variables of the electron fluid, in which case the closed set of equations (117) – (120) reduces to

$$\Delta \mathbf{a} - \frac{\partial^2 \mathbf{a}}{\partial t^2} = n_e \boldsymbol{\beta}, \tag{122}$$

$$\Delta \phi - \frac{\partial^2 \phi}{\partial t^2} = n_e - 1, \tag{123}$$

$$\frac{\partial n_e}{\partial t} + \nabla \cdot (n_e \boldsymbol{\beta}) = 0, \tag{124}$$

$$\frac{\partial}{\partial t} (\mathbf{p} - \mathbf{a}) = \nabla (\phi - \gamma) + \boldsymbol{\beta} \times \nabla \times (\mathbf{p} - \mathbf{a}). \tag{125}$$

Taking the curl of Eq. (125), we get identically $\nabla \times \nabla(\phi - \gamma) = 0$ and the remaining terms become

$$\frac{1}{c} \frac{\partial}{\partial t} [\nabla \times (\mathbf{p} - \mathbf{a})] = \nabla \times [\boldsymbol{\beta} \times \nabla \times (\mathbf{p} - \mathbf{a})]. \tag{126}$$

The quantity $\Omega = \nabla \times (\mathbf{p} - \mathbf{a})$ is known as *generalized vorticity* [Chen et al., 1984; Hasegawa and Mima, 1977; Bulanov et al., 2001]. Eq. (126) is a variant of the *frozen-in flux theorem* for generalized vorticity Ω, sometimes also called induction equation. If $\Omega = 0$ initially, before the electromagnetic field enters plasma, Eq. (126) tells us that $\Omega = 0$ holds for all time. In this case, we say that the plasma is *initially irrotational* and the vorticity of electrons is bound to magnetic field lines, $\nabla \times \mathbf{p} = \nabla \times \mathbf{a} = e\mathbf{B}/m_e c$. For initially irrotational plasma, Eq. (125) reduces to

$$\frac{1}{c} \frac{\partial}{\partial t} (\mathbf{p} - \mathbf{a}) = \nabla (\phi - \gamma). \tag{127}$$

According to Eqs. (52) and (123), the scalar potential is determined by the electron (charge) density distribution. Therefore, the first term $\nabla \phi$ describes the electrostatic *space-charge force* arising due to a charge distribution. The second term $-\nabla \gamma$ is known as *generalized nonlinear ponderomotive force* [Sprangle et al., 1992; Chen and Sudan, 1993].

Eq. (127) admits the solution $\mathbf{p} = \mathbf{a}$, which requires that the electrostatic space-charge force is exactly compensated by the ponderomotive force, $\nabla(\phi - \gamma) = 0$. In this case, we have exactly $\gamma = \sqrt{1 + |\mathbf{p}|^2} = \sqrt{1 + |\mathbf{a}|^2}$, and the ponderomotive force becomes $f_{pond} = -\nabla \gamma = -\frac{1}{2\gamma} \nabla |\mathbf{a}|^2$. The ponderomotive force pushes electrons out from the regions of high intensity to regions of low intensity. More precisely, the force is strongest when the gradient of the radiation intensity ($\nabla |\mathbf{a}|^2 \sim \nabla I$) is largest [Sprangle et al., 1992; Chen and Sudan, 1993]. At the same time, an electrostatic field emerges due to the created space-charge inhomogeneity, which creates an equal and opposite force that pushes the electrons back into the region from which the ponderomotive force expelled them. For transverse components of momentum,

---

[18]For a review of the kinetic theory and algorithms for numerical solutions known as *particle-in-cell method*, see Refs. [Birdsall and Langdon, 2004; Arber et al., 2015].

$\mathbf{p}_\perp = \mathbf{a}$ also holds in the case when the laser beam is transversally large, in which case the transverse derivatives can be neglected. We also satisfy $\nabla_\perp(\phi - \gamma) \approx 0$. Note that these electrostatic fields, which arise due to the collective motion of plasma, act to cancel the longitudinal drift that is present in the motion of free electrons interacting with relativistic electromagnetic field (28) [Gibbon, 2005].

Creating such electrostatic fields with the strength of the order comparable to ponderomotive force due to laser fields is an essential feature of relativistic laser-plasma interactions. A laser pushing with ponderomotive force on plasma through which it propagates creates a copropagating electrostatic field due to space-charge force. If charged particles are injected into the correct phase of the copropagating electrostatic field, it can act as an accelerator. In the case of electrons, this is known as *laser wakefield acceleration* (LWFA) [Tajima and Dawson, 1979; Andreev et al., 1992; Pukhov and Meyer-ter Vehn, 2002; Esirkepov et al., 2006; Lu et al., 2006; Lu et al., 2007; Esarey et al., 2009; Bulanov et al., 2016a], where accelerating gradients four orders of magnitude larger than those produced in conventional radiofrequency accelerators can be achieved [Dawson, 1959; Faure et al., 2004; Geddes et al., 2004; Mangles et al., 2004], enabling compact laser-driven acceleration of electrons to multi-GeV energies in centimeter-scale plasma [Kim et al., 2013; Leemans et al., 2014; Gonsalves et al., 2019; Aniculaesei et al., 2024]. Plasma can be, therefore, used as an efficient optical rectifier. This concept will be discussed in more detail in the following sections.

2.3.2 Relativistic transparency

Let us now focus on the evolution of an electromagnetic wave when the ponderomotive and the space-charge force compensate each other, i.e., $\mathbf{p} = \mathbf{a}$. The Lorentz factor is then $\gamma(\mathbf{r}, t) = \sqrt{1 + |\mathbf{a}(\mathbf{r}, t)|^2}$. Using that the velocity of the electrons is now $\boldsymbol{\beta} = \mathbf{p}/\gamma = \mathbf{a}/\gamma$, the wave equation (123) can be written in the form of Klein-Gordon equation (in dimensional units), as

$$\left(c^2 \Delta - \frac{\partial^2}{\partial t^2} - \omega_{p,r}^2(\mathbf{r}, t) \right) \mathbf{a}(\mathbf{r}, t) = 0, \tag{128}$$

where $\omega_{p,r} = \omega_{pe}/\sqrt{\gamma}$ is the inhomogeneous relativistic plasma frequency, which can vary in both space and time since both the Lorentz factor γ and the electron density n_e are generally functions of space and time coordinates. To obtain the dispersion relation of electromagnetic waves, we now consider only a single monochromatic plane wave propagating in plasma, $\mathbf{a}(\mathbf{r}, t) = \mathbf{a}_0 \exp(i\varphi)$, where the phase of the wave is given as $\varphi = \mathbf{k} \cdot \mathbf{r} - \omega t$. We get the following dispersion relation, valid for any constant amplitude $\mathbf{a}_0$,

$$\left(-c^2 k^2 + \omega^2 - \omega_{p,r}^2 \right) \mathbf{a}_0 = 0, \tag{129}$$

in other words,

$$\omega^2 = c^2 k^2 + \omega_{p,r}^2. \tag{130}$$

Note that the dispersion relation (130) derived from the wave equation for $\mathbf{A}$ must indeed equal the dispersion relation for the linear waves described by the real fields $\mathbf{E}$ and $\mathbf{B}$, since their phase can differ from the phase of $\mathbf{A}$ only up to a constant phase shift φ_0, which is determined by the derivative of $\mathbf{A}$, according to the definition of the real fields (6) – (7). A particular phase front propagates according to $\varphi = const$. For example, the first crest of the wave satisfies $\varphi = 0$, i.e., $\mathbf{k} \cdot \mathbf{r} = \omega t$. If we choose the coordinate system such that axis x is parallel with the wave vector $\mathbf{k}$, we can get the velocity of this phase using dispersion

relation (130), referred to as *phase velocity* [Born and Wolf, 1959],

$$v_p = \frac{\mathrm{d}x}{\mathrm{d}t} = \frac{\omega}{k} = \frac{c}{n}, \tag{131}$$

where we have introduced the *refractive index* of inhomogeneous relativistic plasma [Gibbon, 2005]

$$n(\mathbf{r}, t) = \sqrt{1 - \left(\frac{\omega_{p,r}}{\omega}\right)^2} = \sqrt{1 - \frac{n_e}{\gamma n_c}}, \tag{132}$$

where $n_c = \omega^2 \epsilon_0 m_e / e^2$ is the critical density. The phase velocity of electromagnetic waves defines two regimes of interaction. For $\omega > \omega_{p,r}$, the phase velocity is real, and the wave can travel in plasma, which is therefore described as *relativistically underdense*. For $\omega < \omega_{p,r}$, the phase velocity is imaginary, and the wave is reflected upon entry into the plasma; such plasma is described as *relativistically overdense*. Within the plasma, the evanescent wave has the wave vector magnitude $k \approx i\omega_{p,r}/c = i/\delta_{p,r}$ [Chen et al., 1984]. The electromagnetic field can, therefore, penetrate the plasma upon entry from vacuum up to a length which is approximately equal to the *relativistic skin depth* $\delta_{p,r} = c/\omega_{p,r}$. In a non-relativistic scenario, where $\gamma \sim 1$, we retrieve the well-known behavior of plasma or ideal metals, where waves with frequency smaller than the linear plasma frequency become reflected from the metal back into vacuum [Born and Wolf, 1959].

For the superposition of monochromatic waves, the velocity of such an electromagnetic pulse corresponds to the slope of the dispersion relation (130), known as *group velocity* [Born and Wolf, 1959],

$$v_g = \frac{\partial \omega}{\partial k} = cn, \tag{133}$$

where the last equality is valid specifically for plasma. The phase and group velocities in plasma, therefore, satisfy $v_p v_g = c^2$. Note that the phase velocity in plasma is larger than the speed of light, $v_p > c$, since $n < 1$. Fortunately, causality is preserved if we understand that information can propagate between two spacetime events only through changes in the electromagnetic field, which correspond to electromagnetic pulses propagating with group velocity (133), which is smaller than the speed of light.

While we have derived the refractive index for a monochromatic wave, this result can be generalized to an electromagnetic pulse with a slowly varying envelope. Averaging Eq. (128) over a single laser cycle, we get an equation for a slowly varying amplitude envelope $\mathbf{a}_0(\mathbf{r}, t)$, with a refractive index that has the same form as Eq. (132), except that now the Lorentz factor is averaged over in time and polarization independent. Such averaging over the laser envelope amounts to the following simple substitution, $\gamma \to \gamma_0 = \sqrt{1 + \langle |\mathbf{a}|^2 \rangle} = \sqrt{1 + \frac{a_0^2}{2}}$, in Eq. (132).

A laser pulse can therefore penetrate even *overdense* ($n_e > n_c$) plasma when $\gamma_0 > n_e/n_c$. This is a unique feature of relativistic optics known as *self-induced relativistic transparency* (SIT). For ultra-relativistic amplitudes with $a_0 \gg 1$, we have $\gamma_0 \approx a_0/\sqrt{2}$ and from Eq. (132) the condition for SIT takes a simple form [Kaw and Dawson, 1970]

$$a_0 > \sqrt{2}\frac{n_e}{n_c}. \tag{134}$$

Another kind of wave that can propagate in plasma, apart from the electromagnetic wave with $\mathbf{a} \neq 0$, is the electrostatic wave with $\mathbf{a} = 0$. These waves do not carry magnetic field, since $\nabla \times \mathbf{a} = 0$, and the Lorenz condition gives $\partial_t \phi = c^2 \nabla \cdot \mathbf{a} = 0$. Therefore, Eq. (123)

reduces to Poisson's equation, $\Delta\phi = n_e - 1$. If we consider a plane wave solution for the scalar potential, $\phi \sim \exp(i\mathbf{k}\cdot\mathbf{r} - i\omega t)$, we can linearize Eqs. (122) – (125) to obtain the following dispersion relation for electrostatic waves propagating in plasma, $\omega = \omega_{pe}$ [Chen et al., 1984; Gibbon, 2005]. This tells us that the wave vector k is not determined by the wave equation for scalar potential, and the phase velocity $v_p = \omega_p/k$ may have arbitrary values. This also means that the group velocity (133) equals zero. These waves are known as electron *plasma waves* since they exist thanks to the plasma electron density modulations given by the right-hand side of Poisson's equation. Additionally, from the definition of the scalar potential, we see that the waves are *longitudinal*, since the electric field is polarized in the direction of wave motion, $\mathbf{E} = -\nabla\phi = -i\mathbf{k}\phi$. Since the longitudinal plasma waves can propagate even with $v_p \lesssim c$, they are the key that unlocks plasma-based acceleration of well-injected charged particles to relativistic velocities [Tajima and Dawson, 1979]. Also, this electrostatic field is responsible for canceling the longitudinal drift of free electrons [Gibbon, 2005]. The averaged Lorentz factor of laser-driven plasma electrons initially at rest is, therefore, smaller in plasma, as shown above. It can be related to the averaged Lorentz factor of free electrons as $\langle\gamma_{free}\rangle = \langle\gamma_{plasma}\rangle^2$. Note that this does not mean that vacuum acceleration is more efficient. As we will show later, electrons injected into the accelerating phase of the wave can achieve significantly higher energy.

The nonlinear refractive index given by Eq. (132) foreshadows that relativistic laser-plasma interactions can yield abundant nonlinear optical effects, such as the already introduced self-induced transparency. The refractive index also clearly splits the remaining physical discussion into two different cases: a) relativistically underdense plasma ($\omega > \omega_{pe}/\sqrt{\gamma}$), where the laser freely propagates, and b) relativistically overdense plasma ($\omega < \omega_{pe}/\sqrt{\gamma}$), where region of interest narrows down to the surface of the plasma target, from which the laser field must reflect according to the refractive index. Therefore, the following sections reflect this disjunction, and we focus on these two cases individually, with a selection of topics.

2.4 Relativistically underdense plasma

When the plasma is relativistically transparent, we return to the wave equation (128) to understand the nonlinear evolution of the laser field throughout its propagation. The laser propagates in plasma with normalized group velocity $\beta_g \approx ck_0/\omega_0$. It, therefore, seems convenient to express wave equation (122) in terms of the following coordinates, $t = \tau$ and $\xi = z - v_g t$, where ξ is the copropagating coordinate which measures the relative distance from the propagating laser pulse. The derivatives transform as

$$\frac{\partial}{\partial t} = \frac{\partial\xi}{\partial t}\frac{\partial}{\partial\xi} + \frac{\partial\tau}{\partial t}\frac{\partial}{\partial\tau} = -v_g\frac{\partial}{\partial\xi} + \frac{\partial}{\partial\tau}, \tag{135}$$

$$\frac{\partial}{\partial z} = \frac{\partial\xi}{\partial z}\frac{\partial}{\partial\xi} + \frac{\partial\tau}{\partial z}\frac{\partial}{\partial\tau} = \frac{\partial}{\partial\xi}, \tag{136}$$

which gives us the wave equation[19] as [Bulanov et al., 1992; Decker et al., 1996; Mori, 1997; Bulanov et al., 2001]

$$\left[\frac{1}{\gamma_g^2}\frac{\partial^2}{\partial\xi^2} + \nabla_\perp^2 + 2\beta_g\frac{\partial^2}{\partial\xi\partial\tau} - \frac{\partial^2}{\partial\tau^2}\right]\mathbf{a} = n_e\boldsymbol{\beta_e}, \tag{137}$$

---

[19]In normalized units as before – length is given in units of c/ω_{pe}, and time in units of $1/\omega_{pe}$.

where $\gamma_g = 1/\sqrt{1 - \beta_g^2}$ is the Lorentz factor of the laser pulse and β_g is the normalized group velocity. The first term on the left-hand side of Eq. (137) disperses the laser pulses longitudinally. The laser pulse is longitudinally increasingly more stable in the relativistic limit $\gamma_g \gg 1$. This is equivalent to propagation in low-density plasma, since $(v_g/c)^2 \approx 1 - (\omega_{pe}/\omega_0)^2$. The second term is responsible for the transverse modulation of the laser beam. As we will show later, this can lead to nonlinear effects such as *self-focusing* [Litvak, 1970; Bulanov and Sakharov, 1991; Sprangle et al., 1992; Chen and Sudan, 1993; Askaryan et al., 1994; Bulanov et al., 1995], which can enable self-guiding of the laser on distances significantly larger than the typical Rayleigh length. The third term describes variations in the laser group velocity, and the fourth term is responsible for fast variations of a forward-going wave and can be typically neglected. The right-hand side is once again the source term. In the previous sections, we have shown that the transverse momentum can be taken as $\mathbf{p} = \mathbf{a}$ for ponderomotive and space-charge force compensation or one-dimensional approximation. In other scenarios, it is nevertheless the leading order contribution [Esarey et al., 2009]. We therefore take $\boldsymbol{\beta}_e \approx \mathbf{a}/\gamma_e$.

Let us now consider a forward propagating wave with the following normalized vector potential $\mathbf{a}(r, \xi, \tau)e^{ik\xi}$, where $\mathbf{a}$ is the envelope of the laser which evolves slowly in time and $r = \sqrt{x^2 + y^2}$ is the transverse distance from the beam center. We assume that $\gamma_g \gg 1$, and the wave equation (137) in the slowly varying envelope approximation[20] (SVEA) can be written as

$$\left[2i\omega_0 \frac{\partial}{\partial \tau} + \nabla_\perp^2 + 2\beta_g \frac{\partial^2}{\partial \xi \partial \tau} \right] \mathbf{a} = \frac{n_e}{\gamma_e} \mathbf{a}. \tag{138}$$

It is helpful to note that the source term on the right-hand side is related to the refractive index of plasma (132), as $(n_e/\gamma_e)\mathbf{a} = n_c(1 - n^2)\mathbf{a}$, which can help draw analogies between Eq. (138) and well known nonlinear optical effects based on modulations of refractive index [Mori, 1997]. We see that the refractive index, as well as group and phase velocities, can be altered by changes in plasma density and laser amplitude or frequency [Esarey et al., 1990; Bulanov et al., 1992; Mori, 1997].

We first assume the *quasistatic approximation* [Gibbon, 2005] to see how the plasma evolves with the laser pulse as it propagates. This approximation assumes that plasma electrons evolve on a much faster timescale than the laser envelope, allowing us to approximate changes in plasma quantities as instantaneous, i.e., for normalized potential $\partial_t \phi \approx 0$. Additionally, we assume that the plasma response is due to a wide laser beam ($k_p w_0 \gg 1$, where w_0 is the laser waist), allowing us to approximate the transverse changes of the beam with respect to the longitudinal ones as $\nabla_\perp \phi \ll \partial_\xi \phi$. The continuity equation (124) in the Eulerian coordinates then becomes $\partial_\xi n_e(\beta_g - \beta_e) = 0$, where we have assumed that the transverse modulations of the plasma are negligible. Assuming that the plasma is at rest at $\xi = 0$, we have after integration (in normalized units) $n_e = 1/(1 - \beta_e/\beta_g)$. Note that the plasma density diverges for electrons approaching the group velocity of the laser pulse. This divergence indicates a singularity in the fluid description of the dynamics. It corresponds to so-called *wave breaking*, through which individual electrons become released from the fluid-like motion of plasma. Similarly, we can integrate the longitudinal component of the momentum equation (127) to obtain the following constant of motion of plasma electrons,

$$\gamma_e(1 - \beta_g \beta_e) = 1 + \phi. \tag{139}$$

---

[20]This approximation assumes that the laser pulse evolves slowly compared to the plasma electrons, and therefore it neglects the second derivative with respect to time in Eq. 137.

Plugging these into Eq. (123), we get the following equation for the evolution of the plasma waves [Esarey et al., 1997]

$$\frac{\partial \phi^2}{\partial \xi^2} = \gamma_g^2 \left[\beta_g \left(1 - \frac{1 + a^2}{\gamma_g^2 (1 + \phi)^2} \right)^{-1/2} - 1 \right] - \rho, \tag{140}$$

where $\gamma_g = 1/\sqrt{1 - \beta_g^2}$ is the Lorentz factor corresponding to the velocity of the wave coordinates, and ρ is the externally injected charge distribution propagating within the plasma, and $a = |\mathbf{a}|$ is the magnitude of the normalized vector potential. To simplify the following discussion, we assume the ultra-relativistic limit $\gamma_g \gg 1$, i.e., low-density plasma and $v_g \approx c$, and $\rho \approx 0$, i.e., no external charged particle beam is injected into the plasma[21]. The ultra-relativistic approximation neglects the effects of plasma wave breaking, i.e., plasma wave steepening due to the accumulation of electrons as they approach the phase velocity of the plasma wave, $\beta_e \to \beta_g$ [Bulanov et al., 1992; Bulanov et al., 1998; Bulanov et al., 2001; Panchenko et al., 2008]. Now, we are primarily interested in describing plasma waves copropagating with a laser pulse.

The nonlinear plasma wave equation in the ultra-relativistic limit simplifies to the following form [Bulanov et al., 1989; Berezhiani and Murusidze, 1990; Esarey et al., 2009; Bulanov et al., 2016a; Bulanov, 2021]

$$\frac{\partial \phi^2}{\partial \xi^2} = \frac{1}{2} \left(\frac{1 + a^2}{(1 + \phi)^2} - 1 \right). \tag{141}$$

Assuming a laser pulse with constant amplitude $a = const.$, and that the plasma is undisturbed at the pulse front, $\phi(\xi = 0) = \partial_\xi \phi(\xi = 0) = 0$[22], Eq. (141) can be integrated to get the following equation for the longitudinal electric field ($E_\parallel = -\partial_\xi \phi$) as

$$E_\parallel^2 = \left(\frac{\partial \phi}{\partial \xi} \right)^2 = \frac{\phi(a^2 - \phi)}{1 + \phi}. \tag{142}$$

Indeed, this is the equation for an oscillating electric field; the condition for the existence of periodic solutions is given by $\phi'' = 0$, which can be easily checked to be equivalent to $a^2 > 0$. This condition is satisfied for any laser pulse shape or amplitude. Therefore, plasma waves are excited and copropagate with any laser pulse in plasma. Additionally, we see that the potential oscillates within the laser pulse between the values $\phi_{\min} = 0 < \phi < \phi_{\max} = a^2$. To calculate the wavelength of the plasma wave, we invert and integrate Eq. (142) to obtain an implicit solution

$$\xi(\phi, a^2) = \int_0^\phi \sqrt{\frac{1 + \varphi}{\varphi(a^2 - \varphi)}} \mathrm{d}\varphi. \tag{143}$$

The roots of the electric field of the oscillating plasma wave are given by the condition $\phi' = 0$, which gives their presence from Eq. (142) at the points where either $\phi_{\min} = 0$ or $\phi_{\max} = a^2$. Integrating the implicit solution from $\phi = 0$ up to $\phi = a^2$, we get the distance between the first two zeroes of the electric field, which yields the following formula for the

---

[21]See contents of paper B.2 for an overview of beam-driven plasma wakefields.

[22]To obtain analytical results which qualitatively describe properties of plasma waves excited by more realistic pulse shapes, we are considering a flat-top laser pulse shape for the moment.
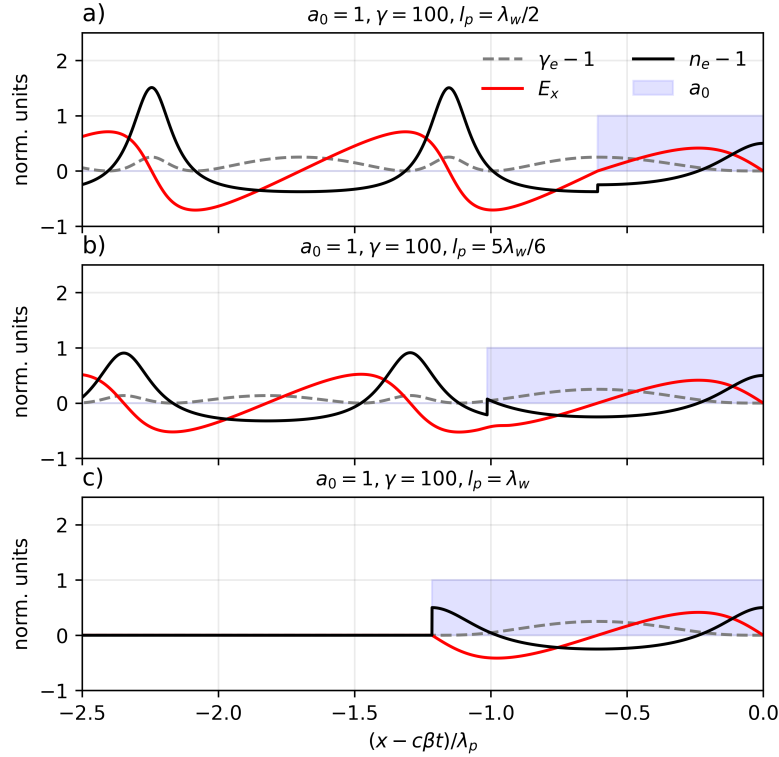
Figure 12: Numerical solutions of Eq. (140) showing the effect of laser pulse length
l_p **on plasma wave excitation.** Normalized laser amplitude (blue), normalized electron density
(black), longitudinal electric field (red) and Lorentz factor of the plasma electrons (grey, dashed) for
different pulse durations: $l_p = l_{opt} = \lambda_w/2$ (a), $l_p = 5\lambda_w/6$ (b) and $l_p = \lambda_w$ (c), which corresponds to
the no-wakefield condition. Since the ultra-relativistic limit applies ($\gamma_w = \gamma_g = 100$), the wavelength
of the interior plasma wave is given by Eq. (144), and the electric field amplitude of the wake plasma
wave is given by Eq. (147). The plasma wave amplitude is largest in the optimal case (146).

nonlinear plasma wavelength λ_w [Bulanov et al., 2016a],

$$\frac{\lambda_w}{\lambda_{pe}} = \frac{2\xi(\phi_{\max}, a^2)}{2\pi} = \frac{1}{\pi} \int_0^{a^2} \sqrt{\frac{1+\varphi}{\varphi(a^2 - \varphi)}} \mathrm{d}\varphi = \frac{2}{\pi} E(-a^2), \tag{144}$$

where $E(k)$ is the complete elliptic integral of the second kind [Gradshteyn and Ryzhik, 1965],
and $\lambda_{pe} = 2\pi c/\omega_{pe}$ is the linear plasma wavelength[23]. In the limit $a_0^2 \ll 1$, the wavelength
reduces to the linear plasma wavelength $\lambda_w \approx \lambda_{pe}$. In the large amplitude limit $a_0^2 \gg 1$,
the plasma wavelength is elongated, as $\lambda_w \approx \lambda_{pe}(2a_0/\pi)$. In the same manner, we can find
the amplitude of the electric field from the condition $E' = -\phi'' = 0$, which occurs when
$\phi_\pm = \pm\sqrt{1 + a^2} - 1$. Plugging this into Eq. (142), we get the electric field amplitude of the
interior laser-driven plasma waves as $E_{\max} = \sqrt{1 + a^2} - 1$. Therefore, the laser amplitude
directly dictates the nonlinearity of the electron plasma wave response.

We note that plasma waves can also be excited in the wake of a laser pulse. Such a

---

[23]$\lambda_{pe} = 2\pi$ in the dimensionless units used throughout the derivation.

plasma wave is often referred to as *laser wakefield*. If we consider a laser with pulse length $l_{pulse} = l_{opt} = \lambda_w/2$ such that it ends exactly after the first half-cycle of the plasma wave, $\phi'(-l_{opt}) = 0$, the electrostatic potential at the trailing edge of the pulse becomes maximized, $\phi(-l_{opt}) = a^2$. Taking these values as the boundary conditions for the evolution behind the laser pulse, we integrate Eq. (141) again to obtain an equation for the longitudinal electric field of the wake wave

$$E_\parallel^2 = \left(\frac{\partial \phi}{\partial \xi}\right)^2 = (a^2 - \phi)\left(1 - \frac{1}{(1 + a^2)(1 + \phi)}\right). \tag{145}$$

Note that the potential maxima and minima in the wake can be obtained as $\phi_{\max} = a^2$ and $\phi_{\min} = -a^2/(1 + a^2)$. Indeed, the potential is also maximized in the wakefield due to our choice of pulse length. That is, any other choice would produce $\phi_{\max} < a^2$. The condition for resonant wakefield excitation can be, therefore, formulated in terms of the following requirement for the optimal pulse duration

$$l_{opt} = \frac{\lambda_w}{2}, \tag{146}$$

with the nonlinear plasma wavelength λ_w given by Eq. (144). The optimal pulse duration also implies that a flat-top pulse with a length of $l_p = 2l_{opt}$ excites no wakefield. An interior plasma wave is excited, but at the pulse rear, which equals a full cycle of the plasma wave, we have $\phi = 0$. That is, the pulse does not transfer any energy into the wake. While this is, in principle, possible, the interior plasma wave modulates the refractive index. This quickly changes the flat-top pulse shape such that the no-wakefield condition $l_p = 2l_{opt}$ is quickly broken, and wakefield amplitude grows. This is shown in Fig. 12, which shows excitation of both the interior plasma wave with wavelength given by Eq. (144) and the plasma wake wave.

The potentials corresponding to the minima and maxima of the oscillating electric field, $E = -\phi'$, were derived above as $\phi_\pm = \pm\sqrt{1 + a^2} - 1$ from the condition $\phi''_\pm = 0$. Plugging $\phi_\pm$ (with $a^2 = 0$ for the wake region) into Eq. (145), we find that the longitudinal electric field of the plasma wave oscillates between the values $-E_{\max} < E < E_{\max}$, where the electric field amplitude of the wake $E_{\max}$ is given in dimensional units as

$$E_{\max} = \frac{m_e c \omega_{pe}}{e} \frac{a^2}{\sqrt{1 + a^2}}. \tag{147}$$

It is also useful to note that for weakly relativistic lasers with $a^2 \ll 1$, Eq. (141) can be linearized, since $\phi < a^2 \ll 1$. The result is the following linear equation for plasma waves (valid for $a^2 \ll 1$),

$$\frac{\partial \phi^2}{\partial \xi^2} + \phi = \frac{a^2}{2}. \tag{148}$$

Solution for arbitrary laser pulse shape can be then found immediately through convolution of the right-hand side with the fundamental solution of the equation, $\phi_0(\xi) = \theta(\xi)\sin(\xi)$ where $\theta(\xi)$ [Riley et al., 2006] is the Heaviside theta function [Gradshteyn and Ryzhik, 1965], as (in dimensional units)

$$\phi(\xi) = k_{pe}^2 \int_{-\infty}^{\xi} \sin\left[k_{pe}(\xi - \xi')\right] \frac{a^2(\xi')}{2} d\xi', \tag{149}$$

where $k_{pe} = c/\omega_{pe}$ is the linear plasma wave number. In the linear regime $a^2 \ll 1$, analytic solutions can be readily obtained by evaluation of Eq. (149). Longitudinal electric field and electron density then follow from the first and second derivative of the normalized potential, $E_{\parallel} = -\partial_{\xi}\phi$ and $\delta n_e = \partial_{\xi}^2\phi$. We continue the discussion of laser-driven plasma waves in section 2.4.4, where we expand the discussion of their properties in the context of laser wakefield acceleration.

We now return to discuss the effect of copropagating plasma waves described above on the laser pulse evolution. We proceed to reveal a crucially important conservative property of electromagnetic pulses propagating in plasmas with slowly evolving envelopes. First, we multiply the equation for the evolution of the vector potential envelope (138) by the conjugate of the complex envelope $\mathbf{a}^*$ and then we add the complex conjugate of the resulting equation, we obtain

$$\frac{\partial}{\partial\tau}\left[|\mathbf{a}|^2 - i\frac{\beta_g}{\omega_0}\left(\mathbf{a}^*\frac{\partial\mathbf{a}}{\partial\xi} - \mathbf{a}\frac{\partial\mathbf{a}^*}{\partial\xi}\right)\right] = \frac{i}{2}\mathbf{a}\nabla_{\perp}^2\mathbf{a}^* - \frac{i}{2}\mathbf{a}^*\nabla_{\perp}^2\mathbf{a}. \tag{150}$$

Note that the source term on the right-hand side of Eq. (138) is now canceled out. Integrating over the beam area πr^2, we get [Gibbon, 2005]

$$\pi\int_0^\infty \frac{\partial}{\partial\tau}\left[|\mathbf{a}|^2 - i\frac{\beta_g}{\omega_0}\left(\mathbf{a}^*\frac{\partial\mathbf{a}}{\partial\xi} - \mathbf{a}\frac{\partial\mathbf{a}^*}{\partial\xi}\right)\right]\mathrm{d}r^2 = \frac{i\pi}{2}\int_0^\infty\left(\mathbf{a}\nabla_{\perp}^2\mathbf{a}^* - \mathbf{a}^*\nabla_{\perp}^2\mathbf{a}\right)2r\mathrm{d}r \tag{151}$$

$$= \pi i\int_0^\infty\left[\mathbf{a}^*\left(\frac{\partial^2}{\partial r^2} + \frac{1}{r}\frac{\partial}{\partial r}\right)\mathbf{a}r - c.c.\right]\mathrm{d}r = \pi i\int_0^\infty\left(r\left|\frac{\partial\mathbf{a}}{\partial r}\right|^2 - r\left|\frac{\partial\mathbf{a}}{\partial r}\right|^2\right)\mathrm{d}r = 0. \tag{152}$$

Therefore, we see that Eq. (138) has the following integral of motion

$$\pi\int_0^\infty \frac{\partial}{\partial\tau}\left[|\mathbf{a}|^2 - i\frac{\beta_g}{\omega_0}\left(\mathbf{a}^*\frac{\partial\mathbf{a}}{\partial\xi} - \mathbf{a}\frac{\partial\mathbf{a}^*}{\partial\xi}\right)\right]\mathrm{d}r^2 = 0. \tag{153}$$

To clearly understand the conserved quantity, we rewrite the normalized complex amplitude, without loss of generality, in the form $\mathbf{a} = |\mathbf{a}|e^{i\nu(\xi,\tau)}$. Reminding ourselves that the instantaneous frequency of an electromagnetic pulse is defined as a time derivative of the phase $\varphi(z,t) = \omega_0 t - \nu(z - \beta_g t, t)$, explicitly written as

$$\omega(t) = \frac{\mathrm{d}\varphi}{\mathrm{d}t} = \omega_0 - \beta_g\frac{\partial\nu}{\partial\xi}, \tag{154}$$

we can rewrite Eq. (153), after integrating over the longitudinal coordinate ξ, in the following form

$$\frac{\partial}{\partial\tau}\int\left(\pi\int_0^\infty|\mathbf{a}|^2\omega\mathrm{d}r^2\right)\mathrm{d}\xi = \frac{\partial}{\partial\tau}\int|\mathbf{a}|^2\omega\mathrm{d}^3\mathbf{r} = 0. \tag{155}$$

Since the electric field envelope (in normalized units) is $|\mathbf{E}| = |\mathbf{a}|\omega$, the integrand can be interpreted as *photon number density*, $|\mathbf{a}|^2\omega = |\mathbf{E}|^2/\omega = \mathcal{E}/\omega$, where $\mathcal{E}$ is the energy density of the electromagnetic field. This quantity is sometimes referred to as *wave action density*, which has the form of an adiabatic invariant $J = \mathcal{E}/\omega$ [Chen et al., 1984]. Therefore, the total wave action (photon number) is conserved [Bulanov et al., 1992; Mori, 1997; Bulanov et al., 2001],

$$\int|\mathbf{a}|^2\omega\,\mathrm{d}^3\mathbf{r} = const. \tag{156}$$

In other words, the conservation of wave action (156) can be interpreted as the conservation of

total photon number, which states that if a slowly evolving electromagnetic pulse propagating in plasma loses energy, the frequency of the laser must decrease proportionally. This effect is known as *pump depletion*, which we will discuss in more detail later. Over time, this effect redshifts the entire spectrum of the laser as it propagates through plasma[24]. Eq. (156) can be estimated as $a^2 \omega r^2 L = const$, where $a = |\mathbf{a}|$ is the amplitude envelope and L is the pulse length. We see that the amplitude of a laser propagating in plasma can be affected by slow changes both in size and frequency. For example, the amplitude can be increased through either longitudinal compression ($L \downarrow \implies a^2 \uparrow$), transverse focusing ($r^2 \downarrow \implies a^2 \uparrow$), or frequency redshift ($\omega \downarrow \implies a^2 \uparrow$). Using Eq. (153), we may also obtain the following rate of change of the transverse electromagnetic field energy

$$\frac{\partial}{\partial \tau} \mathcal{E}_\perp \approx \frac{\partial}{\partial \xi} \left(\frac{E_\parallel^2}{2} \right), \tag{157}$$

where the transverse electromagnetic field energy density is given as $\mathcal{E}_\perp = E_\perp^2/2 = (-\partial_t \mathbf{a})^2/2 = (\partial_\tau |\mathbf{a}|^2 - 2\partial_\tau \mathbf{a} \cdot \partial_\xi \mathbf{a} + 2\partial_\xi |\mathbf{a}|^2)/2$ and the longitudinal electric field is given as $E_\parallel = -\partial_\xi (1 + \phi)$. Using Gauss' law, the right-hand side can also be expressed as $\partial_\xi E_\parallel^2/2 = -\delta n_e E_\parallel$, where $-\partial_\xi E_\parallel = \delta n_e = n_e - 1$ is the normalized electron charge density perturbation. We can now make a general observation: a local loss of laser pulse energy requires in an equal manner two things: a) the presence of charge density perturbation δn_e and b) the longitudinal electrostatic field $E_\parallel$. Both of them arise through the laser-driven electron plasma waves discussed before.

The physical picture of the laser pulse evolution can be obtained by considering modulations of the plasma refractive index [Mori, 1997]. In general, the laser pulse evolves in the plasma due to spatiotemporal changes in the refractive index, which can occur from the excitation of electron plasma waves discussed above or from other effects, which we will discuss momentarily. The refractive index (132) can be expanded for relativistically underdense plasma ($n_e/\gamma n_c \ll 1$) as [Decker et al., 1996; Mori, 1997]

$$n(\mathbf{r}, t) = \frac{v_g}{c} \approx 1 - \frac{1}{2} \left(\frac{n_e}{\gamma n_c} \right), \tag{158}$$

where $\gamma = \sqrt{1 + a_0^2/2}$ is the averaged Lorentz factor of plasma electrons and $a_0(\mathbf{r}, t)$ is the averaged amplitude of the normalized vector potential. The phase velocity (131) is then given (in dimensional units) as

$$\frac{v_p}{c} \approx 1 + \frac{1}{2} \left(\frac{n_e}{\gamma n_c} \right). \tag{159}$$

Generally, the laser pulse evolution can be described briefly as follows: transverse evolution occurs due to transverse modulation of phase velocity, longitudinal evolution occurs due to longitudinal modulation in group velocity, and frequency shift occurs due to longitudinal modulation of phase velocity. These effects can also be directly described by solving Eq. (138). The role and timescale of the individual terms on the left-hand side are then estimated by keeping only one term at a time and comparing the amplification factor's time dependence with the refractive index's initial perturbations [Bulanov et al., 2001].

---

[24]We remind ourselves that this result was obtained only for lasers with envelopes that evolve *adiabatically*, i.e., slowly in time with respect to the laser phase which evolves on a timescale $\sim 1/\omega_0$.

2.4.1 Stimulated Raman scattering and nonlinear laser depletion

From our discussion of plasma waves, it is clear that even weakly relativistic pulses introduce refractive index modulations due to the occurrence of plasma waves copropagating with the driving laser pulse. The electron plasma waves evolve fast ($\tau \sim 1/\omega_{pe}$) and can seed a host of instabilities within the laser pulse [Forslund et al., 1975b; Bers, 1983; Decker et al., 1996; Mori, 1997; Bulanov et al., 2001; Gibbon, 2005], which can quickly modulate and erode the laser pulse envelope [Forslund et al., 1985; Bulanov et al., 1992]. Plasma wave seeds can also arise from thermal fluctuations of electrons, which occur even ahead of the laser pulse. The fastest instability (and therefore the most relevant one for ultrashort laser pulses) is the stimulated Raman scattering (SRS) [Forslund et al., 1975b; Forslund et al., 1985; Antonsen and Mora, 1992; Darrow et al., 1992; Mori, 1997]. The slower stimulated Brillouin scattering (SBS) could also grow from an ion acoustic wave seed in a long laser pulse [Chen et al., 1984]. However, for ultrashort laser pulses it can be neglected as long as the static ion approximation holds.

SRS occurs due to the presence of small amplitude electron plasma waves, which can modulate the refractive index at the frequency of ω_{pe}, a time (length) scale much shorter than the typical Rayleigh diffraction time (length) $\tau_R = z_R/c$ [Bulanov et al., 2001], which is the natural time (length) scale for the slowly evolving laser envelope [Born and Wolf, 1959]. SRS can be described in the wave-wave interaction picture. An electromagnetic pump wave with $(\omega_0, \mathbf{k}_0)$ is scattered by a seed plasma wave with $(\omega_{pe}, \mathbf{k}_{pe})$, which is then further reinforced by the ponderomotive beating between the pump and scattered waves $(\omega_\pm, \mathbf{k}_\pm)$. The linearization of the wave and fluid plasma equations yields the following phase matching conditions for the scattered waves [Forslund et al., 1975b; Bers, 1983; Decker et al., 1996; Mori, 1997; Bulanov et al., 2001; Gibbon, 2005]

$$\omega_\pm = \omega_0 \pm \omega_{pe}, \tag{160}$$

$$\mathbf{k}_\pm = \mathbf{k}_0 \pm \mathbf{k}_{pe}, \tag{161}$$

where the $\pm$ corresponds to the anti-Stokes and Stokes shift of the pump wave, respectively, both of which are allowed in the first-order linearization of the wave equation [Bers, 1983]. Note that, since we have in underdense plasma $\omega_0 > \omega_{pe}$, the wave must have frequency of at least $\omega_0 > 2\omega_{pe}$, such that a scattered wave with $\omega_\pm > \omega_{pe}$ and a plasma wave with ω_{pe} can be generated. This sets the condition for plasma density in which SRS can occur as $n_e < n_c/4$. It was experimentally verified that for pump waves scattered from nonlinear electron plasma waves, the amplitude-dependent nonlinear plasma wave frequency should be used for the phase-matching conditions, i.e., $\omega_{pe} \to \omega_{p,r} = \omega_{pe}/\sqrt{\gamma}$, where $\gamma = \sqrt{1 + a_0^2/2}$. We note that scattered waves themselves can undergo SRS, which leads to cascading that creates frequency sidebands at $\omega_0 \pm n\omega_{pe}$, where n is an integer.

In the case when the scattered wave is nearly parallel with the pump wave, $\mathbf{k}_\pm \approx \mathbf{k}_0$, we have $\mathbf{k}_e \ll \mathbf{k}_0$. This scenario is known as the stimulated forward Raman scattering (SFRS). This instability leads to longitudinal modulation of the laser pulse, with modulation wavelength $\lambda_{pe} \approx 2\pi c/\omega_{pe}$. The growth rate of SFRS can be obtained through standard instability analysis as [Forslund et al., 1975b; Kruer, 1988; Decker et al., 1996; Gibbon, 2005]

$$\frac{\Gamma_{\mathrm{SFRS}}}{\omega_{pe}} = \frac{1}{\sqrt{8}} \frac{\omega_{pe}}{\omega_0} \frac{a_0}{1 + a_0^2/2}. \tag{162}$$

The characteristic rise time of the laser pulse modulation is of the order $\tau_{\theta=0} \sim 1/(\tau_p \gamma_F^2)$, where τ_p is the laser pulse duration. The resonant growth of the plasma wave makes SFRS

crucial in LWFA since the laser pulse excites a strong copropagating longitudinal field. Note that the growth rate has a maximum for $a_0 = \sqrt{2}$, and drops off as $\sim 1/a_0$ for $a_0 \gg 1$. Yet, phase matching enables SRS under any angle. For small angles close to the propagation axis ($\theta \sim 1/(k_p w_0) \ll 1$), the stimulated side Raman scattering (SSRS) can also affect the laser beam in the transverse direction, in a time of the order $c\tau_{0<\theta\ll1} \sim (z_R/c) \times (P/P_c)^{-1/2} \times (\omega_{pe}\tau_p)^{-1/2}$, where $z_R = k_0 w_0^2/2$ is the Rayleigh length, P is the laser power and P_c is the self-focusing critical power, which will be calculated in the next section. It was shown [Andreev et al., 1992; Esarey et al., 1994; Decker et al., 1996; Mori, 1997] that longitudinal instability due to electron plasma wave seed dominates when $4\omega_0/\omega_{pe} \ll k_p w_0$, while transverse instability dominates when $1 + a_0^2 \omega_{pe}\tau_p \ll [4\omega_0/(\omega_{pe}k_p w_0)]^2$. In the case when the following inequality is satisfied [Bulanov et al., 2001]

$$1 \ll \left(\frac{4\omega_0}{\omega_{pe} k_p w_0}\right)^2 \ll a_0^2 \omega_{pe}\tau_p, \tag{163}$$

the laser pulse evolves in two stages. In the first stage, the instability starts as a longitudinal modulation. In the second stage, the transverse modulation of the laser spot size dominates. The transverse modulation always evolves faster than the Rayleigh diffraction time if $(16P/P_c)\omega_{pe}\tau_p \gg 1$

In addition to stimulated forward and side Raman scattering, the scattered wave can also propagate antiparallel to the laser wave vector, $\mathbf{k}_\pm \approx -\mathbf{k}_0$. Since the instability growth requires a copropagating plasma wave, we may neglect the anti-Stokes wave as non-resonant, which gives us phase matching for the Stokes backscattered wave $\mathbf{k}_+ \approx -\mathbf{k}_0$ and therefore $\mathbf{k}_{pe} \approx 2\mathbf{k}_0$. This is known as stimulated backward Raman scattering (SBRS). The growth rate can be obtained as [Forslund et al., 1975b; Kruer, 1988; Darrow et al., 1992; Decker et al., 1996]

$$\frac{\Gamma_{\text{SBRS}}}{\omega_{pe}} = \frac{\sqrt{3}}{2}\left(\frac{\omega_0}{3\omega_{pe}}\right)^{1/3} \frac{a_0^{2/3}}{(1+a_0^2/2)^{1/2}}. \tag{164}$$

Note that the growth rate has a maximum for $a_0 = 2$, after which it drops off as $\Gamma_{\text{SBRS}} \sim a_0^{-1/3}$. By direct comparison, we see that SBRS is significantly faster compared to SFRS, $\Gamma_{SBRS}/\Gamma_{SFRS} \sim (\omega_0/\omega_{pe})^{4/3} a_0^{2/3}$. A steady-state solution is established inside the pulse in a time of the order of the pulse duration [Bulanov et al., 2001].

SFRS and SBRS growth rates drop off with increasing a_0. This could lead us to conclude that SRS does not play a significant role in the modulation of intense laser pulses with $a_0 \gg 1$. Indeed, in this case, *nonlinear pump depletion* [Bulanov et al., 1992] starts to play a more significant role. Let us consider a laser pulse much larger than the plasma wavelength, then no substantial plasma wave is initially formed, as the resonance condition (146) is not satisfied. However, for $a_0 \gg 1$, the SRS grows fast at the low amplitude leading edge of the laser pulse where $a \sim 1$. SRS quickly develops a modulation in this region, which feeds the process of plasma wave excitation and nonlinear pump depletion discussed, which locally depletes energy and steepens the leading edge of the pulse [Bulanov et al., 1992; Bulanov et al., 2001]. This steepening of the pulse front can saturate in a distance much shorter than the Rayleigh length, and it effectively *drills a hole*, which acts as a steep shock front (with a size of the order of the nonlinear plasma wavelength $\sim \sqrt{\gamma}\lambda_{pe}$) for efficient plasma wake wave excitation [Bulanov et al., 1992; Esarey et al., 2000; Bulanov et al., 2001; Gordon et al., 2003; Nakajima et al., 2011]. A steep leading edge locally creates a large local density perturbation. Since the refractive index modulation is not as significant in the remainder of the laser, the energy is primarily depleted locally at the pulse shock front. This effect,

which occurs for $a_0 \gg 1$, is known as *pulse etching*, and the etching or erosion velocity can be estimated directly from Eq. (157). Integrating over ξ and then τ up to the time when the energy of the plasma wake wave equals that of the laser, we get $l_{pd}E_\parallel = \int \mathcal{E}_\perp \mathrm{d}\xi = \int E_\perp^2 \mathrm{d}\xi$, where $l_{pd} = c\tau_{pd}$ is the *pump depletion length*, which corresponds to τ_{pd}, which is the time at which the plasma wave energy equals the laser energy. For simplicity, let us consider a flat-top laser pulse with pulse length l_p. The maximum electric field amplitude of the wakefield is $E_{\max} = a^2/(1 + a^2)^{1/2}$ (147), and the total energy in the wakefield at the time of pump depletion can be therefore written as $\mathcal{E}_\parallel = l_{pd}E_{\max}^2 = l_{pd}a^4/(1 + a^2)$. Assuming a flat-top laser pulse, the total energy of the laser can be then written as $\int \mathcal{E}_\perp \mathrm{d}\xi = l_p a^2 \omega_0^2$. From the equality of the two, we obtain the pump depletion length in dimensional units as

$$l_{pd} = l_p \left(\frac{\omega_0}{\omega_{pe}} \right)^2 \frac{a^2}{1 + a^2}. \tag{165}$$

In the limit of linear interaction, $a^2 \ll 1$, we get $l_{pd}/l_p \approx (\omega_0/\omega_{pe})^2/a^2$, and the depletion length decreases with amplitude. In the nonlinear regime, $a^2 \gg 1$, the pump depletion length becomes amplitude-independent, $l_{pd}/l_p \approx (\omega_0/\omega_{pe})^2$. The fact that the pump depletion length is amplitude independent can also be attributed to the diminishing effect of SRS for $a^2 \gg 1$. It is of note that from the pump depletion length we can also obtain the etching velocity of the pulse front, which is the difference between the linear group velocity of the body of the pulse and the pulse front velocity, given as $\beta_{etch} = \beta_g - \beta_{\mathrm{front}} = l_p/l_{pd} \approx (\omega_{pe}/\omega_0)^2$.

Another exciting mechanism occurs due to the nonlinear pump depletion, which is the generation of relativistic solitons [Bulanov et al., 1992; Farina and Bulanov, 2001; Naumova et al., 2001; Esirkepov et al., 2002; Esirkepov et al., 2004]. As the laser loses energy to the plasma wave it generates in its wake, its carrier frequency is adiabatically decreased [Esarey et al., 1990; Bulanov et al., 1992; Esarey et al., 1994; Mori, 1997]. Throughout the nonlinear interaction, it is possible that a significant portion of the pulse energy redshifts down to $\omega \to \omega_{pe}$, at which point the group velocity (133) reaches zero. Therefore, the depleted portions of the electromagnetic pulse can lag behind the main body and convert their energy into solitons, localized packets of electromagnetic energy. It was even shown that these electromagnetic structures might emit coherent synchrotron radiation [Esirkepov et al., 2004], with high-frequency afterglow persisting for tens of plasma wave periods.
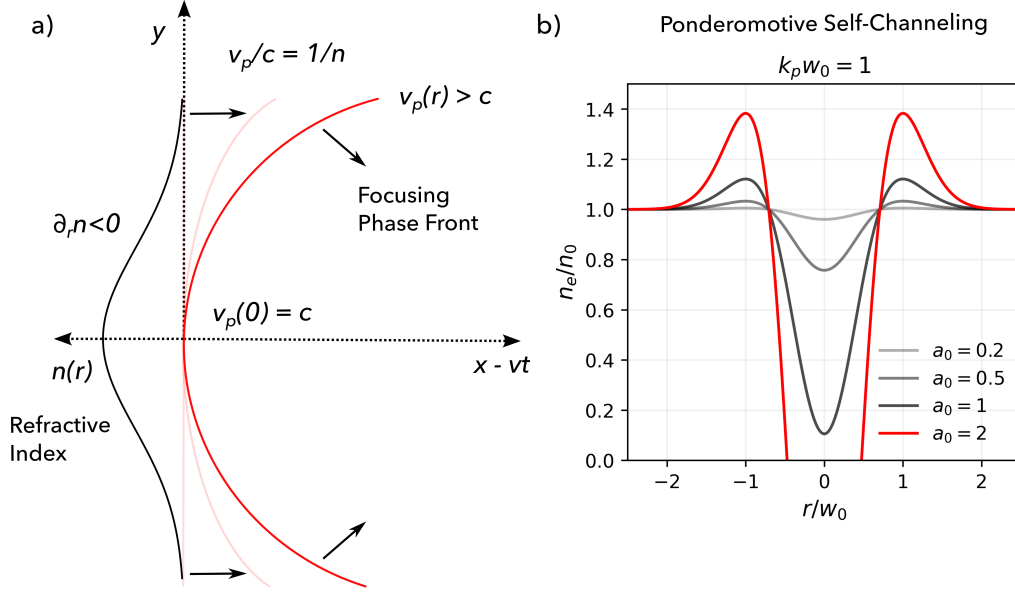
2.4.2 Self-focusing, ponderomotive channeling and filamentation instability

Taking the radial derivative of the refractive index (158), we get

$$\frac{\mathrm{d}n}{\mathrm{d}r} = \frac{n_e}{n_c \gamma^3} \frac{\partial}{\partial r} \left(a^2 \right) - \frac{2}{\gamma} \frac{\partial}{\partial r} \left(\frac{n_e}{n_c} \right). \tag{166}$$

Typically, well-focused lasers have profiles that decrease in amplitude with increasing radial distance. For example, a Gaussian beam. Such a profile satisfies $a^2 > 0$ and $\partial_r a^2 < 0$. That is, the first term tells us that relativistically underdense plasma acts as a converging lens, which is known as *relativistic self-focusing* [Sprangle et al., 1990; Bulanov and Sakharov, 1991; Cohen et al., 1991; Antonsen and Mora, 1992; Borisov et al., 1992; Sprangle et al., 1992; Chen and Sudan, 1993; Esarey et al., 1997; Cattani et al., 2001]. This is immediately clear since the local phase velocity increases away from the axis, $\partial_r v_p > 0$.

We consider the quasistatic approximation to understand the effect of the second term. This approximation again states that the evolution of the plasma is much faster than that of

Figure 13: Physical picture of relativistic self-focusing. A laser beam creates a transverse inhomogeneity (a) in the refractive index due to relativistic plasma oscillations and ponderomotive self-channeling (b), both of which contribute to off-axis phase velocity increase. The density modulation is calculated from Eq. (167). The red curve corresponds to the *blowout regime* (168), in which all electrons are pushed away from the laser pulse region.

the envelope of the laser. Thus we may neglect the time derivative in Eq. (123) to obtain (in dimensional units) $\delta n_e/n_0 = n_e/n_0 - 1 = k_p^{-2}\Delta\phi$. In the quasistatic approximation, the plasma reacts immediately to the slow evolution of the ponderomotive force, which is therefore compensated by the space-charge force, and we can take $\Delta\phi = \Delta\gamma$. Therefore, the density modulation can be calculated for a long pulse Gaussian beam with $a = a_0 \exp(-r^2/w_0^2)$, where w_0 is the laser waist, as

$$\frac{n_e}{n_0} = 1 + k_p^2\Delta\gamma \approx 1 + k_p^2\nabla_\perp^2\gamma = \frac{1}{4\gamma k_p^2}\nabla_\perp^2 a^2 = 2\frac{a_0^2}{\gamma w_0^2 k_p^2}\left(2\frac{r^2}{w_0^2} - 1\right)e^{-2(r/w_0)^2}. \tag{167}$$

The electron density has a minimum on the laser axis $r = 0$ and always increases from the laser axis towards the edge of the laser ($r \approx w_0$). This is known as *ponderomotive self-channeling* [Sun et al., 1987; Kurki-Suonio et al., 1989; Borisov et al., 1992], which is shown in Fig. 13b. A long-pulse laser propagating in plasma creates a density channel and for typical laser beams[25] we have $\partial_r n_e > 1$. Therefore, the second term in Eq. (158) reinforces relativistic self-focusing, and we have in total $\partial_r n < 0$. Additionally, we note that ponderomotive self-channeling can lead to cavitation, where all electrons are expelled from the axis. This can be calculated from Eq. (167) by requiring that $n_e = 0$, which occurs when

---

[25] Except for optical vortices, which have topological phase singularity that results in zero intensity on-axis. See section 2.4.6.

the following *cavitation condition* is satisfied [Gibbon, 2005],

$$a_0\sqrt{\frac{2}{\gamma}} > k_p w_0. \tag{168}$$

Note that for $a_0 \gg 1$, the ponderomotive force is balanced on the axis with the space-charge force when $\sqrt{2}\sqrt{a_0} \approx k_p w_0$. This balance is closely related to a so-called *bubble regime*, where optimal laser guiding in plasma is achieved when the plasma cavity assumes the form of a sphere [Lu et al., 2006; Lu et al., 2007; Esarey et al., 2009], for $a_0 > 2$, if the laser waist and pulse duration satisfy[26]

$$ck_p\tau_p \lesssim k_p w_0 \approx 2\sqrt{a_0}. \tag{169}$$

Cavitation typically leads to the acceleration of ions towards the edges of the plasma channel, which further reinforces evacuation of the channel on the timescale of ion motion $\sim 1/\omega_{pi}$. Such slow changes can be then measured with long pulse optical probes, for example, using interferometry [Matlis et al., 2006; Harilal et al., 2022; Raclavský et al., 2024]. The fact that plasma acts as a converging lens foreshadows that there exists a focusing threshold, at which point the natural diffraction of a laser beam propagating in a vacuum becomes compensated [Mori, 1997]. We note that the Gaussian beam waist evolves in vacuum as $w = w_0\sqrt{1 + (z/z_r)^2}$, where $z_R = k_0 w_0^2/2$ is the Rayleigh length [Born and Wolf, 1959]. It is helpful to calculate the second derivative of the vacuum waist near the focus ($\tau \approx 0$), as we will momentarily use it to calculate the self-focusing threshold, we get $\partial_\tau^2 w \approx 4/(k_0^2 w_0^3)$.

Let us now find the equation for the evolution of the laser waist in plasma. To find it, we will need to calculate the velocity difference across the phase front of a weakly relativistic laser ($a^2 \ll 1$), which is

$$\frac{\Delta v_p}{c}(r) = \frac{v_p(r) - v_p(\infty)}{c} \sim e^{-2(r/w_0)^2}. \tag{170}$$

The phase velocity difference leads to a phase front curvature, which is determined by the relative path difference of different light rays on the phase front, $\Delta L = \Delta v_p \Delta t$, which is illustrated in Fig. 13. The angle that the wavefront bends forward to θ is then related to the beam waist w, and the relative path difference is $\Delta L = w\theta$. Let us now calculate the rate at which the radiation is focused inwards. The rate of change of beam waist is equal to the transverse component of the phase front velocity $\partial_\tau w = -v_p \sin\theta \approx -c\theta$. Taking another time derivative and using the above relationship between the relative path difference and the focusing angle, $\partial_\tau \theta \approx \Delta v_p/w$, we get with the inclusion of vacuum diffraction calculated in the previous paragraph the following equation for beam waist evolution near the focus, which includes both plasma self-focusing and vacuum diffraction [Mori, 1997]

$$\frac{\partial^2 w}{\partial \tau^2} \approx \frac{4}{k_0^2 w_0^3} - \frac{c^2}{w_0}\frac{\Delta v_p(0)}{c} = \frac{4}{k_0^2 w_0^3}\left(1 - \frac{a_0^2 w_0^2 k_p^2}{32}\right). \tag{171}$$

Therefore, self-focusing takes place only when the term in the parenthesis becomes negative, which yields the following *self-focusing condition* [Sun et al., 1987]

$$\frac{a_0^2 k_p^2 w_0^2}{32} \geqslant 1. \tag{172}$$

---

[26]This can be trivially obtained from the cavitation threshold, $1 + k_p^{-2}\Delta\gamma \approx 0$, if we assume spherical symmetry of the laser envelope.

The self-focusing condition can also be cast in terms of the laser power as $P/P_c > 1$, where P is the laser power and $P_c = (8\pi\epsilon_0 m_e^2 c^5 \omega^2)/(e^2 \omega_{pe}^2) \approx (\omega/\omega_{pe})^2 \, 17\,\text{GW}$ is the critical power required for self-focusing [Sun et al., 1987; Mori, 1997].

In addition to self-focusing in plasma, a sufficiently wide ($k_p w_0 \gg 1$) laser pulse evolves according to any transverse modulations of the refractive index, in addition to the ponderomotive density modulation. Linearizing Eq. (138) for small perturbations of the field amplitude, we can obtain the following dispersion relation for the unstable transverse mode [Bulanov et al., 2001]

$$\omega^2 = \frac{k_\perp^2}{4\gamma^2 k_0^2}\left(c^2 k_\perp^2 - \omega_{pe}^2 \frac{a^2}{\gamma}\right).\tag{173}$$

Instability develops (the frequency is imaginary) for $ck_\perp < a\omega_{pe}/\sqrt{\gamma}$. It can be verified that the condition for filamentation instability is the analog of the condition for self-focusing ($P > P_c$) when $k_\perp \sim 1/w_0$, where w_0 is the initial laser beam waist. The laser pulse is self-focused in a time of $\tau_{sf} \approx (z_R/c)(P/P_c - 1)^{1/2}$. For $P \gg P_c$, the filamentation instability can split the laser beam into multiple filaments, each of which can undergo self-focusing [Askaryan et al., 1994; Esarey et al., 1994; Esarey et al., 1997; Mori, 1997; Bulanov et al., 2001; Esarey et al., 2009].

For $a^2 \gg 1$, the plasma electrons can attain significant velocity along the longitudinal direction. An effective current of relativistic electrons that propagates with the laser pulse is created, and a strong transverse magnetic field can be generated, which significantly affects the picture of self-focusing. The fast current filaments attract each other, which changes the refractive index due to the effective local decrease of relativistic plasma frequency. Due to this, in the regions with the highest concentration of electrons [27], the phase velocity is increased. Therefore, additional self-focusing is introduced due to this magnetic attraction. This magnetic interaction between the laser pulse and the plasma yields another mechanism for transporting laser energy over long distances. In addition, the magnetic interaction is polarization dependent, and self-focusing and merging of current and laser filaments can be anisotropic [Askaryan et al., 1994].

2.4.3 Self-compression, photon acceleration, and modulational instability

We may calculate the longitudinal bunching of a laser pulse from the group velocity. A change in the group velocity gives the separation between two positions within the laser pulse $\Delta L = \Delta v_g \Delta t$. For two positions close to each other, we can write $\Delta v_g \approx L \partial_\xi v_g$ [28]. Changing into the copropagating coordinate with $\partial_z = \partial_\xi$, we get

$$\frac{1}{L}\frac{\partial L}{\partial \tau} = \frac{\partial v_g}{\partial \xi} = c\frac{\partial n}{\partial \xi},\tag{174}$$

where we have used $v_g/c = n$. Applying the derivative to the refractive index of plasma (158), we get

$$\frac{1}{cL}\frac{\partial L}{\partial \tau} = \frac{\partial n}{\partial \xi} = \frac{n_e}{n_c \gamma^3}\frac{\partial}{\partial \xi}\left(a^2\right) - \frac{2}{\gamma}\frac{\partial}{\partial \xi}\left(\frac{n_e}{n_c}\right).\tag{175}$$

The analysis of Eq. (175) is now similar to the previous section. At the pulse front, we

---

[27]At the laser beam edges, see Fig. 13.

[28]This is simply Taylor expansion of the group velocity, $v_g(\xi_2 - \xi_1) \approx v_g(\xi_1) + (\xi_2 - \xi_1)\partial_\xi v_g$. The distance between two points is $\xi_2 - \xi_1 = L$, and we get $\Delta v_g = v_g(\xi_2 - \xi_1) - v_g(\xi_1) \approx L\partial_\xi v_g$.
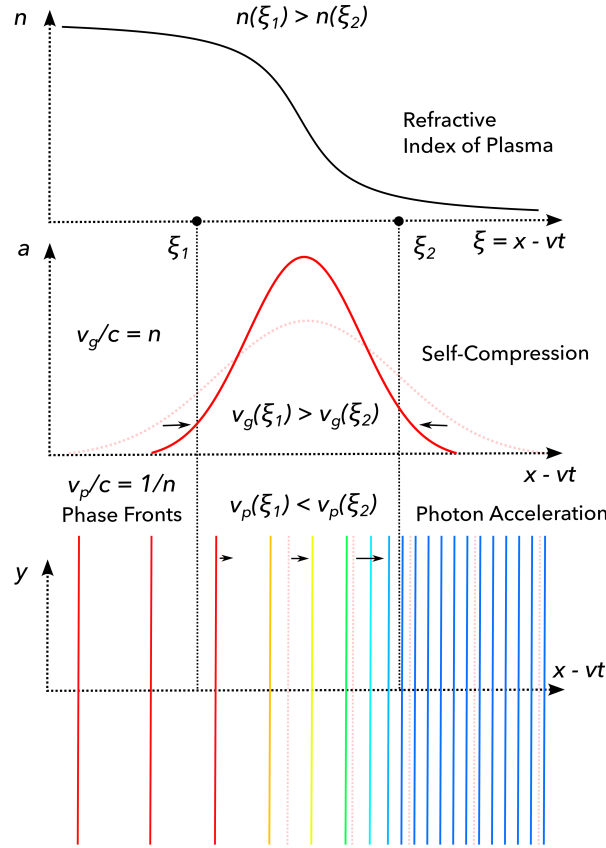
Figure 14: Physical picture of self-compression and photon acceleration. A refractive index inhomogeneity copropagating with the laser pulse leads to longitudinal variations of phase and group velocity. The choice of refractive index profile is illustrative. Generally, the laser redshifts in regions where $\partial_\xi n < 0$, and blueshifts in regions where $\partial_\xi n > 0$, as given by Eq. (177).

have $\partial_\xi a^2 < 0$. The density modulation also grows since the ponderomotive force pushes electrons out of the pulse region, yielding $\partial_\xi n_e > 0$ at the pulse front. Therefore, both the first and second terms give us that the group velocity is decreasing at the pulse front. Vice versa, we have $\partial_\xi a^2 > 0$ and $\partial_\xi n_e > 0$ at the pulse back. In summary, the group velocity increases at the back and decreases at the front, leading to *self-compression* of the pulse.

Derivation of the equation for frequency modulation is the same as above, except that now we consider two different phase fronts, which can travel with two different phase velocities, i.e., the distance between them can be written as $\Delta\lambda = \Delta v_p \Delta t$. If these phase fronts are neighboring, we may write $\Delta v_p \approx \lambda \partial_x v_p$[29], giving us

$$\frac{1}{\lambda}\frac{\partial\lambda}{\partial\tau} = -\frac{\partial v_p}{\partial\xi}, \tag{176}$$

---

[29]Same Taylor expansion as in previous footnote, except for phase velocity. Also, the distance between two neighboring phase fronts is the wavelength, $\xi_2 - \xi_1 = \lambda$. Refer to Fig. 14.

which, using $\partial_\omega \lambda = -\lambda/\omega$, can be rewritten in terms of frequency

$$\frac{1}{\omega}\frac{\partial\omega}{\partial\tau} = \frac{\partial v_p}{\partial\xi} = \frac{c}{n^2}\frac{\partial n}{\partial\xi}. \tag{177}$$

The behavior of the derivative of the refractive index is then the same as for self-compression; a laser pulse propagating in plasma becomes *positively chirped*, i.e., redshifted at the front and blueshifted at the back. This is known as *relativistic self-phase modulation* (SPM) [Andreev et al., 1992; Antonsen and Mora, 1992; Krall et al., 1993; Mori, 1997]. We note that it is possible to place a laser pulse into a phase of a copropagating plasma wave where $\partial_\xi n \approx const. > 0$, in which case Eq. (177) describes what is known as *photon acceleration*, since the whole laser pulse then becomes uniformly blueshifted [Mendonça, 2000], potentially from visible to extreme ultraviolet (XUV) spectral range [Sandberg and Thomas, 2023; Sandberg and Thomas, 2024].

SPM can lead to what is known as *relativistic modulational instability* (RMI), which can be understood as a longitudinal counterpart of self-focusing [Decker et al., 1996]. A relativistic plasma frequency is locally amplitude-modulated, which leads to frequency modulation according to Eq. (177). Correspondingly, this changes the group velocity, which leads to longitudinal energy density modulation according to Eq. (174). RMI is dominant when $c^2 k^2 \ll \omega^2 - \omega_{p,r}^2$, where k and ω are the wave number and frequency of the perturbation, i.e. the seed perturbation is not a plasma wave. The maximum growth rate is given as [Decker et al., 1996]

$$\frac{\Gamma_{\mathrm{RMI}}}{\omega_{pe}} \approx \frac{a_0^2}{(1 + a_0/2)^{3/2}}\frac{\omega_{pe}}{8\omega_0}. \tag{178}$$

2.4.4 Laser wakefield acceleration of electrons

A concept of utmost importance for particle acceleration has arisen in the context of relativistic laser-plasma interactions over the past decades, known as *laser wakefield acceleration* (LWFA) [Tajima and Dawson, 1979; Esarey et al., 1996; Esarey et al., 2009; Esirkepov et al., 2006; Bulanov et al., 2016a]. In the previous sections, we have shown that electron plasma waves propagate within a laser pulse in plasma[30]. However, they can also propagate in the wake of the laser. Large amplitude electron plasma waves can be resonantly excited to propagate behind the laser with the phase velocity $v_w \approx v_g \approx c$, where v_g is the group velocity of the driving laser, which is close to the speed of light for relativistically underdense plasma. Such a wave provides a substantial accelerating gradient for any electron injected within the correct wave phase. An adequately guided laser pulse[31] can propagate over many Rayleigh lengths, up to its depletion length (165), enabling acceleration of electrons to very high energies.

To explore this concept, we return to the equation for the evolution of the normalized scalar potential (140). Multiplying Eq. (140) by $\partial_\xi \phi = \phi'$ and integrating over the wave coordinate ξ, we obtain the following equation

$$\frac{1}{2}\left(\frac{\partial\phi}{\partial\xi}\right)^2 = \gamma_w^2(1 + \phi)\left[\beta_w\left(1 - \frac{1 + a^2}{\gamma_w^2(1 + \phi)^2}\right)^{1/2} - 1\right] - C, \tag{179}$$

where C is an integration constant, which is given by the values of a^2, ϕ and ϕ' at some initial boundary, e.g. at $\xi = 0$, which may represent the trailing or leading edge of the laser

---

[30]We called them interior plasma waves.

[31]When both Eqs. (169) and (172) are satisfied, or when other guiding techniques are employed.

pulse, depending on whether we investigate interior plasma waves or wakefield, it can be written as

$$C = \gamma_w^2(1 + \phi_0)\left[\beta_w\left(1 - \frac{1 + a_0^2}{\gamma_w^2(1 + \phi_0)^2}\right)^{1/2} - 1\right] - \frac{1}{2}(\phi_0')^2, \tag{180}$$

where $a_0 = a(\xi_0)$, $\phi_0 = \phi(\xi_0)$ and $\phi_0' = \phi'(\xi_0)$ are the initial conditions for the normalized vector potential, scalar potential, and its derivative, respectively. The phase velocity of the plasma wave is again given by the group velocity of the driver, $\beta_w = \beta_g$. Using the constant of motion for plasma electrons initially at rest (139), we can find the Lorentz factor of the plasma electrons, given explicitly in terms of the normalized potential as

$$\gamma_e = \gamma_w^2(1 + \phi)\left[1 - \beta_w\left(1 - \frac{1 + a^2}{\gamma_w^2(1 + \phi)^2}\right)^{1/2}\right]. \tag{181}$$

Using this and $\phi' = -E$, we see that Eq. (179) can be cast in the following simple form[32]

$$\gamma_e + \frac{1}{2}E^2 = C. \tag{182}$$

The constant of motion then tells us the initial conditions of the electric field and Lorentz factor at $\xi = 0$, i.e., $C = \gamma_e(0) + E^2(0)/2$. Eq. (182) can be rewritten as $E = \sqrt{2(C - \gamma_e)}$. Using the continuity equation, we have previously shown that wave breaking occurs when the electrons catch up to the plasma wave, i.e., $\beta_e \to \beta_w$, or equivalently $\gamma_e \to \gamma_w$, which leads to diverging electron plasma density. This limits the maximum electric field that relativistic plasma waves can produce. To find this limit, suppose that the electrons in the laser wake are initially excited by the laser to oscillate close to the wave-breaking velocity at $\xi = 0$, i.e., $C \approx \gamma_w$. Then, in the region behind the laser pulse, $\xi < 0$, we have $E = \sqrt{2(\gamma_w - \gamma_e)}$, and we see that the maximum electric field occurs at the position $\xi < 0$ where $\gamma_e(\xi) = 1$. This yields the Akhiezer-Polovin wave breaking limit [Akhiezer and Polovin, 1956], which sets the maximum strength for the longitudinal electric field of relativistic plasma waves (excited by any driver), given in dimensional units as

$$E_{wb} = \frac{m_e c \omega_p}{e}\sqrt{2(\gamma_w - 1)}, \tag{183}$$

where γ_w is the Lorentz factor of the plasma wave. For plasma waves excited by a laser pulse, the plasma wave phase velocity is given by the group velocity of the laser, $v_w = v_g$, and the Lorentz factor is $\gamma_w \approx \sqrt{\gamma_\perp}\omega_0/\omega_{pe}$, where $\gamma_\perp = \sqrt{1 + a_0^2/2}$. For plasma waves to break, their maximum electric field amplitude must approach $E_{\max} \approx E_{wb}$. From this condition, we estimate the laser amplitude which breaks the plasma wakefield using Eq. (147) as

$$a_{wb} = \sqrt{\gamma_w(1 + \beta_w) - 1}. \tag{184}$$

We reiterate that Eq. (184) was obtained for flat-top laser pulse, which drives a resonant plasma wake, i.e., the pulse length is $l_{opt} = \lambda_w/2$. For a resonant Gaussian laser pulse, numerical solutions of Eq. (141) indicate that the wave breaking amplitude increases up to $a_{wb} \approx \gamma_w$[33]. A general analytic study of the dependence of wave-breaking amplitude

---

[32]Here the longitudinal electric field E is again given in its dimensionless form. It is least cumbersome first to evaluate all calculations using dimensionless variables and then express final results in SI units, i.e., $E_{\mathrm{SI}} = (m_e\omega_{pe}c/e)E_{\mathrm{norm}}$, using the SI definitions for all the constants and plasma frequency.

[33]This estimate is based on a limited number of one-dimensional particle-in-cell simulations.
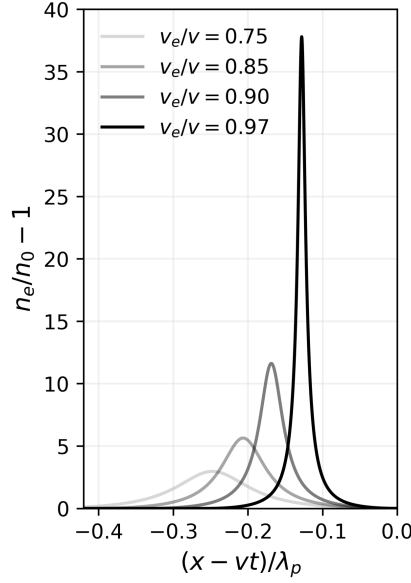
Figure 15: Numerical solutions of Eq. (140) illustrating wave breaking, $\beta_e \to \beta_w$**.** Normalized electron density for various laser amplitudes approaching Eq. (184).

on the laser pulse shape could prove an exciting avenue, among many others, for future theoretical work. Fig. 15 shows a plasma wave approaching the wave-breaking threshold, given by Eq. (184). As discussed before, this leads to nonlinear steepening of the plasma wave and local increase of plasma electron density due to the accumulation of electrons that are "catching up" with the wave.

To find the wavelength of the plasma wake waves, we must first find the zeroes of the electric field, which are given by the condition $\phi' = 0$. Assuming that the excitation of the plasma wave is resonant in the region behind the driver (particle beam or laser), we have $a^2 = 0$. Therefore, the initial conditions in the wake region become $\phi_0 = \phi_{\max}$ and $\phi'_0 = 0$. From the condition $\phi'' = 0$, we can see that the maximum electric field of the wake wave $E_{\max}$ occurs when $\phi_+ = 0$, and its value is given by $E_{\max} = -\phi'(\phi_+)$. This yields $\phi_{\max}$ in terms of $E_{\max}$. The minimum value of the potential, $\phi_{\min}$, is then given from $\phi' = 0$. Finally, both extrema can be then written in the following concise form [Esarey and Pilloff, 1995]

$$\phi_{\max,\min} = \frac{E_{\max}^2}{2} \pm \beta_w \sqrt{\left(1 + \frac{E_{\max}^2}{2}\right)^2 - 1}. \tag{185}$$

The potential difference is

$$\Delta\phi = 2\beta_w \sqrt{\left(1 + \frac{E_{\max}^2}{2}\right)^2 - 1}. \tag{186}$$

We note that the relationship between the values of the wakefield potentials $\phi_{\min,\max}$ and $E_{\max}$ is completely general. As an example, the potential difference for laser-driven wakefield can be obtained using $E_{\max} = a^2/\sqrt{1 + a^2}$. To find the maximum potential difference that

a plasma wake can sustain, we consider the Akhiezer-Polovin limit given by Eq. (183) as $E_{\max} = \sqrt{2(\gamma_w - 1)}$. The potential extrema of nonlinear electron plasma waves is then given as

$$\phi_{\max,\min} = \gamma_w - \frac{1}{2} \pm \beta_w \sqrt{\left(\gamma_w + \frac{1}{2}\right)^2 - 1}. \tag{187}$$

The wavelength of plasma wake waves can now be obtained by inverting Eq. (179) and integrating between potential extrema, which correspond to the zeroes of the oscillating electric field. We get the following integral expression

$$\frac{\lambda_w}{\lambda_{pe}} = \frac{1}{\pi} \int_{\phi_{\min}}^{\phi_{\max}} \frac{1}{\sqrt{2\left[\gamma_e(\phi_0) - \gamma_e(\varphi)\right]}} \mathrm{d}\varphi. \tag{188}$$

This integral has no general analytic solution, but it can be integrated numerically to obtain wavelength for any initial conditions. Nonetheless, we may obtain a general solution in the limit $\gamma_w \gg 1$. Then, the integral yields[34]

$$\frac{\lambda_w}{\lambda_{pe}} \approx \frac{2}{\pi} \left(1 + \phi_{\max}\right)^{1/2} E\left(1 - \frac{1}{(1 + \phi_{\max})^2}\right), \tag{189}$$

where $E(k) = \int_0^{\pi/2} \left(1 - k^2 \sin^2\theta\right)^{1/2} \mathrm{d}\theta$ is the complete elliptic integral of the second kind. In the limit $E_{\max} \gg 1$, the nonlinear plasma wavelength is $\lambda_w \approx \lambda_{pe}(2/\pi)E_{\max}$, while in the linear limit $E_{\max} \ll 1$, we get the usual linear plasma wavelength $\lambda_w \approx \lambda_{pe}$. The wavelength of a nonlinear plasma wake is elongated compared to the linear plasma wave by a factor of $\lambda_w/\lambda_{pe} \sim (2/\pi)E_{\max}$. For laser-driven wakefields, Eq. (147) gives $\lambda_w/\lambda_{pe} \approx (2/\pi)a^2/\sqrt{1 + a^2}$. For wakefields driven close to the wave-breaking threshold given by Eq. (183), we have $\lambda_w \approx \lambda_{pe}(2/\pi)\sqrt{2\gamma_w - 1}$.

For typical plasma density and laser frequency, simple estimates of Eq. (183) yield electric fields that provide accelerating gradients up to 4 orders of magnitude larger than conventional radiofrequency accelerators. This is extraordinary since it enables acceleration of charged particles in very short distances compared to conventional technology [Dawson, 1959; Faure et al., 2004; Geddes et al., 2004; Mangles et al., 2004; Lazzarini et al., 2024]. For example, acceleration of electrons to GeV energies requires tens of meters long conventional accelerators, while the same energy gain was achieved in just a few centimeters within the laser-driven wakefields [Kim et al., 2013; Leemans et al., 2014; Gonsalves et al., 2019; Aniculaesei et al., 2024], significantly shrinking the required footprint of the machine. This makes wakefield acceleration an attractive concept for future accelerators [Caldwell et al., 2021].

To understand how the electrons accelerate within the wakefield, let us integrate the momentum equation (120) over the ξ coordinate to obtain the constant of motion

$$\gamma - \beta_w p_\parallel - \phi = h_0, \tag{190}$$

where the constant h_0 is determined by the initial state of the electron, i.e., $h_0 = \gamma_0 - \beta_w p_{\parallel,0} - \phi_0$. While the plasma electrons initially at rest have $h_0 = 1$, we could also consider

---

[34]Our formula for the wavelength of the plasma wakefield differs from that presented in [Esarey et al., 2009], where the argument of the elliptic integral is taken under a square root, which predicts laser-driven wakefields ($\phi_{max} = a_0^2$) with wavelengths smaller than the linear plasma wavelength for $0 < a < 1$, which is unphysical. Numerical solutions of Eq. (140) indicate that our version is correct, and it correctly predicts that $\lambda_w > \lambda_{pe}$ for any a_0. Both formulas converge in the limit $\phi_{max} \to \infty$. Note that the wavelength of the laser-driven plasma wakefield (189) is slightly smaller than the wavelength of the plasma which occurs in the interior of the laser pulse (144). The difference becomes negligible for $a_0 \gg 1$.
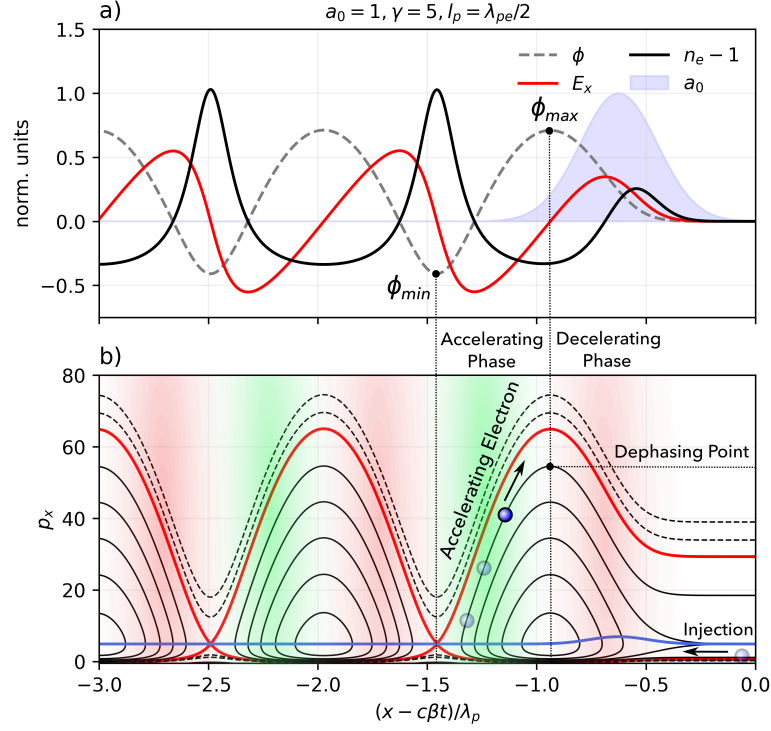
Figure 16: Laser wakefield acceleration illustrated through numerical solutions of Eq. (140). (a) Normalized laser amplitude (blue), normalized electron density (black), longitudinal electric field (red) and normalized potential (grey, dashed). (b) Phase space of electrons (191) due to the plasma wakefield shown in (a). The open orbits (black, dashed) correspond to electrons that have initially $h_0 > h_s$, including the plasma electrons that have $h_0 = 1$. The red orbit marks the separatrix curve (193), along which travel electrons with $h_0 = h_s$. Singular points of the separatrix rest on the blue curve given by Eq. (192). Injection occurs for electrons with $h_0 < h_s$, which can rotate along the closed orbits in the wakefield towards a higher energy position in the phase space. Maximum energy gain (195) is achieved if the acceleration process terminates at the dephasing point, i.e., the laser pulse exits the plasma at the dephasing length (198), which corresponds to the largest maximum potential difference (186).

an electron injected into the wakefield, in which case we have $h_0 \neq 1$. Using Hamilton's equations, it is easy to verify that the constant of motion h_0 is the normalized Hamiltonian describing the electron motion, $h(\xi, p_\parallel) = h_0$. Using $\gamma = \sqrt{1 + p_\parallel^2 + a^2}$, we can solve the integral of motion for the longitudinal momentum $p_\parallel$, which defines the longitudinal phase space for any electron as [Schroeder et al., 2006; Esarey et al., 2009]

$$p_\parallel = \gamma_w^2 (\phi + h_0) \left[\beta_w \pm \sqrt{1 - \frac{1 + a^2}{\gamma_w^2 (\phi + h_0)^2}} \right]. \tag{191}$$

The evolution of the electron within the plasma is then uniquely determined based on its initial state and a given scalar potential, which is obtained by solving Eq. (140). The longitudinal momentum values are joined at a point that is part of a unique phase orbit

known as the *separatrix*, which separates two phase space domains. In the inner domain, the phase orbits are closed, and in the outer domain, they are open. The separatrix is joined at the singular points ξ_s, where the square root in (191) equals zero, which yields $\phi(\xi_s) = \sqrt{1 + a^2(\xi_s)}/\gamma_w - h_s$. Plugging this back into Eq. (191), we see that the singular points lie on a curve defined by the following longitudinal momentum [Esirkepov et al., 2006]

$$|p_\parallel| = \beta_w \gamma_w \sqrt{1 + a^2}. \tag{192}$$

In addition, the singular points coincide with the minima of the potential $\phi(\xi_s) = \phi_{\min}$. The separatrix Hamiltonian can be then written in the following form [Esirkepov et al., 2006; Schroeder et al., 2006; Esarey et al., 2009]

$$h_s = \frac{1}{\gamma_w} - \phi_{\min}. \tag{193}$$

In the same manner as we arrived at the longitudinal momentum, we can express the electron energy as $\gamma_e = \beta_w p_\parallel + \phi + C$. Using $1 + \beta_w^2 \gamma_w^2 = \gamma_w^2$, this becomes [Esarey and Piloff, 1995; Esirkepov et al., 2006; Esarey et al., 2009]

$$\gamma_e(\xi) = \gamma_w^2(\phi(\xi) + h_0)\left[1 \pm \beta_w \sqrt{1 - \frac{1 + a^2}{\gamma_w^2(\phi(\xi) + h_0)^2}}\right]. \tag{194}$$

From Fig. 16, we see that the electrons that can accelerate the most are trapped just inside the closed orbit bound by the separatrix. The maximum energy gain is then achieved for electrons that rotate in the phase space to the position ξ_t, which marks the maximum of the potential, $\phi(\xi_t) = \phi_{\max}$, as well as the electron longitudinal momentum for a given orbit. For an electron to pass close through the minimum of the potential within the closed orbits, we must take for the initial condition $h_0 \approx h_s$. Plugging this into Eq. (194), we get [Esarey and Piloff, 1995]

$$\gamma_{\max} = \gamma_w(1 + \gamma_w \Delta\phi)\left[1 + \beta_w \sqrt{1 - \frac{1}{(1 + \gamma_w \Delta\phi)^2}}\right], \tag{195}$$

where we have assumed that $a^2(\xi_t) \approx 0$, which is equivalent to the requirement that the laser pulse is shorter than half of the nonlinear plasma wave. Barring this assumption, the energy gain given by Eq. (195) is valid for any potential difference $\Delta\phi$. In the limit $\gamma_w \Delta\phi \gg 1$ and $\gamma_w \gg 1$, we have $\gamma_{\max} \approx 2\gamma_w^2 \Delta\phi$, where the potential difference is given by Eq. (186). For $E_{\max} \ll 1$, we have $\gamma_{\max} \approx 4\gamma_w^2 E_{\max}$, while for $E_{\max} \gg 1$, we have $\gamma_{\max} = 2\gamma_w^2 E_{\max}^2$. For example, using the plasma wave amplitude for LWFA (147), we get the maximum energy gain in the case $E_{\max} \gg 1$ (which is equivalent to $a^2 \gg 1$) as

$$\gamma_{\text{LWFA}} \approx 2\gamma_w^2 a^2. \tag{196}$$

The energy gain from linear LWFA, where $E_{\max} \ll 1$, can be also readily evaluated, as $\gamma_{\text{LWFA,lin}} \approx 4\gamma_w^2 a^4$. Yet, we know that the maximum electric field amplitude and the accelerating gradient are produced from plasma waves close to the wave-breaking threshold. In such a wake, the maximum energy gain can be obtained using Eq. (183) as

$$\gamma_{\text{wb}} \approx 4\gamma_w^3. \tag{197}$$

Significant electron energies can be expected from highly relativistic plasma waves

with $\gamma_w \gg 1$. For example, let us consider a plasma with a background density of $n_0 = 2.8 \times 10^{18} \, \text{cm}^{-3}$ and a laser with a wavelength of $\lambda = 1 \, \mu\text{m}$. The phase velocity of the plasma wave, which is equal to the group velocity of the laser, is $\gamma_w \approx \omega_0/\omega_{pe} \approx 20$. The maximum energy gain (197) is then $\mathcal{E}_{\max} = \gamma_{\text{wb}} m_e c^2 \approx 16 \, \text{GeV}$. Since the accelerating field given by Eq. (183) is $E_{\max} \approx 1 \, \text{TV/m}$, it is clear that this energy is reached within an acceleration length of $l_{acc} \approx 1.6 \, \text{cm}$. This is a four orders-of-magnitude footprint reduction when compared to the conventional accelerators, which produce accelerating fields of $E_{\text{rf}} \approx 100 \, \text{MV/m}$ [Tajima and Dawson, 1979].

Maximum energy gain assumes that the acceleration is terminated when the electron reaches the maximum potential $\phi_{\max}$. Otherwise, the electron continues to rotate in the phase space along the closed orbit and loses energy. The length which the accelerated electron must traverse before it reaches the maximum potential is known as the *dephasing length* l_d. It approximately corresponds to the time it takes the electron traveling with velocity β_e to overtake the first half of the nonlinear plasma wave in the accelerating phase, which propagates with velocity β_w. Therefore, the dephasing length is [Bulanov et al., 2016a]

$$l_d \approx \frac{\lambda_w}{2(\beta_e - \beta_w)}. \tag{198}$$

In the limit $\beta_e \approx 1$, the dephasing length becomes $l_d \approx \gamma_w^2 \lambda_w$, where λ_w is the nonlinear wavelength of the wakefield given by Eq. (189). Therefore, maximum energy gain occurs when the acceleration distance coincides with the dephasing length of the electron $l_{acc} \approx l_d$; otherwise, the electron crosses the dephasing point and starts to decelerate. Yet, we have also shown in previous sections that the laser itself loses all of its energy into the plasma wake wave after a time corresponding to the pump depletion length l_{pd}, given by Eq. (165) in the limit $\gamma_w \gg 1$ and $a^2 \gg 1$ as $l_{pd} \approx l_p \gamma_w^2$, where l_p is the laser pulse length. Thus, for the electrons to reach the dephasing point, the acceleration length must satisfy $l_{acc} \approx l_d < l_{pd}$. Additionally, we see that the conversion efficiency of laser-to-electron energy is largest when $l_p \approx \lambda_w$, since then we have $l_{pd} \approx l_d$.

2.4.5 Electron injection and betatron X-ray generation

Let us briefly discuss the initial conditions for external electrons to become trapped in the accelerating phase. This problem is generally known as *electron injection*. The open orbits that follow the fluid motion of plasma correspond to Hamiltonians with $h_0 < h_s$. On the other hand, based on our discussion before, the rotating closed orbits that lead to energy gain must be defined by Hamiltonians with $h_0 > h_s$. From this condition, using Eq. (193), we obtain the following condition in the relativistic limit, $\gamma_e(1 - \beta_w \beta_e) > 1$. Solving this inequality, we obtain the initial electron velocity required for injection as

$$\beta_e > \beta_w. \tag{199}$$

In other words, the injected electron must acquire an initial velocity larger than the relativistic plasma wave to follow the closed orbit. A nice analogy exists to the classical problem of a surfer trying to catch an ocean wave. Like the surfer, an electron must initially catch up with the wave such that an "injection" occurs.

There are numerous methods to achieve electron injection into the plasma wakefield, and we refer to [Esarey et al., 2009; Bulanov et al., 2016a] for more details. To discuss at least one, we note that the condition for electron injection is related to wave breaking, i.e., $\beta_e \rightarrow \beta_w$ [Esarey and Pilloff, 1995; Bulanov et al., 1998; Schroeder et al., 2006; Panchenko

et al., 2008]. Indeed, if the driver excites a sufficiently strong plasma wave such that some electrons oscillate up to $\gamma_e \approx \gamma_w$, these electrons will break out of the fluid-like plasma motion. If the laser amplitude is very close to (but smaller than) the wave-breaking threshold[35] (184), a small laser pulse modulation can "wiggle" some plasma electrons to cross the wave-breaking threshold, creating only a small perturbation within the longitudinal electrostatic field of the plasma wave. These electrons immediately catch up with the wave and become injected into the wakefield. This produces an extremely localized electron bunch. Such localization enables uniform acceleration of the whole electron bunch since most copropagate in a similar phase of the longitudinal electric field. Thus, a high-quality quasi-monoenergetic relativistic electron beam is produced [Faure et al., 2004; Karsch et al., 2007; Lu et al., 2007; Couperus et al., 2017; Gonsalves et al., 2019; Salehi et al., 2021; Lazzarini et al., 2024]. To this date, electron bunches with record energy and total charge, for given laser parameters, were typically self-injected [Lazzarini et al., 2024; Kim et al., 2013; Aniculaesei et al., 2024]. Since this method owes its existence to the extreme nonlinearity of the interaction, a drawback of self-injection is the fluctuation of the electron beam parameters, which occurs due to mostly inevitable fluctuations of both laser and target parameters.

Finally, injection can also occur with non-zero initial transverse momentum [Bulanov et al., 1997; Corde et al., 2013], in which case electrons trapped in the wakefield can perform relativistic oscillations at the relativistic plasma frequency, which is referred to as the *betatron frequency*, $\omega_\beta = \omega_{pe}/\sqrt{2\gamma_e}$ [Corde et al., 2013; Lamač et al., 2021], where γ_e is the instantaneous Lorentz factor of the accelerating electron. Relativistic radiation emission, or synchrotron emission, will occur for electrons with $\gamma \gg 1$, as described generally in Sec. 2.2.3. The radius of curvature can be calculated for transverse betatron oscillations, which have normalized transverse momentum $p_\perp = r_\beta k_\beta \gamma$, as [Corde et al., 2013]

$$\rho \approx 1/(r_\beta k_\beta^2), \tag{200}$$

where r_β is the oscillation amplitude, which is determined by the injection conditions, and $k_\beta = \omega_\beta/c$ is the betatron wave number. The critical frequency (99) then follows as

$$\omega_c = \frac{3}{4c} r_\beta \omega_{pe}^2 \gamma^2, \tag{201}$$

where ω_{pe} is the linear plasma frequency. In the case of optimal guiding, r_β may be estimated from the width of the plasma channel given by Eq. (169). For typical parameters of laser wakefield acceleration[36], the critical frequency is in the X-ray region, and this process is referred to as *betatron X-ray generation*[37]. This yields a compact all-optical source of femtosecond X-ray pulses, which is of significant interest for numerous applications [Albert and Thomas, 2016; Corde et al., 2013; Chaulagain et al., 2022].

2.4.6   Relativistic optical vortices and magnetic field generation

We have previously mentioned that a strong magnetic field can be generated during the nonlinear interaction of a laser pulse with the plasma due to the occurrence of fast charged

---

[35]We remind ourselves that this particular threshold is valid for a flat-top laser pulse. The general formulation is again $\beta_e \to \beta_w$.

[36]Which can be estimated using Eq. (196) or (197), assuming that acceleration is terminated at the dephasing point (198).

[37]See paper B.3 for more details and overview of recent literature on betatron X-ray generation and applications. We also suggest [Attwood and Sakdinawat, 2017; Lamač, 2023] for a historical overview of femtosecond X-ray sources and their applications.

particles, which can arise from the nonlinear depletion of laser energy [Bulanov et al., 2001]. The possibility of creating a long-lasting magnetized plasma with lasers is of eminent interest for laboratory astrophysics and inertial confinement fusion[38]. In the non-relativistic regime, magnetic field generation in plasma can be understood through the lens of the inverse Faraday effect [Ali et al., 2010]. The Faraday effect is the transfer of angular momentum from some medium to a laser, which can, for example, result in a net rotation of the electric field vector of a linearly polarized electromagnetic wave. The inverse Faraday effect is the opposite of this process – a transfer of angular momentum from the laser to the electrons and the associated generation of the magnetic field.

We have already shown that electrons in a vacuum obtain angular momentum along the optical axis, given by Eq. (36). In plasma, in the case when $\mathbf{p} = \mathbf{a}$ (i.e. when $\nabla\gamma = \nabla\phi$, or up to first order in one-dimensional approximation), Eq. (36) also describes the total angular momentum of the plasma electron, which is also collinear with the optical axis. In addition to the angular momentum obtained due to nonlinear polarization, which is sometimes referred to as *spin angular momentum*, electrons can also obtain angular momentum from the *orbital angular momentum* of the electromagnetic wave [Allen et al., 1992; Ali et al., 2010]. The angular momentum density of an electromagnetic field is given by $\mathbf{j} = \mathbf{r} \times \mathbf{g}$, where $\mathbf{g} = \epsilon_0\mu_0\mathbf{S}$ is the linear momentum density, $\mathbf{r}$ is the coordinate vector, and $\mathbf{S} = \mathbf{E} \times \mathbf{H}$ is the Poynting vector.

Let us consider an electromagnetic wave propagating along the z direction with a beam profile defined by the solution of the Helmholtz equation $u(x, y, z)$, i.e., with electric field $\mathbf{E} = \mathbf{E}_0 u(x, y, z) \exp[-i(\omega t - kz)]$. For cylindrically-symmetric beams defined as $u(r, \phi, z) = u(r, z) \exp(il\phi)$, where ϕ is the azimuthal angle and l is the so-called *topological charge*, the angular momentum density can be calculated as [Allen et al., 1992; Ali et al., 2010; Longman, 2021]

$$j_z = \frac{l}{\omega}|u|^2 + \frac{\sigma_z r}{2\omega}\frac{\partial|u|^2}{\partial r}, \tag{202}$$

where $\sigma_z = \pm 1$ for, respectively, right-handed and left-handed circular polarization and $\sigma_z = 0$ for linear polarization.

A non-zero topological charge introduces a helical wavefront into the electromagnetic wave, creating a phase jump at the optical axis and, therefore, a zero in the electromagnetic field. Such electromagnetic waves are sometimes referred to as *optical vortices*. Integrating Eq. (202) with the use of the fact that a single photon has the energy of $\hbar\omega$, we obtain the following well-known formula for the total angular momentum per photon $J_z = (l + \sigma_z)\hbar$. Therefore, it is clear that the first term of the angular momentum density corresponds to *orbital angular momentum*, which is given by the value of the topological charge. The second term corresponds to the *spin angular momentum*, which is given by polarization, i.e., the value of σ_z. Note that in the paraxial approximation, the beam profile is given by the Laguerre-Gaussian modes, $u(r, \phi, z) = u_{lp}^{LG}$ [Saleh and Teich, 1991], and the topological charge l corresponds to the azimuthal index of the mode. Orbital angular momentum density is therefore given by the intensity profile $j_{orb.} \sim |u|^2$, and the spin angular momentum is related to the gradient of the intensity profile, $j_{spin} \sim \partial_r|u|^2$. A simple magnetic field generation model can be obtained if we consider the conservation of angular momentum between the electromagnetic wave and plasma [Ali et al., 2010]. The induced electric field in the plasma is then given as $en_e r E_\phi \approx -\partial_t j_z$, and from Faraday's law, $-(1/r)\partial_r(rE_\phi) = -\partial_t B_z$, we obtain

---

[38]See paper B.4 for motivation, literature review, and more details.
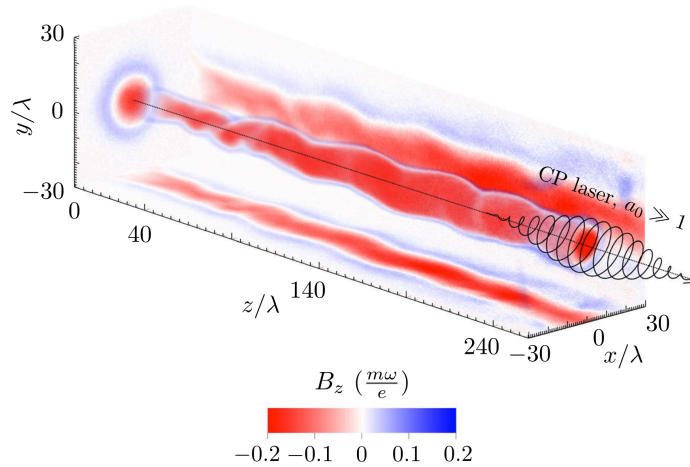
Figure 17: 3D PIC simulation results of magnetic field generation in underdense plasma using relativistic circularly polarized laser pulses. Reprinted under CC BY 4.0 license from [Lamač et al., 2023a]

the following relationship for the rate of change of magnetic field

$$\frac{\partial \mathbf{B}}{\partial t} = \frac{\mathbf{e}_z}{e n_e r} \frac{\partial^2}{\partial t \partial r} \left(\frac{l|u|^2}{\omega c} + \frac{\sigma_z r}{2\omega c} \frac{\partial |u|^2}{\partial r} \right). \tag{203}$$

At the maximum rate of change, using $\partial_r |u|^2 \sim (a_0 \omega / w_0)^2$, the magnetic field scales as $B[\text{MG}] \sim f_{abs} \times (\mu\text{m}/\lambda) \times (a_0^2 n_c/n_e) \times (l + \sigma_z/2) \times (\lambda_0/w_0)^2$, where f_{abs} is the ratio of laser energy absorbed by plasma. This model works well in the linear regime. It is also instructive since it shows us that the magnetic field grows proportionally to both spin and orbital angular momentum, making use of optical vortices attractive for magnetic field generation since they can "rotate" plasma more effectively with $l > 1$ [Ali et al., 2010; Longman, 2021].

Nevertheless, the model breaks in the nonlinear relativistic regime, where electrons achieve relativistic velocities, laser filamentation can occur, and plasma density is significantly modified, all that was neglected in the above treatment. In the nonlinear regime [Askaryan et al., 1994; Askaryan et al., 1997; Berezhiani et al., 1997], as the laser enters the plasma and induces fast currents, *Weibel instability* (also known as *current filamentation instability*) quickly saturates, creating transverse anisotropy within the homogeneous plasma density, with the transverse scale of the saturated channel of the order of the relativistic plasma wavelength, $\lambda_w \sim \sqrt{a_0} c/\omega_{pe}$ [Askaryan et al., 1994]. Longitudinal currents are primarily generated if $l = \sigma_z = 0$, where the magnetic field is primarily azimuthal. If the laser contains angular momentum, $l > 0$ or $\sigma_z > 0$, the electrons follow helical orbits, producing both longitudinal and transverse magnetic field components. These helical current filaments attract each other and create a magnetic field within the plasma channel, which lasts significantly longer than the typical electron plasma timescale $\sim 1/\omega_{pe}$. From Faraday's law, the magnetic field strength can be estimated simply as $B \sim \mu_0 j \lambda_w$. The maximum velocity the electrons can achieve is $v \approx c$. The current density can then be estimated as $j \approx e n_e c$. Using the transverse scale estimated above, we get the maximum magnetic field strength as [Askaryan

et al., 1994; Askaryan et al., 1997; Bulanov et al., 2001; Lamač et al., 2023a]

$$B \approx \frac{m_e \omega}{e} \sqrt{\frac{a_0 n_e}{n_c}}. \tag{204}$$

For initially irrotational plasma, we have shown from Eq. (126) that the vorticity of the plasma electrons is frozen into the magnetic field lines, as $\Omega = \nabla \times \mathbf{p} = e\mathbf{B}/m_e c$ [Hasegawa and Mima, 1977; Chen et al., 1984; Bulanov et al., 2001]. Therefore, the generated magnetic field is initially aligned with symmetrical electron vortices, which are unstable against perturbations and evolve into antisymmetrical rows. This process of magnetic field destabilization is closely related to the von Kármán vortex street known well from fluid mechanics[39]. A motorcyclist driving behind a truck on a highway will feel an oscillating transverse force, corresponding to antisymmetric wind vortices developing behind the truck. In an exactly analogous manner, a laser pulse plowing through plasma creates such a slowly evolving antisymmetric vortex configuration. 3D simulations indicate that long-lasting extremely magnetized plasmas similar to those surrounding supermassive black hole accretion disks, intermediate zones of magnetar magnetosphere, or weakly-magnetized neutron stars are already at reach using available laser technology[40]. Further stabilization of relativistic laser-generated quasi-static magnetic fields in plasma is of significant interest for laboratory astrophysics and, therefore, an exciting avenue for future work.

2.4.7 Relativistic mirrors in underdense plasma

Let us now discuss a concept for producing high-energy coherent electromagnetic radiation based on the idea of a relativistic mirror, envisioned by A. Einstein in his treatise on special relativity [Einstein, 1905]. Let us consider a mirror moving with constant velocity β_w along the x axis and an incident counter-propagating electromagnetic wave with angular frequency ω_0. In the rest frame of the relativistic mirror, spacetime coordinates are given by Lorentz transformation as

$$ct' = \gamma_w(ct - \beta_w x), \tag{205}$$
$$x' = \gamma_w(x - \beta_w ct), \tag{206}$$
$$y' = y, \tag{207}$$
$$z' = z. \tag{208}$$

Due to the relativistic Doppler effect, radiation wavelength and period of the incident radiation must be contracted in the rest frame, with respect to the laboratory frame frequency and wave number as

$$\frac{\omega_0'}{c} = \gamma_w \left(\frac{\omega_0}{c} - \beta_w k_x \right), \tag{209}$$
$$k_x' = \gamma_w \left(k_x - \beta_w \frac{\omega_0}{c} \right). \tag{210}$$

We used $\omega_0/c = k_0$, i.e., we assume a mirror propagating in a vacuum or low-density plasma. In the limit $\gamma_w \gg 1$, we have $\omega_0' = ck_0' \approx 2\gamma_w \omega_0$. Similarly, the electric and magnetic field

---

[39]See paper B.4 for more details.
[40]See [Lamač et al., 2023a], i.e., paper B.4, and references therein.

amplitude of the incident wave transforms as

$$\mathbf{E}'_\| = \mathbf{E}_\|, \tag{211}$$

$$\mathbf{B}'_\| = \mathbf{B}_\|, \tag{212}$$

$$\mathbf{E}'_\perp = \gamma_w \left(\mathbf{E}_\perp + c\boldsymbol{\beta}_w \times \mathbf{B} \right), \tag{213}$$

$$\mathbf{B}'_\perp = \gamma_w \left(\mathbf{B}_\perp - \frac{1}{c}\boldsymbol{\beta}_w \times \mathbf{E} \right). \tag{214}$$

Inverse transformations back to the laboratory frame are the same, except that we have $\boldsymbol{\beta}_w \to -\boldsymbol{\beta}_w$. For an incident laser counter-propagating along the x axis, we have $k_x = -k_0$, and using Eqs. (209)–(214) the counter-propagating laser characteristics take the following form in the rest frame of the mirror

$$\frac{\omega'_0}{\omega_0} = \frac{\tau_p}{\tau'_p} = \frac{E'_0}{E_0} = \sqrt{\frac{1 + \beta_w}{1 - \beta_w}} \approx 2\gamma_w, \tag{215}$$

where τ_p is the pulse duration, which is contracted to τ'_p, and E_0 is the incident laser wave amplitude, which is amplified to E'_0 according to the relativistic Doppler effect. Using the rest frame laser parameters, the description of reflection from the relativistic mirror now reduces to the solution of the wave equation (51) in the rest frame, which has a general solution in three-dimensional space given by Eq. (53). In the far-field limit, it reduces to Eq. (59). Note that all quantities must be expressed in terms of the rest frame variables during the evaluation. For example, current and charge distributions transform according to

$$\rho'c = \gamma_w(\rho c - \beta_w j_\|), \tag{216}$$

$$j'_\| = \gamma_w(j_\| - \beta_w c\rho), \tag{217}$$

$$j'_\perp = j_\perp. \tag{218}$$

Transformation of any variable, including all of the quantities mentioned above[41], is because it is a component of a four-vector in the Minkowski spacetime, which must rotate upon Lorentz transformations, where rotation is meant in the generalized sense, such that distances (dot products given by Minkowski metric) are preserved. For example, the coordinates $x^\mu = (ct, \mathbf{r})$, potentials $A^\mu = (\phi/c, \mathbf{A})$ and currents $j^\mu = (\rho c, \mathbf{j})$, where $\mu \in \{0, 1, 2, 3\}$, are typical examples of four-vectors. Note that in the Lorenz gauge, all of the previously mentioned four-vectors satisfy the following conservation law $\partial_\mu A^\mu = \eta_{\mu\nu}\partial^\nu A^\mu = \partial^0 A^0 - \partial^i A^i = 0$, where $\partial^\mu = (\partial_t/c, -\nabla)$ is the four-gradient and $\eta_{\mu\nu} = \mathrm{diag}(1, -1, -1, -1)$ is the Minkowski metric with the $[+, -, -, -]$ metric signature. Lorentz transformation for any four-vector is then given by a linear transformation $A^{\mu\prime} = \Lambda^{\mu\prime}_\nu A^\nu$. From Eqs. (205), we see that the transformation matrix is given as $\Lambda^{\mu\prime}_\nu = \partial x^{\mu\prime}/\partial x^\nu$, i.e. any component of the matrix can be obtained by calculating derivatives of the rest frame coordinates with respect to laboratory frame coordinates. Scalars, such as the norm of any four-vector, are Lorentz invariant. Though, just like four-vectors, they may depend on coordinates. The invariance tells us that the Lorentz scalar measured in the rest frame at $x' = \Lambda x$ is equal to the same Lorentz scalar measured from the laboratory frame at the corresponding coordinate $x = \Lambda^{-1}x'$, i.e., $\phi'(x') = \phi(x)$.

---

[41]Except for the electromagnetic field components, which are components of a rank-2 antisymmetric tensor, defined from the four-potential as $F^{\mu\nu} = \partial^\mu A^\nu - \partial^\nu A^\mu$. Eqs. (214) – (214) are then obtained from $F^{\mu\prime\nu\prime} = \Lambda^{\nu\prime}_\nu \Lambda^{\mu\prime}_\mu F^{\mu\nu}$.
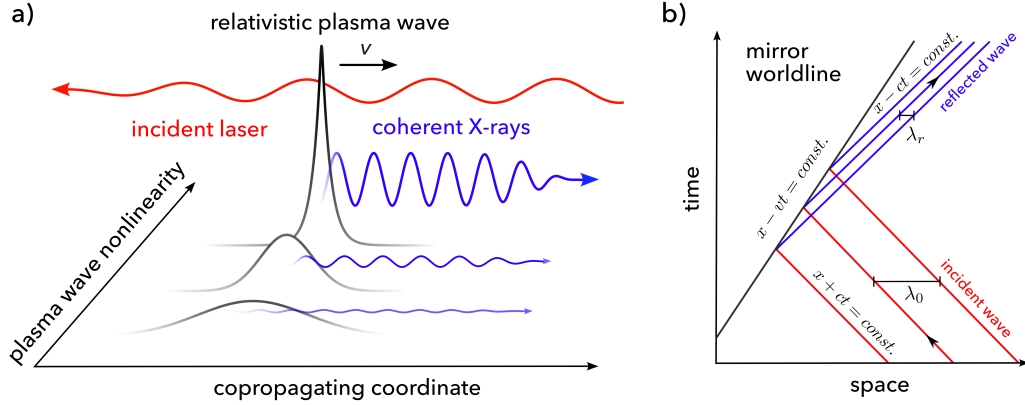
Figure 18: Relativistic mirror based on nonlinear plasma waves driven in plasma. (a) Schematic illustrating the increase of reflection coefficient with plasma wave nonlinearity. (b) Spacetime diagram of a relativistic mirror. Light propagates along the light-cone coordinates $x \pm ct = const.$, which leads to a relativistic double Doppler effect upon reflection. Note that the upshift factor (219) can be derived based on the geometry of (b).

Let us now return to the relativistic mirrors. A. Einstein assumed that his relativistic mirror has ideal reflectivity, but as we will show, any finite distribution of charged particles will introduce a complex reflection coefficient $r = E_r'/E_0'$, where E' is the electric field given in the rest frame of the mirror, and $|r| \leqslant 1$. Therefore, the amplitude of the incident wave is reduced upon reflection in the mirror rest frame. If we transform back into the laboratory frame, the reflected wave undergoes another relativistic Doppler upshift, and the final relationship of incident and reflected frequency, amplitude, and pulse duration follows as

$$\frac{\omega_r}{\omega_0} = \frac{\tau_0}{\tau_r} = \frac{E_r}{rE_0} = \frac{1+\beta_w}{1-\beta_w} \approx 4\gamma_w^2, \tag{219}$$

where the final approximation holds for $\gamma_w \gg 1$. Assuming that the relativistic mirror is composed of electrons, reflection from a planar mirror can be described by the wave equation in the rest frame as

$$\left(\frac{\partial^2}{\partial t'^2} - c^2 \frac{\partial^2}{\partial x'^2} + \omega_{p,r}'^2(x', t') \right) \mathbf{a}(x', t') = 0. \tag{220}$$

Note that according to Eq. (215), the normalized vector potential ($a = E/\omega$) is Lorentz invariant, $a' = a$. Introducing the light-cone coordinates $\xi = x' - ct'$ and $\eta = x' + ct'$[42], which correspond to a $\pi/4$ rotation of spacetime coordinate grid, we obtain the wave equation as [Lamač et al., 2024]

$$\frac{\partial^2 a_r}{\partial \xi \partial \eta} = \frac{1}{4} \frac{k_p'^2}{c^2} \left(\frac{\eta + \xi}{2} \right) a_0 e^{-ik_0'\eta}, \tag{221}$$

where we have assumed that the electron currents composing the mirror oscillate due to the field of the incident radiation, which has amplitude a_0, and that the reflected amplitude satisfies $|a_r| \ll a_0$. Integration of Eq. (221) yields [Bulanov et al., 2013; Bulanov et al., 2016b;

---

[42]These are practical for any problem describing propagating and counter-propagating waves.

Lamač et al., 2024] the complex amplitude reflection coefficient for $r = a_r/a_0$ as

$$r = \frac{1}{2k_0'} \int_{-\infty}^{\infty} k_p'(s) e^{-i2k_0's} \mathrm{d}s, \tag{222}$$

where k_0' is the wave number and $k_p'(x)$ is the inhomogeneous plasma wave number, both transformed to the rest frame of the mirror. We see that the Fourier transform of the inhomogeneous relativistic wave number determines the complex reflection coefficient in the mirror rest frame.

The fact that we denote the velocity of the mirror as β_w, i.e., the same as the phase velocity of relativistic plasma waves discussed in the previous section, is not an accident. Indeed, we have shown before that the density of plasma waves driven close to the wave-breaking threshold diverges, resulting in a highly localized region of high electron density. Such a structure can be considered a relativistic mirror propagating with $\gamma_w \approx \omega_0/\omega_{pe}$ [Bulanov et al., 2003]. The breaking plasma waves have a cusp-like structure [Bulanov et al., 2013; Bulanov et al., 2016b], for which the reflection coefficient can be calculated [Lamač et al., 2024] as

$$r_{\mathrm{wb}} = \frac{\pi}{2^{4/3}3^{2/3}\Gamma\left(\frac{2}{3}\right)} \left(\frac{n_0}{\gamma_w n_c}\right)^{2/3}, \tag{223}$$

where n_0 is the background plasma electron density in the laboratory frame and n_c is the critical density for the incident radiation in the laboratory frame. Laser-driven wakefields are typically driven in background electron plasma density corresponding to $\gamma_w = \omega_{pe}/\omega_{dr} \approx 10 - -100$, where ω_{dr} is the frequency of the laser driving the nonlinear plasma wave. In the case when both the driver and the incident wave have a similar frequency, for example, if the incident one is split from the driving laser, we get a further simplification [Lamač et al., 2024]

$$r_{\mathrm{LWFA}} \approx \frac{0.44}{\gamma_w^2}. \tag{224}$$

For plasma waves with $\gamma_w \gg 1$, the reflected amplitude is $E_r \approx 4\gamma_w^2 r E_0$. Laser-driven plasma waves have typically $\gamma_w \approx 10 - 100$, therefore the reflection coefficient is typically small, $r \approx 10^{-4}$. Nevertheless, the double Doppler frequency upshift can produce an extremely bright beam of coherent radiation. With laser-driven plasma waves, we can tune the pressure of the gas target to change the velocity of the mirror, according to $\gamma_w = \omega_{pe}/\omega_{dr}$. In such a case, Eq. (219) promises an extremely tunable source of coherent X-ray radiation and attosecond pulses [Lamač et al., 2024], with relative spectral bandwidth inherited from the incident laser pulse[43].

Relativistic parabolic mirror

Apart from the double Doppler effect, the intensity of radiation reflected from a relativistic mirror can be further increased if the mirror is curved such that the focusing of radiation occurs. This was first proposed in [Bulanov et al., 2003], where it was shown that nonlinear plasma waves naturally take the shape of a paraboloid [Bulanov et al., 2003; Jeong et al.,

---

[43]In paper B.2, we show that coherent X-ray sources based on relativistic plasma mirrors could rival the spectral brightness of free electron lasers. We guide the reader there for an extended discussion of the properties and applicability of relativistic mirrors based on nonlinear plasma waves. Furthermore, we refer to [Bulanov et al., 2013; Bulanov et al., 2016b; Koga et al., 2018; Kando et al., 2018] for an overview of the current state-of-the-art regarding relativistic mirrors based on nonlinear plasma waves driven in underdense plasma.

2021b; Jeong et al., 2021a]. To obtain the reflected spatiotemporal distribution of radiation, we must first calculate the distribution in the mirror rest frame and perform an inverse transformation into the laboratory frame, done in [Jeong et al., 2021b]. Crucially, the focal length of a relativistic parabolic mirror is reduced by a factor of γ_w in the mirror rest frame. For $\gamma_w \gg 1$, the focal length is extremely short, and the reflection can be approximated as a 4π focusing scenario [Jeong et al., 2020], where radiation is being spherically focused into the spot from a solid angle of 4π, which is a limiting case of tight-focusing, where the ratio of the focal length to beam size, known as f-number, approaches zero [Jeong et al., 2020].

To illustrate the effect of relativistic focusing, we present the case of radial polarization [Jeong et al., 2021b]. We may consider that the incident radiation is described by a Laguerre-Gaussian beam, with an effective radius of $w_{p,l} = w_0\sqrt{2p + l + 1}$, where w_0 is the laser waist of the zeroth-order Gaussian beam and p and $l \geqslant 0$ are the radial and azimuthal index. In the mirror rest frame, the spectral components of the 4π-spherically-focused laser can be expressed in spherical coordinates (r, θ, φ) as

$$\mathbf{E}'_{4\pi}\left(\rho', \theta', \omega'\right) = \mathbf{e}'_\theta\, iE_{0,f}\left(\omega'\right) S_a\left(\rho', \theta', \omega'\right) \exp\left(i\omega't'\right), \tag{225a}$$

$$\mathbf{B}'_{4\pi}\left(\rho', \theta', \omega\right) = -\mathbf{e}'_\varphi\, B_{0,f}\left(\omega'\right) S_b\left(\rho', \theta'; \omega'\right) \exp\left(i\omega't'\right), \tag{225b}$$

where $E_{0,f}\left(\omega'\right)$ and $B_{0,f}\left(\omega'\right)$ are the amplitudes of the Fourier components of electric and magnetic fields in the focus, $\mathbf{e}'_\theta$ and $\mathbf{e}'_\varphi$ are, respectively, the azimuthal and polar unit vectors in the rest frame coordinates, and the spatial distribution functions are given as

$$S_a = \sum_{k=0}^{\infty} \frac{4k+1}{2^{3k}} j_{2k}\left(\frac{\omega'}{c}\rho\right) P_{2k}\left(\cos\theta'\right), \tag{226}$$

$$S_b\left(\omega'\right) = \frac{4}{\pi} j_1\left(\frac{\omega'}{c}\rho\right) P_1^1\left(\cos\theta'\right), \tag{227}$$

where $j_n\left(x\right)$ is the spherical Bessel function of the first kind and n-th order, and $P_n\left(\cdot\right)$ and $P_n^m\left(\cdot\right)$ are, respectively, the Legendre and the associated Legendre functions [Gradshteyn and Ryzhik, 1965]. Note that to obtain the case of azimuthal polarization, we can swap electric and magnetic field components of the radial polarization, $\mathbf{E}_f \leftrightarrow \mathbf{B}_f$ [Jeong et al., 2020; Jeong et al., 2021b]. It is enough to keep only the first two terms of the infinite sum defining the spatial distribution S_a to produce tractable expressions. Summing up the neglected higher-order spherical Bessel functions slightly reduces the size of the focal spot [Jeong et al., 2021b], but this does not affect the qualitative description, which is our primary interest. Therefore, we keep only the first two terms of the sum $(k = 0, 1)$. Performing the inverse Lorentz and Fourier transformations for the 4π-focused fields given by Eqs. (225a)–(225b), we obtain in the laboratory frame the spatiotemporal distribution of a radially polarized laser, focused by a relativistic parabolic mirror, as [Jeong et al., 2021b]

$$\mathbf{E}_r\left(\rho, \theta, \varphi, t\right) = \gamma_w \frac{1+\beta_w}{1-\beta_w\cos\theta}\sqrt{\frac{3\pi^5}{8}}\frac{w_{p,l}}{\lambda_0}E_0$$

$$\times \begin{bmatrix} \left\{-j_0\left(\omega'_0 R/c\right)\sin\left(\omega'_0 T\right)\Upsilon_1 + \beta_w j_1\left(\omega'_0 R/c\right)\cos\left(\omega'_0 T\right)\Upsilon_2\right\}\cos\varphi \\ \left\{-j_0\left(\omega'_0 R/c\right)\sin\left(\omega'_0 T\right)\Upsilon_1 + \beta_w j_1\left(\omega'_0 R/c\right)\cos\left(\omega'_0 T\right)\Upsilon_2\right\}\sin\varphi \\ \left(1/\gamma_w\right)j_0\left(\omega'_0 R/c\right)\sin\left(\omega'_0 T\right)\Upsilon_2 \end{bmatrix}, \tag{228a}$$

$$\mathbf{B}_r\left(\rho,\theta,\varphi,t\right) = \gamma_w \frac{1+\beta_w}{1-\beta_w\cos\theta}\sqrt{\frac{3\pi^5}{8}}\frac{w_{p,l}}{\lambda_0}\frac{E_0}{c}$$

$$\times \begin{bmatrix} \left\{-j_1\left(\omega_0'R/c\right)\cos\left(\omega_0'T\right)\Upsilon_2 + \beta_w j_0\left(\omega_0'R/c\right)\sin\left(\omega_0'T\right)\Upsilon_1\right\}\sin\varphi \\ \left\{j_1\left(\omega_0'R/c\right)\cos\left(\omega_0'T\right)\Upsilon_2 - \beta_w j_0\left(\omega_0'R/c\right)\sin\left(\omega_0'T\right)\Upsilon_1\right\}\cos\varphi \\ 0 \end{bmatrix}, \tag{228b}$$

where $\lambda_0 = 2\pi c/\omega_0$ is the wavelength of the incident laser in the laboratory frame. The envelope functions are given as

$$\Upsilon_1\left(T,R\right) = \frac{1}{2}\left\{\frac{\cos\theta+\beta_w}{1+\beta_w\cos\theta}\exp\left[-\frac{\Delta\omega'^2}{4}\left(T+\frac{R}{c}\right)^2\right]\right.$$
$$\left. + \frac{\cos\theta-\beta_w}{1-\beta_w\cos\theta}\exp\left[-\frac{\Delta\omega'^2}{4}\left(T-\frac{R}{c}\right)^2\right]\right\}, \tag{229}$$

$$\Upsilon_2\left(T,R\right) = \frac{1}{2}\left\{\frac{\sin\theta}{\gamma_w\left(1-\beta_w\cos\theta\right)}\exp\left[-\frac{\Delta\omega'^2}{4}\left(T-\frac{R}{c}\right)^2\right]\right.$$
$$\left. + \frac{\sin\theta}{\gamma_w\left(1+\beta_w\cos\theta\right)}\exp\left[-\frac{\Delta\omega'^2}{4}\left(T+\frac{R}{c}\right)^2\right]\right\}, \tag{230}$$

where $\Delta\omega' = 1/\tau'$ is the spectral bandwidth of the incident laser pulse in the mirror rest frame. Finally, the time-like T and space-like R functions are defined as

$$T\left(\rho;t\right) = \frac{t-\left(\rho/c\right)\beta_w\cos\theta}{\gamma_w\left(1-\beta_w^2\cos^2\theta\right)}, \tag{231}$$

$$R\left(\rho;t\right) = \frac{\rho-ct\beta_w\cos\theta}{\gamma_w\left(1-\beta_w^2\cos^2\theta\right)}. \tag{232}$$

The frequency and pulse duration of the reflected laser is given by [Jeong et al., 2021b]

$$\frac{\omega_r}{\omega_0} = \frac{\tau_0}{\tau_r} = \frac{1+\beta_w}{1-\beta_w\cos\theta}, \tag{233}$$

which corresponds to the relativistic double Doppler effect [Einstein, 1905]. On the axis of symmetry of the parabolic mirror ($\theta=0$), the frequency upshift corresponds to the case of a flat relativistic mirror given by Eq. (219). From Eqs. (228a)–(228b), we can estimate the field strength at the focus of a relativistic parabolic mirror as

$$\frac{E_r}{E_0} \approx 4\gamma_w^3\sqrt{\frac{3\pi^5}{8}}\frac{w_{p,l}}{\lambda_0}, \tag{234}$$

Compared to the flat relativistic mirror, we see that the relativistic parabolic mirror introduces another enhancement factor of $E_{par}/E_{flat} \approx \gamma_w(w_0/\lambda_0)$, which can be significant for highly relativistic mirrors. To give an example, let us consider a laser pulse with $\lambda_0 = 0.8\ \mu$m, initial beam radius of $w_0 = 3\ \mu$m, and incident intensity $I_0 = 10^{18}$ W/cm². Then, being reflected from an ideal ($r=1$) relativistic parabolic mirror with $\gamma_w = 10$, one obtains reflected intensity of $I_r \approx 2.6 \times 10^{28}$ W/cm² at focus, assuming reflection coefficient of $r = 1$. An
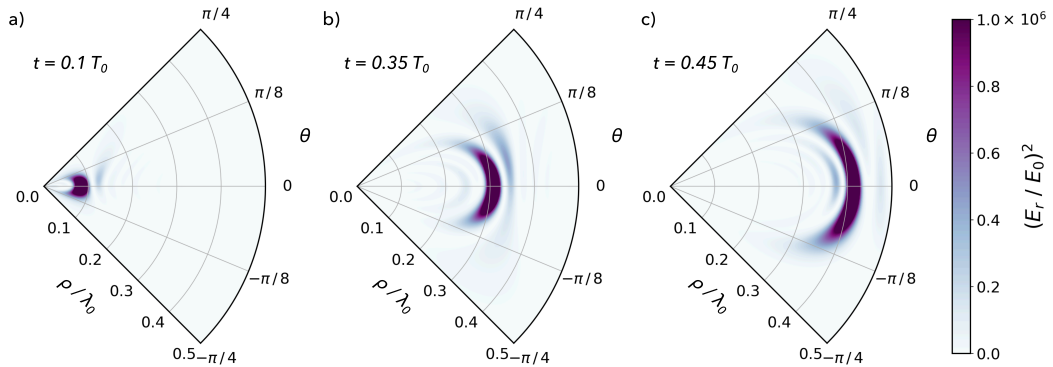
Figure 19: Temporal evolution of radiation energy density, $(\mathbf{E}_r/E_0)^2$, of an electromagnetic pulse reflected from a parabolic relativistic mirror propagating with $\beta_w = 0.9$, with the electric field calculated using Eq. (228a) for $\varphi = 0$. The laser waist is given as $w_e = 5.2\lambda_0$ with pulse duration of $\tau_{\text{FWHM}} \approx 6\, T_0$, where $T_0 = \lambda_0/c$ is the period of the incident laser. The value of the electric field at the focus ($t = 0$) is given by Eq. (234). The color bar is saturated to show the relative differences between individual snapshots.

example of the spatiotemporal evolution of the reflected electromagnetic field was calculated using Eqs. (228a)–(228b), and is presented in Fig. 19. Crucially, the possibility to achieve such intensities would allow us to study a realm of nonlinear quantum electrodynamics in a manner that is not accessible to conventional accelerators, for example, through light-light interaction [Heisenberg and Euler, 1936; Schwinger, 1951; Di Piazza et al., 2012].

Let us consider an electric field strength that could accelerate an electron to an energy of $2m_ec^2$ over a distance corresponding to the Compton wavelength $\lambda_c = 2\pi c/\omega_c$, which corresponds to a photon with energy of $\hbar\omega_c = m_ec^2$. In such a field, electron and positron pairs can be produced out of a vacuum, known as the *Schwinger effect*. The corresponding electric field value is known as the *Schwinger limit* [Heisenberg and Euler, 1936; Schwinger, 1951; Bulanov et al., 2003; Mourou et al., 2006; Di Piazza et al., 2012],

$$E_s = \frac{m_ec^2c^3}{q_e\hbar} \approx 1.32 \times 10^{18} \text{ V/m}, \tag{235}$$

which corresponds to an intensity of $I_s \approx 10^{29}$ W/cm^2. The Schwinger limit corresponds to the breakdown of vacuum and the surprising onset of nonlinear electrodynamics *in vacuum* [Heisenberg and Euler, 1936; Schwinger, 1951; Di Piazza et al., 2012]. For electric fields close to E_s, the vacuum can become significantly polarized, and nonlinear processes occur, such as photon-photon scattering or birefringence of light [Schwinger, 1951; Di Piazza et al., 2012]. Studying the effects of such electromagnetic fields would prove invaluable for fundamental physics [Di Piazza et al., 2012], which drives motivation into accelerated research of laser amplification processes, which could enable us to probe $E \approx E_s$ in the laboratory. While this intensity may not yet be readily attainable with today's technology, we can use Lorentz invariance to study these processes within the rest frame of relativistic charged particles, specifically the readily available relativistic electron.

The parameter which dictates the onset of nonlinear effects through the interaction of an electron with the electromagnetic field is known as the electron quantum parameter [Di Piazza

et al., 2012; Blackburn, 2020], which is given as

$$\chi = \frac{\gamma}{E_s}\sqrt{(\mathbf{E} + c\boldsymbol{\beta} \times \mathbf{B})^2 - (\mathbf{E} \cdot \boldsymbol{\beta})^2}.$$ (236)

For electromagnetic plane waves we have $\mathbf{B} = \mathbf{n} \times \mathbf{E}$, and since $\mathbf{n} \cdot \mathbf{E} = 0$, we get

$$\chi = \gamma \frac{E}{E_s}\sqrt{(1 - \boldsymbol{\beta} \cdot \mathbf{n})^2}.$$ (237)

In counter-propagating geometry, we have $\mathbf{n} \cdot \boldsymbol{\beta} \approx -1$. Therefore, $\chi = 2\gamma(E/E_c)$. Today, electrons are routinely accelerated to $\gamma \sim 10^4$ using laser wakefield acceleration [Leemans et al., 2014; Gonsalves et al., 2019; Aniculaesei et al., 2024], or even $\gamma > 10^5$ with conventional accelerators [Decking et al., 2017]. To explore nonlinear effects at $\chi \sim 1$, the electric field intensity requirement decreases proportionally with increasing γ. This scheme could enable all-optical experiments studying the effects of nonlinear quantum electrodynamics, where both of the scattering components, accelerated electrons and intensely focused radiation, could be produced using lasers [Mourou et al., 2006; Di Piazza et al., 2012; Blackburn, 2020; Lamač et al., 2023a].

2.5 Relativistically overdense plasma

In this section, we consider the interaction of electromagnetic radiation with relativistically opaque plasma, which occurs when $\omega < \omega_{p,r} = \omega_{pe}/\sqrt{\gamma}$. This regime is of great importance to problems such as inertial confinement fusion, high-harmonic generation, particle acceleration, or emission of gamma radiation. Typically, the interaction of laser pulses with plasma often involves some form of plasma inhomogeneity. Femtosecond laser pulses are usually accompanied by spontaneously amplified emission at the picosecond or nanosecond scale. These pre-pulses can be significant and ionize target material long before the main pulse arrives. In such a scenario, the plasma surface can expand into the vacuum with a natural gradient, which can be estimated with a scale length $L \approx [(1/n_e)\partial_x n_e]^{-1}$. The interaction then takes place in an inhomogeneous plasma, where the laser pulse propagates up to the region of plasma resonance[44], where $\omega = \omega_{pe}$. Today, some techniques enable us to clean pre-pulses such that plasma gradients with scale length $kL \ll 1$ can be produced [Teubner and Gibbon, 2009; Kahaly et al., 2013], where k is the wave number of incident radiation. In this scenario, a sharp plasma-vacuum interface allows the laser to easily extract electrons from the plasma and accelerate them towards the vacuum region in the first half-cycle of the electromagnetic wave. A process known as *vacuum heating of electrons* [Brunel, 1987; Gibbon, 2005; Teubner and Gibbon, 2009]. Thus, it is sensible that we begin this chapter by discussing the propagation of electromagnetic waves in inhomogeneous plasmas [Landau and Lifshitz, 1960; Kruer, 1988].

2.5.1 Propagation of electromagnetic waves in inhomogeneous plasmas

Let us assume that the electromagnetic wave is obliquely incident on an inhomogeneous plasma with density $n_e = n_e(x)$, which has a positive gradient pointing in the x-direction ($\partial_x n_e > 0$), and which is located in the region $x > 0$. The angle of incidence θ is given with

---

[44]As we will show later, the laser is reflected even earlier at oblique incidence.

respect to the plasma surface normal vector[45]. In vacuum, the wave satisfies $\omega^2 = c^2(k_x^2 + k_y^2)$, where $k_y = k_x \cos\theta, k_y = k \sin\theta$. For $k_y = 0$, the wave is said to be incident *normally*, while in the case of $k_y \neq 0$, it is said to pass *obliquely*. For oblique incidence, two different cases of polarization must be distinguished. In the case of *S-polarization*, the electric field vector is perpendicular to the plane of incidence, $\mathbf{E} = E_z \exp(-i\omega t)\mathbf{e}_z$. In the opposite case of *P-polarization*, the electric field vector $\mathbf{E}$ lies in the plane of incidence, and the magnetic field vector lies perpendicular to this plane, $\mathbf{B} = B_z \exp(-i\omega t)\mathbf{e}_z$.

S-polarization

The wave equation for the S-polarized electric field is given as [Landau and Lifshitz, 1960; Kruer, 1988; Eliezer, 2002]

$$\frac{\mathrm{d}^2 E_z}{\mathrm{d}x^2} + \frac{\mathrm{d}^2 E_z}{\mathrm{d}y^2} + \frac{\omega^2 n^2}{c^2} E_z = 0, \tag{238}$$

where $n(x) = \sqrt{1 - (\omega_{pe}(x)/\omega)^2}$ is the refractive index of the inhomogeneous plasma. Since the refractive index varies only in the x-direction, the perpendicular component of the wave vector $k_y = k \sin\theta$ must be conserved. Therefore, we can write the electric field component as $E_z = E \exp(ik_y y)$. Then, we have

$$\frac{\mathrm{d}^2 E}{\mathrm{d}x^2} + \left(\frac{\omega^2 n^2}{c^2} - k_y^2 \right) E = 0, \tag{239}$$

Note that the term within the parentheses corresponds to the local wave vector component in the x-direction, $k_x^2 = k^2 n^2 - k_y^2$, where k is the vacuum wave number of the incident laser. Also note that the laser wave must reflect when k_x changes sign, i.e., at a *reflection point x_r* where $k_x = 0$, which yields the following condition $\omega \cos\theta = \omega_{pe}(x_r)$. The exact position of the reflection point x_r generally depends on the inhomogeneous plasma density profile. A solution for *S*-polarization can be obtained if we assume slow variation of the longitudinal wave number, $|(1/k_x)\partial_x k_x| \ll |k_x|$, which can be rewritten more concisely as

$$\left| \frac{\partial}{\partial x} \frac{1}{k_x} \right| \ll 1. \tag{240}$$

This is often referred to as *Wentzel-Kramers-Brillouin approximation*, which yields the following solution for the electric field of the *S*-polarized wave [Landau and Lifshitz, 1960; Kruer, 1988; Eliezer, 2002]

$$E(x) = \frac{E_0}{\sqrt{ck_x/\omega}} \exp\left(i \int_0^x k_x(\eta)\mathrm{d}\eta \right), \tag{241}$$

where E_0 is the electric field amplitude in the vacuum region $x < 0$. The amplitude of the electric field increases as the light wave propagates towards higher electron density, as $|E = E_0/\sqrt{k_x(x)}$. This can be explained if we note that the energy density of the wave is conserved, $|E(x)|^2 v_g/c = E_0^2$, where $v_g/c = ck_x/\omega$ is the group velocity of the wave. Therefore, since the local group velocity of the electromagnetic wave decreases as the wave enters higher density, the electric field amplitude must swell.

It is clear that the condition given by Eq. (240) is not satisfied at the reflection point

---

[45]See Fig. 20 for the geometry.

x_r, where $k_x \to 0$. To find an analytic solution, we expand the longitudinal wave vector k_x in the neighborhood of the reflection point and keep only the leading order linear term, $k_x^2 \approx -\alpha(x - x_r)$. This yields the *Airy-Stokes equation* [Gradshteyn and Ryzhik, 1965], $\mathrm{d}^2 E/\mathrm{d}x^2 - \alpha(x - x_r)E = 0$. Without loss of generality, let us assume that the plasma density is growing. Then, $\alpha > 0$, and it is clear that the solution is oscillatory for $x < x_r$ and exponential for $x > x_r$. A solution that satisfies this behavior and is finite for all x exists and is given as

$$E(x) = \mathcal{A}\mathrm{Ai}\,(\eta)\,, \tag{242}$$

where $\mathrm{Ai}(\eta) = (1/\pi)\int_0^\infty \cos(u^3/3 + u\eta)\mathrm{d}u$ is the *Airy function* [Gradshteyn and Ryzhik, 1965], $\mathcal{A}$ is a constant and $\eta = \alpha^{1/3}(x - x_r)$. It is also important to mention that this solution is exact for inhomogeneous plasma with a constant gradient, i.e. $\omega_{pe}^2(x) = \omega^2 x/L$. In such a case, we have $x_r = L\cos^2\theta$ and $\alpha = \omega^2/(c^2 L) = k^2/L$[46]. To see how the constant $\mathcal{A}$ relates to the amplitude of the incident wave E_0, we expand Eq. (242) far away from the reflection point. At $x = 0$, we have $\eta = -(kL)^{1/3}\cos^2\theta$, and for $(kL)^{1/3}\cos^2\theta \gg 1$ we get $\mathrm{Ai}(-\eta) \approx (\eta^{-1/4}/\sqrt{\pi})\cos\left[(2/3)\eta^{3/2} - \pi/4\right]$ [Gradshteyn and Ryzhik, 1965], and the electric field can be written as [Kruer, 1988; Eliezer, 2002]

$$E(\eta) \approx \frac{\mathcal{A}}{2\sqrt{\pi}\eta^{1/4}}\,\exp\left[i\left(\frac{2\eta^{2/3}}{3} - \frac{\pi}{4}\right)\right] + \frac{\mathcal{A}}{2\sqrt{\pi}\eta^{1/4}}\,\exp\left[-i\left(\frac{2\eta^{2/3}}{3} - \frac{\pi}{4}\right)\right]. \tag{243}$$

Eq. (243) represents the stationary wave formed by the superposition of the incident wave propagating in the positive x-direction, and the wave reflected at $x = x_r$, which propagates in the negative x-direction. For $x \gg x_r$, the expansion of Eq. (242) shows that the incident wave decays exponentially, as [Kruer, 1988; Eliezer, 2002]

$$E(x \gg x_r) \approx \frac{\mathcal{A}}{2\sqrt{\pi}\eta^{1/4}}\,\exp\left[-\left(\frac{2\eta^{3/2}}{3}\right)\right]. \tag{244}$$

Since the wave is reflected at $x = x_r$ and evanescent for $x > x_r$, the reflection coefficient must be equal to unity, $r = 1$. Therefore, in the vacuum region $x < 0$, Eq. (242) is equal to the sum of the incident and reflected waves, $E(x = 0) = E_0 + E_0\exp(i\varphi)$, where $\phi = 4kL/3 - \pi/2$ is the phase acquired by the reflected wave throughout its propagation in plasma. This gives us $\mathcal{A} = 2\sqrt{\pi}(kL)^{1/6}E_0 e^{i\phi}$, and the general solution (242) can be now written in terms of the incident laser amplitude as [Kruer, 1988; Eliezer, 2002]

$$E(x) = 2\sqrt{\pi}(kL)^{1/6}E_0 e^{i\phi}\mathrm{Ai}\,(\eta)\,. \tag{245}$$

The Airy function has a maximum at $\eta = -1$, $\mathrm{Ai}(-1) \approx 0.54$. The maximum value of the electric field in plasma is therefore $|E_{max}/E_0| \approx 1.9(kL)^{1/6}$. As an example, for an inhomogeneous plasma with scale length $L = 100\,\mu$m and laser wavelength $\lambda_0 = 1\,\mu$m, the maximum field is $E_{max}/E_0 \approx 5.57$. The magnetic field $\mathbf{B} = B\mathbf{e}_y$ is given from Faraday's law as $B(x) = -(i/\omega)\partial_z E(x)$, which yields

$$B(x) = -i2\sqrt{\pi}(kL)^{-1/6}B_0 e^{i\phi}\mathrm{Ai}'\,(\eta)\,. \tag{246}$$

We point out that as the electric field increases, the magnetic field decreases. Additionally, B is zero when E is maximum. At the reflection point $x = x_r = L\cos^2\theta$, where $\eta = 0$, the

---

[46]Note that the full solution also includes the phase factor $\exp(-i\omega t + ik_x x)$.

values of the electric and magnetic field are given as [Eliezer, 2002]

$$\left|\frac{E_s(\eta = 0)}{E_0}\right| \approx 1.26(kL)^{1/6}, \tag{247}$$

$$\left|\frac{B_s(\eta = 0)}{B_0}\right| \approx 0.92(kL)^{-1/6}. \tag{248}$$

P-polarization

In the case the electric field vector lies in the plane of incidence, the wave equation for the out-of-plane magnetic field $\mathbf{B} = B(x)\exp\left(-i\omega t + ik_y y\right)\mathbf{e}_z$ is [Kruer, 1988; Eliezer, 2002]

$$\frac{\mathrm{d}^2 B}{\mathrm{d}x^2} + \frac{1}{n^2}\frac{\partial B}{\partial x} + \left(\frac{\omega^2}{c^2} - \frac{k_y^2}{n^2}\right)B = 0. \tag{249}$$

It is immediately clear that the equation has a singularity at $n^2 \to 0$, which corresponds to the point where $\omega = \omega_{pe}$. Let us again consider the linear density profile, $\omega_{pe}^2(x) = \omega^2 x/L$. Substituting $\eta = (k^2/L)^{1/3}(x - L)$ and $\tau = (kL)^{1/3}\sin\theta$, Eq. (249) then becomes [Eliezer, 2002]

$$\frac{\partial^2 B}{\partial \eta^2} - \frac{1}{\eta}\frac{\partial B}{\partial \xi} - (\eta + \tau^2) = 0. \tag{250}$$

The equation has a singularity at $\eta = 0$, which corresponds to $x = L$, and thus $\omega_{pe} = \omega$. We consider the evolution of the magnetic field close to the resonance point, where $\eta \ll \tau^2$,

$$\frac{\partial^2 B}{\partial \eta^2} - \frac{1}{\eta}\frac{\partial B}{\partial \xi} - \tau^2 = 0. \tag{251}$$

It can be verified with direct substitution that the solution is given by

$$B(\eta) = B_0\left(1 + \frac{1}{2}\tau^2\eta^2\ln\eta\right). \tag{252}$$

At the resonance point $\eta \to 0$, the magnetic field tends to a constant value of B_0 [Landau and Lifshitz, 1960; Kruer, 1988; Eliezer, 2002]. To find how this value relates to the amplitude of the incident wave E_0, we first mention that far from the resonance point ($\eta \gg \tau^2$), the magnetic field is effectively described by the Airy-Stokes equation, and the results from previous sections apply. The magnetic field at the reflection point $x_r = L\cos^2\theta$ can therefore be taken using Eq. (248), as $B(x_r) \approx B_0 0.92E_0(kL)^{-1/6}$. The decay of the magnetic field as it tunnels beyond the reflection point $x_r = L\cos^2\theta$ onwards to the resonance point $x_p = L$ can be estimated by a decay factor $e^{-\beta}$, which corresponds to the phase factor of a wave propagating beyond the turning point, $\beta = \int_{L\cos^2\theta}^{L}(1/c)(\omega_{pe}^2(x) - \omega^2\cos^2\theta)^{1/2}\mathrm{d}x$. Thus, we obtain the following value for the magnetic field close to the resonance point,

$$B(x = L) \approx 0.9B_0(kL)^{-1/6}\exp\left[-\frac{2}{3}kL\sin^3\theta\right]. \tag{253}$$

The electric field at the resonance point can now be obtained from Faraday's law,
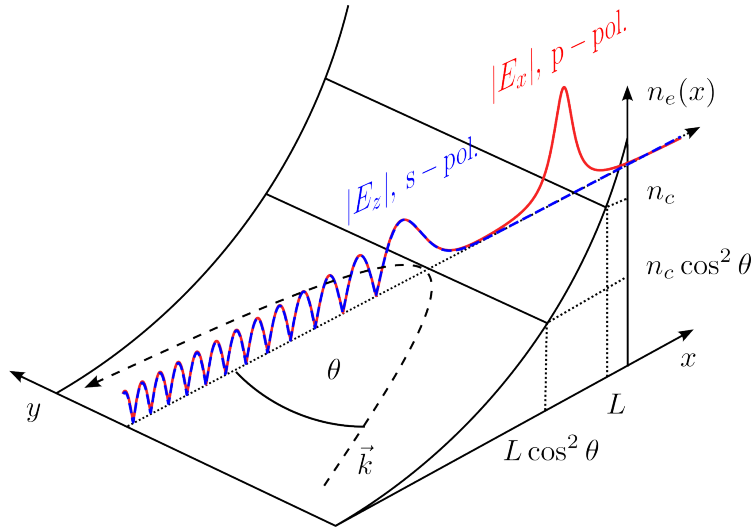
Figure 20: Schematic illustrating the difference between the interaction of a P and S-polarized electromagnetic wave with inhomogeneous plasma. The electromagnetic wave has an initial wave vector **k** and is incident at an angle of θ away from the surface normal. The dashed line indicates the evolution of the wave vector. In the case of S-polarization, the electric field of the wave is given by E_z, the wave is reflected at $x_r = L \cos^2 \theta$ and forms a standing wave pattern described by Eq. (245). For P-polarization, the situation is analogous for E_x up until the reflection point, where the electric field swells like S polarization. However, in the case of P-polarization, the electromagnetic wave tunnels through onwards to the critical density positioned at $x_p = L$, where the E_x grows linearly with time. This growth is due to resonant oscillations of the plasma electrons since at $x_p = L$, we have $\omega = \omega_{pe}$. The resonant growth is then saturated due to laser energy absorption, or the end of interaction. Eq. (257) gives the electric field of the saturated resonance.

$\nabla \times \mathbf{B} = -ikn^2 \mathbf{E}$, which gives us the magnitude of the x-component of the electric field as

$$|E_x| = \left| i \frac{\partial_y B_z}{kn^2} \right| = \frac{\sin \theta B(x)}{n^2(x)}. \tag{254}$$

While the magnetic field is constant at the resonance point, it is clear that the electric field becomes singular at the resonance point $x \to L$, where $n^2 \to 0$. The physical interpretation of Eq. (254) is revealed when we realize that the dielectric function $\epsilon = n^2$ describes the response of the oscillating plasma electrons [Landau and Lifshitz, 1960; Kruer, 1988; Bulanov et al., 2001; Eliezer, 2002]. At the same time, $E_d = B(x = L) \sin \theta$ represents the evanescent amplitude of the incident wave at the resonance point $x = L$, which drives the electron oscillations. Using the magnetic field at the resonance point (253), we can express the driving electric field as

$$E_d = \frac{E_0}{\sqrt{2\pi kL}} \phi(\tau), \tag{255}$$

where $\phi(\tau) \approx 2.3\tau \exp\left(-2\tau^3/3\right)$. The driving field vanishes for $\tau \to 0$, corresponding to normal incidence. Normal incidence is, therefore, analogous to the case of S-polarization discussed before, where no resonance occurs.

Resonance saturation and laser absorption

We now reveal an essential property of plasma resonance. In general, the amplitude of the electric field $E_x(t)$ cannot grow indefinitely. Several saturation processes can occur for ultrashort laser pulses [Bulanov et al., 1994; Bulanov et al., 1998; Bulanov et al., 2001]. To discuss a few, the electromagnetic wave might have a finite pulse duration, in which case the resonance will saturate following the pulse duration. Saturation also occurs when the electrons are driven with such strength that they are ejected from the resonance region, i.e., wave breaking occurs. Relativistic detuning of the resonant frequency may also happen, where the resonant plasma frequency increases with the increasing inertia of plasma electrons performing relativistic oscillations. Apart from these collisionless processes, we may also consider the collisional ones, such as electron-ion collisions [Chen et al., 1984], which can be important for long pulse durations and small normalized amplitudes.

Resonance saturation is equivalent to the occurrence of an imaginary part of the dielectric function, which can be, therefore, generally written as [Kruer, 1988; Eliezer, 2002]

$$\epsilon = n^2 = 1 - \frac{\omega_{pe}^2(x)}{\omega^2} - is, \tag{256}$$

where s is a dimensionless number that can characterize any saturation process, such as the ones mentioned above. It can be related to an effective frequency of the saturation process ν as $s = \nu/\omega$, where ω is the angular frequency of the incident laser. The electric field in the resonance region can then be written as

$$E_x(x,t) = \mathcal{R}\left[\frac{E_d \exp(-i\omega t)}{1 - (\omega_{pe}/\omega)^2 - is}\right], \tag{257}$$

where $\mathcal{R}[\cdot]$ is the real part of the complex electric field and $(\omega_{pe}/\omega)^2 = x/L$ for the linear plasma density profile. The maximum amplitude, spatial width, saturation time of the resonance, and its relative bandwidth are approximately

$$E_{max} = \frac{E_d}{s}, \qquad \Delta x = sL, \qquad \Delta t = \frac{1}{s\omega}, \qquad \frac{\Delta\omega}{\omega} = s. \tag{258}$$

We note that the relative bandwidth is related to the quality factor Q of the resonance, as $Q = \omega_{pe}/\Delta\omega = 1/s$. As noted before, at low temperatures and incident wave amplitudes, saturation due to the electron-ion collisions may also occur [Chen et al., 1984], in which case $s = \nu_{ei}/\omega$ where ν_{ei} is the collision frequency. At weakly relativistic amplitudes, collisionless processes will be more dominant. For ultrashort pulses, saturation can occur due to finite laser pulse duration, in which case we have $s_T = 1/(\pi N_p)$, where N_p is the number of wave periods contained within the pulse. In the case of self-intersection of the electron trajectories, i.e. wave breaking, we have $s_N = (r_e/L)^{1/2}$, where L is the plasma density scale length and $r_e = eE_0/(m_e\omega^2) = a_0/k$ is the oscillation amplitude due to the incident wave with normalized amplitude E_0. Finally, for saturation due to relativistic detuning of the plasma frequency, we have $s_R = a_0^{2/3}$[47], where a is the normalized vector potential of the laser, $a_0 = eE_0/(m_e c\omega)$. Finally, the dimensionless saturation parameter in Eqs. (258) is then given

---

[47]Dimensionless parameters for relativistic detuning and wave breaking can be obtained based on the displacement equation (267) presented in the next section, which was done in Refs. [Bulanov et al., 1994; Bulanov et al., 1998].

by the largest one [Bulanov et al., 1994; Bulanov et al., 1998; Bulanov et al., 2001],

$$s = \max\left[s_N = \left(\frac{a_0}{kL}\right)^{1/2}, s_R = a^{2/3}, s_T = \frac{1}{\pi N_p} \right] \tag{259}$$

Regardless of the saturation mechanism, the absorbed energy flux can be calculated as [Kruer, 1988]

$$I_{abs} \sim \int_0^\infty s\omega |E_z|^2 \mathrm{d}x = \int_0^\infty s\omega \frac{E_d^2}{|\epsilon|^2} \mathrm{d}x, \tag{260}$$

where for the case of linear density profile, we have

$$|\epsilon|^2 = \left(1 - \frac{x}{L}\right)^2 + s^2. \tag{261}$$

The resonance region size is proportional to s, and the electric field's maximum value is proportional to $1/s$, which enables us to evaluate the energy absorbed through electrostatic wave excitation without specification of the absorption process. Evaluation of the integral yields $I_{abs} \approx \omega L E_d^2$. Conservation of energy requires that $I_{abs} \approx f_{abs} c E_0^2$. Using Eq. (255), we obtain the fraction of absorbed energy flux as [Kruer, 1988; Gibbon, 2005]

$$f_{abs} \approx \frac{\phi^2(\tau)}{2}, \tag{262}$$

where $\phi(\tau)$ is defined as in Eq. (255). Just like the amplitude of the driving field, the absorbed energy flux is maximized when $\tau = (kL)^{1/3}\sin\theta \approx 0.8$. This simplified model captures the features of numerical results obtained by [Forslund et al., 1975a; Estabrook et al., 1975; Speziale and Catto, 1977] but somewhat overestimates the peak absorption. Detailed calculations using a linear density profile show peak resonance absorption of about $f_{max} \approx 0.5$, which can be used as a normalization constant for Eq. (262) to obtain a quantitatively more precise analytical model. Using these results, collisionless absorption can be modeled with hydrodynamics models by introducing a phenomenological dimensionless parameter s in the vicinity of the critical surface, such that one retrieves $f_{max} \approx 0.5$ at an angle given by $\tau \approx 0.8$, in the limit $kL \gg 1$.

Electron displacement and density distribution near the resonance point

We now express the Eulerian coordinate x in terms of the Lagrangian variable x_0, which is the initial position of an electron. They are related by [Dawson, 1959]

$$x = x_0 + \xi(x_0), \tag{263}$$

where $\xi(x_0)$ is the displacement of the electron from x_0. In both descriptions, the total number of particles in some volume must remain the same, $n(x)dV = n(x_0)dV_0$. The volume elements are related to each other through the determinant of the Jacobian matrix, as $dV = JdV_0$. In one dimension, the determinant is $J = \partial_x/\partial_{x0} = 1 + \partial\xi/\partial_{x_0}$. Therefore, the densities are related as $n(x) = n(x_0)/J$, which can be expressed as [Dawson, 1959]

$$n_e(x) = \frac{n_e(x_0)}{1 + \partial\xi/\partial x_0}, \tag{264}$$

where $n_e(x_0) = n_0$ corresponds to the initial unperturbed electron density. The fluid-like motion of the plasma electrons breaks when their trajectories start to intersect, which occurs when $J \to 0$, or $\partial \xi / \partial_{x_0} \to -1$. At such points, the electron density grows unbounded, and wave breaking occurs. The solution of the Poisson equation shows that the electron displacement and density is related to the electric field as [Bulanov et al., 1994; Bulanov et al., 1998; Bulanov et al., 2001]

$$E_x = \frac{e}{\epsilon_0} \int_0^{\xi(x_0, t)} n_0 \left(x_0 + \alpha \right) \mathrm{d}\alpha, \tag{265}$$

where x_0 is the initial electron position. For a linear density profile, $n_e = n_c x / L$, the electric field is given as [Bulanov et al., 1994; Bulanov et al., 2001]

$$E_x = \begin{cases} (e n_c / \epsilon_0)(x_0 \xi + \xi^2 / 2) / L, & x_0 + \xi > 0 \\ -(e n_c / \epsilon_0)(x_0^2 / 2) / L, & x_0 + \xi < 0 \end{cases} \tag{266}$$

where $x = x_0 + \xi > 0$ corresponds to the plasma region solution and $x = x_0 + \xi < 0$ corresponds to the vacuum region solution. Additionally, it is useful to note that for step-like density, which can approximate the case when $kL \ll 1$, the longitudinal electric field due to plasma displacement is given as $E_{x,step} = e n_0 \xi / \epsilon_0$ in the plasma region and $E_{x,step} = -e n_0 x_0 / \epsilon_0$ in the vacuum region. For weakly relativistic driving field, we obtain from the Lorentz force the following equation describing nonlinear oscillations [Bulanov et al., 1994; Bulanov et al., 2001],

$$\frac{\partial^2 \xi}{\partial t^2} + \frac{3}{2c^2} \frac{\partial^2 \xi}{\partial t^2} \left(\frac{\partial \xi}{\partial t} \right)^2 = -\frac{e}{m_e} (E_x + E_d), \tag{267}$$

where E_d is the driving field and E_x is the space-charge restoring field due to the electron displacement, given by Eq (266). On the left-hand side, we see that nonlinearity, and therefore saturation, occurs due to relativistic effects. In contrast, the nonlinearity on the right-hand side, given by Eq. (266), arises due to the inhomogeneity of the plasma. For non-relativistic oscillations, we may neglect the nonlinear terms and obtain for electrons close to the resonance point ($x_p = L$) the following displacement $\xi \approx -(r_e/2) t \cos \omega t$. The oscillations grow linearly with time, while the resonance bandwidth decreases as $\Delta \omega \approx 1/(\omega t)$. At the time when the displacement equals the resonance width $\Delta x \approx L(r_e/L)^{1/2}$, the electron trajectories start to self-intersect, and saturation occurs [Bulanov et al., 1994]. The maximum displacement is therefore limited to $\xi_{max} \approx r_e \approx \Delta x \approx s_n L$.

For plasma with large scale length L and non-relativistic saturation, the oscillations are effectively linear, and the displacement can be approximated as $\ddot{\xi} \approx -e E_x / m_e$ in both cases. In this case, using equations (254) and (255), we obtain

$$\xi = r_e \frac{(1 - x/L) \cos(\omega t) + s \sin(\omega t)}{(1 - x/L)^2 + s^2}, \tag{268}$$

where x now represents the initial electron position[48]. Eq. (268) describes an oscillating localized plasma wave with a width of $\Delta x = sL$, in accordance with Eqs. (258). The

---

[48]This is because the initial positions x_0 coincide with the coordinate grid. In the following, we omit the subscript for clarity and use x instead of x_0 in all the formulas and plots, as that is the usual label for coordinates.
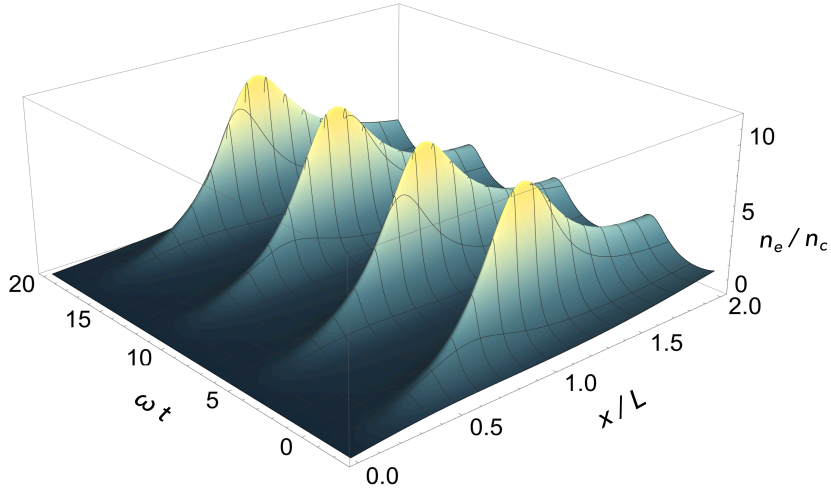
Figure 21: Evolution of initially linear electron plasma density profile $n_e = n_c x/L$. Calculated from Eq. (270) for $s = \omega = L = 1$ and $r_e = 0.9$.

displacement velocity follows as

$$\dot{\xi} = \frac{r_e s \omega}{\left(1 - x/L\right)^2 + s^2} \cos(\omega t). \tag{269}$$

The phase velocity of the plasma oscillation is equal to $v_{ph} = \omega/k \approx \omega/\Delta x = \omega s L$. We see that the displacement of the plasma electrons is evolving in time, and the density distribution can be calculated accordingly, using Eq. (263), as

$$\frac{n_e}{n_0} = \left[1 - \frac{r_e}{L} \frac{\cos(\omega t)}{s^2 + (1 - x/L)^2} + \frac{2r_e(1 - x/L)}{L} \frac{(1 - x/L)\cos(\omega t) + s\sin(\omega t)}{\left(s^2 + (1 - x/L)^2\right)^2} \right]^{-1}, \tag{270}$$

where $n_0 = n_c x/L$ is the unperturbed density profile and n_c is the critical frequency for the incident laser. Fig. 21 shows that the electron density forms a reappearing overcritical density spike with a peak at the resonance point $x_p = L$.

Our previous discussion has considered the case when the displacement of the electrons is much smaller than the plasma scale length, $\xi \approx r_e \ll L$. In the opposite case, of a very sharp plasma gradient, $\xi \approx r_e \gg L$, the electrons can be ejected out of the vacuum and find themselves accelerated directly by the laser field, i.e., vacuum acceleration of electrons occurs [Brunel, 1987; Bulanov et al., 1994; Bulanov et al., 2001]. If we estimate the initial velocity of the electrons pulled by the laser into the vacuum as $v_0/c \approx a_0$, the displacement can be calculated as

$$\xi_{vac} = -v_0 t + \frac{\omega^2}{4L} x_0^2 t^2, \tag{271}$$

where x_0 is the initial position of the electrons. The electron density can be again calculated using Eq. (264). Near the leading front where $x \approx -v_0 t$, the electron density has a linear profile, given as $n \approx n_{cr}(x + v_0 t)/L$, where the Lagrangian and Eulerian coordinates are again related as $x = x_0 + \xi(x_0, t)$.
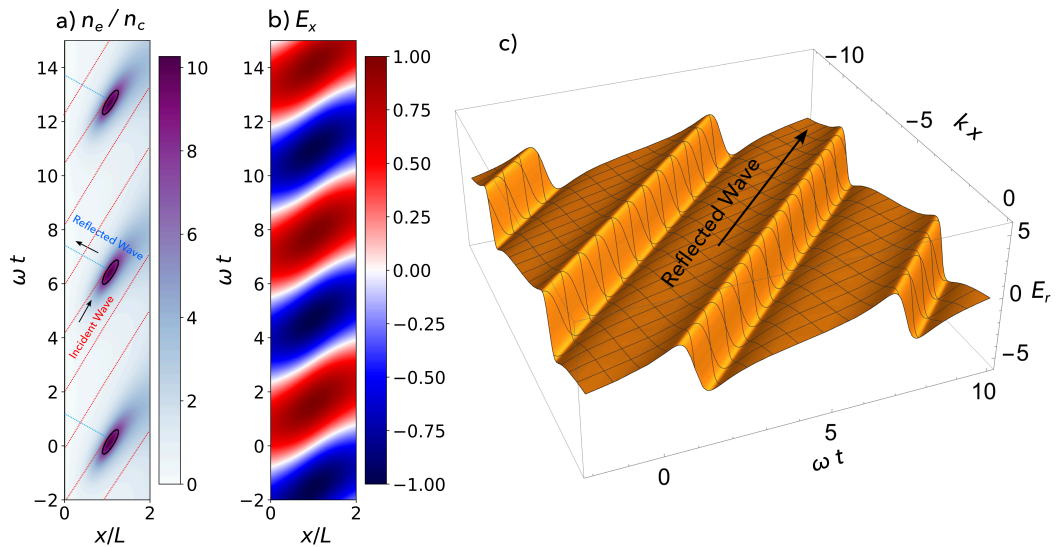
Figure 22: High harmonic generation from the resonant relativistic oscillating mirror.
(a) The electron plasma density evolution, given by Eq. (270). The black contour line indicates a threshold, beyond which $n_e > n_c$. In the interior of this boundary, radiation can be reflected into the vacuum, as indicated by the colored dotted lines. (b) Longitudinal electric field of the saturated plasma resonance (257). (c) Spatiotemporal evolution of reflected radiation, calculated using the model of a narrow resonance given by Eq. (274).

2.5.2 High-harmonics and attosecond pulse generation

We have shown in the previous sections that dense regions of oscillating electrons can be produced due to nonlinear laser-plasma interaction. In the case when the density of the electrons is sufficiently large, such that $n_e > n_c$, the incident driving field can even be reflected into the vacuum, as illustrated in Fig. 22a. A dense oscillating plasma inhomogeneity can produce periodic trains of ultrashort pulses [Bulanov et al., 1994; Naumova et al., 2005; Mourou et al., 2006; Teubner and Gibbon, 2009; Bulanov et al., 2016b]. When the plasma-vacuum interface is sharp, electrons can be pulled violently towards the vacuum side to oscillate directly within the laser field [Brunel, 1987]. For sufficiently dense vacuum-accelerated electron bunches, periodic bursts of reflected ultrashort pulses again occur due to laser-driven nonlinear oscillations [Bulanov et al., 1994; Bulanov et al., 2001; Mourou et al., 2002; Naumova et al., 2005; Naumova et al., 2006; Mourou et al., 2006; Baeva et al., 2006; Teubner and Gibbon, 2009; Pukhov et al., 2010; Wheeler et al., 2012; Bulanov et al., 2016b; Blackburn et al., 2018; Vincenti, 2019; Edwards and Mikhailova, 2020; Quéré and Vincenti, 2021; Lamač et al., 2023b]. The process of high-harmonic and attosecond pulse generation is commonly referred to as the *relativistic oscillating mirror* [Bulanov et al., 1994; Naumova et al., 2005; Teubner and Gibbon, 2009; Edwards and Mikhailova, 2020], as the radiation occurs due to strong currents formed by periodically oscillating relativistic plasma electrons.

Here, we present a model of high harmonic generation, which we call *resonant relativistic oscillating mirror*[49], which captures key features of high harmonic generation from overdense plasmas. The radiation generated by the saturated resonant plasma oscillations discussed in

---

[49]The idea of high harmonic generation from the saturated plasma resonance was first hypothesized in [Bulanov et al., 2016b], on which we build upon here.

the previous section can be obtained by solving the wave equation (51). For a transversally homogeneous incident laser, i.e., such that its beam size is much larger than its wavelength, we may neglect the transverse derivatives and obtain the following solution for the electric field

$$\mathbf{E}(x,t) = -\frac{1}{2\epsilon_0 c} \int \mathbf{j}\left(x', t - \frac{|x - x'|}{c}\right) \mathrm{d}x', \tag{272}$$

where the current distribution is given as $\mathbf{j} = -ec\boldsymbol{\beta}_\perp n_e(x,t)$, where $\boldsymbol{\beta}_\perp$ is the normalized velocity of electron oscillations perpendicular to the propagation direction of the reflected wave. For the saturated resonant oscillations discussed in the previous section, the rapidly evolving plasma density is given by Eq. (270). Transverse velocity evolves in the field of the incident laser as $\dot{\beta}_\perp \approx -(eE_0/m_e c)\exp(-i\omega t)$. Therefore, the real part of the velocity is $\beta_\perp \approx -a_0 \sin(\omega t)$. For such a current distribution, we may integrate Eq. (272) to obtain the radiation emitted for a given set of parameters (r_e, L, ω, s). The oscillating mirror imprints its spatiotemporal properties (258) into the reflected pulses, which is illustrated in Fig. 22a. The duration and bandwidth of each reflected pulse are then given as $\Delta\omega \approx 1/\tau \approx \omega s$, where ω is the frequency of incident radiation and s is the dimensionless saturation parameter (259). Due to the periodicity of the process, the spectrum is composed of harmonics of the laser frequency, as discussed in section 2.2.1. Let us show this explicitly in the case of narrow resonance, $\Delta x \approx sL \ll 1$. Then, we may take the current distribution as $\mathbf{j} = -e\boldsymbol{\beta}_\perp n_e(x,t)\delta(x - L)$. Integration of Eq. (272) yields

$$E(x,t) = -\frac{en_c a_0}{2\epsilon_0}\frac{\sin\varphi}{1 - \frac{a_0}{kLs^2}\cos\varphi}, \tag{273}$$

where $\varphi = \omega t + k(x - L)$ is the phase of the reflected wave. For weakly nonlinear oscillations, $a_0/(kLs^2) \ll 1$, we can expand the denominator as

$$E(x,t) = -\frac{en_c a_0}{2\epsilon_0}\sin\varphi \sum_{n=0}\left(\frac{a_0}{kLs^2}\right)^n \cos^n\varphi. \tag{274}$$

The harmonic content is explicit, and the coefficients of the $\sim \sin(n\varphi)$ terms can be obtained using the binominal theorem[50] [Gradshteyn and Ryzhik, 1965; Riley et al., 2006]. A growing presence of harmonics leads to nonlinear wave steepening, which is shown in Figs. (22)–(23).

Crucially, the harmonics are phase-locked. That is, the relative phase factors of the individual harmonics are not random, and there is a fixed phase relationship. Synchronization of high harmonics leads to the possibility of generating ultrashort attosecond pulses [Mourou et al., 2002; Naumova et al., 2005; Naumova et al., 2006; Teubner and Gibbon, 2009].

The plasma response is effectively immediate in the case of very sharp plasma scale lengths $kL \ll 1$ and for $\omega_{pe} \gg \omega$. Then, we can approximate the plasma as a perfect conductor, and the following boundary condition applies $\mathbf{a}[x_m(t), t] = \mathbf{a}_r[x_m(t), t] + \mathbf{a}_i[x_m(t), t] = 0$. In other words, the tangential vector potential equals zero on the critical surface x_m. The temporal profile of reflected radiation in the vacuum is then uniquely determined by the motion of the critical surface, $\mathbf{a}_r = -\mathbf{a}_i = -a_0 \exp\left[-i\omega t + ikx_m(t)\right]$. In the case of a sharp interface, the critical surface is directly exposed to the laser field. In general, we may consider that it oscillates with some frequency Ω, then its motion is (relative to the observer at the angle of reflection) given as $x_m(t) = x_s \sin(\Omega t)$. According to our discussion of laser interaction with electrons in vacuum, it is reasonable to assume that the oscillation frequency can be approximated as $\Omega = \omega$ at oblique incidence. In such a case, the discussion of the

---

[50]$\cos^n\varphi = (e^{i\varphi} + e^{-i\varphi})^n/2^n = (1/2^n)\sum_{k=0}^n \binom{n}{k}\exp\left[i(n - 2k)\varphi\right].$
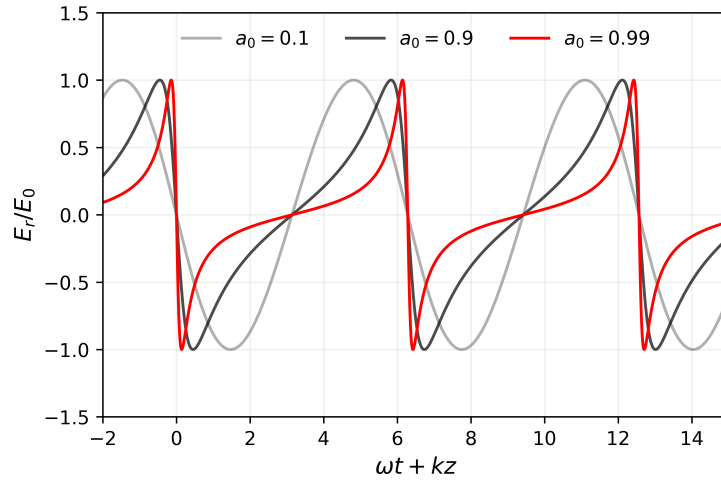
Figure 23: Ultrashort pulse train generation due to phase-locked harmonics produced from the relativistic mirror. The radiation profile was calculated from Eq. (274) using $\omega = k = L = s = 1$. Nonlinear wave steepening occurs due to the growing presence of harmonics, which compress the reflected electromagnetic wave into ultrashort pulses. This is thanks to the inherent phase synchronization of wave reflection from a resonant relativistic oscillating mirror.

properties of the reflected field follows that of Eq. (274), and the reflected signal is composed of both *even and odd* harmonics [Gibbon, 2005; Teubner and Gibbon, 2009]. At normal incidence, the nonlinear $\mathbf{v} \times \mathbf{B}$ part of the Lorentz force drives the critical surface oscillations at $\Omega = 2\omega$. A similar analysis as the one above can be done to reveal that the harmonic spectrum is now composed of only *odd* harmonics of the laser frequency [Gibbon, 2005; Teubner and Gibbon, 2009].

In section 2.2.3, we have shown the characteristics of emission due to extremely relativistic motion, which results in an ultrashort radiation burst with duration of the order $\Delta t \approx \rho/(\gamma^3 c) = 1/\omega_c$, where ρ is the instantaneous radius of curvature at the time of emission. Then, the motion at the turning point can be approximated with an instantaneously circular motion. Expanding the motion close to the turning point and taking the Fourier transform of the one-dimensional field given by Eq. (272), we can find that the spectrum can be described in terms of a derivative of the Airy function, and for $\omega \ll \omega_c$ we find that the intensity spectrum follows the power law [Pukhov et al., 2010]

$$\frac{I_n}{I_0} \sim n^{-4/3}, \tag{275}$$

where n is the harmonic order. The critical frequency ω_c gives the harmonic frequency cut-off, beyond which the spectrum drops exponentially. Radiation produced by such ultra-relativistic nonlinear electron oscillations has been called *coherent synchrotron emission*, due to the similarity of their such to the relativistic instantaneously circular emission described in section 2.2.3. Experimental results agree with the power law of the form [Teubner and Gibbon, 2009]

$$\frac{I_n}{I_0} = n^{-\alpha}, \tag{276}$$
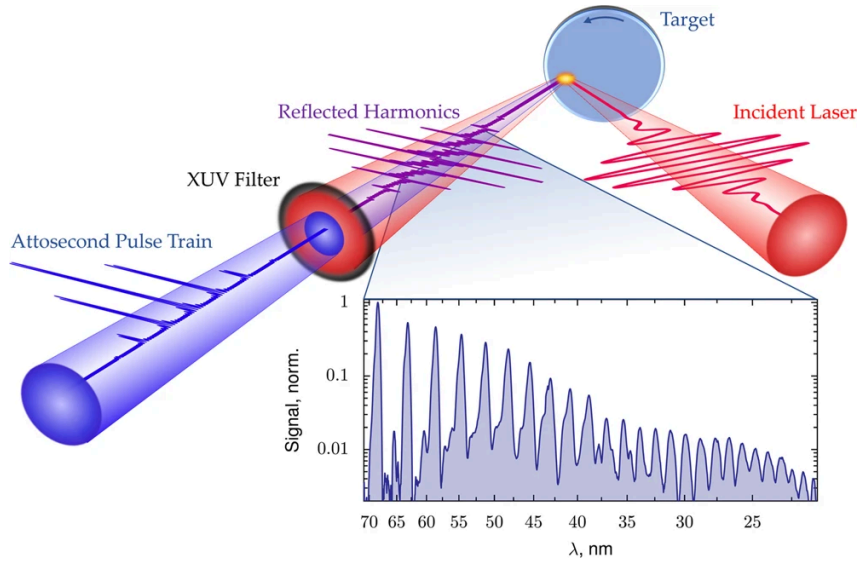
Figure 24: Schematic of high-harmonic generation from relativistic plasma mirror.
Inset shows experimentally measured spectrum using the Princeton 20 TW Ti:sapphire laser system
(Amplitude Technologies), with 70 mJ incident on a rotating BK7 target in 25 fs, producing a
peak intensity of 8×10^{19} W/cm^2. The central laser wavelength is 800 nm. The reflected single-shot
spectrum was passed through a 150 nm aluminum filter, to remove the infrared part of the spectrum,
and imaged with a flat-field diffraction-grating spectrometer. Note that the harmonic structure
appears because the driving laser pulse is multi-cycle; a single-cycle driver would produce an isolated
attosecond pulse and a continuum spectrum. Reprinted under CC BY 4.0 license from [Edwards
and Mikhailova, 2020].

with the power law index typically being $\alpha = 1.5 - 3$ [Baeva et al., 2006; Teubner and Gibbon,
2009; Pukhov et al., 2010], which was found to vary in dependence on plasma scale length L,
incident laser amplitude a_0, focal spot size d_{fwhm} or the plasma density ratio n_e/n_c [Teubner
and Gibbon, 2009; Blackburn et al., 2018; Edwards and Mikhailova, 2020]. Results from
a PIC parametric scan performed in Ref. [Edwards and Mikhailova, 2020] are shown in
Fig. 26. The simulations show that the index tends to $\alpha = 4/3$ in the ultra-relativistic limit
$a_0 \to \infty$. However, we must remark that these results do not consider the effects of quantum
electrodynamics, which are expected to occur at these intensities [Di Piazza et al., 2012].
They also neglect the spatial inhomogeneity of the laser and the ion dynamics [Lamač et al.,
2023b]. Nevertheless, they reveal the limits on the HHG spectrum obtained due to relativistic
effects, presented by Eq. (275).

Recently, we have shown that collisionless absorption (i.e., vacuum acceleration of electrons
for $kL \ll 1$ or resonant collisionless absorption for $kL \gg 1$) can swiftly lead to the occurrence
of strong electron-ion surface currents, which grow unstable and modulate the spatial profile
of the oscillating relativistic electrons on the order of the plasma wavelength. In addition,
strong quasistatic electric and magnetic fields are sustained by these currents, confining the
oscillating electron nanobunches close to the surface. This process leads to highly efficient
emission of broadband XUV radiation in an anomalous direction parallel to the surface of
the plasma. This process was named *relativistic instability modulated emission* [Lamač et al.,
2023b], and it holds promise for applications requiring broadband, attosecond, and intense
XUV radiation, such as ultrafast nonlinear XUV spectroscopy. This surface-parallel emission,
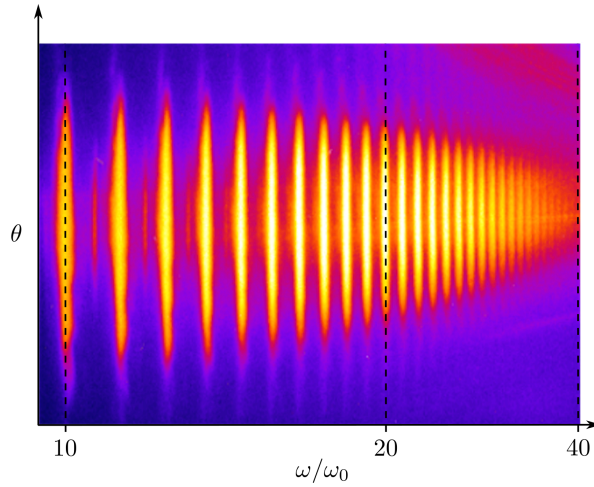
Figure 25: Experimental result of the harmonic spectrum measurement, with orders from $n = 10$ (left) to $n = 40$ (right), obtained upon reflection of the UHI 100 TW laser (CEA Saclay) on a relativistic plasma mirror. Note the decreasing divergence with increasing harmonic order. Reprinted under CC BY 4.0 license from [Quéré and Vincenti, 2021].

as a function of plasma scale length, is anti-correlated with the emission of phase-locked harmonics propagating at the angle of reflection, which was found to be optimal when $kL \approx 1$ [Kahaly et al., 2013; Blackburn et al., 2018; Lamač et al., 2023b].

2.5.3 Focusing of high harmonics due to laser-induced relativistic mirror curvature

In the focus of an intense laser pulse, the critical surface is pushed inward inside the plasma due to a deformation induced by the laser envelope $a(\mathbf{r}, t)$. The displacement is given by [Vshivkov et al., 1998; Bulanov et al., 2001]

$$\xi = a(\mathbf{r}, t) \left(\frac{m_e n_c}{m_i n_e} \right)^{1/2} ct, \tag{277}$$

where m_i is the mass of the ions, m_e is the electron mass, n_e is the initial electron density of a homogeneous plasma target, and n_c is the critical density for the frequency of the incident laser ω. Close to the laser beam axis, we may approximate the beam profile as $a(r) \approx a_0[1 - r^2/(2w_0^2)]$, where w_0 is the laser waist. We obtain that the deformed mirror has a parabolic profile given by

$$x = \xi_0(t) \left(1 - \frac{r^2}{2w_0^2} \right). \tag{278}$$

The parabolic mirror has a focus given by $f = w_0^2/(2\xi_0(t))$, where $\xi_0(t)$ is given by Eq. (277) for $a = a_0$. Approximating the focal length at the time of largest amplitude, as

83
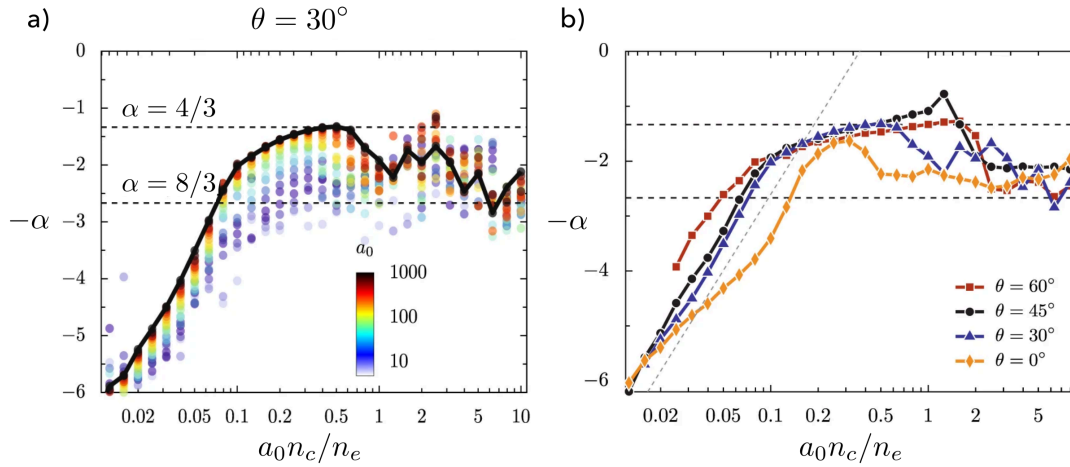
Figure 26: Power law index obtained from Lorentz-boosted 1D3V (one dimension of space, three dimensions in velocity) particle-in-cell simulations. (a) The power law index obtained for various combinations of parameters a_0 and n_e/n_c at the angle of incidence $\theta = 30°$. (b) Power law index obtained for varying θ in the ultra-relativistic limit $a_0 = 1000$. The diagonal line is given by $p = 2\ln[n_e/(n_c a_0)] + C$. Reprinted and adapted under CC BY 4.0 license from [Edwards and Mikhailova, 2020].

$ct = c\tau_{pulse}/2$, we get the focal length of the laser-induced parabolic mirror as

$$f \approx \frac{w_0^2}{a_0 c\tau_p} \left(\frac{m_i n_e}{m_e n_c} \right)^{1/2}. \tag{279}$$

The focal spot diameter can be written for individual harmonics as

$$2w_n \approx \frac{4\lambda_n}{\pi} \frac{f}{D}. \tag{280}$$

Taking the diameter as the focal spot size incident on the plasma mirror, $D \approx 2w_0$, we get the amplitude enhancement factor for the n-th harmonic as

$$\frac{w_0}{w_n} \approx \frac{\pi n a_0 c\tau_p}{\lambda_0} \left(\frac{m_e n_c}{m_i n_e} \right)^{1/2}. \tag{281}$$

For the spectral intensity, if we include the power law scaling $I_n/I_0 \sim n^{-\alpha}$, which is valid up to the cut-off harmonic order $n_{\text{cut-off}} \approx \omega_c/\omega_0$ (275), where ω_c is the critical frequency[51]. We get

$$\frac{I_n}{I_0} = \left(\frac{w_0}{w_n} \right)^2 n^{-\alpha} \approx n^{2-\alpha} \left(\frac{\pi a_0 c\tau_p}{\lambda_0} \right)^2 \frac{m_e n_c}{m_i n_e}. \tag{282}$$

Clearly, Eq. (282) shows that the intensity of the harmonics at the focus of a parabolic oscillating mirror scales as $I_n/I_0 \sim n^{2-\alpha}$. For the power law index of $\alpha = 2$, the spectrum at the focus forms a harmonic plateau up to the cut-off harmonic. The intensity roll-off

---

[51]Maximum cut-off order corresponds to the ultra-relativistic coherent synchrotron emission, as discussed in the previous section.
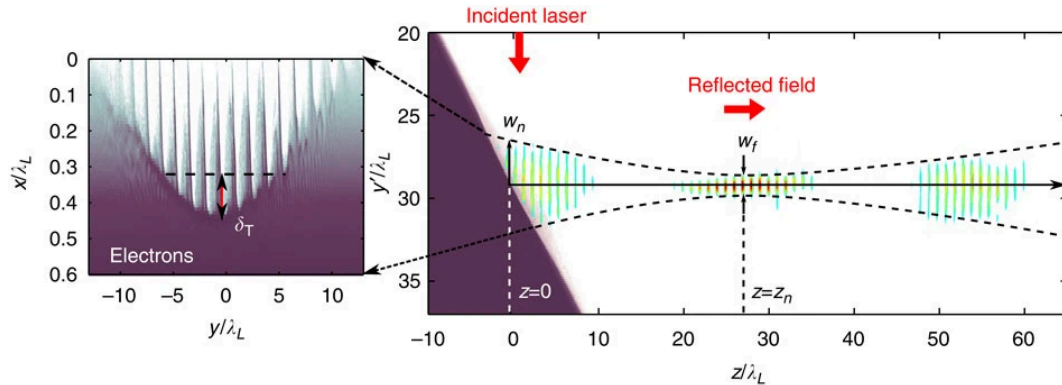
Figure 27: Results of 2D particle-in-cell simulations showing focusing of harmonics from a curved relativistic oscillating mirror. The laser-induced curvature of the relativistic plasma mirror tends to focus on reflected light. The divergence of harmonics, and therefore focal spot size, is reduced proportionally to the increasing harmonic number. The right panel shows the plasma electron density n_e (dark purple) at the maximum of the laser pulse. A zoom of the dented surface is shown in the left panel. The multi-color map shows the intensity of the train of attosecond pulses obtained by filtering harmonics from order 4 - 8 at three different times during its propagation away from the plasma mirror. Focusing of this attosecond train occurs at a distance from the plasma mirror of $z_n \approx f \cos \theta$, where f is the laser-induced focal length and θ is the incidence angle with respect to the surface normal. Reprinted under CC BY-NC-ND 3.0 license from [Vincenti et al., 2014].

of the harmonics becomes *spectrally rectified* in the focus of a laser-curved relativistic oscillating mirror. We have shown in the previous section that the optimal power law index for ultra-relativistic oscillations is given as $\alpha = 4/3 \approx 1.33 < 2$ [Pukhov et al., 2010], which indicates that the high harmonics could potentially even *dominate* the spectral content of the electromagnetic field at the focus.

Let us now estimate the maximum intensity enhancement that could be achieved in the focus of such a parabolic mirror. We consider the optimal scenario of $\alpha = 4/3$. Taking the radius of curvature as $\rho \approx \lambda_0$[52], the spectral intensity of the cut-off harmonic with frequency $\omega = \omega_c \approx \omega_0 \gamma^3$ at the focus can be written as

$$\frac{I_c}{I_0} \approx \gamma_e^2 \left(\frac{\pi a_0 c \tau_p}{\lambda_0} \right)^2 \frac{m_e n_c}{m_i n_e}. \tag{283}$$

Let us now consider a typical 30 fs Ti:Sapphire laser pulse, $c\tau_p \approx 11.3\lambda_0$. The electron energy can be estimated to correspond to the relativistic quiver energy, $\gamma \approx a_0$. For plasma density with $n_e \approx n_c$, we get the intensity enhancement factor as $I_c/I_0 \approx \gamma^4$. Today, multi-petawatt laser systems can produce incident laser intensities above $I_0 \approx 10^{22} \, \text{W.cm}^{-2}$ [Danson et al., 2019], which corresponds to $a_0 \approx \gamma_e \approx 68$. Then, the intensity enhancement factor in the focus becomes $I_c/I_0 \approx 10^7$ and the peak intensity in the focal spot of the parabolic mirror can be estimated as $I_c \approx 10^{29} \, \text{W.cm}^{-2}$, which is of the order of the Schwinger field (235). Our estimate based on Eq. (283) is in agreement with PIC simulations performed in [Quéré and Vincenti, 2021] for $n_e/n_c \sim 10^2$, results of which are shown in Fig 28. Indeed,

---

[52]A more precise estimate can be obtained by calculating the polarization-dependent radius of curvature of the laser-driven electron orbits. For circular polarization, we have $\rho = \lambda_0 a_0/(2\pi)$.
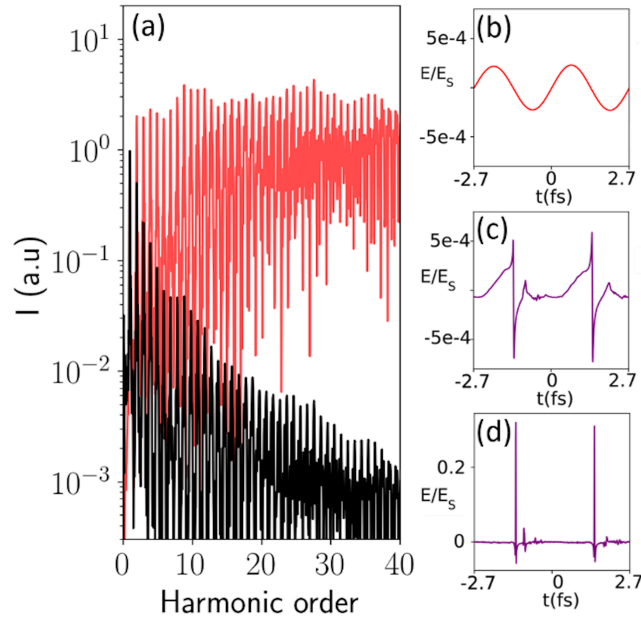
Figure 28: (a) Spectral and (b)–(d) temporal effects of the reflection of an ultraintense laser field from a curved relativistic plasma mirror, from PIC simulations. The spectral rectification effect is highlighted in (a) by comparing the harmonic spectrum right after reflection (black) and at the center of its focus (red). The big difference between (c) and (d) is due to the spectral rectification effect introduced by the plasma mirror curvature, as shown in (a). Electric fields are given in units of the Schwinger field E_s. The intensity of the incident laser is $I_0 = 10^{22}$ W.cm^{-2}. Reprinted under CC BY 4.0 license from [Quéré and Vincenti, 2021].

Refs. [Quéré and Vincenti, 2021; Vincenti, 2019] emphasize that the spectral rectification due to the curvature of a relativistic plasma mirror opens a realistic path toward the Schwinger limit.

We compare the relativistic flying parabolic mirror discussed in section 2.4.7. There, we have discussed that the intensity enhancement factor scales as $I_r/I_0 \sim \gamma^6$, which is a factor of γ^2 more than the parabolic oscillating plasma mirror, which could lead us to conclude that it offers a more exciting route for amplification towards the Schwinger field. Yet, it is, in practice, extremely challenging to obtain amplitude reflection coefficients larger than $r \sim 10^{-3} - 10^{-4}$, while the oscillating overdense mirror has a reflection coefficient of the order $r \sim 1$. To leverage the additional γ^2-scaling of the flying parabolic mirror due to focal length Lorentz contraction, new techniques must be developed to increase the reflection coefficient and secure sufficient stability of a nonlinear plasma wave. Today, the path towards the Schwinger field seems less resistant within the concept of a laser-curved relativistic oscillating mirror [Vincenti, 2019; Quéré and Vincenti, 2021].

Nevertheless, the flying relativistic mirror concept has another application besides the possibility of serving as an amplifier towards the Schwinger limit. Since it propagates with constant velocity, while the velocity of the relativistic oscillating mirror changes at each instant, the reflection of a quasi-monochromatic laser from the flying mirror yields an X-ray laser with the same relative spectral bandwidth as the incident laser radiation. We have shown that quasi-monochromatic reflected waves with spectral brightness potentially rivaling X-ray free-electron lasers can be obtained using relativistic flying mirrors, with a six orders-

of-magnitude smaller radiation gain length [Lamač et al., 2024]. Based on our exposition of and to the topics, both concepts currently offer much potential to the scientific community at large, with significant promise for future research and applications. o presented through oral contribution at the SPIE Optics + Photonics international conference in Prague, Czech Republic (2023).

3
A selection of author's results

This chapter presents an overview of all the first-author publications produced throughout the postgraduate studies. It includes a brief description of the results and a detailed account of the author's role and contributions. The publications are available with permission from copyright holders in the Appendix B.

3.1 On the anomalous relativistic emission

The Nobel's Prize in Physics 2023 Award to Anne L'Huillier, Ferenc Krausz, and Pierre Agostini for "experimental methods that generate attosecond pulses of light for the study of electron dynamics in the matter" and the Nobel's Prize in Physics 2018 Award to Gerard Mourou and Donna Strickland for "groundbreaking inventions in the field of laser physics," in particular "for their method of generating high-intensity, ultra-short optical pulses" underline the fundamental importance of ultrashort laser pulse generation to the scientific community.

Due to their large reflectivity and the lack of damage threshold, relativistic oscillating mirrors open a new way toward producing extremely short pulses composed of high harmonics at significantly higher incident laser intensity. In paper I., we have theoretically studied the efficiency of high harmonic generation from the relativistic oscillating mirror in dependence on the inhomogeneous plasma scale length. We have confirmed previously experimentally measured efficiency curves, which confirm that the high harmonic yield is anti-correlated with collisionless absorption of laser energy. Surprisingly, we have found that this anticorrelation also translates into a new radiation emission mechanism, where coherent XUV radiation is emitted in an anomalous direction, parallel to the plasma surface.

Collisionless absorption of laser energy disrupts the quasi-neutrality at the plasma surface, leading to strong electron-ion return currents that induce quasistatic electric and magnetic fields. These fields create a potential minimum close to the surface for the laser-driven oscillating electrons, forcing them to propagate along the surface as they oscillate. This translates to collimated relativistic emission discussed in section 2.2.3. Additionally, these electron currents are modulated by a surface instability with a wavelength of the order, or less than, the plasma wavelength, which significantly enhances the efficiency of XUV generation.

The author formulated a theoretical description of the origin of the anomalous radiation

emission in active collaboration with Sergei Bulanov and Kunioki Mima, who was a visiting senior scientist at the ELI Beamlines Facility at the time. Under the supervision of all co-authors, the author has employed and analyzed numerical simulations, wrote the manuscript, and assumed the role of the corresponding author throughout the peer review. All co-authors helped in reviewing and editing the final manuscript.

The results of this study have been reported on by a number of science news outlets, with the most prominent report being a *featured article* in Phys.ORG: An anomalous relativistic emission arising from the intense interaction of lasers with plasma mirrors. The results were also presented in the form of an oral contribution at the International Symposium on Compact Synchrotron X-ray Sources in Munich (2024) and 50th European Physical Society Conference on Plasma Physics in Salamanca, Spain (2024), and they were also presented in the form of a poster at the The Laser and Plasma Accelerators Workshop in Sagres, Portugal (2023) and international conference SPIE Optics + Optoelectronics in Prague, Czech Republic (2023).

3.2 On the beam-driven relativistic mirrors

In section 2.4.7, we discussed the realization of laser-driven relativistic mirrors in underdense plasmas. A relativistic mirror propagating at constant velocity is of significant interest, as the incident radiation undergoes a double Doppler upshift, significantly increasing the radiation frequency and potentially also the amplitude of reflected radiation, for relativistic mirrors with sufficient reflectivity.

Paper II. introduces a novel concept based on charged-particle beam-driven relativistic mirrors. This approach, akin to laser-laser relativistic driven mirrors, demonstrates how a beam of charged particles can drive a nonlinear plasma wave throughout its propagation. Just like a laser pulse, a charged particle beam experiences nonlinear energy depletion due to the occurrence of copropagating plasma waves. However, we show that a charged particle beam with sufficient kinetic energy can propagate for significantly longer distances in plasma undisturbed, sustaining a nonlinear wave close to the wave-breaking threshold over an impressively long distance. The stability of a relativistic plasma mirror close to the wave-breaking threshold is critical, as it is close to this threshold where the reflectivity is maximized.

We find that a laser pulse can be reflected from such a mirror with a stable phase for tens or even hundreds of laser periods, which enables the production of narrowband coherent X-ray sources. In the paper, we show the generation of both intense attosecond X-ray pulses and narrowband X-ray radiation, with spectral brightness rivaling that of X-ray free electron lasers. We guide the reader to the full article to examine the implications of creating such a compact, coherent X-ray source.

As the primary contributor, the author formulated the idea, developed the theory, and wrote the manuscript. Petr Valenta, a key collaborator, performed the numerical simulations, and the author and Petr Valenta analyzed the results. The invaluable contributions of all the co-authors in reviewing and editing the final manuscript are also acknowledged.

The results of this study were presented as an oral contribution at the International Symposium on Compact Synchrotron X-ray Sources (2024) in Munich, Germany, and the 50th European Physical Society Conference on Plasma Physics (2024) in Salamanca, Spain.

3.3 On the resonant betatron X-ray generation

Section 2.4.5 introduced the mechanism of femtosecond X-ray pulse generation using laser-driven wakefields, referred to as betatron X-ray generation. This process yields a unique source of all-optically generated femtosecond X-ray pulses, which find numerous applications in ultrafast X-ray diffraction and spectroscopy or phase-contrasted X-ray imaging. A sufficiently large X-ray photon flux is required for ultrafast pump-probe schemes to obtain good contrast in the single-shot regime. Therefore, one of the primary directions in research surrounding betatron sources is the increase of energy conversion efficiency.

To support this effort, we have brought forward the two-color resonant betatron X-ray generation concept presented in paper III., where we considered splitting off a small part of the laser pulse into a nonlinear crystal to convert into the second, or even third, harmonic frequency of the laser. A group delay between the leading and trailing pulse is then introduced, such that the accelerating electrons find themselves within the field of the converted laser pulses.

We have found that a two-color laser field leads to resonant betatron X-ray generation throughout the electron acceleration process, significantly boosting the laser-to-X-ray conversion efficiency by up to two orders of magnitude.

The author initiated this project under the close supervision of Jaroslav Nejdl and Uddhab Chaulagain, who played a crucial role in analyzing and focusing the research on experimentally relevant parameters. The author has performed and analyzed multi-dimensional numerical particle-in-cell and single-particle simulations. The theoretical part was formulated in collaboration with Sergei Bulanov. Lucie Jurkovičová invented the conceptual design of the experiment presented in the study. The author wrote the manuscript and assumed the role of the corresponding author throughout the peer-review process. All co-authors significantly contributed to the review and editing of the final manuscript.

The results of this study were presented in the form of a poster contribution at the international conference SPIE Optics + Optoelectronics in Prague, Czech Republic (2023), Laser and Plasma Accelerators Workshop in Sagres, Portugal (2023), and the Plasmas in Super-Intense Laser Fields Summer School in Erice, Italy (2022).

3.4 On the laser-driven magnetic field generation

Section 2.4.6 addressed generating quasistatic magnetic fields in plasmas utilizing relativistic laser pulses. The field of laboratory astrophysics is highly interested in the creation of long-lasting magnetized plasmas with magnetic field strengths comparable to those observed around black hole accretion disks or weakly magnetized neutron stars—this field endeavors to elucidate astronomical observations by investigating magnetized plasmas in controlled laboratory settings.

In paper IV., we have employed three-dimensional and fully relativistic particle-in-cell simulations to investigate the range of magnetic field strengths achievable under typical laboratory conditions. Our parametric scan revealed that magnetic field strengths of the order of multi-gigagauss can be produced with currently available laser technology. To support these results, we have formulated a theoretical model, which was also found to be in accordance with earlier experimental results. Additionally, we scrutinized the temporal stability of these magnetic fields. We revealed their ability to persist notably longer than the laser pulse or the electron plasma oscillation period. The evolution of these fields was attributed to the current filamentation instability, mirroring behavior analogous to the well-documented Kármán vortex street.

The research was initiated by the author, who oversaw the execution and analysis of the numerical particle-in-cell simulations and authored the manuscript. The author cultivated the theoretical framework in collaboration with Sergei Bulanov. All co-authors were actively engaged in reviewing and editing the final manuscript.

The results were also presented through oral contribution at the SPIE Optics + Photonics international conference in Prague, Czech Republic (2023).

– Alan Turing (1950)

4

Conclusion

This chapter summarizes the content of this doctoral thesis and the author's most important results. It marks the currently most active research directions and discusses new research avenues stemming from the author's results.

4.1 Summary

In summary, this doctoral thesis presents the author's main results in relativistic optics and provides an extensive reference for the theory and literature of relativistic optics.

A historical overview of high-power laser development and its relationship to relativistic optics was presented in Chapter 1. We have also defined this thesis's goals and briefly summarized the author's research contributions to the field.

We have presented the theory of relativistic optics relevant to the author's research in Chapter 2. First, we have given a theory for radiation from relativistic electrons. Then, we presented a selection of topics in two regimes of laser-plasma interaction, where the plasma target was either relativistically underdense or overdense. In the case of underdense plasma, a particular focus was placed on laser wakefield acceleration, betatron X-ray generation, magnetic field generation, and relativistic mirrors based on nonlinear plasma waves. For overdense plasma, we have discussed the generation of high harmonics and attosecond pulses from a relativistic oscillating mirror. Finally, we have discussed focusing due to laser-induced mirror curvature.

Chapter 3 presented a brief commentary on the author's main results in the field of relativistic optics, which are presented in the form of four publications available in full in Appendix B, and a list of conferences these results were presented at. The results can be summarized as follows:

Paper I. describes a novel mechanism of highly efficient coherent XUV light emission, which takes place at the surface of a relativistically oscillating plasma mirror. The radiation propagates in an anomalous direction, parallel to the surface of the plasma mirror instead of at the angle of reflection. We have discussed the spatiotemporal properties of the radiation, which are due to an electron-ion surface instability. We have also found that the XUV yield, as a function of the pre-plasma scale length, is anti-correlated

with the emission of high harmonics at the reflection angle, which was related to the collisionless absorption of laser energy.

Paper II. presents a new concept of relativistic mirrors propagating at a constant velocity based on nonlinear plasma waves driven by charged particle beams propagating in plasma. We have found that the beam-driven relativistic mirrors are highly stable and enable the generation of narrowband quasi-monochromatic coherent X-ray radiation or extremely intense attosecond pulses. We have found that this is primarily due to a reduced laser-induced damage threshold compared to laser-driven relativistic flying mirrors.

Paper III. contains the concept of two-color betatron X-ray generation, in which the conversion efficiency of laser energy to betatron X-rays is increased if the accelerating electrons find themselves in the field of copropagating laser pulses with different frequencies. We have found that this technique can improve the laser-to-X-rays energy conversion efficiency by up to two orders of magnitude. We also presented a design of a two-arm experimental setup, where the initial laser pulse splits into multiple pulses with harmonic frequencies through standard techniques using nonlinear crystals.

Paper IV. presents our study of the laser-driven generation of intense, long-lived magnetic fields in plasma. Specifically, we searched for parameters relevant to laboratory astrophysics and experiments related to studying nonlinear quantum electrodynamics. We have performed parametric scans using state-of-the-art three-dimensional particle-in-cell simulations and found parameters for generating picosecond-stable gigagauss magnetic fields using petawatt-class lasers, with numerical scaling laws in good agreement with analytic results.

4.2 Future outlook

Thanks to the prolific research on relativistic laser-plasma interactions that has taken place since the advent of CPA, the shrinking of particle accelerators by at least three orders of magnitude in footprint is part of today's reality. A slew of novel research directions are now open and actively pursued. One of the most active research areas is the control and stabilization of plasma accelerators and scaling to high-repetition-rate operation. Today, GeV laser-driven plasma accelerators are based on petawatt-class laser systems, operating at single shot or $\sim$ Hz repetition rates. On the other hand, laser systems capable of $\sim$ kHz repetition rates are currently limited to peak powers of a few terawatts, limiting the energy of accelerated electrons to a few tens of MeV. In light of the $\sim$ MHz repetition rate of conventional accelerators, further advancements in laser technology are highly desirable. Specifically, high thermal load during laser operation is one of the critical bottlenecks preventing additional increases to higher repetition rates.

Nonetheless, electron beams from such laser systems are already suitable for applications, mainly compact all-optical generation of bright coherent or incoherent ultrashort X-ray pulses. Such X-ray sources are typically based on inverse Compton scattering or betatron X-ray radiation, suitable for phase-contrasted imaging, ultrafast X-ray absorption spectroscopy, and diffraction. At the same time, the promise of compact free-electron lasers utilizing laser wakefield accelerated electrons is also being pursued all over the world, with coherent FEL operation at 27 nanometers (in the XUV range) using 500 MeV laser wakefield accelerated electron beams reported recently [Graydon, 2022]. The promise of compact acceleration stimulates many research institutes to develop more affordable sources of bright, ultrafast

X-rays. For all-optical radiation sources, such as the betatron or the Compton source, new techniques are actively researched to improve the source brightness, not only through the repetition rate of the laser system but also for each laser shot. This is required by ultrafast pump-probe schemes, which require good single-shot contrast, and novel applications such as ultrafast nonlinear XUV or X-ray spectroscopy.

Following the recent scientific breakeven in inertial confinement fusion [Fujioka, 2024], significant attention is also drawn to this research area, where petawatt-class lasers are considered for concepts such as the fast ignition scheme [Gibbon, 2005].

A particular interest in compact particle acceleration is found in radiotherapy and radiology. There, ultrafast X-rays are also desired due to the FLASH effect [Favaudon et al., 2014], where ultra-high dose-rate ($\geq 40\,\mathrm{Gy/s}$) radiotherapy reduces damage to healthy tissue compared to conventional low dose-rate ($\leq \mathrm{Gy/min}$) radiotherapy source, assuming the same therapeutic total dose. For this purpose, compact acceleration of electrons and protons is also pursued.

Aside from these primary research routes, work continues on novel methods of ultrafast generation of bright coherent radiation pulses, such as the relativistic flying and oscillating plasma mirrors, presented in detail in this thesis. Due to the nonlinear polarization of plasma, which occurs due to relativistic oscillations, these concepts promise enhanced efficiency compared to the conventional non-plasma-based light sources at incident laser intensities orders of magnitude beyond the damage thresholds which limit traditional light sources, such as the high harmonics generated from noble gases, which is currently the premier source for attosecond physics. One of the most exotic and yet fundamental applications of relativistic mirrors is the possibility to produce radiation with intensity comparable to the Schwinger limit, providing us with a tool to study polarization of the quantum vacuum through processes unavailable to conventional accelerator facilities, such as light-light scattering, or the Schwinger effect.

Research directions opened by the findings presented in this doctoral thesis certainly deserve more attention. Additional work on relativistic instability-modulated emission is needed to find optimal operation parameters. For relativistic oscillating mirrors, identifying optimal parameters for focusing toward the Schwinger limit should be studied more. Stabilizing intense quasistatic magnetic fields also requires further attention, and laser-target configurations relevant to laboratory astrophysics applications should be explored theoretically and experimentally. Experimental realization of the two-color betatron X-ray scheme could remove the photon flux bottleneck of the betatron source. Generalization to a more arbitrary single-pulse frequency-varying laser field should also be studied. Finally, the concept of beam-driven relativistic mirrors could lead to the experimental realization of a stable relativistic flying mirror, which is fundamental for applications requiring narrowband bright and tunable coherent hard X-ray laser. In this direction, more work is needed to find an efficient all-optical scheme where driving charged particles and incident radiation could be produced from a single laser to generate coherent X-rays. Furthermore, the focusing properties of relativistic flying mirrors should be studied in more detail using fully relativistic three-dimensional simulations.

The author believes that based on the dynamic evolution of ultrashort light pulse generation in the recent decades, most recently commemorated by the scientific community through the Nobel Prize in Physics 2018 and 2023, new technological techniques and scientific ideas leveraging relativistic optics to their full potential are yet to be found. Just as with the advent of the first laser and CPA, the consequences of the proliferation of such ideas and technology will resonate fundamentally through basic and applied science, spanning physics, chemistry, and medicine.

Acknowledgements

To all of the individuals mentioned below, I express my deepest gratitude for scientific collaboration and for fostering a friendly and academically stimulating work environment.

First and foremost, I would like to thank my supervisor, Jaroslav Nejdl, for guiding me throughout my postgraduate studies and, even more importantly, for giving me the freedom to pursue my ideas, experiment, and make mistakes. My academic successes were only possible with failures and the environment to do both. I am also deeply grateful for being presented with the opportunity to join the Department of Radiation Physics and Electron Acceleration at ELI Beamlines, which opened the way for developing many new personal and professional relationships.

At the same time, I would like to thank Uddhab Chaulagain, who fostered a friendly and supportive work environment and significantly broadened my scientific horizons in the early days. He is also a great friend and colleague, putting his heart into our group work at ELI Beamlines. Last but not least, for taking care of our office plants, which would surely perish without him.

I give my utmost respect to Sergei Bulanov, not only for his persistent and field-defining research activity, which continues to this day but also for his unrelenting curiosity and devotion to our work. I am also profoundly grateful for his guidance, which in no small part defined my scientific interests. Finally, I am thankful for his friendly openness to any discussion, scientific or personal.

I am also grateful to all the students I had the opportunity to advise. For their scientific curiosity, patience to withstand my long lectures on the whiteboard, and all the fun we had together: Orsolya Morvai, Dominik Čáp, and Maroš Bratko.

To Marek Raclavský, for being a good friend, officemate, and a genuinely great person.

I am grateful to Petr Valenta for his persistent and cheerful attitude, collaborative spirit, scientific curiosity, and willingness to harken to and humor my ideas.

I thank Tomáš Kerepecký for his friendly spirit and help when I joined ELI. His help jump-started my initial scientific pursuits, and even years later, these effects resonate.

I also thank Yann Simon for his help with proofreading the thesis and for being a great intern.

The list of great people continues. I am deeply grateful to all my previous and current colleagues and friends: Ondřej Hort, Yelyzaveta Pulnova, Ondřej Finke, Martin Albrecht,

Lucie Jurkovičová, Martin Matys, Gabrielle Grittani, Kim Ta Phuoc, Carlo Lazzarini, Jan Vábek, Victor Malka, Tomáš Parkman, Dong Du Mai, Matyáš Staňek, Kunioki Mima, Ondřej Stránský, Josef Licek, Arujash Mohanty, Stéphane Sebban, Jakub Langer, Vladislav Wohlrath, Vašek Maixner, Jaroslav Nejedlý, Jiří Wollmann, Josef Kadlec, Samuel Van Overloop, Václav Miřátský, Štěpán Šubík, and many others.

Finally, but most importantly, I would like to express gratitude to my family, without which my journey would not be possible. To Michaela Šmucerová for her boundless support and patience, to our two fantastic border collies, Ace and Marley, to my sisters, nieces, mother, and everyone else.

Bibliography

[Akhiezer and Polovin, 1956] Akhiezer, A. and Polovin, R. (1956). Theory of wave motion of an electron plasma. *Soviet Physics - JETP*, **3**(5):696–704.

[Albert and Thomas, 2016] Albert, F. and Thomas, A. G. (2016). Applications of laser wakefield accelerator-based light sources. *Plasma Physics and Controlled Fusion*, **58**(10):103001.

[Ali et al., 2010] Ali, S., Davies, J., and Mendonca, J. (2010). Inverse faraday effect with linearly polarized laser pulses. *Physical Review Letters*, **105**(3):035001.

[Allen et al., 1992] Allen, L., Beijersbergen, M. W., Spreeuw, R., and Woerdman, J. (1992). Orbital angular momentum of light and the transformation of laguerre-gaussian laser modes. *Physical Review A*, **45**(11):8185.

[Andreev et al., 1992] Andreev, N., Gorbunov, L., Kirsanov, V., Pogosova, A., Ramazashvili, R., and Parsons, D. (1992). Resonant excitation of wakefields by a laser pulse in a plasma. *JETP Letters*, **55**(10):571–576.

[Aniculaesei et al., 2024] Aniculaesei, C., Ha, T., Yoffe, S., Labun, L., Milton, S., McCary, E., Spinks, M. M., Quevedo, H. J., Labun, O. Z., Sain, R., et al. (2024). The acceleration of a high-charge electron bunch to 10 gev in a 10-cm nanoparticle-assisted wakefield accelerator. *Matter and Radiation at Extremes*, **9**(1).

[Antonsen and Mora, 1992] Antonsen, T. M. and Mora, P. (1992). Self-focusing and Raman scattering of laser pulses in tenuous plasmas. *Physical Review Letters*, **69**(15):2204–2207.

[Arber et al., 2015] Arber, T., Bennett, K., Brady, C., Lawrence-Douglas, A., Ramsay, M., Sircombe, N. J., Gillies, P., Evans, R., Schmitz, H., Bell, A., et al. (2015). Contemporary particle-in-cell approach to laser-plasma modelling. *Plasma Physics and Controlled Fusion*, **57**(11):113001.

[Armstrong et al., 1962] Armstrong, J. A., Bloembergen, N., Ducuing, J., and Pershan, P. S. (1962). Interactions between light waves in a nonlinear dielectric. *Physical Review*, **127**(6):1918–1939.

[Askaryan et al., 1997] Askaryan, G., Bulanov, S., Dudnikova, G., Esirkepov, T. Z., Lontano, M., Meyer-ter Vehn, J., Pegoraro, F., Pukhov, A., and Vshivkov, V. (1997). Magnetic interaction of ultrashort high-intensity laser pulses in plasmas. *Plasma Physics and Controlled Fusion*, **39**(5A):A137.

[Askaryan et al., 1994] Askaryan, G., Bulanov, S., Pegoraro, F., Pukhov, A., et al. (1994). Magnetic interaction of self-focusing channels and fluxes of electromagnetic-radiation-their coalescence, the accumulation of energy, and the effect of external magnetic-fields on them. *JETP Letters*, **60**(4):251–257.

[Attwood and Sakdinawat, 2017] Attwood, D. and Sakdinawat, A. (2017). *X-Rays and Extreme Ultraviolet Radiation: Principles and Applications.* Cambridge University Press, 2nd edition.

[Baeva et al., 2006] Baeva, T., Gordienko, S., and Pukhov, A. (2006). Theory of high-order harmonic generation in relativistic laser interaction with overdense plasma. *Physical Review E*, **74**(4):046404.

[Bahk et al., 2004] Bahk, S. W., Rousseau, P., Planchon, T. A., Chvykov, V., Kalintchenko, G., Maksimchuk, A., Mourou, G. A., and Yanovsky, V. (2004). Generation and characterization of the highest laser intensities (10^{22} W/cm^2). *Optics Letters*, **29**(24):2837.

[Bass et al., 1962] Bass, M., Franken, P. A., Ward, J. F., and Weinreich, G. (1962). Optical rectification. *Physical Review Letters*, **9**(11):446–448.

[Baumgartner and Byer, 1979] Baumgartner, R. A. and Byer, R. K. (1979). Optical parametric amplification. *IEEE Journal of Quantum Electronics*, **15**(6):432–444.

[Berezhiani et al., 1997] Berezhiani, V., Mahajan, S., and Shatashvili, N. (1997). Theory of magnetic field generation by relativistically strong laser radiation. *Physical Review E*, **55**(1):995.

[Berezhiani and Murusidze, 1990] Berezhiani, V. I. and Murusidze, I. G. (1990). Relativistic wake-field generation by an intense laser pulse in a plasma. *Physics Letters A*, **148**(6-7):338–340.

[Bers, 1983] Bers, A. (1983). Space-time evolution of plasma instabilities-absolute and convective. In *Basic Plasma Physics*, volume 1.

[Bethe and Salpeter, 1957] Bethe, H. A. and Salpeter, E. E. (1957). *Quantum Mechanics of One- and Two-Electron Atoms.* Springer-Verlag Berlin Heidelberg.

[Birdsall and Langdon, 2004] Birdsall, C. K. and Langdon, A. B. (2004). *Plasma Physics via Computer Simulation.* Taylor and Francis, New York.

[Blackburn, 2020] Blackburn, T. (2020). Radiation reaction in electron–beam interactions with high-intensity lasers. *Reviews of Modern Plasma Physics*, **4**(1):5.

[Blackburn et al., 2018] Blackburn, T., Gonoskov, A., and Marklund, M. (2018). Relativistically intense xuv radiation from laser-illuminated near-critical plasmas. *Physical Review A*, **98**(2):023421.

[Borisov et al., 1992] Borisov, A. B., Borovskiy, A. V., Shiryaev, O. B., Korobkin, V. V., Prokhorov, A. M., Solem, J. C., Luk, T. S., Boyer, K., and Rhodes, C. K. (1992). Relativistic and charge-displacement self-channeling of intense ultrashort laser pulses in plasmas. *Physical Review A*, **45**(8):5830–5845.

[Born and Wolf, 1959] Born, M. and Wolf, E. (1959). *Principles of Optics.* Pergamon Press.

[Brunel, 1987] Brunel, F. (1987). Not-so-resonant, resonant absorption. *Physical Review Letters*, **59**(1):52.

[Bulanov et al., 2001] Bulanov, S., Califano, F., Dudnikova, G., Esirkepov, T. Z., Inovenkov, I., Kamenets, F., Liseikina, T., Lontano, M., Mima, K., Naumova, N., et al. (2001). Relativistic interaction of laser pulses with plasmas. *Reviews of Plasma Physics*, pages 227–335.

[Bulanov et al., 1998] Bulanov, S., Naumova, N., Pegoraro, F., and Sakai, J. (1998). Particle injection into the wave acceleration phase due to nonlinear wake wave breaking. *Physical Review E*, **58**(5):R5257.

[Bulanov et al., 1997] Bulanov, S., Pegoraro, F., Pukhov, A., and Sakharov, A. (1997). Transverse-wake wave breaking. *Physical Review Letters*, **78**(22):4205.

[Bulanov, 2021] Bulanov, S. V. (2021). Electron dynamics in the field of strong plasma and electromagnetic waves: A review. *Physics of Wave Phenomena*, **29**(1):1–46.

[Bulanov et al., 2016a] Bulanov, S. V., Esirkepov, T. Z., Hayashi, Y., Kiriyama, H., Koga, J. K., Kotaki, H., Mori, M., and Kando, M. (2016). On some theoretical problems of laser wake-field accelerators. *Journal of Plasma Physics*, **82**(3):905820308.

[Bulanov et al., 2016b] Bulanov, S. V., Esirkepov, T. Z., Kando, M., and Koga, J. (2016). Relativistic mirrors in laser plasmas (analytical methods). *Plasma Sources Science and Technology*, **25**(5):53001.

[Bulanov et al., 2013] Bulanov, S. V., Esirkepov, T. Z., Kando, M., Pirozhkov, A. S., and Rosanov, N. N. (2013). Relativistic mirrors in plasmas. Novel results and perspectives. *Physics-Uspekhi*, **56**(5):429–464.

[Bulanov et al., 2003] Bulanov, S. V., Esirkepov, T. Z., and Tajima, T. (2003). Light intensification towards the Schwinger limit. *Physical Review Letters*, **91**(8):85001.

[Bulanov et al., 1992] Bulanov, S. V., Inovenkov, I. N., Kirsanov, V. I., Naumova, N. M., and Sakharov, A. S. (1992). Nonlinear depletion of ultrashort and relativistically strong laser pulses in an underdense plasma. *Physics of Fluids B*, **4**(7):1935–1942.

[Bulanov et al., 1989] Bulanov, S. V., Kirsanov, V. I., and Sakharov, A. S. (1989). Excitation of ultrarelativistic plasma waves by pulse of electromagnetic radiation. *JETP Letters*, **50**(4):176–178.

[Bulanov et al., 1994] Bulanov, S. V., Naumova, N. M., and Pegoraro, F. (1994). Interaction of an ultrashort, relativistically strong laser pulse with an overdense plasma. *Physics of Plasmas*, **1**(3):745–757.

[Bulanov et al., 1995] Bulanov, S. V., Pegoraro, F., and Pukhov, A. M. (1995). Two-dimensional regimes of self-focusing, wake field generation, and induced focusing of a short intense laser pulse in an underdense plasma. *Physical Review Letters*, **74**(5):710–713.

[Bulanov and Sakharov, 1991] Bulanov, S. V. and Sakharov, A. S. (1991). Induced focusing of electromagnetic wave in a wake plasma wave. *JETP Letters*, **54**(4):203–207.

[Caldwell et al., 2021] Caldwell, A., Gschwendtner, E., Lotov, K., Muggli, P., and Wing, M. (2021). Physics of awake run 2. Technical report.

[Cattani et al., 2001] Cattani, F., Kim, A., Anderson, D., and Lisak, M. (2001). Multifilament structures in relativistic self-focusing. *Physical Review E*, **64**(1):8.

[Chaulagain et al., 2022] Chaulagain, U., Lamač, M., Raclavský, M., Khakurel, K., Rao, K. H., Ta-Phuoc, K., Bulanov, S., and Nejdl, J. (2022). Eli gammatron beamline: a dawn of ultrafast hard x-ray science. **9**(11):853.

[Chen et al., 1984] Chen, F. F. et al. (1984). *Introduction to Plasma Physics and Controlled Fusion*. Springer.

[Chen and Sudan, 1993] Chen, X. L. and Sudan, R. N. (1993). Two-dimensional self-focusing of short intense laser pulse in underdense plasma. *Physics of Fluids B*, **5**(4):1336–1348.

[Chiao et al., 1964a] Chiao, R. Y., Garmire, E., and Townes, C. H. (1964). Self-trapping of optical beams. *Physical Review Letters*, **13**(15):479–482.

[Chiao et al., 1964b] Chiao, R. Y., Townes, C. H., and Stoicheff, B. P. (1964). Stimulated Brillouin scattering and coherent generation of intense hypersonic waves. *Physical Review Letters*, **12**(21):592–595.

[Cohen et al., 1991] Cohen, B. I., Lasinski, B. F., Langdon, A. B., and Cummings, J. C. (1991). Dynamics of ponderomotive self-focusing in plasmas. *Physics of Fluids B*, **3**(3):766–775.

[Corde et al., 2013] Corde, S., Ta Phuoc, K., Lambert, G., Fitour, R., Malka, V., Rousse, A., Beck, A., and Lefebvre, E. (2013). Femtosecond x rays from laser-plasma accelerators. *Reviews of Modern Physics*, **85**(1):1–48.

[Couperus et al., 2017] Couperus, J. P., Pausch, R., Köhler, A., Zarini, O., Krämer, J. M., Garten, M., Huebl, A., Gebhardt, R., Helbig, U., Bock, S., Zeil, K., Debus, A., Bussmann, M., Schramm, U., and Irman, A. (2017). Demonstration of a beam loaded nanocoulomb-class laser wakefield accelerator. *Nature Communications*, **8**(1):487.

[Danson et al., 2019] Danson, C. N., Haefner, C., Bromage, J., Butcher, T., Chanteloup, J.-C. F., Chowdhury, E. A., Galvanauskas, A., Gizzi, L. A., Hein, J., Hillier, D. I., et al. (2019). Petawatt and exawatt class lasers worldwide. *High Power Laser Science and Engineering*, 7:e54.

[Darrow et al., 1992] Darrow, C., Coverdale, C., Perry, M., Mori, W., Clayton, C., Marsh, K., and Joshi, C. (1992). Strongly coupled stimulated raman backscatter from subpicosecond laser-plasma interactions. *Physical Review Letters*, **69**(3):442.

[Dawson, 1959] Dawson, J. M. (1959). Nonlinear electron oscillations in a cold plasma. *Physical Review*, **113**(2):383–387.

[Decker et al., 1996] Decker, C., Mori, W., Tzeng, K.-C., and Katsouleas, T. (1996). The evolution of ultra-intense, short-pulse lasers in underdense plasmas. *Physics of Plasmas*, **3**(5):2047–2056.

[Decking et al., 2017] Decking, W., Weise, H., et al. (2017). Commissioning of the european xfel accelerator. In *Proc. 8th Int. Particle Accelerator Conf.(IPAC'17)*, volume 8, page 1.

[Di Piazza et al., 2012] Di Piazza, A., Müller, C., Hatsagortsyan, K., and Keitel, C. (2012). Extremely high-intensity laser interactions with fundamental quantum systems. *Reviews of Modern Physics*, **84**(3):1177–1228.

[Dubietis et al., 1992] Dubietis, A., Jonušauskas, G., and Piskarskas, A. (1992). Powerful femtosecond pulse generation by chirped and stretched pulse parametric amplification in BBO crystal. *Optics Communications*, **88**(4-6):437–440.

[Edwards and Mikhailova, 2020] Edwards, M. R. and Mikhailova, J. M. (2020). The x-ray emission effectiveness of plasma mirrors: reexamining power-law scaling for relativistic high-order harmonic generation. *Scientific Reports*, **10**(1):5154.

[Einstein, 1905] Einstein, A. (1905). Zur Elektrodynamik bewegter Körper. *Annalen der Physik*, **322**(10):891–921.

[Elder et al., 1947] Elder, F., Gurewitsch, A., Langmuir, R., and Pollock, H. (1947). Radiation from electrons in a synchrotron. *Physical Review*, **71**(11):829.

[Eliezer, 2002] Eliezer, S. (2002). *The Interaction of High-Power Lasers with Plasmas*. CRC press.

[Esarey et al., 1994] Esarey, E., Krall, J., and Sprangle, P. (1994). Envelope analysis of intense laser pulse self-modulation in plasmas. *Physical Review Letters*, **72**(18):2887.

[Esarey and Piloff, 1995] Esarey, E. and Piloff, M. (1995). Trapping and acceleration in nonlinear plasma waves. *Physics of Plasmas*, **2**(5):1432–1436.

[Esarey et al., 2009] Esarey, E., Schroeder, C. B., and Leemans, W. P. (2009). Physics of laser-driven plasma-based electron accelerators. *Reviews of Modern Physics*, **81**(3):1229–1285.

[Esarey et al., 2000] Esarey, E., Schroeder, C. B., Shadwick, B. A., Wurtele, J. S., and Leemans, W. P. (2000). Nonlinear theory of nonparaxial laser pulse propagation in plasma channels. *Physical Review Letters*, **84**(14):3081–3084.

[Esarey et al., 1996] Esarey, E., Sprangle, P., Krall, J., and Ting, A. (1996). Overview of plasma-based accelerator concepts. *IEEE Transactions on Plasma Science*, **24**(2):252–288.

[Esarey et al., 1997] Esarey, E., Sprangle, P., Krall, J., and Ting, A. (1997). Self-focusing and guiding of short laser pulses in ionizing gases and plasmas. *IEEE Journal of Quantum Electronics*, **33**(11):1879–1914.

[Esarey et al., 1990] Esarey, E., Ting, A., and Sprangle, P. (1990). Frequency shifts induced in laser pulses by plasma waves. *Physical Review A*, **42**(6):3526–3531.

[Esirkepov et al., 2004] Esirkepov, T., Bulanov, S. V., Nishihara, K., and Tajima, T. (2004). Soliton synchrotron afterglow in a laser plasma. *Physical Review Letters*, **92**(25):255001.

[Esirkepov et al., 2002] Esirkepov, T., Nishihara, K., Bulanov, S. V., and Pegoraro, F. (2002). Three-dimensional relativistic electromagnetic subcycle solitons. *Physical Review Letters*, **89**(27):275002.

[Esirkepov et al., 2006] Esirkepov, T. Z., Bulanov, S. V., Yamagiwa, M., and Tajima, T. (2006). Electron, positron, and photon wakefield acceleration: Trapping, wake overtaking, and ponderomotive acceleration. *Physical Review Letters*, **96**(1):14803.

[Estabrook et al., 1975] Estabrook, K., Valeo, E., and Kruer, W. (1975). Two-dimensional relativistic simulations of resonance absorption. *The Physics of Fluids*, **18**(9):1151–1159.

[Farina and Bulanov, 2001] Farina, D. and Bulanov, S. V. (2001). Relativistic electromagnetic solitons in the electron-ion plasma. *Physical Review Letters*, **86**(23):5289–5292.

[Faure et al., 2004] Faure, J., Glinec, Y., Pukhov, A., Klselev, S., Gordienko, S., Lefebvre, E., Rousseau, J. P., Burgy, F., and Malka, V. (2004). A laser-plasma accelerator producing monoenergetic electron beams. *Nature*, **431**(7008):541–544.

[Faure et al., 2019] Faure, J., Gustas, D., Guénot, D., Vernier, A., Böhle, F., Ouillé, M., Haessler, S., Lopez-Martens, R., and Lifschitz, A. (2019). A review of recent progress on laser-plasma acceleration at kHz repetition rate. *Plasma Physics and Controlled Fusion*, **61**(1):14012.

[Favaudon et al., 2014] Favaudon, V., Caplier, L., Monceau, V., Pouzoulet, F., Sayarath, M., Fouillade, C., Poupon, M.-F., Brito, I., Hupé, P., Bourhis, J., et al. (2014). Ultrahigh dose-rate flash irradiation increases the differential response between normal and tumor tissue in mice. *Science translational medicine*, **6**(245):245ra93–245ra93.

[Ferray et al., 1988] Ferray, M., L'Huillier, A., Li, X., Lompre, L., Mainfray, G., and Manus, C. (1988). Multiple-harmonic conversion of 1064 nm radiation in rare gases. *Journal of Physics B: Atomic, Molecular and Optical Physics*, **21**(3):L31.

[Forslund et al., 1975a] Forslund, D., Kindel, J., Lee, K., Lindman, E., and Morse, R. (1975). Theory and simulation of resonant absorption in a hot plasma. *Physical Review A*, **11**(2):679.

[Forslund et al., 1975b] Forslund, D., Kindel, J., and Lindman, E. (1975). Theory of stimulated scattering processes in laser-irradiated plasmas. *The Physics of Fluids*, **18**(8):1002–1016.

[Forslund et al., 1985] Forslund, D., Kindel, J., Mori, W., Joshi, C., and Dawson, J. (1985). Two-dimensional simulations of single-frequency and beat-wave laser-plasma heating. *Physical Review Letters*, **54**(6):558.

[Franken et al., 1961] Franken, P. A., Hill, A. E., Peters, C. W., and Weinreich, G. (1961). Generation of optical harmonics. *Physical Review Letters*, **7**(4):118–119.

[Fujioka, 2024] Fujioka, S. (2024). Nuclear-fusion reaction beats breakeven. *Physics*, 17:14.

[Gaumnitz et al., 2017] Gaumnitz, T., Jain, A., Pertot, Y., Huppert, M., Jordan, I., Ardana-Lamas, F., and Wörner, H. J. (2017). Streaking of 43-attosecond soft-x-ray pulses generated by a passively cep-stable mid-infrared driver. *Optics express*, **25**(22):27506–27518.

[Geddes et al., 2004] Geddes, C. G., Toth, C., Van Tilborg, J., Esarey, E., Schroeder, C. B., Bruhwiler, D., Nieter, C., Cary, J., and Leemans, W. P. (2004). High-quality electron beams from a laser wakefield accelerator using plasma-channel guiding. *Nature*, **431**(7008):538–541.

[Gibbon, 2005] Gibbon, P. (2005). *Short Pulse Laser Interactions with Matter: an Introduction.* World Scientific, 2005.

[Giordmaine and Miller, 1965] Giordmaine, J. A. and Miller, R. C. (1965). Tunable coherent parametric oscillation in LiNbO$_3$ at optical frequencies. *Physical Review Letters*, **14**(24):973–976.

[Gonsalves et al., 2019] Gonsalves, A. J., Nakamura, K., Daniels, J., Benedetti, C., Pieronek, C., De Raadt, T. C., Steinke, S., Bin, J. H., Bulanov, S. S., Van Tilborg, J., Geddes, C. G., Schroeder, C. B., Tóth, C., Esarey, E., Swanson, K., Fan-Chiang, L., Bagdasarov, G.,

Bobrova, N., Gasilov, V., Korn, G., Sasorov, P., and Leemans, W. P. (2019). Petawatt laser guiding and electron beam acceleration to 8 GeV in a laser-heated capillary discharge waveguide. *Physical Review Letters*, **122**(8):84801.

[Gordon et al., 2003] Gordon, D. F., Hafizi, B., Hubbard, R. F., Peñano, J. R., Sprangle, P., and Ting, A. (2003). Asymmetric self-phase modulation and compression of short laser pulses in plasma channels. *Physical Review Letters*, **90**(21):4.

[Gordon et al., 1955] Gordon, J. P., Zeiger, H. J., and Townes, C. H. (1955). The maser—new type of microwave amplifier, frequency standard, and spectrometer. *Physical Review*, **99**(4):1264.

[Gradshteyn and Ryzhik, 1965] Gradshteyn, I. S. and Ryzhik, I. M. (1965). *Table of Integrals, Series, and Products*. Academic Press, New York.

[Graydon, 2022] Graydon, O. (2022). The race for wakefield-driven fels. *Nature Photonics*, **16**(11):750–751.

[Haefner et al., 2017] Haefner, C. L., Bayramian, A., Betts, S., Bopp, R., Buck, S., Cupal, J., Drouin, M., Erlandson, A., Horáček, J., Horner, J., Jarboe, J., Kasl, K., Kim, D., Koh, E., Koubíková, L., Maranville, W., Marshall, C., Mason, D., Menapace, J., Miller, P., Mazurek, P., Naylon, A., Novák, J., Peceli, D., Rosso, P., Schaffers, K., Sistrunk, E., Smith, D., Spinka, T., Stanley, J., Steele, R., Stolz, C., Suratwala, T., Telford, S., Thoma, J., VanBlarcom, D., Weiss, J., and Wegner, P. (2017). High average power, diode pumped petawatt laser systems: a new generation of lasers enabling precision science and commercial applications. In Korn, G. and Silva, L. O., editors, *Research Using Extreme Light: Entering New Frontiers with Petawatt-class Lasers III*, volume 10241, page 2. International Society for Optics and Photonics, SPIE.

[Hargrove et al., 1964] Hargrove, L., Fork, R. L., and Pollack, M. (1964). Locking of he–ne laser modes induced by synchronous intracavity modulation. *Applied Physics Letters*, **5**(1):4–5.

[Harilal et al., 2022] Harilal, S., Phillips, M., Froula, D., Anoop, K., Issac, R., and Beg, F. (2022). Optical diagnostics of laser-produced plasmas. *Reviews of Modern Physics*, **94**(3):035002.

[Hasegawa and Mima, 1977] Hasegawa, A. and Mima, K. (1977). Stationary spectrum of strong turbulence in magnetized nonuniform plasma. *Physical Review Letters*, **39**(4):205.

[Heisenberg and Euler, 1936] Heisenberg, W. and Euler, H. (1936). Folgerungen aus der Diracschen Theorie des Positrons. *Zeitschrift für Physik*, **98**(11-12):714–732.

[Jackson, 1962] Jackson, J. D. (1962). *Classical Electrodynamics*. John Wiley & Sons.

[Jeong et al., 2020] Jeong, T. M., Bulanov, S. V., Sasorov, P. V., Bulanov, S. S., Koga, J. K., and Korn, G. (2020). 4π-spherically focused electromagnetic wave: Diffraction optics approach and high-power limits. *Optics Express*, **28**(9):13991.

[Jeong et al., 2021a] Jeong, T. M., Bulanov, S. V., Valenta, P., Korn, G., Esirkepov, T. Z., Koga, J. K., and Pirozhkov, A. S. (2021). Ultra-strong attosecond laser focus produced by a relativistic-flying parabolic mirror. In Bleiner, D., editor, *International Conference on X-ray Lasers 2020*, volume 11886, pages 125–132. International Society for Optics and Photonics, SPIE.

[Jeong et al., 2021b] Jeong, T. M., Bulanov, S. V., Valenta, P., Korn, G., Esirkepov, T. Z., Koga, J. K., Pirozhkov, A. S., Kando, M., and Bulanov, S. S. (2021). Relativistic-flying laser focus by a laser-produced parabolic plasma mirror. *Physical Review A*, **104**(5):53533.

[Kahaly et al., 2013] Kahaly, S., Monchocé, S., Vincenti, H., Dzelzainis, T., Dromey, B., Zepf, M., Martin, P., and Quéré, F. (2013). Direct observation of density-gradient effects in harmonic generation from plasma mirrors. *Physical Review Letters*, **110**(17):175001.

[Kaiser and Garrett, 1961] Kaiser, W. and Garrett, C. G. (1961). Two-photon excitation in CaF_2: Eu^{2+}. *Physical Review Letters*, **7**(6):229–231.

[Kando et al., 2018] Kando, M., Esirkepov, T. Z., Koga, J. K., Pirozhkov, A. S., and Bulanov, S. V. (2018). Coherent, short-pulse x-ray generation via relativistic flying mirrors. *Quantum Beam Science*, **2**(2):9.

[Karsch et al., 2007] Karsch, S., Osterhoff, J., Popp, A., Rowlands-Rees, T. P., Major, Z., Fuchs, M., Marx, B., Hörlein, R., Schmid, K., Veisz, L., Becker, S., Schramm, U., Hidding, B., Pretzler, G., Habs, D., Grüner, F., Krausz, F., and Hooker, S. M. (2007). GeV-scale electron acceleration in a gas-filled capillary discharge waveguide. *New Journal of Physics*, **9**(11):415.

[Kaw and Dawson, 1970] Kaw, P. and Dawson, J. (1970). Relativistic nonlinear propagation of laser beams in cold overdense plasmas. *The Physics of Fluids*, **13**(2):472–481.

[Keldysh, 1965] Keldysh, L. V. (1965). Ionization in the field of a strong electromagnetic wave. *Sov. Phys. JETP*, 20:1307.

[Kim et al., 2013] Kim, H. T., Pae, K. H., Cha, H. J., Kim, I. J., Yu, T. J., Sung, J. H., Lee, S. K., Jeong, T. M., and Lee, J. (2013). Enhancement of electron energy to the multi-GeV regime by a dual-stage laser-wakefield accelerator pumped by petawatt laser pulses. *Physical Review Letters*, **111**(16):165002.

[Koga et al., 2018] Koga, J. K., Bulanov, S. V., Esirkepov, T. Z., Kando, M., Bulanov, S. S., and Pirozhkov, A. S. (2018). Relativisitcally upshifted higher harmonic generation via relativistic flying mirrors. *Plasma Physics and Controlled Fusion*, **60**(7):74007.

[Krall et al., 1993] Krall, J., Ting, A., Esarey, E., and Sprangle, P. (1993). Enhanced acceleration in a self-modulated-laser wake-field accelerator. *Physical Review E*, **48**(3):2157–2161.

[Krausz and Ivanov, 2009] Krausz, F. and Ivanov, M. (2009). Attosecond physics. *Reviews of Modern Physics*, **81**(1):163–234.

[Kruer, 1988] Kruer, W. L. (1988). *Laser-Plasma Interactions*, volume 3. Addison-Wesley Publishing Company.

[Kurki-Suonio et al., 1989] Kurki-Suonio, T., Morrison, P. J., and Tajima, T. (1989). Self-focusing of an optical beam in a plasma. *Physical Review A*, **40**(6):3230–3239.

[Lamač, 2023] Lamač, M. (2023). Laser-driven hard x-ray source for imaging applications.

[Lamač et al., 2021] Lamač, M., Chaulagain, U., Jurkovičová, L., Nejdl, J., and Bulanov, S. (2021). Two-color nonlinear resonances in betatron oscillations of laser accelerated relativistic electrons. *Physical Review Research*, **3**(3):033088.

[Lamač et al., 2023a] Lamač, M., Chaulagain, U., Nejdl, J., and Bulanov, S. V. (2023). Generation of intense magnetic wakes by relativistic laser pulses in plasma. *Scientific Reports*, **13**(1):1701.

[Lamač et al., 2023b] Lamač, M., Mima, K., Nejdl, J., Chaulagain, U., and Bulanov, S. V. (2023). Anomalous relativistic emission from self-modulated plasma mirrors. *Physical Review Letters*, **131**(20):205001.

[Lamač et al., 2024] Lamač, M., Valenta, P., Nejdl, J., Chaulagain, U., Jeong, T. M., and Bulanov, S. V. (2024). Bright coherent attosecond x-ray pulses from beam-driven relativistic mirrors. *arXiv preprint arXiv:2403.03277*.

[Landau and Lifshitz, 1962] Landau, L. and Lifshitz, E. (1962). *Classical Theory of Fields*. Addison-Wesley Publishing Company.

[Landau and Lifshitz, 1960] Landau, L. D. and Lifshitz, E. M. (1960). *Electrodynamics of Continuous Media*. Pergamon Press Oxford.

[Lazzarini et al., 2024] Lazzarini, C., Grittani, G., Valenta, P., Zymak, I., Antipenkov, R., Chaulagain, U., Goncalves, L., Grenfell, A., Lamač, M., Lorenz, S., et al. (2024). Ultrarelativistic electron beams accelerated by terawatt scalable khz laser. *Physics of Plasmas*, **31**(3).

[Leemans et al., 2014] Leemans, W. P., Gonsalves, A. J., Mao, H. S., Nakamura, K., Benedetti, C., Schroeder, C. B., Tóth, C., Daniels, J., Mittelberger, D. E., Bulanov, S. S., Vay, J. L., Geddes, C. G., and Esarey, E. (2014). Multi-Gev electron beams from capillary-discharge-guided subpetawatt laser pulses in the self-trapping regime. *Physical Review Letters*, **113**(24):245002.

[Li et al., 2021] Li, Z., Kato, Y., and Kawanaka, J. (2021). Simulating an ultra-broadband concept for Exawatt-class lasers. *Scientific Reports*, **11**(1):151.

[Litvak, 1970] Litvak, A. (1970). Finite-amplitude wave beams in a magnetoactive plasma. *Sov. Phys. JETP*, **30**(344):166.

[Longman, 2021] Longman, A. M. (2021). Under-dense laser-plasma interactions in relativistic optical vortices.

[Lu et al., 2006] Lu, W., Huang, C., Zhou, M., Mori, W. B., and Katsouleas, T. (2006). Nonlinear theory for relativistic plasma wakefields in the blowout regime. *Physical Review Letters*, **96**(16):165002.

[Lu et al., 2007] Lu, W., Tzoufras, M., Joshi, C., Tsung, F. S., Mori, W. B., Vieira, J., Fonseca, R. A., and Silva, L. O. (2007). Generating multi-GeV electron bunches using single stage laser wakefield acceleration in a 3D nonlinear regime. *Physical Review Special Topics - Accelerators and Beams*, **10**(6):61301.

[Maiman, 1960] Maiman, T. H. (1960). Stimulated optical radiation in Ruby. *Nature*, **187**(4736):493–494.

[Maine and Mourou, 1988] Maine, P. and Mourou, G. (1988). Amplification of 1-nsec pulses in Nd:glass followed by compression to 1 psec. *Optics Letters*, **13**(6):467–469.

[Maker et al., 1964] Maker, P. D., Terhune, R. W., and Savage, C. M. (1964). Intensity-dependent changes in the refractive index of liquids. *Physical Review Letters*, **12**(18):507–509.

[Malka et al., 1997] Malka, G., Fuchs, J., Amiranoff, F., Baton, S., Gaillard, R., Miquel, J., Pépin, H., Rousseaux, C., Bonnaud, G., Busquet, M., et al. (1997). Suprathermal electron generation and channel formation by an ultrarelativistic laser pulse in an underdense preformed plasma. *Physical Review Letters*, **79**(11):2053.

[Mangles et al., 2004] Mangles, S. P., Murphy, C. D., Najmudin, Z., Thomas, A. G., Collier, J. L., Dangor, A. E., Divall, E. J., Foster, P. S., Gallacher, J. G., Hooker, C. J., Jaroszynski, D. A., Langley, A. J., Mori, W. B., Norreys, P. A., Tsung, F. S., Viskup, R., Walton, B. R., and Krushelnick, K. (2004). Monoenergetic beams of relativistic electrons from intense laser-plasma interactions. *Nature*, **431**(7008):535–538.

[Matlis et al., 2006] Matlis, N. H., Reed, S., Bulanov, S. S., Chvykov, V., Kalintchenko, G., Matsuoka, T., Rousseau, P., Yanovsky, V., Maksimchuk, A., Kalmykov, S., Shvets, G., and Downer, M. C. (2006). Snapshots of laser wakefields. *Nature Physics*, **2**(11):749–753.

[Maxwell, 1865] Maxwell, J. C. (1865). Viii. a dynamical theory of the electromagnetic field. *Philosophical transactions of the Royal Society of London*, (155):459–512.

[McClung and Hellwarth, 1962] McClung, F. J. and Hellwarth, R. W. (1962). Giant optical pulsations from ruby. *Journal of Applied Physics*, **33**(3):828–829.

[Mendonça, 2000] Mendonça, J. T. (2000). *Theory of Photon Acceleration*. CRC Press.

[Meyerhofer, 1997] Meyerhofer, D. D. (1997). High-intensity-laser-electron scattering. *IEEE Journal of Quantum Electronics*, **33**(11):1935–1941.

[Mocker and Collins, 1965] Mocker, H. W. and Collins, R. J. (1965). Mode competition and self-locking effects in a Q-switched ruby laser. *Applied Physics Letters*, **7**(10):270–273.

[Moore et al., 1995] Moore, C. I., Knauer, J., and Meyerhofer, D. (1995). Observation of the transition from thomson to compton scattering in multiphoton interactions with low-energy electrons. *Physical Review Letters*, **74**(13):2439.

[Mori, 1997] Mori, W. (1997). The physics of the nonlinear optics of plasmas at relativistic intensities for short-pulse lasers. *IEEE Journal of Quantum Electronics*, **33**(11):1942–1953.

[Mourou et al., 2002] Mourou, G., Chang, Z., Maksimchuk, A., Nees, J., Bulanov, S. V., Bychenkov, V. Y., Esirkepov, T. Z., Naumova, N. M., Pegoraro, F., and Ruhl, H. (2002). On the design of experiments for the study of relativistic nonlinear optics in the limit of single-cycle pulse duration and single-wavelength spot size.

[Mourou et al., 2006] Mourou, G. A., Tajima, T., and Bulanov, S. V. (2006). Optics in the relativistic regime. *Reviews of Modern Physics*, **78**(2):309.

[Nagy et al., 2020] Nagy, T., Kretschmar, M., Vrakking, M. J. J., and Rouzée, A. (2020). Generation of above-terawatt 1.5-cycle visible pulses at 1 kHz by post-compression in a hollow fiber. *Optics Letters*, **45**(12):3313.

[Nakajima et al., 2011] Nakajima, K., Deng, A., Zhang, X., Shen, B., Liu, J., Li, R., Xu, Z., Ostermayr, T., Petrovics, S., Klier, C., Iqbal, K., Ruhl, H., and Tajima, T. (2011). Operating plasma density issues on large-scale laser-plasma accelerators toward high-energy frontier. *Physical Review Special Topics - Accelerators and Beams*, **14**(9):91301.

[Naumova et al., 2001] Naumova, N., Bulanov, S., Esirkepov, T. Z., Farina, D., Nishihara, K., Pegoraro, F., Ruhl, H., and Sakharov, A. (2001). Formation of electromagnetic postsolitons in plasmas. *Physical Review Letters*, **87**(18):185004.

[Naumova et al., 2006] Naumova, N., Nees, J., and Mourou, G. (2006). Efficient attosecond phenomena in the relativistic λ^3 regime. In *AIP Conference Proceedings*, volume 827, pages 65–73. American Institute of Physics.

[Naumova et al., 2005] Naumova, N. M., Nees, J. A., and Mourou, G. A. (2005). Relativistic attosecond physics. *Physics of Plasmas*, **12**(5).

[Nisoli et al., 1996] Nisoli, M., De Silvestri, S., and Svelto, O. (1996). Generation of high energy 10 fs pulses by a new pulse compression technique. *Applied Physics Letters*, **68**(20):2793–2795.

[Ouillé et al., 2020] Ouillé, M., Vernier, A., Böhle, F., Bocoum, M., Jullien, A., Lozano, M., Rousseau, J. P., Cheng, Z., Gustas, D., Blumenstein, A., Simon, P., Haessler, S., Faure, J., Nagy, T., and Lopez-Martens, R. (2020). Relativistic-intensity near-single-cycle light waveforms at kHz repetition rate. *Light: Science and Applications*, **9**(1):47.

[Panchenko et al., 2008] Panchenko, A. V., Esirkepov, T. Z., Pirozhkov, A. S., Kando, M., Kamenets, F. F., and Bulanov, S. V. (2008). Interaction of electromagnetic waves with caustics in plasma flows. *Physical Review E*, **78**(5):56402.

[Perelomov et al., 1966] Perelomov, A., Popov, V., and Terentev, M. (1966). Ionization of atoms in an alternating electric field. *Sov. Phys. JETP*, **23**(5):924–934.

[Perry et al., 1999] Perry, M. D., Pennington, D., Stuart, B. C., Tietbohl, G., Britten, J. A., Brown, C., Herman, S., Golick, B., Kartz, M., Miller, J., Powell, H. T., Vergino, M., and Yanovsky, V. (1999). Petawatt laser pulses. *Optics Letters*, **24**(3):160.

[Pukhov et al., 2010] Pukhov, A. et al. (2010). Enhanced relativistic harmonics by electron nanobunching. *Physics of Plasmas*, **17**(3).

[Pukhov and Meyer-ter Vehn, 2002] Pukhov, A. and Meyer-ter Vehn, J. (2002). Laser wake field acceleration: The highly non-linear broken-wave regime. *Applied Physics B*, **74**(4-5):355–361.

[Quéré and Vincenti, 2021] Quéré, F. and Vincenti, H. (2021). Reflecting petawatt lasers off relativistic plasma mirrors: a realistic path to the schwinger limit. *High Power Laser Science and Engineering*, 9:e6.

[Raclavský et al., 2024] Raclavský, M., Rao, K. H., Chaulagain, U., Lamač, M., and Nejdl, J. (2024). High-sensitivity optical tomography of instabilities in supersonic gas flow. *Optics Letters*, **49**(9):2253–2256.

[Radier et al., 2022] Radier, C., Chalus, O., Charbonneau, M., Thambirajah, S., Deschamps, G., David, S., Barbe, J., Etter, E., Matras, G., Ricaud, S., et al. (2022). 10 pw peak power femtosecond laser pulses at eli-np. *High Power Laser Science and Engineering*, 10:e21.

[Riley et al., 2006] Riley, K. F., Hobson, M. P., and Bence, S. J. (2006). *Mathematical Methods for Physics and Engineering.* Cambridge University Press.

[Rivas et al., 2017] Rivas, D. E., Borot, A., Cardenas, D. E., Marcus, G., Gu, X., Herrmann, D., Xu, J., Tan, J., Kormin, D., Ma, G., Dallari, W., Tsakiris, G. D., Földes, I. B., Chou, S. W., Weidman, M., Bergues, B., Wittmann, T., Schröder, H., Tzallas, P., Charalambidis, D., Razskazovskaya, O., Pervak, V., Krausz, F., and Veisz, L. (2017). Next generation driver for attosecond and laser-plasma physics. *Scientific Reports*, **7**(1):5224.

[Saleh and Teich, 1991] Saleh, B. E. and Teich, M. C. (1991). *Fundamentals of Photonics.* John Wiley & Sons.

[Salehi et al., 2021] Salehi, F., Le, M., Railing, L., Kolesik, M., and Milchberg, H. M. (2021). Laser-accelerated, low-divergence 15-MeV quasimonoenergetic electron bunches at 1 kHz. *Physical Review X*, **11**(2):21055.

[Sandberg and Thomas, 2023] Sandberg, R. and Thomas, A. (2023). Photon acceleration from optical to xuv. *Physical Review Letters*, **130**(8):085001.

[Sandberg and Thomas, 2024] Sandberg, R. and Thomas, A. (2024). Dephasingless plasma wakefield photon acceleration. *Physical Review E*, **109**(2):025210.

[Sarachik and Schappert, 1970] Sarachik, E. and Schappert, G. (1970). Classical theory of the scattering of intense laser radiation by free electrons. *Physical Review D*, **1**(10):2738.

[Schroeder et al., 2006] Schroeder, C. B., Esarey, E., Shadwick, B. A., and Leemans, W. P. (2006). Trapping, dark current, and wave breaking in nonlinear plasma waves. *Physics of Plasmas*, **13**(3):33103.

[Schwinger, 1951] Schwinger, J. (1951). On gauge invariance and vacuum polarization. *Physical Review*, **82**(5):664–679.

[Shank et al., 1982] Shank, C., Fork, R., Yen, R., Stolen, R., and Tomlinson, W. J. (1982). Compression of femtosecond optical pulses. *Applied Physics Letters*, **40**(9):761–763.

[Spence et al., 1991] Spence, D. E., Kean, P. N., and Sibbett, W. (1991). 60-fsec pulse generation from a self-mode-locked ti: sapphire laser. *Optics Letters*, **16**(1):42–44.

[Speziale and Catto, 1977] Speziale, T. and Catto, P. (1977). Linear wave conversion in an unmagnetized, collisionless plasma. *The Physics of Fluids*, **20**(6):990–997.

[Sprangle et al., 1992] Sprangle, P., Esarey, E., Krall, J., and Joyce, G. (1992). Propagation and guiding of intense laser pulses in plasmas. *Physical Review Letters*, **69**(15):2200–2203.

[Sprangle et al., 1990] Sprangle, P., Esarey, E., and Ting, A. (1990). Nonlinear theory of intense laser-plasma interactions. *Physical Review Letters*, **64**(17):2011–2014.

[Strickland and Mourou, 1985] Strickland, D. and Mourou, G. (1985). Compression of amplified chirped optical pulses. *Optics Communications*, **56**(3):219–221.

[Sun et al., 1987] Sun, G.-Z., Ott, E., Lee, Y. C., and Guzdar, P. (1987). Self-focusing of short intense pulses in plasmas. *Physics of Fluids*, **30**(2):526.

[Ta Phuoc et al., 2012] Ta Phuoc, K., Corde, S., Thaury, C., Malka, V., Tafzi, A., Goddet, J. P., Shah, R. C., Sebban, S., and Rousse, A. (2012). All-optical Compton gamma-ray source. *Nature Photonics*, **6**(5):308–311.

[Tajima and Dawson, 1979] Tajima, T. and Dawson, J. M. (1979). Laser electron accelerator. *Physical Review Letters*, **43**(4):267–270.

[Tanaka et al., 2020] Tanaka, K. A., Spohr, K. M., Balabanski, D. L., Balascuta, S., Capponi, L., Cernaianu, M. O., Cuciuc, M., Cucoanes, A., Dancus, I., Dhal, A., Diaconescu, B., Doria, D., Ghenuche, P., Ghita, D. G., Kisyov, S., Nastasa, V., Ong, J. F., Rotaru, F., Sangwan, D., Söderström, P. A., Stutman, D., Suliman, G., Tesileanu, O., Tudor, L., Tsoneva, N., Ur, C. A., Ursescu, D., and Zamfir, N. V. (2020). Current status and highlights of the ELI-NP research program. *Matter and Radiation at Extremes*, **5**(2):24402.

[Teubner and Gibbon, 2009] Teubner, U. and Gibbon, P. (2009). High-order harmonics from laser-irradiated plasma surfaces. *Reviews of Modern Physics*, **81**(2):445.

[Toth et al., 2020] Toth, S., Stanislauskas, T., Balciunas, I., Budriunas, R., Adamonis, J., Danilevicius, R., Viskontas, K., Lengvinas, D., Veitas, G., Gadonas, D., Varanavičius, A., Csontos, J., Somoskoi, T., Toth, L., Borzsonyi, A., and Osvay, K. (2020). SYLOS lasers - The frontier of few-cycle, multi-TW, kHz lasers for ultrafast applications at extreme light infrastructure attosecond light pulse source. *Journal of Physics: Photonics*, **2**(4):45003.

[Vincenti, 2019] Vincenti, H. (2019). Achieving extreme light intensities using optically curved relativistic plasma mirrors. *Physical Review Letters*, **123**(10):105001.

[Vincenti et al., 2014] Vincenti, H., Monchocé, S., Kahaly, S., Bonnaud, G., Martin, P., and Quéré, F. (2014). Optical properties of relativistic plasma mirrors. *Nature Communications*, **5**(1):3403.

[Voronov and Delone, 1966] Voronov, G. and Delone, N. (1966). Many-photon ionization of the xenon atom by ruby laser radiation. *Soviet Physics - JETP*, **23**(1):54.

[Vshivkov et al., 1998] Vshivkov, V. A., Naumova, N. M., Pegoraro, F., and Bulanov, S. V. (1998). Nonlinear electrodynamics of the interaction of ultra-intense laser pulses with a thin foil. *Physics of Plasmas*, **5**(7):2727–2741.

[Wheeler et al., 2012] Wheeler, J., Borot, A., Malvache, A., Ricci, A., Jullien, A., Lopez-Martens, R., Monchocé, S., Vincenti, H., and Quéré, F. (2012). Attosecond lighthouses from plasma mirrors. *Nature Photonics*, **6**(12):829–833.

[Woodbury and Ng, 1962] Woodbury, E. J. and Ng, W. K. (1962). Ruby laser operation in near IR. *Proceedings of the Institute of Radio Engineers*, **50**(11):2367.

[Yoon et al., 2021] Yoon, J. W., Kim, Y. G., Choi, I. W., Sung, J. H., Lee, H. W., Lee, S. K., and Nam, C. H. (2021). Realization of laser intensity over 10^{23} W/cm^2. *Optica*, **8**(5):630.

[Zangwill, 2013] Zangwill, A. (2013). *Modern Electrodynamics*. Cambridge University Press.

[Zeng et al., 2017] Zeng, X., Zhou, K., Zuo, Y., Zhu, Q., Su, J., Wang, X., Wang, X., Huang, X., Jiang, X., Jiang, D., Guo, Y., Xie, N., Zhou, S., Wu, Z., Mu, J., Peng, H., and Jing, F. (2017). Multi-petawatt laser facility fully based on optical parametric chirped-pulse amplification. *Optics Letters*, **42**(10):2014.

Appendices

A

List of author's publications

The list of all publications in peer-reviewed journals, preprint archives, and conference proceedings in which the author took part is presented in this section. The publications are listed in order of author's contribution.

A.1 Preprints

- M. Lamač, P. Valenta, J. Nejdl, U. Chaulagain, T. M. Jeong and S. V. Bulanov (2024). Bright coherent attosecond X-ray pulses from beam-driven relativistic mirrors. *arXiv*, preprint arXiv:2403.03277. (submitted)

A.2 Publications in peer-reviewed journals

- M. Lamač, K. Mima, J. Nejdl, U. Chaulagain, and S. V. Bulanov (2023). Anomalous relativistic emission from self-modulated plasma mirrors. *Physical Review Letters*, **131**(20), 205001

- M. Lamač, U. Chaulagain, L. Jurkovičová, J. Nejdl, and S. V. Bulanov (2021). Two-color nonlinear resonances in betatron oscillations of laser accelerated relativistic electrons. *Physical Review Research*, **3**(3), 033088.

- M. Lamač, U. Chaulagain, J. Nejdl and S. V. Bulanov (2023). Generation of intense magnetic wakes by relativistic laser pulses in plasma. *Scientific Reports*, **13**(1), 1701.

- U. Chaulagain, M. Lamač, M. Raclavský, K. P. Khakurel, K. H. Rao, K. T. Phuoc, S. V. Bulanov and J. Nejdl (2022). ELI Gammatron Beamline: A Dawn of Ultrafast Hard X-ray Science. *Photonics*, **9**(11), 853.

- M. Raclavský, K. H. Rao, U. Chaulagain, M. Lamač and J. Nejdl (2021). High-sensitivity optical tomography of instabilities in supersonic gas flow. *Optics Letters*, **49**(9), 2253-2256.

■ M. Raclavský, K. P. Khakurel, U. Chaulagain, <u>M. Lamač</u> and J. Nejdl (2021). Multi-lane mirror for broadband applications of the betatron x-ray source. *Photonics*, **8**(12), 579.

■ C. M. Lazzarini, G. M. Grittani, P. Valenta, I. Zymak, R. Antipenkov, U. Chaulagain, L. V. N. Goncalves, A. Grenfell, <u>M. Lamač</u>, S. Lorenz, M. Nevrkla, A. Špaček, V. Šobr, W. Szuba, P. Bakule, G. Korn and S. V. Bulanov (2024). Ultrarelativistic electron beams accelerated by terawatt scalable kHz laser. *Physics of Plasmas*, **31**(3), 030703. (Featured Article)

A.3   Publications in conference proceedings

■ U. Chaulagain, <u>M. Lamač</u>, M. Raclavský, S. Karatodorov, J. Nejdl and S. V. Bulanov (2021). Ultrafast hard X-ray sources based on relativistic electrons at ELI beamlines. *47th EPS Conference on Plasma Physics*, EPS 2021, p. 1195-1198.

■ U. Chaulagain, <u>M. Lamač</u>, M. Raclavský, K. H. Rao, O. Morvai, F. Vaňek, K. Ta-Phuoc, S. V. Bulanov and J. Nejdl (2023). Development of the multidisciplinary X-ray sources at ELI Beamlines facility. *Compact Radiation Sources from EUV to Gamma-Rays: Development and Applications 2023*, SPIE Optics + Optoelectronics 2023, **12582**, 1258208.

■ U. Chaulagain, <u>M. Lamač</u>, M. Raclavský, K. H. Rao, J. Nejdl, S. A. Weber and S. V. Bulanov (2022). Development of LPA based hard X-ray sources at ELI Beamlines. *48th EPS Conference on Plasma Physics*, EPS 2022, **12578**, 125780A.

■ U. Chaulagain, <u>M. Lamač</u>, M. Raclavský, K. Khakurel and J. Nejdl (2022). Update on LPA based X-ray sources at ELI Beamlines. *Compact EUV & X-ray Light Sources 2022*, High-brightness Sources and Light-driven Interactions Congress 2022, EW3A. 4.

■ M. Raclavský, K. H. Rao, <u>M. Lamač</u>, U. Chaulagain and J. Nejdl (2023). Advanced measurement of gas jet density using a wavefront sensor. *Compact Radiation Sources from EUV to Gamma-Rays: Development and Applications 2023*, SPIE Optics + Optoelectronics 2023, **12582**, 125820H.

■ U. Chaulagain, S. Karatodorov, <u>M. Lamač</u>, M. Raclavský, M. Kozlová, S. A. Weber and J Nejdl (2020). LWFA driven hard X-ray sources at ELI Beamlines. *High-brightness Sources and Light-driven Interactions Congress 2020*, JW1A. 3.

■ M. Raclavský, S Karatodorov, U. Chaulagain, <u>M. Lamač</u> and J. Nejdl (2020). High sensitivity characterization of lwfa gas jet targets. *High-brightness Sources and Light-driven Interactions Congress 2020*, JW1A. 4.

■ U. Chaulagain, S. Karatodorov, M. Raclavský, S. Lorenz, <u>M. Lamač</u>, M. Albrecht, V. Tomkus, J. Dudutis, M. Mackevičiūtė, P. Gečys and J Nejdl (2021). Tomographic characterization of gas jets for laser-plasma acceleration with increased sensitivity. *International Conference on X-Ray Lasers 2020*, **11886**, 61-67.

■ U. Chaulagain, K. Boháček, J. Vančura, <u>M. Lamač</u>, W. Yan, Y. Gu, M. Kozlová, K. Ta-Phuoc, S. A. Weber and J. Nejdl (2020). LWFA-driven betatron source for Plasma Physics Platform at ELI Beamlines. *X-Ray Lasers 2018: Proceedings of the 16th International Conference on X-Ray Lasers 16*, **241**, 117-123.

- J. Nejdl, U. Chaulagain, D. Mai, O. Hort, <u>M. Lamač</u>, M. Raclavský, M. Albrecht, L. Jurkovičová, O. Finke, J. Vábek, Y. Pulnova and S. V. Bulanov (2022). Update on laser-driven X-ray sources at ELI Beamlines. *Compact EUV & X-ray Light Sources 2022*, High-brightness Sources and Light-driven Interactions Congress 2022, ETh5A. 6.

- J. Nejdl, U. Chaulagain, O. Hort, D. Mai, R. Lera, S. Karatodorov, M. Albrecht, M. Jurkovič, O. Finke, <u>M. Lamač</u>, M. Raclavský and J. Vábek (2020). New Generation of Laser-driven X-ray Sources at ELI Beamlines. *High-brightness Sources and Light-driven Interactions Congress 2020*, ETh3A. 7.

B
Selected publications

B.1 Anomalous relativistic emission from self-modulated plasma mirrors

The following article is reproduced from M. Lamač, K. Mima, J. Nejdl, U. Chaulagain, and S. V. Bulanov (2023). Anomalous relativistic emission from self-modulated plasma mirrors. *Physical Review Letters*, **131**(20), 205001, with the permission of APS.

Anomalous Relativistic Emission from Self-Modulated Plasma Mirrors

M. Lamač[1,2,*] K. Mima,[3] J. Nejdl[1,4] U. Chaulagain,[1] and S. V. Bulanov[1,5]

[1]*ELI Beamlines Facility, The Extreme Light Infrastructure ERIC, Za Radnicí 835, Dolní Břežany 25241, Czechia*
[2]*Faculty of Mathematics and Physics, Charles University, Ke Karlovu 3, Prague 2, 12116, Czechia*
[3]*Institute of Laser Engineering, Osaka University, 2-6 Yamadaoka, Suita, Osaka 565-0871, Japan*
[4]*Faculty of Nuclear Science and Physical Engineering, Czech Technical University in Prague, Břehová 7, Prague 1, 11519, Czechia*
[5]*Kansai Photon Science Institute, National Institutes for Quantum and Radiological Science and Technology,*
8-1-7 Umemidai, Kizugawa, 619-0215 Kyoto, Japan

The interaction of intense laser pulses with plasma mirrors has demonstrated the ability to generate high-order harmonics, producing a bright source of extreme ultraviolet (XUV) radiation and attosecond pulses. Here, we report an unexpected transition in this process. We show that the loss of spatiotemporal coherence in the reflected high harmonics can lead to a new regime of highly efficient coherent XUV generation, with an extraordinary property where the radiation is directionally anomalous, propagating parallel to the mirror surface. With analytical calculations and numerical particle-in-cell simulations, we discover that the radiation emission is due to laser-driven oscillations of relativistic electron nanobunches that originate from a plasma surface instability.

Generation of attosecond pulses and extreme ultraviolet radiation (XUV) originating from the interaction of a relativistically intense laser with a plasma mirror has now been investigated for almost three decades [1–5]. With experimental results supporting its potential for applications in fundamental science, ultrafast science, attosecond interferometry or imaging [2,6–12], this mechanism presents a competitive alternative to the contemporary workhorse of attosecond science, which is high-harmonic generation (HHG) from noble gases originating from nonlinear laser-atom interactions [11,13–15]. The potential of relativistic high-harmonic generation reveals itself in the lack of ionization thresholds, which pose a hard limit on intensity of conventional gas or solid HHG sources. With the growing availability of commercial high-repetition rate laser systems with peak powers in the terawatt range, relativistic generation of broadband, bright, and ultrashort radiation will be attractive even at small university-scale laboratories. The emission of relativistic high harmonics originates from plasma surface electrons performing nonlinear oscillations within the laser field, with velocity close to the speed of light. This occurs when the amplitude of the incident laser exceeds the threshold amplitude of relativistic optics [16], which is characterized in terms of the normalized laser amplitude as $a_0 = eE_0/m_e\omega_0 c \geq 1$, where e is the elementary charge, m_e the electron mass, c the speed of light, ω_0 is the angular frequency of the laser, and E_0 the amplitude of the laser electric field. The coherent reflection from the plasma surface can be additionally affected for very high laser intensities such that the ions can accelerate to a fraction of the speed of light in a single laser cycle,

$a_0 \geq (m_i/Zm_e)^{1/2}$ [17,18], where m_i is the ion mass and Z is the ion charge number.

In this Letter, we report the discovery of a new regime of XUV light generation, which we call relativistic instability-modulated emission (RIME), originating from the interaction of an intense laser pulse with a plasma mirror, which is self-modulating due to unstable return current induced by the collisionless absorption of the laser. RIME generates broadband XUV radiation with high-efficiency and an anomalous propagation characteristic, where the radiation is emitted parallel to the plasma mirror surface. The mechanism of RIME is illustrated in Fig. 1. An intense P-polarized laser pulse is obliquely incident on the surface of a relativistically overdense plasma mirror, $1 \leq a_0 < n_e/n_c$, where n_e is the electron plasma density, $n_c = m_e\epsilon_0\omega_0^2/e^2$ is the critical plasma density and ϵ_0 is the vacuum permittivity. At the beginning of interaction, the intense incident laser coherently reflects from and accelerates the surface electrons into the plasma bulk [Fig. 1(b)] by the Brunel effect [19,20]. These bulk-penetrating Brunel electrons induce neutrality-restoring return currents flowing along the mirror periphery, consisting of counter-streaming electrons and ions which generate intense quasistatic magnetic field on the mirror surface [21]. The electron-ion two-stream grows unstable with a growth rate $\Gamma \propto \omega_{pe}(Zm_e/m_i)^{1/3}$ [22], which is of the order of the laser frequency for solid high-Z targets with electron plasma densities $n_e/n_c \geq (m_i/Zm_e)^{2/3}$. Therefore, after laser-plasma interaction time of $\approx 1/\Gamma$, the plasma mirror self-modulates with wavelength of the order of the plasma wavelength $\lambda_p = 2\pi c/\omega_{pe}$, where $\omega_{pe} = (e^2n_e/m_e\epsilon_0)^{1/2}$
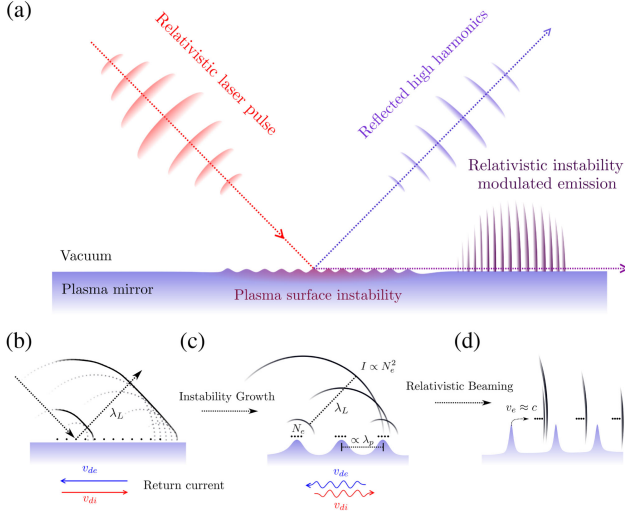
FIG. 1. Principle of RIME. (a) Schematic of radiation emission geometry. (b) Radiation emitted by electrons composing a mirror surface forms a reflected wave. (c) Surface modulation leads to a loss of spatiotemporal coherence in the reflected wave and enhancement of individual bunch emissions. (d) Oscillating electrons move along the surface in the field of a relativistically intense laser, leading to relativistic beaming of individual bunch emissions towards the surface.

is the electron plasma frequency. As the plasma wave grows, the oscillating electrons are bunched and the individual bunch emissions are coherently enhanced while the reflected wave loses its spatiotemporal coherence [Fig. 1(c)]. As the laser amplitude ramps up in the interaction region, the unstable plasma wave grows non-linear and breaks [23], releasing electron nanobunches to be accelerated by the laser across the magnetized plasma surface to velocities close to the speed of light, resulting in surface-parallel relativistic beaming of individual bunch emissions [Fig. 1(d)].

The coherent intensity spectrum of RIME generated over a half-oscillation period by an electron bunch containing N_e electrons can be obtained as (see Supplemental Material [24] for derivation details)

$$I(\omega) = N_e^2 \frac{\sqrt{3}e^2\gamma}{4\pi\epsilon_0 c} \frac{\omega/\omega_c}{(1+(\omega/\omega_b)^2)^2} \int_{\omega/\omega_c}^{\infty} K_{5/3}(\xi)d\xi, \quad (1)$$

where $K_{5/3}(x)$ is the modified Bessel function, $\omega_c = 3c\gamma^3/2\lambda_0$ is the critical frequency indicating an exponential cutoff in the spectrum, λ_0 is the laser wavelength, and γ is the electron Lorentz factor. The electron bunch modulation frequency is given as $\omega_b = c/L_b$, where L_b is the electron bunch length. Bunch modulation frequency indicates a transition in the radiation spectrum, from the coherent regime of radiation emission, where $I \propto N_e^2$ for frequencies smaller than or of the same order $\omega \lesssim \omega_b$, into the regime of incoherent emission, where $I \propto N_e$ for $\omega \gg \omega_b$.

To describe the modulation frequency of the electron bunch, we must consider the origin of the bunch modulating instability. Fast Brunel electrons penetrate into the plasma mirror and induce a return current composed of counter-streaming electrons and ions flowing along the surface. Assuming that the drift velocity of the return electrons is much larger than ions $v_{de} \gg v_{di}$, the ion velocity may be neglected and, following the usual treatment of two-stream instability, we obtain the well-known Buneman instability (BI) dispersion relation for a small perturbation [22],

$$\frac{\omega_{pe}^2}{(\omega - kv_{de})^2} + \frac{\omega_{pi}^2}{\omega^2} = 1, \quad (2)$$

where $\omega_{pi} = (Z^2e^2n_i/m_i\epsilon_0)^{1/2}$ is the ion plasma frequency. For an unstable growing mode, the mirror surface, and therefore the Brunel electrons, will be modulated according to the instability wavelength as illustrated in Fig. 1(c). Solving Eq. (2) for the complex frequency $\omega \rightarrow \omega + i\Gamma$, we obtain from the imaginary part the maximum growth rate of the Buneman instability as

$$\Gamma_m = \omega_{pe} \frac{\sqrt{3}}{2} \left(\frac{Z^2 m_e}{2m_i}\right)^{1/3}, \quad (3)$$

which is approximately valid for all modes in the band $|kv_{de} - \omega_p| \lesssim (3/2)(\omega_{pe}\omega_{pi}^2)^{1/3}$ [22]. The condition for RIME to occur therefore requires laser pulse duration to be larger than $\approx 1/\Gamma_m$. This straightforward result allows us to see that the plasma surface instability e-folding time can be of the order of a single laser cycle, since $\Gamma_m \approx \omega_0$ for solid density plasma, $n_e \approx 10^3 n_c$, which means that the plasma surface instability can fully manifest already within a few laser cycles.

To study the process in detail, we have performed multidimensional particle-in-cell (PIC) simulations (See Supplemental Material [24] for simulation details). A P-polarized laser pulse defined with pulse duration $\tau_{\text{FWHM}} = 30$ fs, laser wavelength $\lambda_0 = 1$ μm, and peak intensity $I_0 = 10^{22}$ W/cm² corresponding to a normalized laser amplitude $a_0 = 85.5$, was focused with an incidence angle $\theta = 45°$ to a spot size with waist radius $w_0 = 2$ μm upon a plasma mirror composed of uniformly overlapping electrons and ions with matching density $n_i/n_c = n_e/n_c = 1000$ and temperature $k_BT = 100$ eV. Figure 2 shows the analysis of plasma surface instability observed in the PIC simulation. Figure 2(a) shows the temporal evolution of the surface-parallel ion current, revealing an unstable plasma wave propagating in the direction of electron return flow with phase velocity $v_p/c \approx 0.01$. This corresponds to the drift velocity of the electron return current, since from the current neutrality condition $v_{de}/c \approx a_0 n_c/n_e \approx 0.01$ at $t \approx 45$ fs when the amplitude of the incident laser is $a_0 \approx 10$.
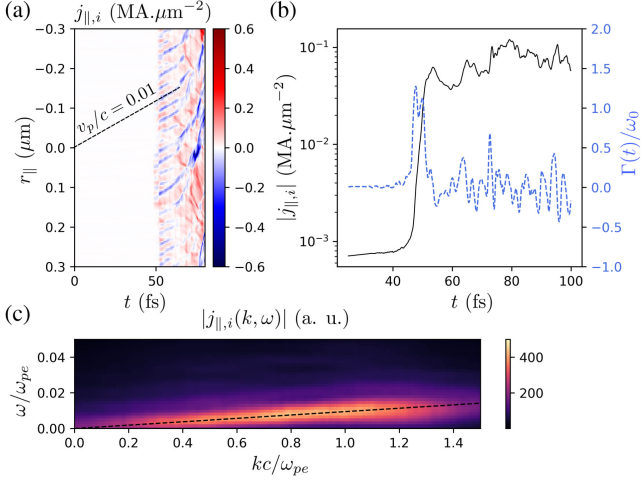
FIG. 2. PIC simulation of the surface instability. (a) Time evolution of the longitudinal component of the ion current, shown up to $t = 80$ fs. Dashed line following linear phase velocity of the surface wave corresponds to $v_p/c = 0.01$. (b) Time evolution of $|j_{i,\parallel}|$ averaged over $r_\parallel \in [-1 \ \mu m, 1 \ \mu m]$ (black) and corresponding instantaneous growth rate $\Gamma(t)$ (blue). (c) Fourier transform of the ion current in the linear phase of the instability, 0 fs $< t <$ 55 fs (colored, smoothened) and the real part of the solution of Eq. (2) (black, dashed) calculated for the electron drift velocity $v_{de}/c = 0.01$, $\omega_p/\omega_0 = 31.6$.

Figure 2(b) presents the time evolution of the instability, showing the instability saturation and clear separation between the linear and nonlinear phases occurring at $t \approx 55$ fs. We note that the maximum instantaneous growth rate matches the prediction given by Eq. (3). Figure 2(c) shows the numerical dispersion of the instability overlaid with the real part of the solution of Eq. (2), showing a match between the PIC and Buneman unstable modes.

Figure 3 presents a detailed view of the RIME origin. In Fig. 3(a), Brunel electrons can be seen penetrating into the bulk in the direction of laser propagation at twice the laser frequency, which is due to the relativistic $\mathbf{j} \times \mathbf{B}$ Lorentz force term. This leads to the growth of unstable return current flowing along the periphery seen in Fig. 3(b). As the unstable plasma wave breaks, oscillating electron nanobunches are accelerated by the laser across the surface within the focal region to relativistic velocities. This is shown with the electron current components in Figs. 3(c) and 3(d). The transverse component highlights the transverse oscillatory turning points of the individual nanobunches occurring at $j_{\perp,e} = 0$. On the other hand, it is at these points where longitudinal velocity is largest, $v_\parallel \approx c$, which leads to relativistic beaming of radiation along the surface. (See Supplemental Material [24] for a movie of the process.) This results in the loss of reflected wave coherence and the emergence of RIME XUV bursts seen in the perpendicular component of the magnetic field B_z shown in Fig. 3(f). Additionally, the magnetic field reveals that the

instability region is extremely magnetized due to the return current, with amplitude of the order of the incident laser. This leads to enhanced confinement of relativistic electrons towards the plasma surface [21]. The electric field component E_y in Fig. 3(e) shows the incident P-polarized laser interfering with the intense RIME bursts.

Radiation characteristics of RIME are presented in Fig. 4. Trajectories of two characteristic electron bunches with $\gamma \approx a_0$ are presented in Fig. 4(c). Calculated radiation power confirms multiple bursts emitted along the bunch trajectory. The intensity spectra of RIME and the wave reflected due to the relativistic oscillations of the mirror (ROM) are shown in Fig. 4(a). The spatiotemporal coherence of the reflected wave is reduced with the onset of RIME, leading to larger XUV conversion efficiency for the emission along the mirror surface. To evaluate coherent enhancement of radiation due to electron bunching, we have performed another PIC simulation with immobile ions. The simulation confirmed that in this case BI and RIME are not present. In this scenario, the coherence of high harmonics composing the reflected wave is significantly improved, as shown in Fig. 4(a). However, compared to the RIME spectrum, the efficiency significantly drops for $\omega/\omega_0 > 10$, which can be explained by the nanobunching effect occurring in the realistic simulation, since the individual bunch sizes can be smaller than $\lambda_{pe} = \lambda_0/31.6 \approx 31$ nm as shown in Figs. 3(c) and 3(d). The continuous RIME spectrum is explained by the fact that the peak laser-plasma interaction, and therefore strongest emission, occurs deep into the nonlinear phase of the instability evolution at $t = 80$ fs, as seen in Fig. 2(b). This leads to nonperiodic trains of electron nanobunches individually producing broadband XUV bursts that add up to a broad, continuous spectrum. We point out that the bunching effect also enhances the low-order harmonics composing the reflected wave, which can be seen when comparing the two ROM spectra shown in Fig. 4(a). This is because the distances between the individual bunches within a single laser oscillation are smaller than the wavelengths of the low-order harmonics, which can be seen in Figs. 3(e) and 3(f). To compare the RIME spectrum with the analytical result given by Eq. (1), we proceed to estimate the bunch modulation frequency. The average value of electron drift velocity inside the return current observed in the PIC simulation is $v_{de}/c \approx 0.18$ at the peak interaction time $t = 80$ fs [Fig. 3(d)]. The bunch modulation frequency due to BI can be therefore estimated as $\omega_b = c/L_b \approx 2c/\lambda_B \approx (c\omega_p/v_{de}\pi) \approx 18\omega_0$, corresponding to an electron bunch length of $L_b \approx 88$ nm and instability wavelength $\lambda_B \approx 0.18 \ \mu m$, which is in agreement with the features seen in Figs. 3(c) and 3(d). Considering such modulation frequency, RIME spectrum as given by Eq. (1), with energy of laser-accelerated electrons given $\gamma \approx a_0 = 85.5$, is presented in Fig. 4(a), showing an excellent agreement with the PIC result. In Fig. 4(b) we show the dependence of emitted radiation on
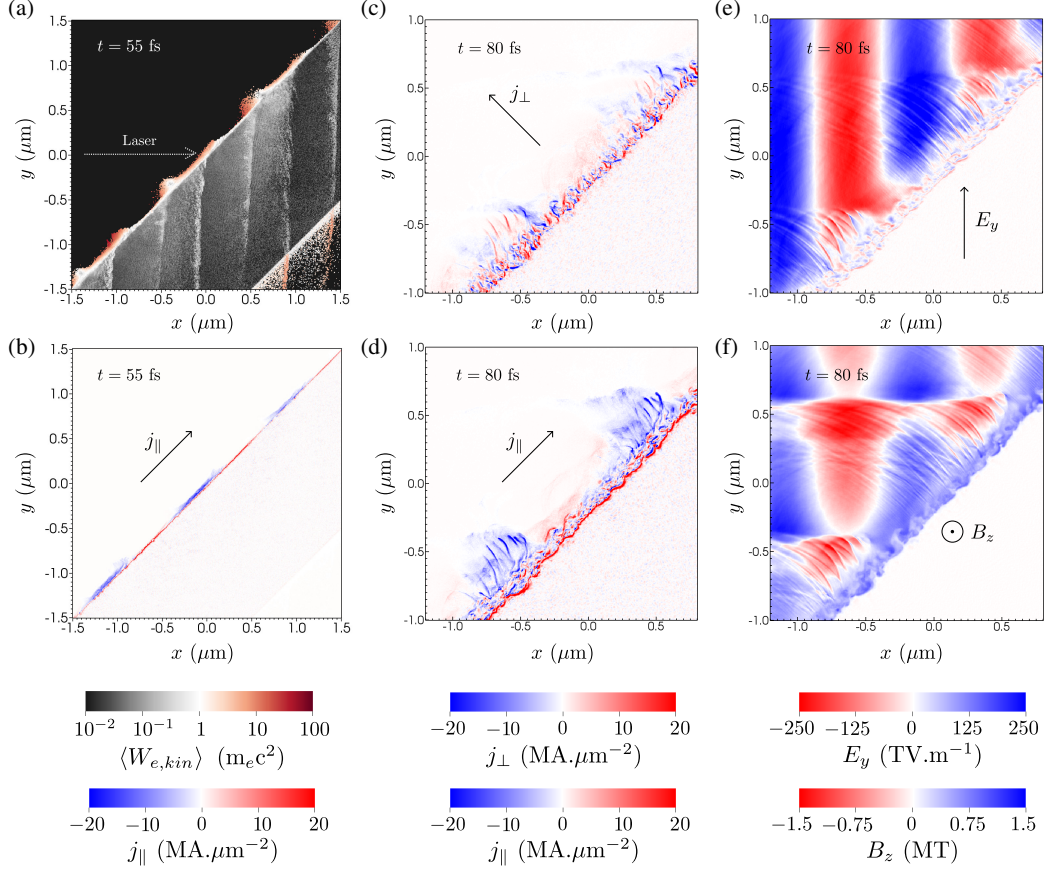
FIG. 3. PIC simulation of RIME. Average kinetic energy of electrons (a) and the longitudinal electron current (b) at the time of instability saturation, $t = 55$ fs. Transverse (c) and longitudinal (d) electron current, and electric (e) and magnetic field (f) components at the time of peak laser amplitude arrival, $t = 80$ fs.

laser polarization. When the incident laser is S polarized, BI and RIME are not present and only ROM-reflected wave remains with less efficient high-harmonic generation, which confirms a well-known property of ROM [2].

Previous studies have demonstrated that the presence of preplasma with scale length satisfying $kL \approx 1$ can optimize ROM conversion efficiency [28,29], where $k = \omega_0/c$ is the laser wave number and L is the pre-plasma scale length. This optimum comes from the balance of the strong electrostatic field due to the space-charge distribution limiting electron oscillations when $kL < 1$, and the growth of plasma waves leading to reflected wave coherence loss when $kL > 1$ [20,30]. In the case when $kL > 1$, the plasma wave growth is resonant for a P-polarized laser incident upon inhomogeneous plasma with a scale length satisfying [30,31]

$$(kL)^{1/3} \sin \theta \approx 0.8, \qquad (4)$$

where θ is the laser incidence angle. To investigate the effect of nonzero pre-plasma scale lengths on RIME, we have conducted PIC simulations in the range $0 \leq kL \leq \pi$.

The results are summarized in Fig. 4(d), where we show the conversion efficiency of laser energy to XUV wavelengths $\lambda \leq 100$ nm. Our numerical results match the experimentally discovered ROM optimum found in [28,29], which occurs when $kL \approx 1$. For such scale length, the total reflectivity reaches up to 60%, with around 0.4% of laser energy converted to XUV. The results for RIME show high XUV efficiency, but more intricate dependence. First, as discussed above, the coherent enhancement due to nano-bunching yields larger XUV conversion efficiency by up to an order of magnitude. Second, the XUV yields are anticorrelated. This is due to the fact that the coherent enhancement of RIME results in the loss of coherence in the reflected wave and vice versa. Finally, the RIME XUV yield reveals an optimal scale length for the simulation with $L/\lambda_0 = 0.25$, where XUV conversion efficiency grows up to 2%. To compare to conventional XUV sources, the widely used gas HHG source operates at XUV energy conversion efficiency of $\approx 10^{-5}$ [14,15], with maximum incident laser intensity limited to $\sim 10^{15}$ W cm^{-2}.

For the simulated incidence angle of 45°, the condition for resonant plasma wave growth given by Eq. (4) gives the
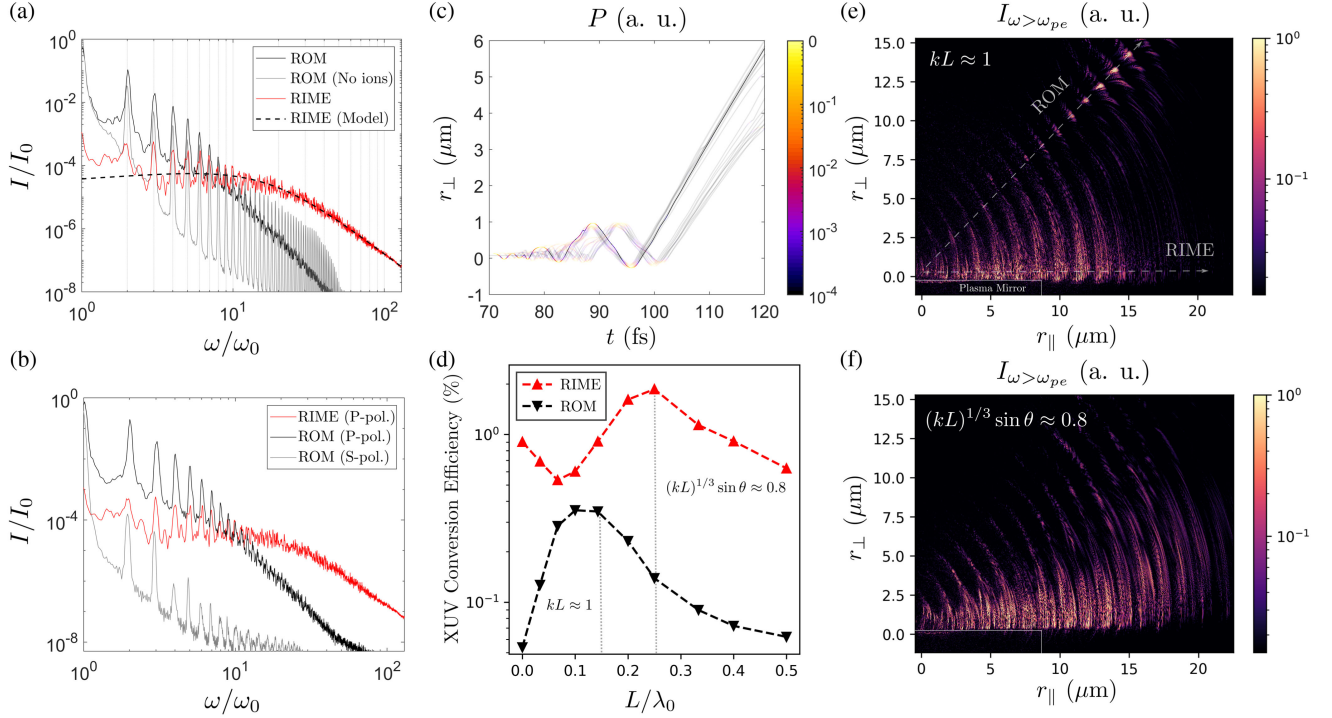
FIG. 4. Radiation properties of RIME. (a) Intensity spectra with the analytical model given by Eq. (1). (b) Intensity spectra for S and P laser polarizations. (c) Instantaneous power of radiation emitted along the surface calculated for two electron bunches oscillating above the surface ($r_\perp = 0$) with $\gamma \approx a_0$. (d) Laser-to-XUV energy conversion efficiency dependence on pre-plasma scale length L. (e) Spatial distribution of XUV intensity for the ROM-optimal and (f) the RIME-optimal pre-plasma.

scale length as $L/\lambda_0 = 0.23$, an excellent match which shows that the origin of the RIME optimum is due to the resonant growth of large-amplitude plasma waves which facilitate faster wave breaking of instability-modulated electrons into the laser field. The XUV intensity distribution for the two optimal cases are shown in Figs. 4(e) and 4(f). In the case of $kL \approx 1$, the laser is initially reflected coherently by ROM. As the unstable plasma wave saturates, the spatiotemporal XUV coherence is reduced and coherent XUV bursts propagating along the mirror surface emerge. In the case of resonant plasma wave growth, $(kL)^{1/3} \sin \theta \approx 0.8$, the reflected wave loses its spatiotemporal coherence almost immediately and most of the XUV radiation is increasingly collimated towards the surface as the laser intensity ramps up.

The angular distribution of RIME is given by the emission angle of laser-accelerated relativistic electrons given by $\tan \theta = [2/(\gamma - 1)]^{1/2}$ [20]. For the electrons oscillating in the peak laser amplitude $\gamma \approx a_0$, the emission angle is therefore $\theta \approx 8.7° = 150$ mrad, which is in reasonable agreement with the XUV intensity distributions shown in Figs. 4(e) and 4(f), and the angular distribution of RIME for the case of $kL \approx 1$ shown in Fig. 5(b). The angular distribution shows clear separation between the high-frequency radiation emitted by ROM and RIME, which is also visible in the corresponding XUV intensity

distribution shown in Fig. 4(e). The temporal profile of XUV radiation for the two optimal cases is shown in Fig. 5(a). In correspondence with Fig. 4(e), the radiation pulse of the ROM-optimal case $L/\lambda_0 = 0.1$ shows initially coherent and smooth reflected wave profile at $t < 55$ fs, losing its coherence at $t = 55$ fs, and then transitioning to the RIME profile modulated by coherent attosecond bursts at $t > 55$ fs. The case of RIME-optimal scale length $L/\lambda_0 = 0.25$ shows that already at the beginning of interaction, $t < 55$ fs, the XUV pulse is modulated with
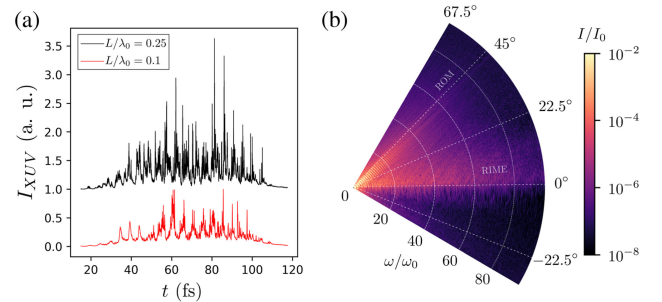
FIG. 5. (a) Temporal profile of XUV radiation for the case of RIME (black) and ROM (red) optimal scale length, offset for clarity. (b) Angular distribution of spectral intensity for ROM-optimal scale length $L/\lambda_0 = 0.1$. Color map is saturated for higher contrast in the XUV region.

the RIME bursts in accordance with Fig. 4(f). As the laser peak arrives at $t = 80$ fs, coherently enhanced giant attosecond XUV pulses emerge due to the strong electron nanobunching from the resonant plasma wave growth.

In conclusion, a new high-yield mechanism of coherent XUV light generation called RIME was discovered to occur during the interaction of relativistically intense P-polarized laser pulse with overdense plasma satisfying $1 \leq a_0 < n_e/n_c$. The radiation emission is directionally anomalous, propagating parallel to the mirror surface. With numerical and analytical methods, we have found that RIME occurs due to laser-driven oscillations of electron nanobunches which emerge from a return current instability induced by collisionless absorption of the incident laser. Furthermore, by varying the preplasma scale length, we have found that RIME is anticorrelated with the reflected high harmonics, showing the possibility to tune between two directionally separated XUV radiation sources in a single experimental configuration. Finally, we have found an optimal preplasma scale length for RIME corresponding to resonant growth of plasma waves at the mirror surface. The optimal XUV conversion efficiency of RIME reaches percent level, presenting a new approach for future experiments aiming to produce high-yield coherent XUV radiation.

---

[*] Corresponding author: marcel.lamac@eli-beams.eu

[1] W. Mori, C. Decker, and W. Leemans, Relativistic harmonic content of nonlinear electromagnetic waves in underdense plasmas, IEEE Trans. Plasma Sci. **21,** 110 (1993).

[2] U. Teubner and P. Gibbon, High-order harmonics from laser-irradiated plasma surfaces, Rev. Mod. Phys. **81,** 445 (2009).

[3] S. V. Bulanov, N. Naumova, and F. Pegoraro, Interaction of an ultrashort, relativistically strong laser pulse with an overdense plasma, Phys. Plasmas **1,** 745 (1994).

[4] H. Vincenti, S. Monchocé, S. Kahaly, G. Bonnaud, P. Martin, and F. Quéré, Optical properties of relativistic plasma mirrors, Nat. Commun. **5,** 3403 (2014).

[5] A. Pirozhkov, M. Kando, T. Z. Esirkepov, P. Gallegos, H. Ahmed, E. Ragozin, A. Y. Faenov, T. Pikuz, T. Kawachi, A. Sagisaka et al., Soft-x-ray harmonic comb from relativistic electron spikes, Phys. Rev. Lett. **108,** 135004 (2012).

[6] B. Dromey, D. Adams, R. Hörlein, Y. Nomura, S. Rykovanov, D. Carroll, P. Foster, S. Kar, K. Markey, P. McKenna et al., Diffraction-limited performance and focusing of high harmonics from relativistic plasmas, Nat. Phys. **5,** 146 (2009).

[7] M. Yeung, B. Dromey, S. Cousens, T. Dzelzainis, D. Kiefer, J. Schreiber, J. Bin, W. Ma, C. Kreuzer, J. Meyer-ter Vehn et al., Dependence of laser-driven coherent synchrotron emission efficiency on pulse ellipticity and implications for polarization gating, Phys. Rev. Lett. **112,** 123902 (2014).

[8] P. Heissler, R. Hörlein, J. M. Mikhailova, L. Waldecker, P. Tzallas, A. Buck, K. Schmid, C. Sears, F. Krausz, L. Veisz et al., Few-cycle driven relativistically oscillating plasma mirrors: A source of intense isolated attosecond pulses, Phys. Rev. Lett. **108,** 235003 (2012).

[9] N. M. Naumova, J. A. Nees, I. V. Sokolov, B. Hou, and G. A. Mourou, Relativistic generation of isolated attosecond pulses in a λ 3 focal volume, Phys. Rev. Lett. **92,** 063902 (2004).

[10] J. A. Wheeler, A. Borot, S. Monchocé, H. Vincenti, A. Ricci, A. Malvache, R. Lopez-Martens, and F. Quéré, Attosecond lighthouses from plasma mirrors, Nat. Photonics **6,** 829 (2012).

[11] O. Smirnova, Y. Mairesse, S. Patchkovskii, N. Dudovich, D. Villeneuve, P. Corkum, and M. Y. Ivanov, High harmonic interferometry of multi-electron dynamics in molecules, Nature (London) **460,** 972 (2009).

[12] R. Neutze, R. Wouts, D. Van der Spoel, E. Weckert, and J. Hajdu, Potential for biomolecular imaging with femtosecond x-ray pulses, Nature (London) **406,** 752 (2000).

[13] F. Krausz and M. Ivanov, Attosecond physics, Rev. Mod. Phys. **81,** 163 (2009).

[14] V. Nefedova, M. Albrecht, M. Kozlová, and J. Nejdl, Development of a high-flux XUV source based on high-order harmonic generation, J. Electron Spectrosc. Relat. Phenom. **220,** 9 (2017).

[15] C. M. Heyl, H. Coudert-Alteirac, M. Miranda, M. Louisy, K. Kovács, V. Tosa, E. Balogh, K. Varjú, A. L'Huillier, A. Couairon et al., Scale-invariant nonlinear optics in gases, Optica **3,** 75 (2016).

[16] G. A. Mourou, T. Tajima, and S. V. Bulanov, Optics in the relativistic regime, Rev. Mod. Phys. **78,** 309 (2006).

[17] A. Macchi, F. Cattani, T. V. Liseykina, and F. Cornolti, Laser acceleration of ion bunches at the front surface of overdense plasmas, Phys. Rev. Lett. **94,** 165003 (2005).

[18] T. Z. Esirkepov, Y. Sentoku, K. Mima, K. Nishihara, F. Califano, F. Pegoraro, N. Naumova, S. Bulanov, Y. Ueshima, T. Liseikina et al., Ion acceleration by superintense laser pulses in plasmas, J. Exp. Theor. Phys. Lett. **70,** 82 (1999).

[19] F. Brunel, Not-so-resonant, resonant absorption, Phys. Rev. Lett. **59,** 52 (1987).

[20] P. Gibbon, *Short Pulse Laser Interactions with Matter: An Introduction* (World Scientific, Singapore, 2005).

[21] T. Nakamura, S. Kato, H. Nagatomo, and K. Mima, Surface-magnetic-field and fast-electron current-layer formation by ultraintense laser irradiation, Phys. Rev. Lett. **93,** 265002 (2004).

[22] O. Buneman, Dissipation of currents in ionized media, Phys. Rev. **115,** 503 (1959).

[23] S. Bulanov and P. Sasorov, Tearing of a current sheet and reconnection of magnetic lines of force, Sov. J. Plasma Phys. **4,** 418 (1978).

[24] See Supplemental Material at http://link.aps.org/supplemental/10.1103/PhysRevLett.131.205001 for more details, which includes Refs. [25–27].

[25] T. Arber, K. Bennett, C. Brady, A. Lawrence-Douglas, M. Ramsay, N. Sircombe, P. Gillies, R. Evans, H. Schmitz,

A. Bell *et al.*, Contemporary particle-in-cell approach to laser-plasma modelling, Plasma Phys. Controlled Fusion **57,** 113001 (2015).

[26] J. D. Jackson, *Classical Electrodynamics* (John Wiley & Sons, New York, 1999).

[27] C. J. Hirschmugl, M. Sagurton, and G. P. Williams, Multi-particle coherence calculations for synchrotron-radiation emission, Phys. Rev. A **44**, 1316 (1991).

[28] S. Kahaly, S. Monchocé, H. Vincenti, T. Dzelzainis, B. Dromey, M. Zepf, P. Martin, and F. Quéré, Direct observation of density-gradient effects in harmonic generation from plasma mirrors, Phys. Rev. Lett. **110**, 175001 (2013).

[29] F. Dollar, P. Cummings, V. Chvykov, L. Willingale, M. Vargas, V. Yanovsky, C. Zulick, A. Maksimchuk, A. Thomas, and K. Krushelnick, Scaling high-order harmonic generation from laser-solid interactions to ultrahigh intensity, Phys. Rev. Lett. **110**, 175002 (2013).

[30] V. L. Ginzburg, *The Propagation of Electromagnetic Waves in Plasma* (Pergamon, New York, 1964).

[31] N. G. Denisov, On a singularity of the field of an electromagnetic wave propagated in an inhomogeneous plasma, Sov. Phys.—JETP **4**, 544 (1957), http://jetp.ras.ru/cgi-bin/e/index/e/4/4/p544?a=list.

B.2 Bright coherent attosecond X-ray pulses from beam-driven relativistic mirrors

The following article is reproduced from M. Lamač, P. Valenta, J. Nejdl, U. Chaulagain, T. M. Jeong and S. V. Bulanov (2024). Bright coherent attosecond X-ray pulses from beam-driven relativistic mirrors. *arXiv*, preprint arXiv:2403.03277.

Copyright © The Authors 2024.

Bright coherent attosecond X-ray pulses from beam-driven relativistic mirrors

Marcel Lamač[1,2*], Petr Valenta[1], Jaroslav Nejdl[1,3], Uddhab Chaulagain[1], Tae Moon Jeong[1], Sergei V. Bulanov[1,4]

[1*]ELI Beamlines Facility, Extreme Light Infrastructure ERIC, Za Radnicí 835, Dolní Břežany, 25241, Czech Republic.
[2]Faculty of Mathematics and Physics, Charles University, Ke Karlovu 3, Prague 2, 12116, Czech Republic.
[3]Faculty of Nuclear Sciences and Physical Engineering, Czech Technical University in Prague, Břehová 7, Prague 1, 11519, Czech Republic.
[4]Kansai Photon Science Institute, National Institutes for Quantum Science and Technology, 8-1-7 Umemidai, Kizugawa, Kyoto, 619-0215, Japan.

*Corresponding author(s). E-mail(s): marcel.lamac@eli-beams.eu;

Abstract

Bright ultrashort X-ray pulses allow scientists to observe ultrafast motion of atoms and molecules. Coherent light sources, such as the X-ray free electron laser (XFEL), enable remarkable discoveries in cell biology, protein crystallography, chemistry or materials science. However, in contrast to optical lasers, lack of X-ray mirrors demands XFELs to amplify radiation over a single pass, requiring tens or hundreds of meters long undulators to produce bright femtosecond X-ray pulses. Here, we propose a new ultrafast coherent light source based on laser reflection from a relativistic mirror driven by a relativistic charged particle beam in micrometer-scale plasma. We show that reflection of millijoule-level laser pulses from such mirrors can produce bright, coherent and bandwidth-tunable attosecond X-ray pulses with peak intensity and spectral brightness comparable to XFELs. In addition, we find that beam-driven relativistic mirrors are highly robust, with laser-induced damage threshold exceeding solid-state components by at least two orders of magnitude. Our results promise a new way for bright coherent attosecond X-ray pulse generation, suitable for unique applications in fundamental physics, biology and chemistry.

Keywords: attosecond pulse generation, coherent X-ray source, relativistic mirrors, laser-plasma interaction

The theory of light reflection from a moving mirror was presented by A. Einstein in his seminal work on theory of special relativity in 1905 [1]. As illustrated in Fig. 1b, an electromagnetic pulse reflected from a mirror counter-propagating at velocity v will undergo a frequency upshift, pulse compression and amplitude increase due to a double Doppler effect, which can be written as [1–4]

$$\frac{\omega_r}{\omega_0} = \frac{\tau_0}{\tau_r} = \frac{E_r}{rE_0} = \frac{1+\beta}{1-\beta}, \qquad (1)$$

where E_r, ω_r, τ_r and E_0, ω_0, τ_0 are respectively the electric field amplitude, angular frequency and pulse duration of reflected and incident radiation,

$\beta = v/c$ is the normalized mirror velocity, r is the complex amplitude reflection coefficient (see Supplementary Information S1 for definition and derivation details) and c is the speed of light in vacuum.

This concept promises a source of coherent electromagnetic radiation with unique properties. A relativistic mirror with tunable velocity could enable measurements with fundamentally limitless spatiotemporal resolution, an ultimate prospect for many novel applications, including spectroscopy and imaging of atomic, molecular, and electronic dynamics with attosecond resolution [5–8], laboratory astrophysics experiments [9] or experimental study of nonlinear properties of quantum vacuum and other topics of fundamental interest [10], such as investigating black hole information paradox with accelerating relativistic mirrors [11].

Most of these applications require a coherent light source with high brightness, which is currently offered mostly by the kilometers-long and access-limited X-ray free electron lasers (XFELs) [7, 8]. Recently, breakthroughs in shrinking free-electron lasers were achieved by using compact plasma accelerators to produce coherent radiation in the XUV [12, 13], UV [14] and infrared [15] spectral range. The next generation of coherent light sources should be compact, while ideally at the same time advancing some of the source characteristics, such as brightness, pulse duration or spectral tunability. Eq. 1 tells us that a robust, highly-reflective relativistic mirror with tunable velocity could satisfy all of these requirements.

The question of producing a relativisitic mirror has been a recurring topic, with reinvigorated interest today due to the availability of high-power lasers that enable its various implementations, see e.g. Refs. [3, 16, 17] (and the references cited therein) for review, with notable examples being the relativistic mirror formed by the plasma wake wave of a laser pulse propagating in underdense plasma [2, 18–23], the oscillating relativistic mirror driven by a laser on the surface of an overdense plasma target [24–29], or the relativistic mirror accelerated by the interaction of an intense laser with a thin solid target [30–32]. The numerous studies of laser-driven relativistic mirrors in the recent years have shown a growing maturity in the field, but none have demonstrated a robust mechanism for bright and highly-tunable coherent X-ray pulse generation.

Relativistic mirrors formed by nonlinear plasma waves driven by lasers propagating in underdense plasma [2, 18–23] are especially attractive. The velocity of the mirror is equal to the driving laser group velocity. Changing the velocity of such a mirror experimentally therefore requires only a simple variation in gas pressure. For the usual wavelength of high-power lasers, $\lambda_0 = 0.8\,\mu m$, the electron density n_e in a laser-driven nonlinear plasma wave can exceed the critical plasma density $n_c \approx 1.7 \times 10^{21}\,\mathrm{cm}^{-3}$, enabling coherent reflection for counter-propagating radiation as illustrated in Fig. 1a.

However, since an increase of laser group velocity equals decrease in background plasma density, the laser amplitude must be also increased to sustain sufficiently high electron density in plasma wave. This makes laser-driven mirrors sensitive to diffraction and laser instabilities, such as self-modulation or stimulated Raman scattering [33, 34], which can rapidly change the laser group velocity, breaking the mirror in process and trapping the oscillating plasma electrons which sustain the nonlinear plasma wave [35, 36]. These detrimental effects make tunable generation of bright coherent attosecond X-ray pulses challenging using laser-driven relativisic mirrors.

In this work, we propose a robust and highly-tunable relativistic mirror based on a large-amplitude nonlinear plasma wave driven by a relativistic charged (both positively and negatively) particle beam propagating in plasma. We show that charged particle beams can drive a highly-reflective and stable relativistic mirrors with well-defined velocity over a relatively long distance, unlocking generation of bright and fully-coherent attosecond X-ray pulses with intensity, bandwidth and peak spectral brightness comparable to XFELs in just a few micrometers.

Results

Relativistic mirrors driven by charged particle beams in plasma

We begin by presenting analytical theory for beam-driven relativistic mirrors. To describe relativistic mirrors based on beam-driven nonlinear
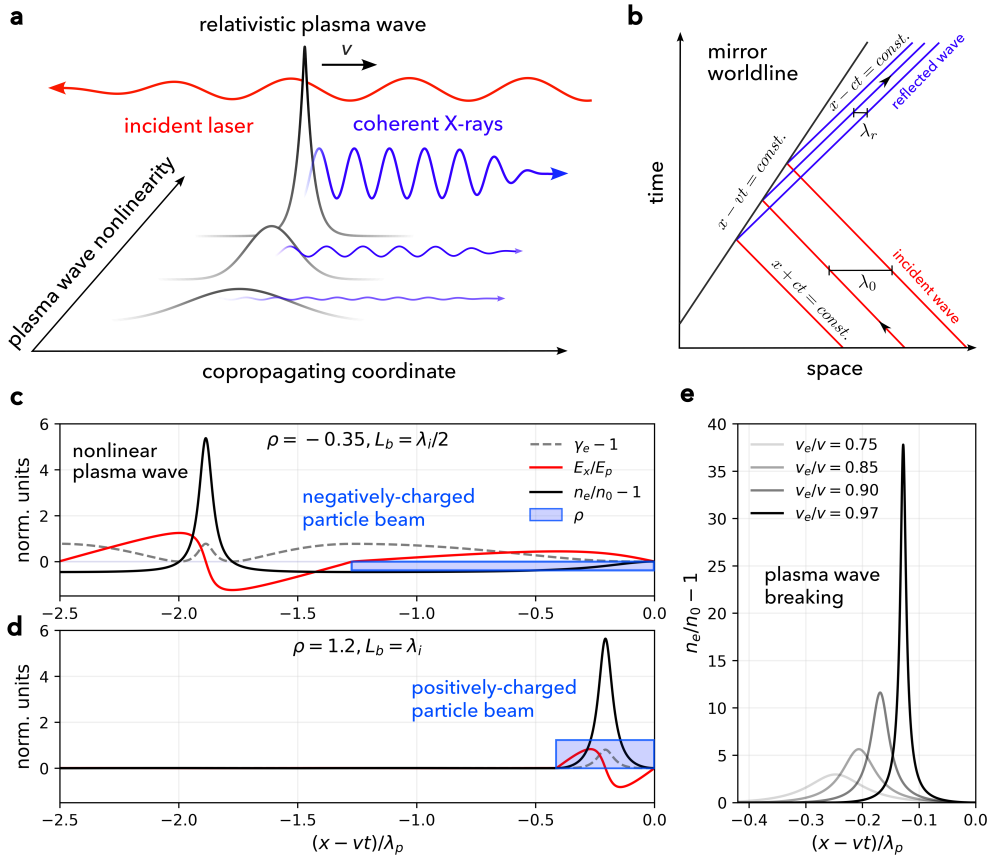
Fig. 1 Relativistic mirrors driven by charged particle beams in plasma. a, Schematic of a laser being reflected from a relativistic mirror formed by a propagating nonlinear plasma wave. Reflection coefficient increases with plasma wave nonlinearity, which increases the density of plasma electrons, with peak velocity v_e, which are catching up with the nonlinear wave, which propagates with velocity $v > v_e$. **b,** Diagram of radiation being fully reflected from a relativistic mirror propagating in spacetime with velocity v. At the reflection point, an electromagnetic wave undergoes a double Doppler effect, as illustrated by the wavefronts of incident (red) and reflected radiation (purple) given by constant wave-periodic values of the light-cone coordinates $x + ct$ and $x - ct$, where x, t are the space and time coordinates, respectively. **c, d,** Numerical solutions of Eq. 2, given in terms of the copropagating coordinate $x - vt$ normalized to the linear plasma wavelength λ_p, showing normalized electron density (black), longitudinal electric field (red) and Lorentz factor of plasma electrons (grey, dashed) driven by negatively (**c**) and positively (**d**) charged relativistic particle beams propagating in plasma with $\gamma = 5$. Normalized charge density of the driving beam ρ (blue, filled) is set according to Eq. 3 in both cases such that electron oscillations reach $\gamma_e = 1.4$, producing comparable nonlinear waves. Particle beam pulse length L_b is set according to Eq. 4 to drive resonant wake (negatively-charged beam, $L_b = \lambda_i/2$) and single-cycle interior (positively-charged beam, $L_b = \lambda_i$) plasma wave. **e,** Numerical solutions of Eq. 2, showing that a nonlinear plasma wave, driven by a relativistic charged particle beam with $\gamma = 5$, can be brought arbitrarily close to the wave breaking threshold by tuning beam density ρ according to Eq. 3.

plasma waves, we consider the one-dimensional approximation, which is justified for wide relativistic particle beams satisfying $k_p r_b \gg 1$, where $k_p = \omega_p/c$ is the plasma wave number, r_b is the radial size of the beam, $\omega_p = \left[e^2 n_0/(m_e \epsilon_0)\right]^{1/2}$ is the linear plasma frequency, n_0 is the background

electron plasma density, m_e is the electron mass, e is the elementary charge and ϵ_0 is the vacuum permittivity. The plasma waves driven by a charged particle beam can be described in terms of a copropagating coordinate $\xi = k_p(x - vt)$, where x is the space coordinate and t represents time, by

3

(see Supp. S2 for derivation details)

$$\frac{\partial^2 \phi}{\partial \xi^2} = \gamma^2 \left[\beta \left(1 - \frac{1}{\gamma^2(1+\phi)^2} \right)^{-1/2} - 1 \right] - \rho, \quad (2)$$

where ϕ is the electric potential normalized by mc^2/e, $\rho = qn_b/n_0$ is the normalized charge density of the driver, n_b is the driver particle density and q is the charge number of the driver, e.g. $q = -1$ for electrons or muons, $q = +1$ for protons or positrons and $q \geq 1$ for positively-charged ions.

We approximate the driver in the laboratory frame with a flat-top density profile, $\rho = $ const., normalized velocity β and pulse length L_b. Plasma waves obtained by solving Eq. 2 numerically for such a charged (negatively and positively) driver are shown in Fig. 1c, d. Highly-reflective large-amplitude electron density wave can be produced if the plasma wave is brought close to the threshold of wave breaking, where the electrons composing the plasma wave catch up with the driver, $v_e \to v$, or equivalently, $\gamma_e \to \gamma$. We solve Eq. 2 analytically and obtain the following maximum Lorentz factor of electrons composing the beam-driven plasma wave (see Supp. S3 for derivation details)

$$\gamma_e = 1 + \frac{2\rho^2\beta^2}{2\rho + 1 + (\rho/\gamma)^2}, \quad (3)$$

Solving Eq. 3 at the wave breaking threshold, $\gamma_e = \gamma$, we obtain the beam charge density which causes immediate plasma wave breaking, as $\rho_{wb,+} = \gamma$ for $q > 0$ and $\rho_{wb,-} = -\gamma/(2\gamma+1) \approx -1/2$ for $q < 0$. Therefore, to drive a large-amplitude density wave over any distance, the particle beam density must be initially set below the wave breaking threshold, as $\rho/\rho_{wb} < 1$.

Large-amplitude electron density waves can be excited close to the wave breaking threshold in the wake of a charged particle beam, but if the normalized beam charge density satisfies $\rho > -1/(1+\beta) \approx -1/2$, it can be excited also in its interior as shown in Fig. 1d. The following expression can be derived for the interior wave wavelength λ_i in the limit $\gamma \gg 1$ (see Supp. S4 for a more general form, valid for any γ, and derivation details)

$$\frac{\lambda_i}{\lambda_p} = \frac{2}{\pi} \frac{E\left[2\rho/(2\rho+1) \right]}{\sqrt{2\rho+1}}, \quad (4)$$

where $\lambda_p = 2\pi c/\omega_p$ is the linear plasma wave wavelength and $E(k)$ is the complete elliptic integral of the second kind. Eq. 4 shows that interior waves contract (for $\rho > 0$) and expand (for $\rho < 0$) with respect to the linear plasma wave. The pulse length L_b can be set to excite resonant nonlinear plasma wake wave when $L_b = (m - 1/2)\lambda_i$, or to excite multi-cycle interior plasma waves with no wake excitation when $L_b = m\lambda_i$, where m is a natural number (see Supp. S5 for derivation details). Interior plasma waves can therefore serve either as a single mirror, or a periodic train of relativistic mirrors, similarly to wake waves.

For $\rho \leq -1/(1+\beta) \approx -1/2$, the interior wave wavelength (4) diverges and no plasma oscillations occur in the beam interior. In such a case, large-amplitude density waves can occur only in the wake of a negatively-charged particle beam which has large enough pulse length, such that plasma electrons are accelerated throughout the beam interior up to $\gamma_e \approx \gamma$, which can be obtained by solving Eq. 2 numerically.

Beam-driven plasma waves close to the wave breaking threshold cannot propagate in plasma indefinitely. The longitudinal field of the interior plasma wave modulates the charged particle beam as it propagates. Eventually, the mirror breaks due to this relativistic beam-plasma instability. The distance L_{wb} traveled by the mirror before it breaks can be obtained as (see Supp. S6 for derivation details)

$$\frac{L_{wb}}{\lambda_p} \approx \frac{\gamma}{5} \left(\frac{M}{qm_e} \right)^{1/2} \left(1 - \frac{\rho}{\rho_{wb}} \right)^{1/2}, \quad (5)$$

where M is mass of the driver particles. Eq. 5 explicitly reiterates that the mirror propagates for any significant distance only when $\rho/\rho_{wb} < 1$. In this case, we see that the mirror can be set extremely resilient, since the breaking distance grows with driver velocity and particle mass, as $L_{wb} \approx \gamma(M/m)^{1/2}$. In the following, we show that tunability of the breaking distance of beam-driven relativistic mirrors is the key that unlocks tunable generation of extremely-bright attosecond X-ray pulses.

Coherent attosecond X-ray pulses

The most important parameter of a mirror is the reflection coefficient, r. According to Eq. 1, it

4
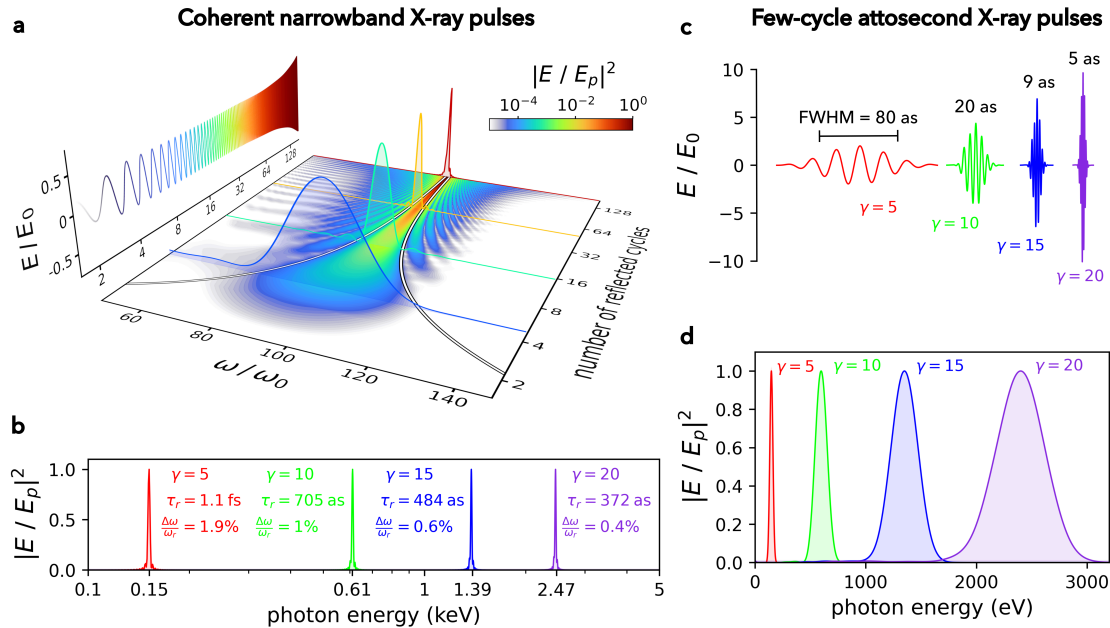
Fig. 2 PIC simulation results of attosecond X-ray pulses from beam-driven relativistic plasma mirrors.
a, Normalized energy spectrum evolution and temporal profile of reflected radiation obtained from PIC simulations for proton-driven relativistic mirror with $\gamma = 5$ propagating in underdense plasma with $n_0/n_c = 0.01$, where $n_c \approx 10^{21}$ cm^{-3} is the critical density for the incident laser wavelength 800 nm. Theoretical bandwidth (white lines, black outline) given by $\Delta\omega/\omega_r = 1/N$, where N is the number of reflected cycles. The inset shows temporal profile of reflected radiation corresponding to the time of spectral peak saturation. The temporal profile is colour-coded to the time (number of reflected cycles in) of corresponding normalized energy spectrum lineouts. **b**, Normalized energy spectrum of radiation reflected from relativistic mirrors driven in underdense plasma with $n_0/n_c = 0.08$ by protons with $\gamma \in \{5, 10, 15, 20\}$ and the incident laser amplitude $E_0 = 10^{-3} m_e c\omega_0/e$. The relative spectral bandwidths $\Delta\omega/\omega_r$ decrease with increasing γ due to increasing mirror propagation distance, given by Eq. 5. **c**, Temporal profile of attosecond X-ray pulses generated from beam-driven relativistic mirrors with $\gamma \in \{5, 10, 15\}$, $n_0/n_c = 0.08$ and incident laser pulse amplitude $E_0 = 0.1 m_e c\omega_0/e$. **d**, Corresponding energy spectra showing tunability from XUV to X-rays.

determines the reflected wave amplitude, but also the number of reflected X-ray photons, $N_{\gamma,r} = |r|^2 N_{\gamma,0}$, where $N_{\gamma,0}$ is the number of incident laser photons.

Reflection coefficient of beam-driven relativistic mirrors can be calculated as (see Supp. S7-S8 for derivation details)

$$r \approx 0.3 \left(\frac{n_0}{\gamma n_c}\right)^{2/3}, \qquad (6)$$

where $n_c = m_e \epsilon_0 \omega_0^2/e^2$ is the critical plasma density calculated for the incident laser with frequency ω_0. While $r \to 0$ as $\gamma \to \infty$, the reflected amplitude according to Eq. 1 follows $E_r/E_0 \approx 4\gamma^2 r \propto \gamma^{4/3}$ due to double Doppler

effect. The peak power of reflected radiation is therefore amplified as $P_r/P_0 \propto \gamma^{8/3}$. Using Eq. 1, we see that incident-to-reflected energy conversion efficiency also grows with mirror velocity, as $\eta = \mathcal{E}_r/\mathcal{E}_0 \propto \gamma^{2/3}$, where $\mathcal{E}_r$ and $\mathcal{E}_0$ are, respectively, the total energy of reflected and incident radiation. This is valid as long as the total reflected energy does not exceed total energy of the electrons composing the relativistic mirror, $N_{\gamma,r}\hbar\omega_r \ll N_e\gamma m_e c^2$ [22]. In the following section, the exact threshold is formulated in terms of maximum laser fluence incident on the relativistic mirror.

To evaluate our analytical results with self-consistent and energy-conserving numerical calculations, we have employed fully-relativistic

5

particle-in-cell (PIC) simulations. Here, we present the results of a relativistic mirror formed by the nonlinear interior plasma wave driven by a flat-top proton beam (see Methods for simulation details), as depicted in Fig. 1d, with varying mass-to-charge ratio considered in the next section. For the considered parameters, the minimum number of protons required in a beam would correspond to $N_p \approx \gamma n_0 \lambda_i^3 \approx 10^7$, which is well within the means of conventional accelerators, which can reach $N_p \approx 10^{11}$ [37–40]. To investigate bandwidth tunability of reflected radiation, we consider two different cases for the incident counter-propagating laser. A low-amplitude, narrowband continuous wave (CW) and a high-amplitude, broadband few-cycle pulse. In both cases, the central wavelength is $\lambda_0 = 0.8\,\mu m$.

Continuous wave. The spectrum evolution and the temporal profile of reflected radiation, for the case with $n_0/n_c = 0.01$ and $\gamma = 5$, are shown in Fig. 2a. The CW is upshifted in accordance with Eq. 1, $\omega_r/\omega_0 \approx 98$. The energy spectrum peak grows quadratically in time and saturates at the the mirror breaking distance L_{wb} with $N \approx 140$ reflected cycles and relative spectral bandwidth $\Delta\omega/\omega_r = 0.7\%$, where $\Delta\omega$ is the full-width at half-maximum (FWHM) of the reflected radiation energy spectrum.

The energy spectrum of a reflected continuous wave can be calculated analytically (see Supp. S9 for derivation) as $|E(\omega)|^2 = E_p^2 \, \mathrm{sinc}\,((\omega - \omega_r)\tau_r/2)$, where $E_p^2 = |E_r|^2 \tau_r^2$ is the spectral peak value and $\mathrm{sinc}(x) = \sin(x)/x$. The FWHM spectral bandwidth directly follows as $\Delta\omega \approx \omega_r/N$, where N is the number of reflected cycles. This is in accordance with the PIC results, which highlights that relative spectral bandwidth is conserved upon reflection from a stable beam-driven relativistic mirror, producing a pulse with properties given exactly by Eq. 1, up to the mirror breaking distance given by Eq. 5.

Fig. 2b shows normalized energy spectra saturated at the mirror breaking distance produced by proton beams, with $\gamma \in \{5, 10, 15, 20\}$ and $\rho = 0.96\rho_{wb}$, propagating in plasma with $n_0/n_c = 0.08$. While increasing background plasma density increases reflection coefficient, the number of reflected cycles drops, since the mirror breaks faster according to Eq. 5, as $L_{wb} \propto \lambda_p$. The fastest mirror with $\gamma = 20$ produces a fully-coherent

X-ray pulse with narrow bandwidth of $10\,eV$ centered at $2.47\,keV$, and pulse duration $\tau_r \approx 372\,as$ in accordance with Eq. 1.

Few-cycle pulses. To investigate the possibility of bright few-cycle X-ray pulse generation, we set a counter-propagating few-cycle pulse with Gaussian profile incident on the nonlinear wave with peak amplitude increased to $a_0 = 0.1$ and FWHM pulse duration $\tau_{\mathrm{FWHM}} = 3T_0 \approx 8\,fs$. Fig. 2c shows the temporal profiles of radiation reflected from relativistic mirrors with three different velocities. The fastest considered mirror, with $\gamma = 20$, reflects a bright coherent X-ray pulse, as short as $\tau_r = 5$ attoseconds, with energy centered around $2.4\,keV$ and peak electric field amplitude $E_r \approx 4\,TV/m$, corresponding to intensity of $I_r \approx 2.3 \times 10^{18}\,W/cm^2$, which is of the same order as XFELs [7]. Fig. 2d shows the corresponding normalized energy spectra. By changing the γ of the driver, the bright few-cycle pulses are tuned according to Eq. 1 from XUV to X-rays.

Such coherent attosecond X-ray pulses could serve as an extremely bright source for unique applications which require high brightness and short pulse durations at the same time, such as ultrafast coherent X-ray spectroscopy [41], nonlinear XUV spectroscopy [42, 43] or coherent diffractive imaging of biomolecules [44].

Properties of beam-driven relativistic mirrors and laser-induced damage threshold

Figs. 3a,b, show an excellent match between the reflected amplitude given by Eqs. 1,6, and the dependence of reflected peak amplitude on normalized background plasma density and mirror velocity obtained from PIC simulations.

Driver particle type. To investigate negatively-charged drivers, as well as to verify Eq. 5, we again simulated the case with a low-amplitude CW laser with $a_0 = 10^{-3}$, $n_0/n_c = 0.08$ and $\gamma = 5$ for protons, muons, their antiparticles, and also the case of $\gamma = 20$ for positrons. Positrons were set faster, because the breaking distance for $\gamma = 5$ is less than the laser wavelength, $L_{wb} \approx 0.7\lambda_0$. Similarly, the case of electron drivers is reserved for future study, since the computational requirements necessary to sufficiently resolve the entire elongated nonlinear wake, as well as reflected radiation for

6
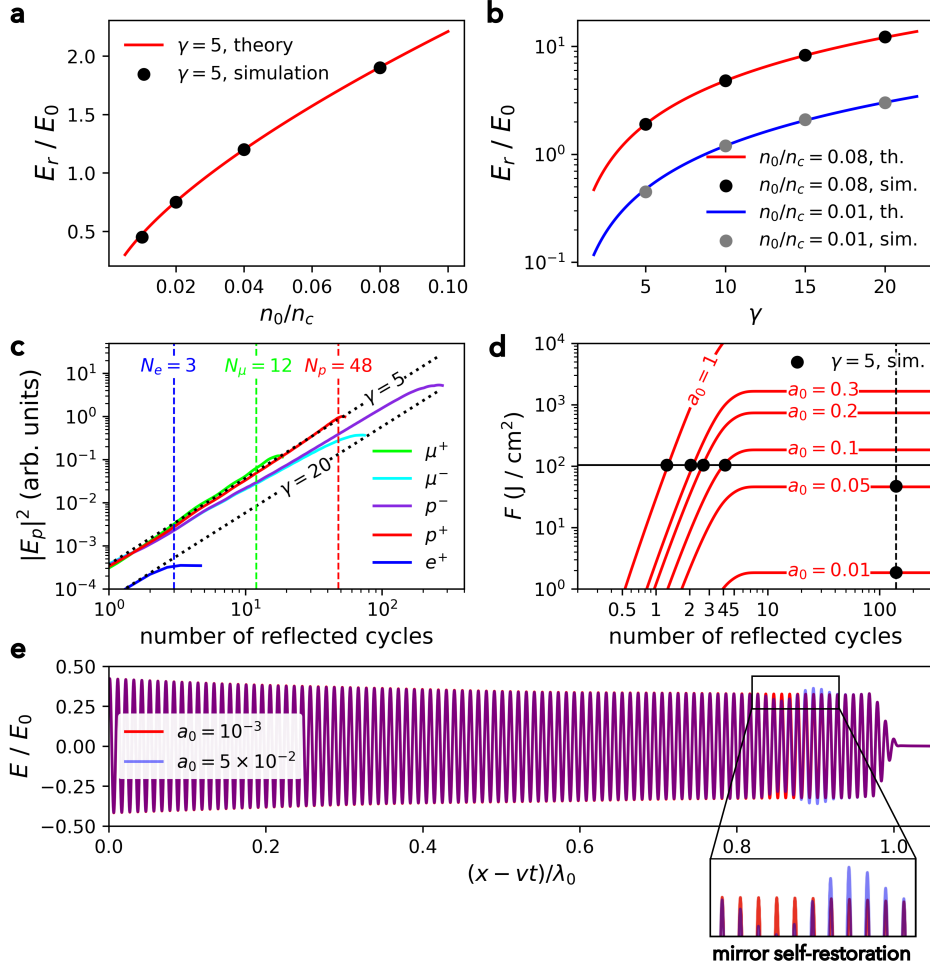
Fig. 3 Properties of beam-driven relativistic mirrors in plasma. Dependence of reflected amplitude on normalized background plasma density for $\gamma = 5$ (**a**), and driver Lorentz factor for $n_0/n_c \in \{0.01, 0.08\}$ (**b**). Theoretical curves are calculated from Eqs. 1,6. **c**, Evolution of energy spectrum peak E_p, in terms of number of reflected cycles, for various driver particle types. Theoretical curves are given by $|E_p|^2 \approx |E_r|^2 \tau_r^2$, which is calculated using Eqs. 1, 6 for $\gamma \in \{5, 20\}$ (dotted). The theoretical number of reflected cycles (vertical, dashed) predicted by Eq. 5 is calculated as $N \approx 2(L_{wb} - x_0)/\lambda_0$, where x_0 is the position where the counter-propagating laser initially collides with the mirror. For positrons, muons and protons we have set, respectively, $x_0/\lambda_0 \in \{1.3, 4, 7\}$. Lorentz factor for all particles is set as $\gamma = 5$, except for positrons where $\gamma = 20$. **d**, Evolution of optical fluence F incident on a relativistic mirror (red, solid) with $\gamma = 5$, $n_0/n_c = 0.01$ for various values of normalized laser amplitude. The theoretical value of laser-induced damage threshold (black, solid, horizontal) is given by Eq. 7 for $n_0/n_c = 0.01$, and the number of reflected cycles limited due to mirror breaking distance (black, dashed, vertical) is given by Eq. 5 as $N \approx 140$ for $x_0 = 17\lambda_0$. **e**, Temporal profile of coherent X-ray radiation from beam-driven relativistic mirror with $\gamma = 5$, $n_0/n_c = 0.01$ and $a_0 \in \{10^{-3}, 0.05\}$. The case of $a_0 = 0.05$ exhibits the self-restoration property of relativistic mirrors, where the fluence incident on the continuously replenishing nonlinear plasma wave saturates below the damage threshold, if the mirror restoration time t_r is short enough, which can be also seen in Fig. 3**d**.

$\gamma \geq 20$, are extremely demanding with standard numerical methods.

Fig. 3c shows the spectrum peak evolution for various drivers. The reflection coefficient for the negatively-charged beams is roughly 70% of the value given by Eq. 6, but the maximum number of reflected cycles can be up to 5 times larger when comparing antiprotons and protons. As shown in Figs. 1c,d, this is because stronger longitudinal interior wave modulates the positively-charged

7

drivers as they propagate. Therefore, irrespective of charge number, Eq. 5 can be interpreted as the minimum mirror propagation distance for a driving beam with particle mass M. The number of reflected cycles for the positron case is $N \approx 2.5$, in accordance with Eq. 5 for $M/m_e \approx 1, \gamma = 20$. This highlights the possibility for all-optical beam-driven relativistic mirrors, where positron or electron beams could be produced using compact laser wakefield accelerators [35, 45, 46].

Laser-induced damage threshold. Analogous to standard optical components, relativistic plasma mirrors are susceptible to laser-induced damage [22]. If the reflected energy is too large, damage can occur due to recoil of the mirror. This recoil threshold can be expressed in terms of maximum fluence on the relativistic mirror, also known as laser-induced damage threshold (LIDT)

$$\text{LIDT} = \kappa m_e c^2 \frac{n_0 \lambda_i}{8|r|^2 \gamma}. \tag{7}$$

Here, κ represents the coefficient of proportionality between the total reflected energy and the total energy of the electrons forming the mirror. Based on simulations with a_0 ranging from 10^{-3} to 1, we deduce that for beam-driven relativistic mirrors $\kappa \approx 6 \times 10^{-4}$. This yields LIDT ≈ 100 J/cm^2 for mirrors with $\gamma = 5$, which is two orders of magnitude higher compared to their solid-state counterparts [47, 48]. Fig. 3d compares the LIDT given by Eq. 7 and the threshold fluence obtained from simulations. Once the LIDT is exceeded, the number of reflected cycles with frequency given by Eq. 1 saturates, but the reflection process does not necessarily cease. However, the properties of reflected radiation may start to differ significantly from those obtained in regime well below the LIDT [22].

Furthermore, since beam-driven relativistic mirrors are composed of electrons continuously flowing through, the mirrors possess the ability to self-restore, with a characteristic restoration time of $t_r \approx \lambda_i/c\beta$. The restoration time is particularly short (a few fs) for the mirrors realized by interior waves, given their substantially shorter wavelengths compared to wake waves. Self-restoration must be taken into account when assessing the limits of applicability of Eq. 7, i.e., even if the fluence accumulated over a period of time $\gg t_r$ exceeds the LIDT, the mirror properties remain unaffected, as the impact of laser is fully compensated by the mirror restoration process. The onset of self-restoration is highlighted for the case of $a_0 = 0.05$ in Figs. 3e, where the mirror restoration time is calculated as approximately four laser cycles. The mirror replenishes completely before it is damaged, leading to effective saturation of fluence on the mirror and significantly more reflected cycles than predicted by Eq. 7, as shown in Fig. 3d for $a_0 \in \{0.01, 0.05\}$.

To summarize, if the time over which the incident laser deposits damage threshold fluence given by Eq. 7 is much larger than the mirror restoration time, the mirror will self-restore and continue to produce phase and amplitude stable coherent X-ray radiation. Therefore, large-amplitude few-cycle laser pulses should be used to maximize amplitude of reflected radiation, whereas smaller values of a_0 should be considered for a narrowband attosecond X-ray source.

Peak brightness and energy conversion efficiency

The figure-of-merit for coherent light sources is the peak spectral brightness, $\mathcal{B}$ [7, 49]. For coherent X-ray pulses from beam-driven relativistic mirrors, it can be derived as (see Supp. S10 for details)

$$\mathcal{B} \left[\frac{\text{photons}}{\text{s mm}^2 \text{ mrad}^2 \text{ 0.1\% BW}} \right] = \frac{32c\gamma^6 N_{\gamma,i} |r|^2}{10^{15}\lambda_0^3}$$
$$\approx 5 \times 10^{30} \gamma^4 \left(\frac{n_0}{n_c} \right)^{4/3} \lambda_0^{-4}[\mu\text{m}]\mathcal{E}_0[\text{J}], \tag{8}$$

where $\mathcal{E}_0$ is the energy of the incident laser pulse. Fig. 4a compares Eq. 8 with PIC simulation results and the peak spectral brightness of other currently available coherent light sources [7]. The simulations correspond to background density $n_0/n_c = 0.08$, proton-driven mirror with $\gamma \in \{5, 10, 15, 20\}$ and incident laser pulse with energy of 10 mJ. At photon energy of 2.5 keV, the peak brightness obtained is $\mathcal{B} \approx 10^{33}$ photons/(s mm^2 mrad^2 0.1% BW). Fig. 4b compares the theoretical conversion efficiency obtained from Eqs. 1,6 as $\eta \approx 0.36 \, (n_0/n_c)^{4/3} \gamma^{2/3}$ to the PIC simulation results. In accordance, conversion efficiency grows with mirror velocity, up to $\eta \approx 9\%$ at 2.5 keV.

8
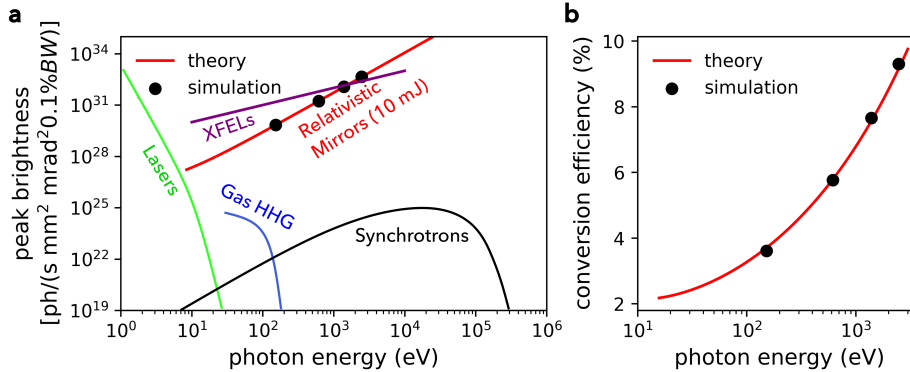
Fig. 4 Properties of coherent X-ray light from beam-driven relativistic mirrors. a, Peak spectral brightness of 10 mJ laser pulse reflected from beam-driven relativistic mirrors propagating with $\gamma \in \{5, 10, 15, 20\}$ (black dots) in plasma with normalized electron density $n_0/n_c = 0.08$. Data for other light sources taken from [8]. **b,** Incident-to-reflected laser energy conversion efficiency for $n_0/n_c = 0.08$. Different photon energies correspond respectively to different mirror velocities, $\gamma \in \{5, 10, 15, 20\}$.

Beam-driven relativistic mirrors have the potential to be one of the most efficient sources of bright coherent X-ray radiation. Indeed, as long as the maximum fluence on the self-restoring relativistic mirror does not exceed LIDT given by Eq. 7, reflected radiation properties are defined by Eqs. 1,6, and conversion efficiency increases with reflected photon energy. In this case, beam-driven relativistic mirrors could even realize a novel scheme for laser energy amplification, since $\eta > 1$ for $\gamma > 4.63 \, (n_c/n_0)^2$.

Discussion

We have presented a new way for generation of bright coherent attosecond X-ray pulses based on laser reflection from relativistic mirrors driven by charged particle beams in plasma.

In excellent agreement with presented theory, simulation results show that beam-driven relativistic mirrors enable extremely efficient generation of bright, tunable and coherent attosecond X-ray pulses, with simulations showing peak spectral brightness up to $\mathcal{B} \approx 10^{33}$ photons/(s mm² mrad² 0.1% BW) at X-ray photon energy of 2.5 keV, which is of the order of X-ray free electron lasers. Furthermore, reflectivity of beam-driven relativistic mirrors is robust with respect to mass of the driving particles, differing only in mirror propagation distance, which highlights the possibility for compact all-optical

beam-driven relativistic mirrors based on laser wakefield accelerated electron or positron beams.

The coherent attosecond X-ray pulses are found to be generated over a distance of few micrometers, facilitating a compact source for novel applications where both high intensity and ultrashort pulse pulse duration are required, such as coherent nonlinear X-ray spectroscopy or coherent diffractive imaging of biomolecules.

Finally, we have found the laser-induced damage threshold of beam-driven relativistic mirrors to be at least two orders of magnitude higher than optical solid-state components. The relativistic mirrors carry a unique property, where the mirror is not damaged unless the threshold fluence accumulates faster than the mirror replenishes itself. In this case, beam-driven relativistic mirrors could be even used as a novel scheme for laser energy amplification.

Methods

Particle-In-Cell simulations

We carried out fully-relativistic 1D3V (one spatial and three velocity dimensions) particle-in-cell (PIC) simulations using the code EPOCH [50]. The parameters of the PIC simulations are defined as follows: The driving particle beams have flat-top profile with length L_b, particle mass $M/m_e \in \{1, 207, 1836\}$, charge density ρ, and the Lorentz factor is varied as $\gamma \in \{5, 10, 15, 20\}$.

9

For positively-charged drivers, $L_b = \lambda_i$ and $\rho = 0.96\,\rho_{wb,+} = 0.96\gamma$, i.e., slightly below the wavebreaking threshold in order to ensure high reflectivity over sufficiently long distance according to Eq. 5. For negatively-charged drivers, resolving the full interior plasma wave in addition to the wakefield and the reflected wavelength proved computationally challenging. To reduce the necessary simulation box length required to observe beam-driven wake wave breaking, we shrunk the pulse length and set the particle number density of the driver slightly above the wavebreaking threshold, according to $\rho = -1/2 < \rho_{wb,-} = -\gamma/(2\gamma + 1)$. The pulse length required to achieve wake wave breaking at $\gamma = 5$ was then obtained by numerically solving Eq. 2, as $L_b \approx 10.7\,c/\omega_p$. The pulse length was then correspondingly set slightly below this wave breaking threshold, as $0.96\,L_b$, for the same reasons as in the case of positively-charged drivers.

The driving particle beam propagates in a pre-ionized homogeneous plasma with number density n_0, where $n_0/n_c \in \{0.01, 0.02, 0.04, 0.08\}$. Here, n_c stands for the critical plasma density corresponding to the wavelength of the counter-propagating laser pulse $\lambda_0 = 800$ nm. The laser pulse has flat-top profile with smooth $4\,T_0$ long up-ramp, where $T_0 = \lambda_0/c \approx 2.66$ fs is the laser period, and its normalized amplitude a_0 is varied from 10^{-3} to 1. For the case of a few-cycle Gaussian laser pulse, we have set $a_0 = 0.1$ for all simulations.

The simulations utilize moving window technique; the window, which moves at the velocity of the driving particle beam, has length of $3\,L_b$. The underlying Cartesian grid is uniform with the resolution of 100 cells per analytically calculated wavelength of the reflected radiation. The plasma is cold and collisionless, represented with electron quasi-particles moving on the static neutralizing background. Initially, there are 10 electron quasi-particles per grid cell. The electromagnetic field evolution is calculated using the 2nd order finite-difference time-domain method, whereas the equations of motion for quasi-particles are solved using the Boris algorithm. Absorbing boundary conditions are applied on each of the simulation window boundaries for both the electromagnetic fields and quasi-particles.

Data Availability

The data that support the findings of this study are available from the corresponding author upon reasonable request.

Code Availability

Numerical PIC simulations were performed with the open source massively parallelized PIC code EPOCH, available at https://github.com/Warwick-Plasma/epoch. Data analysis and visualization were done using open-source programming language Python and commercial software Wolfram Mathematica. Code used in this study is available from the corresponding author upon reasonable request.

References

[1] Einstein, A.: Zur elektrodynamik bewegter körper. Annalen der physik **4** (1905)

[2] Bulanov, S.V., Esirkepov, T., Tajima, T.: Light intensification towards the schwinger limit. Physical review letters **91**(8), 085001 (2003)

[3] Bulanov, S.V., Esirkepov, T.Z., Kando, M., Pirozhkov, A.S., Rosanov, N.N.: Relativistic mirrors in plasmas. novel results and perspectives. Physics-Uspekhi **56**(5), 429 (2013)

[4] Esirkepov, T.Z., Bulanov, S.V.: Luminal mirror. Phys. Rev. E **109**, 023202 (2024) https://doi.org/10.1103/PhysRevE.109.L023202

[5] Krausz, F., Ivanov, M.: Attosecond physics. Reviews of modern physics **81**(1), 163 (2009)

[6] Neutze, R., Wouts, R., Spoel, D., Weckert, E., Hajdu, J.: Potential for biomolecular imaging with femtosecond x-ray pulses. Nature **406**(6797), 752–757 (2000)

[7] O'Shea, P.G., Freund, H.P.: Free-electron lasers: Status and applications. Science **292**(5523), 1853–1858 (2001)

[8] Boutet, S., Fromme, P., Hunter, M.S.: X-ray Free Electron Lasers. Springer

[9] Bulanov, S., Esirkepov, T.Z., Kando, M., Koga, J., Kondo, K., Korn, G.: On the problems of relativistic laboratory astrophysics and fundamental physics with super powerful lasers. Plasma Physics Reports **41**, 1–51 (2015)

[10] Mourou, G.A., Tajima, T., Bulanov, S.V.: Optics in the relativistic regime. Reviews of modern physics **78**(2), 309 (2006)

[11] Chen, P., Mourou, G.: Accelerating plasma mirrors to investigate the black hole information loss paradox. Physical review letters **118**(4), 045001 (2017)

[12] Wang, W., Feng, K., Ke, L., Yu, C., Xu, Y., Qi, R., Chen, Y., Qin, Z., Zhang, Z., Fang, M., *et al.*: Free-electron lasing at 27 nanometres based on a laser wakefield accelerator. Nature **595**(7868), 516–520 (2021)

[13] Malaca, B., Pardal, M., Ramsey, D., Pierce, J., Weichman, K., Andriyash, I., Mori, W., Palastro, J., Fonseca, R., Vieira, J.: Coherence and superradiance from a plasma-based quasiparticle accelerator. Nature Photonics **18**(1), 39–45 (2024)

[14] Labat, M., Cabadağ, J.C., Ghaith, A., Irman, A., Berlioux, A., Berteaud, P., Blache, F., Bock, S., Bouvet, F., Briquez, F., *et al.*: Seeded free-electron laser driven by a compact laser plasma accelerator. Nature Photonics **17**(2), 150–156 (2023)

[15] Pompili, R., Alesini, D., Anania, M., Arjmand, S., Behtouei, M., Bellaveglia, M., Biagioni, A., Buonomo, B., Cardelli, F., Carpanese, M., *et al.*: Free-electron lasing with compact beam-driven plasma wakefield accelerator. Nature **605**(7911), 659–662 (2022)

[16] Kando, M., Esirkepov, T.Z., Koga, J.K., Pirozhkov, A.S., Bulanov, S.V.: Coherent, short-pulse x-ray generation via relativistic flying mirrors. Quantum Beam Science **2**(2), 9 (2018)

[17] Teubner, U., Gibbon, P.: High-order harmonics from laser-irradiated plasma surfaces. Reviews of Modern Physics **81**(2), 445 (2009)

[18] Kando, M., Fukuda, Y., Pirozhkov, A., Ma, J., Daito, I., Chen, L.-M., Esirkepov, T.Z., Ogura, K., Homma, T., Hayashi, Y., *et al.*: Demonstration of laser-frequency upshift by electron-density modulations in a plasma wakefield. Physical review letters **99**(13), 135001 (2007)

[19] Pirozhkov, A., Ma, J., Kando, M., Esirkepov, T.Z., Fukuda, Y., Chen, L.-M., Daito, I., Ogura, K., Homma, T., Hayashi, Y., *et al.*: Frequency multiplication of light back-reflected from a relativistic wake wave. Physics of Plasmas **14**(12), 123106 (2007)

[20] Kando, M., Pirozhkov, A., Kawase, K., Esirkepov, T.Z., Fukuda, Y., Kiriyama, H., Okada, H., Daito, I., Kameshima, T., Hayashi, Y., *et al.*: Enhancement of photon number reflected by the relativistic flying mirror. Physical review letters **103**(23), 235003 (2009)

[21] Moghadasin, H., Niknam, A.R., Komaizi, D., Banjafar, M.: Attosecond pulse generation by relativistic flying mirrors in laser-plasma interaction: Effect of plasma density and driver amplitude on the generated pulse. Physics of Plasmas **26**(9), 093105 (2019)

[22] Valenta, P., Esirkepov, T.Z., Koga, J., Pirozhkov, A., Kando, M., Kawachi, T., Liu, Y.-K., Fang, P., Chen, P., Mu, J., *et al.*: Recoil effects on reflection from relativistic mirrors in laser plasmas. Physics of Plasmas **27**(3), 032109 (2020)

[23] Mu, J., Esirkepov, T.Z., Valenta, P., Gu, Y., Jeong, T.M., Pirozhkov, A.S., Koga, J.K., Kando, M., Korn, G., Bulanov, S.V.: Relativistic flying forcibly oscillating reflective diffraction grating. Physical Review E **102**(5), 053202 (2020)

[24] Bulanov, S.V., Naumova, N., Pegoraro, F.: Interaction of an ultrashort, relativistically strong laser pulse with an overdense plasma. Physics of Plasmas **1**(3), 745–757 (1994)

[25] Lichters, R., Meyer-ter-Vehn, J., Pukhov,

A.: Short-pulse laser harmonics from oscillating plasma surfaces driven at relativistic intensity. Physics of Plasmas **3**(9), 3425–3437 (1996)

[26] Vincenti, H.: Achieving extreme light intensities using optically curved relativistic plasma mirrors. Physical review letters **123**(10), 105001 (2019)

[27] Quéré, F., Vincenti, H.: Reflecting petawatt lasers off relativistic plasma mirrors: a realistic path to the schwinger limit. High Power Laser Science and Engineering **9**, 6 (2021)

[28] Chopineau, L., Blaclard, G., Denoeud, A., Vincenti, H., Quéré, F., Haessler, S.: Sublaser-cycle control of relativistic plasma mirrors. Physical Review Research **4**(1), 012030 (2022)

[29] Lamač, M., Mima, K., Nejdl, J., Chaulagain, U., Bulanov, S.V.: Anomalous relativistic emission from self-modulated plasma mirrors. Phys. Rev. Lett. **131**, 205001 (2023) https://doi.org/10.1103/PhysRevLett.131.205001

[30] Kulagin, V.V., Cherepenin, V.A., Hur, M.S., Suk, H.: Theoretical investigation of controlled generation of a dense attosecond relativistic electron bunch from the interaction of an ultrashort laser pulse with a nanofilm. Physical review letters **99**(12), 124801 (2007)

[31] Kiefer, D., Yeung, M., Dzelzainis, T., Foster, P., Rykovanov, S., Lewis, C.L., Marjoribanks, R., Ruhl, H., Habs, D., Schreiber, J., *et al.*: Relativistic electron mirrors from nanoscale foils for coherent frequency upshift to the extreme ultraviolet. Nature communications **4**(1), 1763 (2013)

[32] Ma, W., Bin, J., Wang, H., Yeung, M., Kreuzer, C., Streeter, M., Foster, P., Cousens, S., Kiefer, D., Dromey, B., *et al.*: Bright subcycle extreme ultraviolet bursts from a single dense relativistic electron sheet. Physical Review Letters **113**(23), 235002 (2014)

[33] Gibbon, P.: Short Pulse Laser Interactions with Matter: an Introduction. World Scientific, 2005

[34] Kruer, W.: The Physics of Laser Plasma Interactions. CRC Press, 2019

[35] Esarey, E., Schroeder, C.B., Leemans, W.P.: Physics of laser-driven plasma-based electron accelerators. Reviews of modern physics **81**(3), 1229 (2009)

[36] Bulanov, S., Pegoraro, F., Pukhov, A., Sakharov, A.: Transverse-wake wave breaking. Physical review letters **78**(22), 4205 (1997)

[37] Muggli, P., Adli, E., Apsimon, R., Asmus, F., Baartman, R., Bachmann, A.-M., Marin, M.B., Batsch, F., Bauche, J., Olsen, V.B., *et al.*: Awake readiness for the study of the seeded self-modulation of a 400 gev proton bunch. Plasma Physics and Controlled Fusion **60**(1), 014046 (2017)

[38] Verra, L., Della Porta, G.Z., Pucek, J., Nechaeva, T., Wyler, S., Bergamaschi, M., Senes, E., Guran, E., Moody, J., Kedves, M., *et al.*: Controlled growth of the self-modulation of a relativistic proton bunch in plasma. Physical review letters **129**(2), 024802 (2022)

[39] Caldwell, A., Lotov, K., Pukhov, A., Simon, F.: Proton-driven plasma-wakefield acceleration. Nature Physics **5**(5), 363–367 (2009)

[40] Lotov, K.: Simulation of proton driven plasma wakefield acceleration. Physical Review Special Topics-Accelerators and Beams **13**(4), 041301 (2010)

[41] Ju, G., Xu, D., Highland, M.J., Thompson, C., Zhou, H., Eastman, J.A., Fuoss, P.H., Zapol, P., Kim, H., Stephenson, G.B.: Coherent x-ray spectroscopy reveals the persistence of island arrangements during layer-by-layer growth. Nature Physics **15**(6), 589–594 (2019)

[42] Bencivenga, F., Cucini, R., Capotondi, F., Battistoni, A., Mincigrucci, R., Giangrisostomi, E., Gessini, A., Manfredda, M., Nikolov, I., Pedersoli, E., *et al.*: Four-wave mixing experiments with extreme ultraviolet

transient gratings. Nature **520**(7546), 205–208 (2015)

[43] Fidler, A.P., Camp, S.J., Warrick, E.R., Bloch, E., Marroux, H.J., Neumark, D.M., Schafer, K.J., Gaarde, M.B., Leone, S.R.: Nonlinear xuv signal generation probed by transient grating spectroscopy with attosecond pulses. Nature communications **10**(1), 1384 (2019)

[44] Chapman, H.N., Fromme, P., Barty, A., White, T.A., Kirian, R.A., Aquila, A., Hunter, M.S., Schulz, J., DePonte, D.P., Weierstall, U., *et al.*: Femtosecond x-ray protein nanocrystallography. Nature **470**(7332), 73–77 (2011)

[45] Corde, S., Adli, E., Allen, J., An, W., Clarke, C., Clayton, C., Delahaye, J., Frederico, J., Gessner, S., Green, S., *et al.*: Multi-gigaelectronvolt acceleration of positrons in a self-loaded plasma wakefield. Nature **524**(7566), 442–445 (2015)

[46] Terzani, D., Benedetti, C., Bulanov, S.S., Schroeder, C.B., Esarey, E.: Compact, all-optical positron production and collection scheme. Physical Review Accelerators and Beams **26**(11), 113401 (2023)

[47] Gallais, L., Commandré, M.: Laser-induced damage thresholds of bulk and coating optical materials at 1030 nm, 500 fs. Applied optics **53**(4), 186–196 (2014)

[48] Willemsen, T., Chaulagain, U., Havlíčková, I., Borneis, S., Ebert, W., Ehlers, H., Gauch, M., Groß, T., Kramer, D., Laštovička, T., *et al.*: Large area ion beam sputtered dielectric ultrafast mirrors for petawatt laser beamlines. Optics Express **30**(4), 6129–6141 (2022)

[49] Attwood, D., Sakdinawat, A.: X-Rays and Extreme Ultraviolet Radiation: Principles and Applications, 2nd edn. Cambridge University Press, 2017

[50] Arber, T., Bennett, K., Brady, C., Lawrence-Douglas, A., Ramsay, M., Sircombe, N., Gillies, P., Evans, R., Schmitz, H., Bell, A., *et al.*: Contemporary particle-in-cell approach to laser-plasma modelling. Plasma Physics and Controlled Fusion **57**(11), 113001 (2015)

Acknowledgements

Author Information

Affiliations

ELI Beamlines Facility, Extreme Light Infrastructure ERIC, Za Radnicí 835, Dolní Břežany, 25241, Czech Republic

Marcel Lamač, Petr Valenta, Uddhab Chaulagain, Jaroslav Nejdl, Tae-Moon Jeong and Sergei V. Bulanov

Faculty of Mathematics and Physics, Charles University, Ke Karlovu 3, Prague 2, 12116, Czech Republic

Marcel Lamač

Faculty of Nuclear Sciences and Physical Engineering, Czech Technical University in Prague, Břehová 7, Prague 1, 11519, Czech Republic

Jaroslav Nejdl

Kansai Photon Science Institute, National Institutes for Quantum Science and Technology, 8-1-7 Umemidai, Kizugawa, 619-0215, Kyoto, Japan

Sergei V. Bulanov

Contributions

M.L. conceived the research, derived the analytical results and calculated numerical solutions, P.V. performed the particle-in-cell simulations, M.L. and P.V performed analysis of the simulations, processed the data, produced the figures and wrote the manuscript. U.C., J.N., T.M.J. and S.V.B. provided feedback, oversaw and helped to shape the research and the manuscript. All authors reviewed the final manuscript.

Corresponding Author

Correspondence to Marcel Lamač.

Ethics Declaration

Competing Interests

The authors declare no competing interests.

Bright coherent attosecond X-ray pulses from beam-driven relativistic mirrors (Supplementary Information)

Marcel Lamač[1,2*], Petr Valenta[1], Jaroslav Nejdl[1,3], Uddhab Chaulagain[1], Tae Moon Jeong[1], Sergey V. Bulanov[1,4]

[1*]ELI Beamlines Facility, Extreme Light Infrastructure ERIC, Za Radnicí 835, Dolní Břežany, 25241, Czechia.
[2]Faculty of Mathematics and Physics, Charles University, Ke Karlovu 3, Prague 2, 12116, Czechia.
[3]Faculty of Nuclear Science and Physical Engineering, Czech Technical University in Prague, Břehová 7, Prague 1, 11519, Czechia.
[4]Kansai Photon Science Institute, National Institutes for Quantum and Radiological Science and Technology, 8-1-7 Umemidai, Kizugawa, Kyoto, 619-0215, Japan.

*Corresponding author(s). E-mail(s): marcel.lamac@eli-beams.eu;

Contents

1 Theory of weak reflection from relativistic mirrors

Combining Maxwell's equations and using the Lorenz gauge condition $\partial_\mu A^\mu = \nabla \cdot \mathbf{A} + \partial_t \phi / c^2 = 0$, we obtain the inhomogenous wave equation

$$\left(\frac{\partial^2}{\partial t^2} - c^2 \nabla^2 \right) \mathbf{A} = \frac{\mathbf{j}}{\epsilon_0}, \qquad (1)$$

where $\mathbf{A}$ is the magnetic vector potential, ϵ_0 is the vacuum permittivity and $\mathbf{j}$ is the current density, acting as a source of radiation. We consider only the one-dimensional geometry of a planar mirror, with a counter-propagating incident laser. Therefore, we have for the transverse derivatives $\partial_y \mathbf{A} = \partial_z \mathbf{A} = 0$. To further simplify the analysis, we consider only linear polarization in the y direction and define the dimensionless vector potential $\mathbf{a} = e\mathbf{A}/m_e c$, reducing Eq. 1 into a scalar form. We assume that the radiative currents are due to a propagating electron distribution oscillating in electromagnetic field, therefore $j = -en_e v = -ecn_e a / \gamma$, where γ is the Lorentz factor of the plasma electrons, which gives us the one-dimensional Klein-Gordon equation describing propagation of electromagnetic waves in plasma

$$\left(\frac{\partial^2}{\partial t^2} - c^2 \frac{\partial^2}{\partial x^2} + \omega_p^2(x,t) \right) a(x,t) = 0, \qquad (2)$$

where $\omega_p = \sqrt{e^2 n_e(x,t)/(m_e \epsilon_0 \gamma)}$ is the relativistic plasma frequency and $n_e(x,t)$ is the electron density distribution propagating with normalized velocity $\beta = v/c = \sqrt{1 - (1/\gamma)^2}$. Counter-propagating radiation scattered from such a relativistic electron distribution is Doppler shifted in frequency, which makes analysis of Eq. 2 a nontrivial task in the laboratory frame. We therefore perform a Lorentz boost into the mirror reference frame where both incident and reflected radiation have the same frequency ω'. The x coordinate then transforms as $x' = \gamma(x - vt)$. Since the operator $\Box = (\partial_t^2 - c^2 \partial_x^2)$ is Lorentz-invariant, the form of the equation doesn't change and it can be written in the mirror reference frame as

$$\left(\frac{\partial^2}{\partial t'^2} - c^2 \frac{\partial^2}{\partial x'^2} + \omega_p'^2(x') \right) a(x',t') = 0, \quad (3)$$

where the apostrophe denotes quantities transformed to the mirror rest frame. The normalized vector potential is transformed only in coordinates, because the normalized amplitude ($a_0 \propto E_0/\omega_0$) is Lorentz-invariant.

For clarity of the following rest frame analysis, we drop apostrophes for all the transformed variables and return them when necessary. The solution to Eq. 3 can be written generally as a superposition of the incident and reflected waves

$$a(x,t) = a_0 e^{-i(\omega t + kx - \frac{\pi}{2})} + a_r(x,t), \qquad (4)$$

where ω is the radiation frequency and $k = \omega/c$ is the wave number, both evaluated in the mirror rest frame. We include the phase factor $\pi/2$ so that the real part of the incident wave corresponds to a sine wave, such that the real part of the incident wave is zero at spacetime origin $x = ct = 0$. Plugging (4) into (3) while assuming small reflection, $a_r(x,t) \ll a_0 \approx const.$, gives us the following equation for the reflected wave

$$\left(\frac{\partial^2}{\partial t^2} - c^2 \frac{\partial^2}{\partial x^2} \right) a_r(x,t) = -i\omega_p^2(x)a_0 e^{-i(\omega t + kx)}. \tag{5}$$

We note that the approximation of weak reflection is equivalent to the physically reasonable assumption that the electrons oscillate with the same phase and normalized transverse momentum as the incident wave, $j = -(ecn_e a_0/\gamma)e^{-i(\omega t + kx - \frac{\pi}{2})}$. The incident wave $a_0(x,t)$ then represents a homogeneous solution to the differential equation 1, while the particular solution $a_r(x,t)$ is obtained by solving Eq. 1 with the approximated current.

The natural coordinate system for this problem are the light-cone coordinates $\xi = x - ct, \eta = x + ct$, which correspond to a clockwise $\pi/4$ rotation of the spacetime coordinate system. The derivatives transform as $\partial_t + c\partial_x = 2c\partial_\eta$ and $\partial_t - c\partial_x = -2c\partial_\xi$, which using $\partial_t^2 - c^2\partial_x^2 = (\partial_t + c\partial_x)(\partial_t - c\partial_x)$ gives us the reflected wave equation in terms of the light-cone coordinates as

$$\frac{\partial^2 a_r}{\partial \eta \partial \xi}(\xi, \eta) = \frac{i}{4}k_p^2 \left(\frac{\eta + \xi}{2} \right) a_0 e^{-ik\eta}, \qquad (6)$$

where $k_p(x) = \omega_p(x)/c$ is the inhomogeneous relativistic plasma wave number corresponding to the
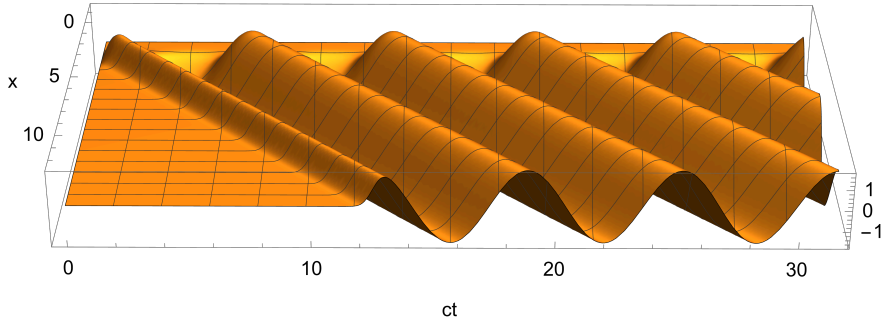
Fig. 1 Analytical solution of Eq. 9 for $k_p^2(x) = e^{-2x^2}$ showing reflected radiation with light rays of constant phase propagating along the light-cone variables $x - ct = const$.

electron distribution. Eq. 6 can be solved by direct integration and application of boundary conditions. We first apply the boundary condition that the reflection occurs only for $t > 0$, therefore at $t = 0$ we have $a_r(x, 0) = 0$. This also implies that the solution exists when $x + ct \geq x - ct$ for all x. Integrating the equation over η, where $\eta \geq \xi$, gives us the derivative of the reflected wave as

$$\frac{\partial a_r}{\partial \xi}(\xi, \eta) = \int_\xi^\eta \frac{i}{4} k_p^2 \left(\frac{\zeta + \xi}{2} \right) a_0 e^{-ik\zeta} d\zeta. \quad (7)$$

Note that, at $t = 0$, Eq. 7 satisfies $\partial_\xi a_r(\eta = x, \xi = x) = 0$, i.e. no radiation is initially emitted along the light cone coordinate ξ. To clearly show that Eq. 8 describes the reflected radiation, we substitute $\zeta + \xi = 2s$ in the integrand, giving us

$$\frac{\partial a_r}{\partial \xi}(\xi, \eta) = a_0 \frac{i e^{ik\xi}}{2} \int_\xi^{\frac{\eta + \xi}{2}} k_p^2(s) e^{-i2ks} ds. \quad (8)$$

If we assume the radiation condition $\partial_\xi a_r \approx ik a_r$, we obtain the spatiotemporal profile of the reflected radiation in spacetime coordinates of the mirror rest frame as

$$a_r(x, t) = a_0 e^{-i(\omega t - kx)} \frac{1}{2k} \int_{x-ct}^x k_p^2(s) e^{-i2ks} ds. \quad (9)$$

Eq. 9 satisfies the radiation boundary condition $\partial_\xi a_r = ik a_r$ exactly for $t \to \infty$, since then $(\eta + \xi)/2 = x$ and $\xi = x - ct \to -\infty$, and only the plane wave phase keeps the ξ dependence. This is equivalent to the assumption that, compared to the phase, the amplitude of the wave described by the integral term varies slowly with ξ. A more precise solution near could be obtained near the

spacetime origin by direct integration of Eq. 7, which leads to a more complicated form. Since we are mostly interested in the far-field behavior, we only keep the term given by Eq. 9 which well describes radiation behavior for large t and $x < ct$.

Finally, the spatiotemporal profile of the reflected wave is obtained by taking the real part of Eq. 9, which is shown in Fig. 2 where a sine wave is reflecting from a Gaussian electron profile. We see that the error of our far-field approximation is small and leads to a small phase shift and reflected amplitude reduction near the line $x = ct$, while the behavior at $x < ct$ shows propagation of reflected radiation with amplitude corresponding to the exact limit value. Precise integration without any approximations of Eq. 7 would give us correct phase behavior near the spacetime origin. The absolute value of Eq. 9, corresponding to the amplitude of the reflected wave, reduces in the limit $x \to \infty$ to the Fourier transform of electron distribution in the mirror rest frame, which was obtained in previous work on relativistic mirrors [1], and the complex amplitude reflection coefficient $r = a_r/a_0$ in the far-field limit can be therefore expressed as

$$r = \frac{1}{2k} \int_{-\infty}^\infty k_p^2(s) e^{-i2ks} ds, \quad (10)$$

where $k = \sqrt{\frac{1+\beta}{1-\beta}} k_0$ is the wave number in the mirror rest frame. The reflected amplitude in the laboratory frame is then simply $E_r/(rE_0) = (1+\beta)/(1-\beta)$, where E_0 is the electric field amplitude of the incident laser in the laboratory frame.

In the following sections, we first analyze and identify properties of beam-driven relativistic mirrors to consequently obtain the electron density distribution required to calculate Eqs. 9-10.

## 2 Beam-driven nonlinear plasma wave equation

We proceed to analyze plasma waves driven by a charged particle beam in one-dimensional approximation, which is valid for broad drivers satisfying $k_p r_b \gg 1$, where $k_p = \omega_p/c$ is the linear plasma wave number, $\omega_p = \sqrt{e^2 n_0/\epsilon_0 m_e}$ is the linear electron plasma frequency, n_0 is the electron plasma density and r_b is the radial size of the beam. The Poisson equation and the continuity equation for plasma electrons are then given as

$$\frac{\partial^2 \phi}{\partial x^2} = \frac{e}{\epsilon_0}(n_e - n_0 - q n_b), \qquad (11)$$

$$\frac{\partial j_x}{\partial x} - e\frac{\partial n_e}{\partial t} = 0, \qquad (12)$$

where n_b is the number density of the driving beam and q is the charge number of the driving particles, e.g. it is positive for positrons and protons ($q = 1$) or ions ($q \geq 1$) and it is negative for electrons ($q = -1$). We assume that the driver density satisfies $n_b(x,t) = n_b(x - vt)$, which means that it propagates in the x-direction and its shape does not evolve in time, an assumption that is valid over a relatively long time for ultra-relativistic beams with $\gamma \gg 1$, where $\gamma = 1/\sqrt{1 - (v/c)^2}$ is the relativistic Lorentz factor of the driving beam and c is the speed of light in vacuum. We now assume that all the plasma quantities also depend only on the Lagrangian coordinate of the driving beam $\xi = x - vt$. This gives us the following transformations for the spatial and temporal derivatives, respectively $\partial_x f(\xi(x,t)) = (\partial_\xi/\partial_x)\partial_\xi f(\xi) = \partial_\xi f(\xi)$ and $\partial_t f(\xi(x,t)) = (\partial_\xi/\partial_t)\partial_\xi f(\xi) = -v\partial_\xi f(\xi)$. Using these transformations and introducing the following normalized units $\omega_p \xi/c = \xi$, $e\phi/m_e c^2 \to \phi$, $eE/m_e c\omega_p \to E$, $n_e/n_0 \to n_e$, $q n_b/n_0 = \rho$, $v/c = \beta$, $j/en_0 c \to j$, $p/m_e c \to p$, equations 11-12 become

$$\frac{\partial^2 \phi}{\partial \xi^2} = (n_e - 1 - \rho), \qquad (13)$$
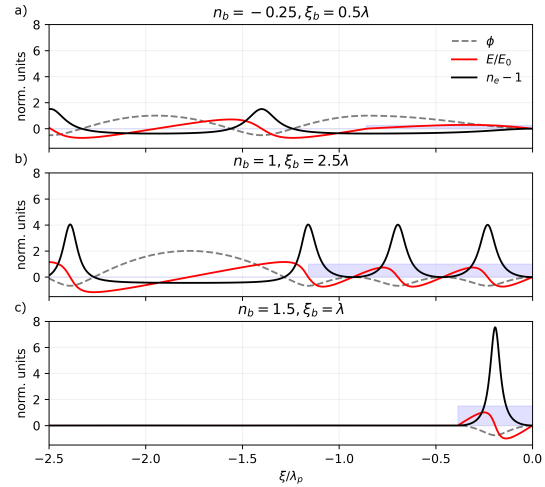
Fig. 2 Poisson equation (16) numerical solutions in the limit $\gamma^2 \gg \rho^2$. Wakefield-optimal solutions with bunch length given by Eq. 25 for (a) $\rho = -0.25$ and (b) $\rho = 1$. Single-cycle interior-wave-optimal solution with bunch length with given by Eq. 24 for $\rho = 1.5$.

$$\frac{\partial}{\partial \xi}(n_e \beta - n_e \beta_e) = 0, \qquad (14)$$

where β_e is the normalized velocity of the plasma electrons. Integrating Eq. 14 with the initial conditions $n_e(\xi = 0) = 1$ and $\beta(\xi = 0) = 0$, which are satisfied by plasma initially at rest, we obtain $n_e = 1/(1 - \beta_e/\beta)$, which shows that extremely large density waves are produced when $\beta_e \to \beta$, and Eq. 13 becomes

$$\frac{\partial^2 \phi}{\partial \xi^2} = \frac{\beta}{\beta - \beta_e} - 1 - \rho. \qquad (15)$$

It can be shown that the motion of an electron in a one-dimensional nonlinear plasma wave is given by the normalized one-dimensional Hamiltonian, $H(\xi, p_x) = \gamma - \beta p_x - \phi(\xi)$. For plasma electrons which are initially at rest, the following quantity is conserved, $\gamma - \beta p_x = 1 + \phi$. Since only longitudinal fields are considered, the Lorentz factor is simply $\gamma = \sqrt{1 + p_x^2}$ and Eq. 15 can be cast as

$$\frac{\partial^2 \phi}{\partial \xi^2} = \gamma^2 \left[\beta\left(1 - \frac{1}{\gamma^2(1 + \phi)^2}\right)^{-1/2} - 1\right] - \rho, . \qquad (16)$$

4

To obtain analytical results, we approximate the driver as a flat-top beam, $\rho(\xi) = \rho = const.$ for $-L_b < \xi < 0$ and zero otherwise, where L_b is the normalized driver length. We now proceed to analyze the plasma waves in the region of the ultra-relativistic particle beam, where $-L_b < \xi < 0$. Multiplying Eq. 16 by ϕ' and integrating with the initial conditions $\phi(\xi = 0) = \phi'(\xi = 0) = 0$, we get the following equation for the electric field of the plasma wave within the driving particle beam,

$$
\left(\frac{\partial\phi}{\partial\xi}\right)^2 = -2(\rho + \gamma^2)\phi \\
+ 2\beta\gamma^2\left(\sqrt{(1+\phi)^2 - \frac{1}{\gamma^2}} - \beta\right). \tag{17}
$$

The existence of plasma oscillations requires the existence of electric field stationary points, which is stated through Eq. 16 as $\phi'' = 0$. From this condition we obtain that real solutions exist only if $\rho > -1/(1 + \beta) \approx -1/2$, which tells us that for dense, negatively-charged drivers with $\rho \ll -1/2$, the background plasma cannot support oscillations in the region of the driver due to the strong electrostatic field of the charged beam. For $\rho > -1/(1 + \beta)$, equations 16-17 allow us to find the amplitude of the nonlinear plasma wave which exists in the interior region of the driver, which we call interior plasma wave from now on. From the electric field null-point condition $\phi' = 0$, we obtain the solutions $\phi_0 = 0$ and $\phi_{min} = -2\rho(1 - 1/\gamma^2)/(2\rho + 1 + \rho^2/\gamma^2)$, where the zero and non-zero solutions correspond respectively to the interior electron density wave trough and crest, respectively, in the case when $\rho > 0$ and vice versa for $\rho < 0$.

3 Lorentz factor of plasma electrons and wave breaking threshold

Using the conserved Hamiltonian of plasma electrons initially at rest, the electron Lorentz factor can be expressed explicitly in terms of the normalized potential as $\gamma_e = \gamma^2(1 + \phi)\left[1 - \beta\sqrt{1 - 1/(\gamma(1 + \phi))^2}\right]$, which gives us the Lorentz factor of the electrons in the density peak (corresponding to ϕ_{min}) of the nonlinear interior wave as

$$
\gamma_e = 1 + \frac{2\rho^2\beta^2}{2\rho + 1 + (\rho/\gamma)^2}. \tag{18}
$$

The wavebreaking limit of interior plasma waves is given by $\gamma_e \to \gamma$. Solving Eq. 18 in this limit gives us the following normalized driver density for which wavebreaking occurs immediately upon beam entry into the plasma,

$$
\rho_{wb,\pm} = \begin{cases} \gamma, & \text{if } q > 0. \\ -\frac{\gamma}{2\gamma+1}, & \text{if } q < 0. \end{cases} \tag{19}
$$

The driver density corresponding to wavebreaking (19) has two solutions, which correspond to positively and negatively charged drivers, respectively.

4 Wavelength of interior plasma waves

Inverting Eq. 17 and integrating from $\xi(\phi) < 0$ to $\xi = 0$, we get an explicit dependence of the normalized Lagrangian coordinate ξ on the normalized potential and driver velocity as

$$
\xi(\phi, \gamma) = \int_\phi^0 \left[-2(\rho + \gamma^2)\phi \\
+ 2\beta\gamma^2\left(\sqrt{(1+\phi)^2 - \frac{1}{\gamma^2}} - \beta\right) \right]^{-1/2} d\phi. \tag{20}
$$

Finally, to obtain the wavelength of the interior plasma waves, we integrate Eq. 20 between the two null-points of the electric field given by $\phi_0 = 0$ and $\phi_{min} = -2\rho(1-1/\gamma^2)/(2\rho+1+\rho^2/\gamma^2)$, which gives us the half-period of the interior wave. The wavelength of the nonlinear interior wave normalized to the linear plasma wavelength is then

$\lambda_i/\lambda_p = -2\xi(\phi_{min})/2\pi$. Therefore

$$\frac{\lambda_i}{\lambda_p}(\gamma,\rho) = \frac{1}{\pi} \int_{\frac{-2\rho(1-1/\gamma^2)}{(2\rho+1+\rho^2/\gamma^2)}}^{0} \left[-2(\rho+\gamma^2)\phi' \right.$$
$$\left. +2\beta\gamma^2 \left(\sqrt{(1+\phi')^2 - \frac{1}{\gamma^2}} - \beta \right) \right]^{-1/2} d\phi', \tag{21}$$

which is valid when the condition for interior plasma wave existence is satisfied, $\rho > -1/(1+\beta)$. Evaluating the integral 21 in the limit $\gamma \gg 1$, we get the following expression for the nonlinear interior plasma wave wavelength

$$\frac{\lambda_i}{\lambda_p} = \frac{2}{\pi} \frac{E\left(\frac{2\rho}{2\rho+1}\right)}{\sqrt{2\rho+1}}, \tag{22}$$

where $E(k)$ is the complete elliptic integral of the second kind. For negatively-charged drivers with $-1/2 < \rho \le 0$, the plasma wavelength grows with increasing negative charge density and diverges at $\rho \to -1/2$. For positively-charged drivers with $\rho \gg 1$, expansion of Eq. 22 yields $\lambda_i/\lambda_p \approx (2/\rho)^{1/2}/\pi$, which reveals a unique mechanism of relativistic nonlinear plasma waves with extremely short-wavelengths, driven by positively-charged particle beams.

At the wavebreaking limit $\rho \to \gamma \gg 1$, the wavelength of the nonlinear wave slightly decreases from Eq. 22, which can be estimated from Eq. 20 in this limit as $\pi\lambda_i/\lambda_p \approx (2/\gamma)^{1/2}$. This stands in stark contrast to plasma wakefields driven by either negatively-charged beams or laser pulses, in which case the plasma wave elongates with increasing driver velocity as $\pi\lambda_i/\lambda_p \approx (2\gamma)^{1/2}$ [2, 3].

5 Optimal driver length

Now we proceed to analyze the plasma waves behind the driver, where $\xi < -L_b$. The Poisson equation (16) with $\rho = 0$ is satisfied with initial conditions given by $\phi(-L_b), \phi'(-L_b)$, which correspond to the solutions obtained in the driver region $-L_b \le \xi \le 0$ due to the continuity of the electric field. Integrating Eq. 16 for $\rho = 0$ with non-zero initial conditions, Eq. 17 takes the following form [4]

$$\gamma_e + \frac{1}{2} \left(\frac{E_{wake}}{E_0} \right)^2 = C_0, \tag{23}$$

where $C_0 = \gamma_e(-L_b) + (-\phi'(-L_b))^2/2$ is a constant given by initial conditions $\phi(-L_b), \phi'(-L_b)$ at the driver rear $\xi = -L_b$.

When the driver length is exactly the length of a single cycle of the nonlinear plasma wave, $L_b = \lambda_i$, the potential after a full-cycle gives, as shown above, the initial conditions as $\phi(-L_b) = \phi'(-L_b) = 0$, and we have $C_0 = 1$ and the maximum amplitude of the wake is $E_{wake}/E_0 = \sqrt{2(C_0 - \gamma_e)} = 0$, since $1 \le \gamma_e \le C_0 = 1$. Therefore, a single-cycle plasma wave is driven optimally and no plasma oscillations occur outside of the region occupied by the ultra-relativistic particle beam. The same analysis holds for optimal multi-cycle waves, in such a case the initial conditions for the Poisson equation are the same and the driver length condition for optimal multi-cycle nonlinear plasma wave generation becomes

$$L_b = n\lambda_i, \tag{24}$$

where n is a natural number and λ is given by Eq. 22. Any deviation from Eq. 24 gives $C_0 > 1$ and therefore non-zero plasma wakefield amplitude. The wakefield amplitude is maximized when $\phi'(-L_b) = 0$ and $C_0 = \gamma_e$, where γ_e is given by Eq. 18. These boundary conditions correspond to a driver whose length L_b ends exactly at the density peak of the interior plasma wave, as shown in Figs. 2a,b. The strongest wakefield is therefore created when the driver length satisfies the following resonance condition,

$$L_b = \left(n - \frac{1}{2} \right) \lambda_i, \tag{25}$$

i.e. for the single-cycle wave $m = 1$, the driver length fits the first half-cycle of the interior plasma wave, $L_b = \lambda_i/2$, and the plasma wakefield amplitude is maximized for given driver density and velocity, as shown in Fig. 2a.

6 Mirror propagation distance due to relativistic beam-plasma instability

As a relativistic charged particle beam propagates through plasma, an instability develops which modulates its initially uniform charge density. This modulation eventually breaks the coherent nonlinear oscillations of plasma electrons which sustain the relativistic mirror. To calculate the distance in plasma a beam-driven relativistic mirror propagates before it breaks, we need to find the instability growth rate.

Let us consider a relativistic charged particle beam with normalized charge density $\rho_b = qn_b/n_0$, mass M and velocity v propagating along the positive direction of the x-axis in plasma composed of electrons and ions with particle number density n_0. However, since the beam is relativistic, and its longitudinal size is of the order of the electron plasma wave $L_b \propto \lambda_p$, the influence of slow ions is negligible compared to the fast plasma electrons. The continuity equation and the Euler momentum equation are then given for both relativistic particle beam and plasma electron species as

$$\frac{\partial n_i}{\partial t} + \frac{\partial (n_i v_i)}{\partial x} = 0, \tag{26}$$

$$m\frac{\partial (\gamma_i v_i)}{\partial t} + mv_i\frac{\partial (\gamma_i v_i)}{\partial x} = qE_x, \tag{27}$$

where $i = b, e$ is the species index and the plasma electrons are initially at rest, $\gamma_e \approx 1$. Now, we consider the small-amplitude modes which perturb the the relativistic beam, as $n_i \approx n_0 + \delta n_{i0}$ and $v_i \approx v_{i0} + \delta v_i$, where $\delta n_i, \delta E_x, \delta v_i \propto e^{i(kx - \omega t)}$. Expanding the momentum in terms of the small perturbation, we get $p_i = \gamma_i v_i \approx \gamma_{i0} v_{i0} + \gamma_{i0}^3 \delta v_i$. Combining the linearized Eqs. 26,27 with the Poisson equation, $\epsilon_0 ik\delta E_x = \delta\rho_b + \delta\rho_e$, we get the following dispersion relation for the relativistic two-stream instability

$$\frac{\omega_b^2}{\gamma_b^3(\omega - kv_b)^2} + \frac{\omega_p^2}{\omega^2} = 1, \tag{28}$$

where $\omega_p^2 = e^2 n_0/(m_e\epsilon_0)$ and $\omega_b^2 = (qe)^2 n_b/(M\epsilon_0) = (q\rho_b m/M)\omega_p^2$. The γ_b^3 factor in the dispersion relation can be intuitively

$$\omega/\omega_p$$
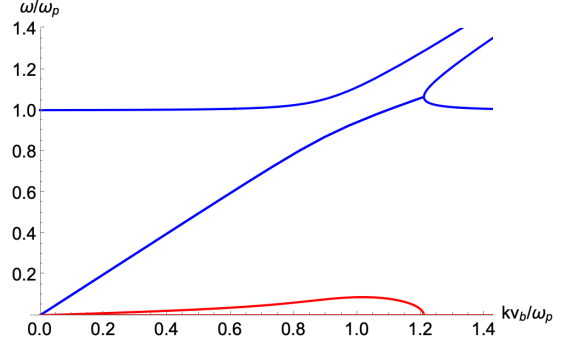
Fig. 3 Real (blue) and imaginary (red) parts of solution of Eq. 28, calculated for a positively-charged relativistic particle beam with $qn_b/n_0 = \rho_{wb,+} = \gamma$, $M = m_e$ and $\gamma = 20$ (positron). The real part corresponding to the growing unstable modes is given by linearly growing branch, $\omega_r \approx kv_b \approx kc$.

understood as the well-known concept of the longitudinal mass of a particle oscillating along the direction of its relativistic motion, $M \rightarrow \gamma_b^3 M$. Eq. 28 can be rewritten as

$$\frac{1}{\omega - kv_b} = \pm\frac{\gamma_b^{3/2}}{\omega_b}\sqrt{1 - \left(\frac{\omega_p}{\omega}\right)^2}. \tag{29}$$

Using $\omega = \omega_r + i\Gamma$, where $\omega_r = \mathcal{R}(\omega)$, and expanding by $\omega_r - kv_b - i\Gamma$, we get

$$\frac{\omega_r - kv_b - i\Gamma}{\omega_r^2 - 2\omega_r kv_b + (kv_b)^2 + \Gamma^2} = \pm\frac{\gamma_b^{3/2}}{\omega_b}\sqrt{1 - \left(\frac{\omega_p}{\omega}\right)^2}. \tag{30}$$

For even moderately relativistic beams satisfying $v_b \approx c$, unstable copropagating electrostatic modes must be also relativistic, with constant phase velocity given by $\omega_r \approx ck$. Subsequently, the growth rate must be very small, $\omega = \omega_r + i\Gamma \approx \omega_r < \omega_p$, which can be verified by solving Eq. 28 numerically, as shown in Fig. 3. Using this in Eq. 30, we get the following estimate for the growth rate of the relativistic non-resonant two-stream unstable modes

$$\frac{\omega_p}{\Gamma} \approx \gamma_b^{3/2}\left(\frac{M}{qm_e\rho_b}\right)^{1/2}\frac{\omega_p}{kv_b}. \tag{31}$$

Finally, the unstable spectrum observed in PIC simulations is broadband. Typically, the modulation occurs only within a very small region

surrounding the copropagating electron density peak of the nonlinear wave (Fig. 2c), where the electrons pile-up and modulate the driving particle beam. This makes single mode interpretation complicated.

To proceed, we make a generalizing heuristic estimate. Requiring that the mirror breaks immediately, $\tau_{wb} \to 0$, when $Q \geq Q_{wb}$, where Q the total charge of the relativistic beam and Q_{wb} is the total charge required to produce wave breaking, we get the following estimate that correctly reproduces the timescale ($\tau_{wb} \propto 1/\Gamma$) of the unstable broadband spectra observed in the PIC simulations, written as $\omega_p/kv_b \to \sqrt{1 - Q/Q_{wb}}$. This yields the following expression for the beam-driven relativistic mirror propagation distance

$$k_p L_{wb} \approx N_e \gamma_b^{3/2} \left(\frac{M}{qm_e\rho_b} \right)^{1/2} \left(1 - \frac{Q}{Q_{wb}} \right)^{1/2},$$
$$(32)$$

where the factor N_e corresponds to the number of e-folds observed in PIC simulations before the mirror breaks. Typically, $N_e \approx 1$. For positively-charged drivers with $\rho_b \lesssim \rho_{wb,+} \approx \gamma$, we have $Q_b/Q_{wb} \approx \rho_b/\rho_{wb,+}$ and the mirror propagation distance, for $N_e \approx 2\pi/5$, takes the form presented in the main text

$$\frac{L_{wb,+}}{\lambda_p} \approx \frac{\gamma_b}{5} \left(\frac{M}{qm_e} \right)^{1/2} \left(1 - \frac{\rho_b}{\rho_{wb}} \right)^{1/2}. \quad (33)$$

For negatively-charged drivers with $\rho_b \approx \rho_{wb,-} = -1/(2 + (1/\gamma)) \approx -1/2$ and $Q_b/Q_{wb} \approx L_b/L_{wb} < 1$, the mirror propagation distance can be estimated as

$$\frac{L_{wb,-}}{\lambda_p} \approx \frac{\gamma_b^{3/2}}{5} \left(\frac{2M}{|q|m_e} \right)^{1/2} \left(1 - \frac{L_b}{L_{wb}} \right)^{1/2}. \quad (34)$$

7 Structure of beam-driven interior plasma wave breaking

As we have shown in S1, evaluating reflection of radiation requires electron plasma density distribution of the breaking wave. To gain a foothold, we return to the Poisson equation (15) to analyze the structure of interior plasma waves at the wavebreaking threshold, $\gamma_e \to \gamma$. We use the integral of motion $\gamma_e - \beta p_x - 1 = \phi$ and the identity

$1/(1 - \beta_e/\beta) - 1 = p_x/(\beta\gamma_e - p_x)$ to rewrite Eq. 15 as

$$(\gamma_e - \beta p_x)'' = \frac{p_x}{\beta\gamma_e - p_x} - \rho. \quad (35)$$

We now expand the momentum around the peak of the nonlinear plasma wave, $p = p_m + \delta p + \mathcal{O}(\delta p^2)$, where $p_m = \sqrt{\gamma_e^2 - 1}$, where γ_e is given by Eq. 18. At the wavebreaking threshold we have $\gamma_e \to \gamma$, therefore we proceed to use the following power series expansion for left-hand side of Eq. 35, $\gamma - \beta p_x = \sqrt{1 + p_x^2} - \beta p_x \approx 1/\gamma + \delta p^2/(2\gamma^3) + \mathcal{O}(\delta p^3)$. For the right-hand side of Eq. 35 we use $\gamma_e \to \gamma$ and therefore $\beta\gamma - p_x = \beta\sqrt{1 + p_x^2} - p_x \approx -\delta p/\gamma^2 + \beta\delta p^2/(2\gamma^3) + \mathcal{O}(\delta p^3)$. Keeping only the leading order terms in Eq. 35, we get

$$(\delta p^2)'' = -2\gamma^6 \frac{\beta}{\delta p} - \gamma. \quad (36)$$

Multiplying Eq. 36 by $(\delta p^2)'$ and integrating over ξ, we get

$$(\delta p' \delta p)^2 + 2\gamma^6 \beta\delta p + \gamma\delta p^2/2 = C, \quad (37)$$

where C is an integration constant. In the limit $\delta p \to 0$, the solution of Eq. 37 is given by the value of the integration constant C. If $\delta p' \delta p \to 0$ when $\delta p \to 0$, then we have $C = 0$ and up to the leading order Eq. 37 takes the following form

$$(\delta p')^2 = -2\gamma^6 \frac{\beta}{\delta p}. \quad (38)$$

In the limit $\xi \to 0$, where ξ is the distance from the position of the density peak, a solution of Eq. 37 is given as

$$\delta p = - \left(\frac{3}{\sqrt{2}} \gamma^3 \beta^{1/2} \xi \right)^{2/3}. \quad (39)$$

The velocity can be expanded up to the first order as $\beta_e \approx \beta + \frac{\delta p}{\gamma^3} + \mathcal{O}(\delta p^2)$, therefore $\beta_e \approx \beta - \frac{1}{\gamma} \left(\frac{3}{\sqrt{2}} \beta^{1/2} \xi \right)^{2/3}$ and the normalized electron density becomes

$$\frac{n_e}{n_0} = \frac{\beta}{\beta - \beta_e} \approx \gamma \left(\frac{\sqrt{2}}{3} \frac{\beta}{\xi} \right)^{2/3}. \quad (40)$$

Eq. 40 shows that the density structure of a breaking interior plasma wave has the form of a

cusp caustic [5], which has an integrable singularity at $\xi \to 0$, therefore the total number of electrons remains finite even for the asymptotic leading-order term given by Eq. 40. It was previously shown that such a cusp singularity is a general feature of electron plasma wave breaking [1, 6, 7]. The structure of beam-driven wave breaking is not different, since the effect of driver density represented by the third term of Eq. 37 only contributes in the higher order corrections.

8 Reflection coefficient of beam-driven relativistic mirror at the wave breaking threshold

In the laboratory frame, the electron distribution given by the asymptotic cusp distribution (40) can be written as

$$\frac{n_e}{n_0} = \gamma \left(\frac{\sqrt{2}}{3} \frac{\beta}{k_p(x - vt)} \right)^{2/3}. \qquad (41)$$

We now transforming into the mirror rest frame using $x' = \gamma(x - vt)$. The electron charge density is part of the four-current which satisfies the continuity equation $\partial_\mu j^\mu = 0$, and it must therefore transform as $\rho' = \gamma(\rho - j_x \beta/c)$ due to charge conservation. Transforming the spacetime coordinates, the rest frame electron density distribution then becomes $n'_e/n'_0 = \gamma(\sqrt{2}\beta\gamma/3)^{2/3}(x')^{-2/3}$, where $n'_0 = n_0/\gamma$ is the background plasma density in the mirror rest frame. We therefore have the following inhomogenous relativistic plasma wave number (using $\beta \approx 1$)

$$k'^2_p(x') = \left(\frac{2}{9} \right)^{1/3} \frac{k_p^{4/3} \gamma^{2/3}}{x'^{2/3}}, \qquad (42)$$

where $k_p = \omega_{p0}/c$ is the linear plasma wave number calculated in the laboratory frame. Using Eq. 42 to calculate the amplitude reflection coefficient given by Eq. 10, we get

$$r = \kappa \left(\frac{n_0}{\gamma n_c} \right)^{2/3}, \qquad (43)$$

where $\kappa = \pi/(2^{4/3}3^{2/3}\Gamma\left(\frac{2}{3}\right)) \approx 0.44$ and $\Gamma(z)$ is the Euler gamma function. Complex amplitude reflection coefficient (43) was previously obtained
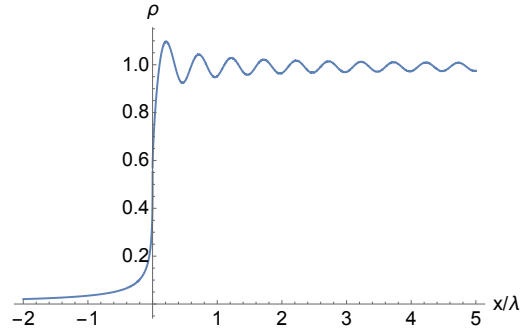
Fig. 4 Spatial profile of complex amplitude reflection coefficient near the origin of the mirror rest frame ($x = 0$). Here λ represents the rest frame radiation wavelength. The reflected wave amplitude is modulated at the second harmonic of the incident radiation near the mirror origin. In the limit $x \to \infty$, the amplitude stabilizes at the value given by Eq. 43.

in the context of laser-driven relativistic mirrors [1, 6]. Calculating Eq. 9 in the limit $t \to \infty$, we can further obtain the spatial profile of the reflected amplitude around the mirror position, which is shown in Fig. 4.

In PIC simulations, we observe that Eq. 43 overestimates amplitude of the reflected radiation. Indeed, Eq. 43 is derived using the singular cusp distribution. However, in fully kinetic simulations electron density is finite both before, during and after wavebreaking, which is the expected behavior due to the discrete number of electrons (and macroparticles in the case of particle-in-cell simulations), which compose nonlinear plasma waves.

To amend this, we introduce the finite distribution scale length l, also known as sharpness parameter [1], and generalize the electron distribution in the laboratory frame, given by Eq. 41, as

$$\frac{n_e}{n_0} = \frac{\gamma 2^{1/3}}{3^{2/3} k_p^{2/3}} \left(\frac{\beta^2}{l^2 + (x - vt)^2} \right)^{1/3}, \qquad (44)$$

where the limit $l \to 0$ reproduces the dominant asymptotic cusp structure obtained by solving Eq. 35. Transforming Eq. 44 into the rest frame, we get the following rest frame inhomogeneous plasma

9

wave number

$$k_p'^2(x') = \left(\frac{2}{9}\right)^{1/3} \frac{k_p^{4/3}\gamma^{2/3}}{l'^2 + x'^2}, \qquad (45)$$

where $l' = \gamma l$ is the finite distribution length scale in the mirror rest frame. The rest frame reflection coefficient evaluated in terms of laboratory frame parameters then becomes

$$r \approx \frac{\pi^{1/2}}{2^{5/6}3^{2/3}\Gamma\left(\frac{1}{3}\right)} \frac{k_p^{4/3}l^{1/6}}{\gamma^{1/3}k_0^{7/6}} K_{1/6}\left(4\gamma^2 k_0 l\right), \quad (46)$$

where $K_n(x)$ is the modified Bessel function of the second kind. By measuring the finite distribution scale length l from simulations, the reflection coefficient is precisely given by Eq. 46. Fully-coherent emission will occur when a distribution of radiating particles satisfies $k_r l \ll 1$, where k_r is the wave number of the reflected radiation in the laboratory frame, $k_r \approx 4\gamma^2 k_0$.

In the PIC simulations, we observe finite distribution length scales of the order $k_r l_{sim} \approx 3.5 \times 10^{-2}$, therefore we estimate $4\gamma^2 k_0 l \approx 1/(9\pi)$ and the rest frame amplitude reflection coefficient can be written in the following simple form

$$r \approx \alpha \left(\frac{n_0}{n_c\gamma}\right)^{2/3}, \qquad (47)$$

where $\alpha = \frac{\pi^{1/3}}{2^{1/6}3^2\Gamma(1/3)}K_{1/6}\left(\frac{1}{3^2\pi}\right) \approx 0.3$ is the proportionality constant obtained by introducing finite distribution length scale l. The scaling follows that of the cusp reflection coefficient given by Eq. 43, but the coefficient is roughly 30% smaller due to the electron density finiteness. As shown with the results presented in the main text, Eq. 47 perfectly describes the particle-in-cell simulation results of relativistic mirrors close to the wave breaking threshold in the parameter range $\gamma \in \{5, 10, 15, 20\}$ and $n_0/n_c \in \{0.01, 0.02, 0.04, 0.08\}$.

9 Energy spectrum of reflected coherent radiation

If we assume that the radiation is reflected with constant amplitude reflection coefficient, the electric field in the spectral domain of a signal with duration τ_r can be expressed in the laboratory frame as

$$\begin{aligned} E_r(x, \omega) &= E_r \int_{-\infty}^{\infty} e^{-i(\omega_r t - k_r x)} e^{i\omega t} dt \\ &= E_r e^{ik_r x} \int_0^{\tau_r} e^{i(\omega - \omega_r)t} dt, \end{aligned} \qquad (48)$$

where $E_r = rE_0(1 + \beta)/(1 - \beta)$ is the reflected amplitude and E_0 is the incident electric field amplitude. Therefore, after directly evaluating the last integral in Eq. 48, the normalized energy spectrum can be expressed as

$$\left|\frac{E(\omega)}{E_p}\right|^2 = \text{sinc}^2\left(\frac{(\omega - \omega_r)\tau_r}{2}\right), \qquad (49)$$

where $\text{sinc}(x) = \sin(x)/x$ is the cardinal sine function, $E_p^2 = |E_r|^2 \tau_r^2$ is the value of the spectrum peak at $\omega = \omega_r$, which grows quadratically in time due to temporal coherence, and τ_r, ω_r are respectively the double Doppler shifted reflected angular frequency and pulse duration.

10 Peak spectral brightness

The value of peak spectral brightness for a monochromatic light source reflected from a homogeneous mirror in terms of the conventional unit of photons per second per relative spectral bandwidth of 10^{-3} per transverse radiation phase space can be written as

$$\mathcal{B} = \frac{N_{ph,r}(N/1000)}{2\pi^2\theta^2\sigma^2\tau_r}, \qquad (50)$$

where N is the number of reflected cycles corresponding to the relative spectral bandwidth as $\Delta\omega/\omega = 1/N$, $N_{ph,r}$ is the total number of reflected photons, θ is the half-angle divergence of reflected radiation and ρ is the waist of the incident laser. The reflected divergence is $\theta \approx \theta_0/(2\gamma)^2$, where θ_0 is the half-angle divergence of the incident laser. If we consider a diffraction limited incident laser and a homogeneous mirror, the beam parameter product characterizing transverse phase space of incident radiation becomes $\rho\theta_0 = \lambda_0/\pi$, where λ_0 is the incident laser wavelength. The peak spectral brightness is then

$$\mathcal{B} = \frac{8\gamma^4 N_{ph,r}(N/1000)}{\lambda_0^2\tau_r}. \qquad (51)$$

Finally, considering the reflected pulse duration satisfies $\tau_r \approx \tau_0/(2\gamma)^2 \approx (N\lambda_0/c)/(2\gamma)^2$, we obtain the final formula for the peak spectral brightness of radiation reflected from a homogeneous beam-driven relativistic mirror,

$$\mathcal{B} = \frac{32c\gamma^6 N_{ph,r}}{1000\lambda_0^3}. \tag{52}$$

The ratio of reflected to incident number of photons can be calculated using the rest frame reflection coefficient as $N_{ph,r}/N_{ph,i} = |r|^2$. Finally, to convert to the conventional synchrotron unit of photons/(s mm^2 mrad^2 0.1%BW), we use m^{2}rad$^2 = 10^{12}$mm^{2}mrad^2 to obtain

$$\mathcal{B}\left[\frac{\text{photons}}{\text{s mm}^2 \text{ mrad}^2 \text{ 0.1\% BW}}\right] = \frac{32c\gamma^6 N_{ph,i}|r|^2}{10^{15}\lambda_0^3}, \tag{53}$$

where the reflection coefficient is given by Eq. 47.

References

[1] Bulanov, S.V., Esirkepov, T.Z., Kando, M., Pirozhkov, A.S., Rosanov, N.N.: Relativistic mirrors in plasmas. novel results and perspectives. Physics-Uspekhi **56**(5), 429 (2013)

[2] Esarey, E., Schroeder, C.B., Leemans, W.P.: Physics of laser-driven plasma-based electron accelerators. Reviews of modern physics **81**(3), 1229 (2009)

[3] Rosenzweig, J.: Nonlinear plasma dynamics in the plasma wakefield accelerator. IEEE transactions on plasma science **15**(2), 186–191 (1987)

[4] Akhiezer, A.I., Polovin, R.: Theory of wave motion of an electron plasma. Soviet Phys. JETP **3** (1956)

[5] Arnold, V.I.: Catastrophe Theory. Berlin Springer-Verlag, 1986

[6] Panchenko, A., Esirkepov, T.Z., Pirozhkov, A., Kando, M., Kamenets, F., Bulanov, S.: Interaction of electromagnetic waves with caustics in plasma flows. Physical Review E **78**(5), 056402 (2008)

[7] Bulanov, S., Naumova, N., Pegoraro, F., Sakai, J.: Particle injection into the wave acceleration phase due to nonlinear wake wave breaking. Physical Review E **58**(5), 5257 (1998)

B.3 Two-color nonlinear resonances in betatron oscillations of laser accelerated relativistic electrons

The following article is reproduced from M. Lamač, U. Chaulagain, L. Jurkovičová, J. Nejdl, and S. V. Bulanov (2021). Two-color nonlinear resonances in betatron oscillations of laser accelerated relativistic electrons. *Physical Review Research*, **3**(3), 033088.

Two-color nonlinear resonances in betatron oscillations of laser accelerated relativistic electrons

M. Lamač [1,2,*] U. Chaulagain [1], L. Jurkovičová [1,3] J. Nejdl [1], and S. V. Bulanov [1]

[1]*ELI Beamlines Center, Institute of Physics, Czech Academy of Sciences, Za Radnicí 835, 25241 Dolní Břežany, Czech Republic*
[2]*Faculty of Mathematics and Physics, Charles University, Ke Karlovu 3, 12116 Prague, Czech Republic*
[3]*Faculty of Nuclear Sciences and Physical Engineering, Czech Technical University, Břehová 78/7, 11519 Prague, Czech Republic*

X-ray radiation from laser wakefield accelerated (LWFA) electrons provides a collimated broadband femtosecond x-ray source with micron-scale source size. However, the photon flux is still inadequate for a range of applications. By interaction of LWFA relativistic electrons with the second and the third harmonic of the laser driving the wakefield, we report more than an order of magnitude enhancement of photon flux emitted by the electrons undergoing betatron oscillations resonant with the harmonics. This phenomenon is demonstrated with analytical and numerical models, as well as particle-in-cell simulations.

I. INTRODUCTION

Laser wakefield acceleration (LWFA) has received considerable attention since its conception [1]. Recent experimental work reports 8 GeV electron bunches being produced in a 20-cm capillary plasma with a petawatt-class laser driver [2]. Betatron x-ray generation is connected to LWFA within the blowout regime [3,4]. The plasma cavity acts as a wiggler forcing electrons to oscillate and consequently radiate x rays known as betatron radiation [5,6]. The short duration of the x-ray pulses, small source size, synchronization with the driving laser, and all-optical compactness of the betatron x-ray source provide a competitive alternative to conventional sources [7–9].

The applications of such ultrafast x-ray sources range from high-resolution x-ray imaging to ultrafast x-ray science [9–15]. The hard x-ray source can be also employed in industrial applications such as x-ray computed tomography of dense objects [14]. An attempt on measurement of single-shot ultrafast x-ray absorption spectroscopy of a warm dense matter has been performed using this broadband x-ray source; however, the photon flux is a limiting factor that prevents routine use of the source with single-shot measurements [15].

Features of betatron x-ray radiation depend on the electron Lorentz factor γ, betatron oscillation frequency $\omega_\beta = \omega_p/\sqrt{2\gamma}$, and betatron oscillation amplitude r_β, where $\omega_p = \sqrt{n_e e^2/m_e \epsilon_0}$ is the electron plasma frequency, n_e the electron density, m_e the electron mass, c the speed of light, ϵ_0 the vacuum permittivity, and e the elementary charge. We introduce the normalized transverse momentum amplitude

$\tilde{p}_x = p_x/m_e c$, known as undulator parameter K [7,16,17], since $\tilde{p}_x = K = r_\beta k_\beta \gamma$, where k_β is the betatron wave number. In the wiggler regime, where $K \gg 1$, the most important radiation parameters become the number of emitted photons per electron per oscillation period $N_\gamma \approx K/30$ and the critical frequency of the synchrotron spectrum $\omega_c = \frac{3}{2}K\gamma^2\omega_\beta$ [7,18]. We see that enhancement of transverse momentum is a crucial step toward achieving high-energy, high-flux x-ray radiation.

In recent years, many works demonstrating an increase of high-energy radiation emission from LWFA electrons have been published [19–25]. However, most of them report on generation of higher photon energy [19,20,22,24] with a limited number of works focusing on the photon flux enhancement of betatron x-ray radiation in the kiloelectronvolt range [21,25]. Enhancement of betatron radiation photon flux in this energy range is critical for many applications such as single-shot time-resolved x-ray absorption spectroscopy and ultrafast x-ray diffraction [9,15].

In this paper, we show that the presence of the second harmonic (SH) and third harmonic (TH) of the fundamental laser frequency copropagating with the relativistic electrons enhance the photon flux of betatron x-ray radiation by an order of magnitude. This enhancement originates from nonlinear resonances in betatron oscillations induced by two laser pulses with different frequencies interacting with the electrons. This resonance results in a boost of the transverse momentum p_x. The geometry of two-color betatron resonance is schematically shown in Fig. 1. The figure depicts a plasma cavity generated during the process of LWFA in a two-dimensional (2D) particle-in-cell (PIC) simulation, where a laser pulse with frequency ω_d drives a strong wakefield, causing self-injected electrons to accelerate and oscillate within the plasma cavity. Betatron oscillation resonance with frequencies ω_1 and ω_2 is achieved when either of the shifted frequencies seen by the electron ω_i matches its betatron frequency $\omega_i \approx \omega_\beta$, where $\omega_i = (1 - v_z/v_{pi})\omega_{0i}$ is the laser angular frequency seen by the electron, $i = 1, 2$, ω_{0i} is the laser angular frequency, v_{pi} is the phase velocity of the lasers, and v_z is the longitudinal
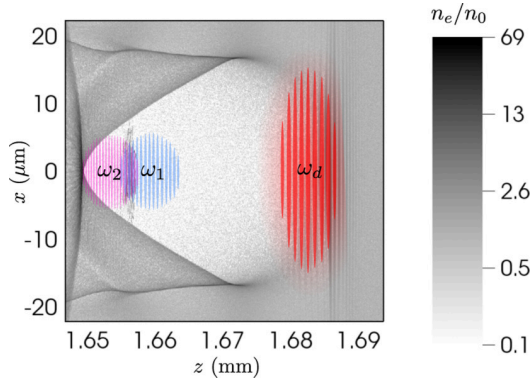
*marcel.lamac@eli-beams.eu

FIG. 1. Schematic of two-color betatron resonance. Normalized electron plasma density snapshot in grayscale from particle-in-cell (PIC) simulation of the two-color case presented in Sec. IV. Resonance is achieved due to the interaction of electrons with lasers of frequency ω_1 and ω_2. Laser with frequency ω_d drives laser wakefield acceleration (LWFA).

velocity of the electron. Such resonance results in significant transverse momentum enhancement [20,26,27].

This paper is organized as follows: In Sec. II, we show that, in the case of relativistic electrons close to dephasing under the paraxial approximation $p_x \ll p_z$, the driven electron oscillations can be described with the Duffing equation, which reveals the conditions for nonlinear resonances [28]. Section III shows solutions for full equations of motion for a more general case of a relativistic electron interacting with two lasers under the paraxial approximation, where the analytic resonance conditions from Sec. II are validated and the resonance dependency on plasma density n_e is explored. Results from PIC simulations showing a presence of nonlinear resonances in the most general case, where laser and plasma evolution as well as acceleration are considered, are presented in Sec. IV. Analysis of emitted x-ray radiation from PIC results showing an order of magnitude enhancement in the case of a two-color scheme is presented in Sec. V. In Sec. VI, we propose an experimental setup capable of providing multicolor laser interaction in plasma targets based on our theoretical results with tunable laser polarizations and delays. Lastly, our results are summarized in the concluding Sec. VII.

II. TWO-COLOR NONLINEAR RESONANCES IN PARAXIAL APPROXIMATION

In this section, we derive the equation that reveals the resonances leading to transverse momentum enhancement present in relativistic electrons oscillating in a plasma channel while interacting with two laser frequencies. The equations of motion of an electron are

$$\frac{d\mathbf{p}}{dt} = -e(\mathbf{E} + \mathbf{v} \times \mathbf{B}), \tag{1}$$

$$\frac{d\mathbf{r}}{dt} = \mathbf{v} = \frac{\mathbf{p}}{m_e \gamma}. \tag{2}$$

The electromagnetic fields of the plasma cavity in the cylindrical coordinate system (r, θ, z), where $r = \sqrt{x^2 + y^2}$

is the radial coordinate, are given by the longitudinal electric field $E_z/E_{wb} = k_p \xi/2$, radial electric field $E_r/E_{wb} = k_p r/4$, and azimuthal magnetic field $cB_\theta/E_{wb} = -k_p r/4$, where $\xi = z - v_\phi t$ is the wake comoving variable, v_ϕ is the phase velocity of the wake, k_p is the plasma wave number, and $E_{wb} = m\omega_p c/e$ is the cold nonrelativistic wave-breaking field [4,29–31]. The equations of motion for an electron in such a cavity without any additional fields are then $\dot{\mathbf{p}} = -e(\mathbf{E} + \mathbf{v} \times \mathbf{B}) = \mathbf{F}_\parallel + \mathbf{F}_\perp \approx -m\omega_p^2(\xi \mathbf{e}_z/2 + r\mathbf{e}_r/2)$, where the last expression assumes $p_\perp/p_z \ll 1$ [7]. Furthermore, for electrons near the dephasing point $\xi \approx 0$, we only have the radial component of the force $\dot{\mathbf{p}} \approx -m\omega_p^2 \mathbf{e}_r r/2$. The laser field in the plane-wave approximation is given as $E_{\mathrm{laser}} = E_1 \sin(\phi_1) + E_2 \sin(\phi_2)$, and the corresponding magnetic field is given as $B_{\mathrm{laser}} = (E_1/v_{p1})\sin(\phi_1) + (E_2/v_{p2})\sin(\phi_2)$, where E_i is the electric intensity amplitude, $\phi_i = \omega_{0i}(t - z/v_{pi}) + \theta_i$ is the laser phase, and θ_i is the initial phase, $i = 1, 2$. The laser field is linearly polarized in the x direction. By restricting the electron to planar motion [$p_y(t) = 0$], the momentum Eqs. (1) and (2), with both the cavity and laser fields included, become

$$\frac{dp_x}{dt} = -e[\eta_1 E_1 \sin(\phi_1) + \eta_2 E_2 \sin(\phi_2)] - \frac{m_e \omega_p^2}{2} x, \tag{3}$$

$$\frac{dp_z}{dt} = -e v_x \left[\frac{E_1}{v_{p1}} \sin(\phi_1) + \frac{E_2}{v_{p2}} \sin(\phi_2) \right], \tag{4}$$

where the factor $\eta_i = 1 - v_z/v_{pi}$ comes from the sum of the electric field and vector product of velocity and magnetic field in Eq. (1). Taking the time derivative of Eq. (3) with the use of normalized transverse momentum $\tilde{p} = p/m_e c$ gives us the following equation for a nonlinear oscillator:

$$\frac{d^2\tilde{p}_x}{dt^2} + \omega_\beta^2 \tilde{p}_x = \tilde{a}_1 \cos(\phi_1) + \tilde{a}_2 \cos(\phi_2), \tag{5}$$

where $\tilde{a}_i = a_i \omega_i^2$, and $a_i = eE_i/(mc\omega_{0i})$ is the normalized laser field amplitude, $i = 1, 2$. By excluding the electrostatic longitudinal wakefield generated during LWFA in Eqs. (1) and (2), we restrict ourselves to the case of wakefield pre-accelerated relativistic electrons with $\gamma \gg 1$ close to dephasing, at which point the wakefield contribution is negligible. This description is also applicable for direct laser accelerated electrons oscillating in self-generated transverse quasistatic fields of plasma channels generated by long laser pulses with relativistic intensities [26,32], generalized to the case when two laser frequencies are present. We are interested in the dynamics of LWFA ultrarelativistic oscillating electrons for which the paraxial approximation $p_z \gg p_x$ with $v_z \approx c$ is valid, and we have $p_x/p_z \approx v_x/c \ll 1$; therefore, $v_x \ll c < v_{pi}$, which means that the contribution from the magnetic field to the transverse momentum p_x through p_z is minor compared with the electrical field contribution in Eq. (3). In other words, variables p_x and x are oscillating fast compared with slowly varying variables v_z and γ [32]. It is therefore reasonable to assume for slow variables that $\dot{\gamma}, \dot{v}_z, \dot{p}_z \approx 0$ on a suitable timescale, and therefore, $p_z = p_z(0) =: p_{z0}$ on the timescale of betatron oscillations $\sim \omega_\beta^{-1}$. The Lorentz factor can be then

approximated as

$$\gamma = \sqrt{1 + \tilde{p}_x^2 + \tilde{p}_{z0}^2} = \sqrt{1 + \tilde{p}_{z0}^2}\sqrt{1 + \frac{\tilde{p}_x^2}{1 + \tilde{p}_{z0}^2}} \quad (6)$$

$$\approx \gamma_0\left(1 + \frac{\tilde{p}_x^2}{2\gamma_0^2}\right), \quad (7)$$

where $\gamma_0 = \sqrt{1 + \tilde{p}_{z0}^2}$, which is the initial Lorentz factor, and since we are considering pre-accelerated relativistic electrons also, $\gamma_0 \gg 1$. Further on, we have

$$\omega_\beta^2 = \frac{\omega_p^2}{2\gamma} \approx \frac{\omega_p^2}{2\gamma_0}\left(1 - \frac{\tilde{p}_x^2}{2\gamma_0^2}\right) = \omega_{\beta_0}^2\left(1 - \frac{\tilde{p}_x^2}{2\gamma_0^2}\right). \quad (8)$$

The paraxial approximation $p_x \ll p_z$ with $v_z \approx c$ further allows us to approximate frequency seen by electrons as $\dot{\phi}_i = (1 - v_z/v_{pi})\omega_{0i} = \eta_i\omega_{0i} = \omega_i \approx$ const.; therefore, the laser phase satisfies $\phi_i(t) \approx \omega_i t + \theta_i$. We note that the relative laser phase $(\theta_2 - \theta_1)$ influences the detailed structure of simultaneous resonances, as discussed in Ref. [28]; however, the maximum attainable transverse momentum amplitude, which we are interested in, remains the same for all relative phase shifts. Therefore, we do not concern ourselves further with this parameter and, for brevity, set $\theta_2 = \theta_1 = 0$. Plugging Eq. (8) into Eq. (5) gives

$$\frac{d^2\tilde{p}_x}{dt^2} + \omega_{\beta_0}^2\tilde{p}_x - \frac{\omega_{\beta_0}^2}{2\gamma_0^2}\tilde{p}_x^3 = \sum_{i=1}^2 \tilde{a}_i \cos(\omega_i t). \quad (9)$$

Equation (9) has the form of the Duffing equation with two-frequency forcing [28]. We will summarize the most important consequences of nonlinear Eq. (9), as discussed in Ref. [28]. We see that the nonlinearity coefficient of $\tilde{p}_x^3$ in Eq. (9), i.e., $-\omega_{\beta_0}^2/2\gamma_0^2$, has a negative sign, indicating a softening nonlinearity of the system, which means that the multivalued amplitude-frequency response curve bends toward frequencies below $\omega_i \approx \omega_{\beta_0}$. For a fixed γ_0, the nonlinearity changes only with electron density n_e. In addition, nonlinearity in Eq. (9) allows for multiple nonlinear resonances apart from the primary resonance $\omega_i \approx \omega_{\beta_0}$. The condition for these resonances can be generally given as

$$\omega_{\beta_0} \approx \frac{m}{n}\omega_i, \quad (10)$$

where m and n are natural numbers, $i = 1, 2$, and either $m = n = 1$ (primary resonance), $m = 1, n \neq 1$ (subharmonic resonances), or $n = 1, m \neq 1$ (superharmonic resonances). The strengths and widths of the frequency ranges in which these resonances occur decrease dramatically for large m, n; therefore, only small values of m, n are usually observed [28,33]. We note that harmonic resonances in Eq. (10) arise even in single-frequency-driven nonlinear oscillations. Multifrequency forcing, however, generates additional combination resonances in nonlinear oscillations. The principal combination resonances are given by the following conditions:

$$\omega_{\beta_0} \approx |\pm 2\omega_i \pm \omega_j|, \quad (11)$$

$$\omega_{\beta_0} \approx \frac{1}{2}(\omega_i \pm \omega_j), \quad (12)$$

where $i, j = 1, 2$ [28]. The presence of two forcing terms also enables simultaneous resonances to occur, i.e., for given frequencies ω_i, the resonance conditions in Eqs. (10)–(12) may overlap.

The main physical mechanism behind transverse momentum enhancement in two-color forced oscillations is therefore twofold. First, we have superposed primary, subharmonic, and superharmonic resonances from respective laser fields given by Eq. (10). Second, we obtain the combination resonances Eqs. (11) and (12), which are unique to multifrequency forcing, further enriching the range of possible resonances as well as enabling simultaneous resonances for oscillating electrons. The immediate consequence of the presence of such resonances in electron oscillations is the enhancement of betatron x-ray radiation due to transverse momentum enhancement, as it is discussed in Sec. I.

We note that this model of forced betatron oscillations of relativistic electrons close to dephasing with $\gamma \gg 1$ is qualitatively valid, even when weak longitudinal electrostatic wakefield is included in the equations of motion in Eqs. (1) and (2). Such inclusion causes the decrease of the betatron frequency $\omega_\beta \approx \gamma^{-1/2}$ and slow increase of the strength parameter $K \approx \gamma^{1/4}$ due to electron energy gain $\sim \gamma$ on a timescale much longer than the timescale of betatron oscillations $\tau_\beta \approx \omega_\beta^{-1}$ [7]. To be precise, our description is valid for slowly varying betatron frequency satisfying the condition $\omega_\beta^2 \gg |\dot{\omega}_\beta| \approx 0$, for which the nonlinear oscillator model is not affected by the negligible betatron frequency change. The previous assumption is further validated for relativistic electrons close to dephasing in Sec. IV, where it is also shown that the conditions for transverse momentum resonance hold even in full PIC simulations.

III. SINGLE-PARTICLE SIMULATIONS

The equations of motion in Eqs. (1) and (2), for a relativistic electron oscillating in plasma cavity with a presence of one or two laser fields in the paraxial approximation, were solved numerically using the fourth-order Runge-Kutta scheme of numerical integration with time step small enough to achieve numerical convergence. The calculation is simplified considerably due to the paraxial approximation $p_x \ll p_z$, $v_z \approx c$, which allows us to consider the laser phase as $\phi_i(t) \approx \omega_i t$. Note that, here, we do not consider the approximation $\dot{p}_z \approx 0$ as in Sec. II. The structure of resonances does not depend on the choice of initial transverse momentum [28], and therefore, we set it for all cases as $\tilde{p}_x(0) = 0$. We neglect the presence of the longitudinal wakefield since we consider relativistic electrons close to dephasing, as discussed in Sec. II. We set field strengths as $a_1 \approx a_2 \approx 1$, corresponding to experimentally accessible values for harmonics of the driving laser. We consider both cases of single and two-color configuration. Lastly, we conduct simulations for a large range of plasma densities beyond the $n_e \approx 10^{19}$ cm^{-3} that is usually used for betatron x-ray generation to reveal the structure of resonances even in the strongly nonlinear regime.

In the *single-color case*, a relativistic electron interacts only with a single laser field with ω_1, which corresponds to the schematic in Fig. 1 when laser with ω_2 is not present. In Figs. 2(a) and 2(b), we show the frequency response of
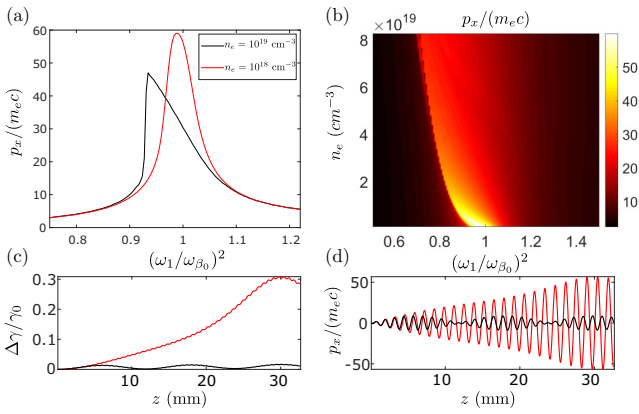
FIG. 2. Single-color case. (a) Frequency response of $\tilde{p}_x$ for $p_x(0) = 0$. Nonlinearity emerges for higher values of electron plasma density n_e. For $n_e = 5 \times 10^{18}$ cm^{-3} (red), we see linear response for resonance conditions in the range $(\omega_1/\omega_{\beta_0})^2 \in (0.8, 1.2)$ corresponding to initial energies $\gamma_0 \in (1.5, 2.5) \times 10^4$, and we see strong nonlinear response for higher density $n_e = 5 \times 10^{19}$ cm^{-3} (black) for $(\omega_1/\omega_{\beta_0})^2 \in (0.8, 1.2)$ corresponding to $\gamma_0 \in (1.5, 2.5) \times 10^3$. (b) Frequency response of $\tilde{p}_x$ for varying n_e. (c) Normalized energy gain and (d) transverse momentum evolution for $n_e = 5 \times 10^{18}$ cm^{-3}, $(\omega_1/\omega_{\beta_0})^2 = 0.8$, $\gamma_0 = 3.2 \times 10^3$ (black), and $(\omega_1/\omega_{\beta_0})^2 = 0.9$, $\gamma_0 = 3.6 \times 10^3$ (red). The nonshifted laser wavelength is $\lambda_1 = 404$ nm.

normalized transverse momentum amplitude, which is the maximum transverse momentum an electron achieves during periodic resonant oscillations. The frequency ratio $\omega_1/\omega_{\beta_0}$ is tuned by varying the initial electron energy since, for a fixed laser frequency and density, we have $(\omega_1/\omega_{\beta_0})^2 \approx \gamma_0$. We observe the emergence of nonlinear response for increasing plasma density n_e featuring up-jump discontinuity and the bending of the frequency response curve as predicted by Eq. (9). We note that the initial condition $\tilde{p}_x(0) = 0$ leads to the lower branch of the resonance curve for frequencies smaller than that corresponding to the up-jump discontinuity [28]. Larger initial momenta $p_x(0) \neq 0$ may lead to upper-branch amplitudes producing larger transverse momentum amplitudes left of the jump discontinuity, as is usual in multivariate frequency responses of nonlinear oscillators. The structure of the resonances, however, does not depend on the initial condition as previously noted. Figures 2(c) and 2(d) show that, within the paraxial approximation, resonant interaction leads to substantial energy and normalized transverse momentum gain even in the single-color case.

In the *two-color case*, two laser fields are interacting with electrons, as shown schematically in Fig. 1. The frequency response of the normalized transverse momentum amplitude with varying electron plasma density is shown in Fig. 3(a). We see two primary resonance regions due to ω_1 and ω_2. We also see that increasing density leads to stronger nonlinearity, as predicted by Eq. (9). For high values of electron plasma density n_e, the emergence of harmonic and simultaneous resonances creates detached regions of large transverse momentum. Figure 3(b) shows a strongly nonlinear region with $n_e > 5 \times 10^{19}$ cm^{-3}, where complex structures of simultaneous, combination, and harmonic resonances emerge. We
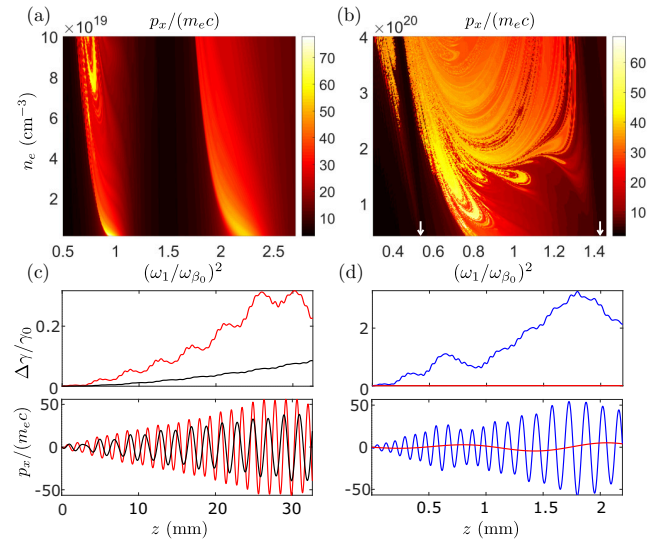

FIG. 3. Two-color case. (a) Frequency response of $\tilde{p}_x$ for $p_x(0) = 0$ with varying n_e. (b) The strongly nonlinear region for $n_e > 5 \times 10^{19}$ cm^{-3}. (c) Normalized energy gain and (d) transverse momentum evolution for $n_e = 5 \times 10^{18}$ cm^{-3}, $(\omega_1/\omega_{\beta_0})^2 = 0.9$, $\gamma_0 = 3.6 \times 10^3$ (red), and $(\omega_1/\omega_{\beta_0})^2 = 2.1$, $\gamma_0 = 8.6 \times 10^3$ (black), and for $n_e = 8 \times 10^{19}$ cm^{-3}, $(\omega_1/\omega_{\beta_0})^2 = 0.8$, $\gamma_0 = 2 \times 10^2$ (blue). White arrows indicate emergence of nonlinear resonances $(\omega_1/\omega_{\beta_0})^2 = 0.5625, 1.44$. The nonshifted laser wavelengths are $\lambda_1 = 404$ nm and $\lambda_2 = 269$ nm.

indicate [white arrows in Fig. 3(b)] emergence of some of the nonlinear resonances predicted by Eqs. (10)–(12). For example, since the shifted frequency of the TH is $\omega_2 \approx (\frac{2}{3})\omega_1$, Eq. (12) gives combination resonance $[\omega_1 + (\frac{2}{3})\omega_1]/2 = \omega_{\beta_0}$; therefore, $(\omega_1/\omega_{\beta_0})^2 \approx 1.44$ (white arrow on the right). An interesting feature seen in Fig. 3(a) is that, since for a fixed electron density n_e we have $(\omega_i/\omega_{\beta_0})^2 \approx \gamma_0$, nonlinearity is strongly suppressed in the primary resonance region from ω_2, which is positioned at $(\omega_1/\omega_{\beta_0})^2 = 2.25$. This is predicted by the inverse cube dependence of the nonlinearity coefficient on high initial electron energy in Eq. (9), i.e., $\omega_{\beta_0}^2/2\gamma_0^2 = \omega_p^2/4\gamma_0^3$. Figures 3(c) and 3(d) show selected resonant evolutions. We draw attention to the benefit of employment of higher frequency lasers, in this case ω_2, since they induce otherwise unattainable primary resonance for electrons accelerated through LWFA to high energies $\gamma_0 \approx (\omega_2/\omega_{\beta_0})^2$, boosting their $\tilde{p}_x$.

Single-particle simulations reveal the structure of the resonances present in betatron oscillations of relativistic electrons close to dephasing when interacting with a two-color laser field in the paraxial approximation. We have shown the emergence of nonlinear resonances in Eqs. (10)–(12) predicted by Eq. (9). We note that single-particle simulations neglect the spatial and temporal profile of the laser pulses as well as its self-focusing and depletion or the presence of accelerating longitudinal plasma wakefield and its evolution. To account for full dynamics, we conducted PIC simulations described in the following section.

IV. PIC SIMULATIONS

To confirm the presence of two-color nonlinear resonances beyond the paraxial approximation in full detail throughout the LWFA process, we performed 2D PIC simulations within the fully relativistic, massively parallelized PIC code EPOCH [34]. The approximation of 2D geometry is reasonable since all lasers are set with the same linear polarization in the x direction within the x-z plane of the simulation, which forces the dynamics of the electron oscillations and the associated resonances induced by the interacting lasers into a 2D plane. The second-order Yee scheme Maxwell solver was used in the PIC simulations. To reduce numerical dispersion in the second-order scheme, the Courant-Friedrichs-Lewy number was set as $c\Delta t/\Delta z = 0.99$. The moving window simulation box was set as $100\times70\,\mu$m with grid size 6000×1000, which corresponds to 16 cells per wavelength for the shortest laser wavelength in the simulation $\lambda_2 = 269$ nm, ensuring proper resolution of all wavelengths involved. Furthermore, third-order interpolation of fields to particles was used to further suppress numerical heating and time-staggering error [35,36]. The number of macro-particles per cell was two. The lasers were focused upon the entrance into the 5-mm-long homogeneous pre-ionized helium gas target with smooth edges and plateau value of electron plasma density $n_e = 4\times10^{18}$ cm^{-3}. Such gas targets are routinely used in plasma betatron x-ray sources [6,17,21]. The value of plasma density was selected this low to generate a larger bubble and therefore prevent interaction of the accelerating electrons with the laser tail of the LWFA-driving frequency ω_d. To simplify the analysis, we focus purely on the dynamics of the electrons and the laser. We therefore neglect collisions, ionization, or quantum electrodynamics effects, although we note that interference effects can play a role in two-color laser ionization injection [34,37,38].

In the *nonresonant case*, only the LWFA-driving laser with ω_d shown in Fig. 1 is present with $\lambda_0 = 808$ nm. Laser strength was set as $a_0 = 5.3$, full width at half maximum (FWHM) pulse duration $\tau_0 = 28$ fs, and waist diameter $d_0 = 28\,\mu$m. This case corresponds to standard LWFA and betatron x-ray generation since the laser does not interact with the accelerating electrons due to low plasma density and consequently large bubble radius.

In the *single-color case*, the driving laser was set as in the previous case. The SH was set with $\lambda_1 = 404$ nm, $a_1 = 1.2$, $\tau_1 = 56$ fs, and $d_1 = 10\,\mu$m. To place the peak of the SH in the interaction region where electrons oscillate, the peak-to-peak time delay between the two pulses was set to 100 fs. The time delay was set to place the SH in the interaction region where electrons accelerate without overlapping with the electron bubble sheath. This case corresponds to single-color betatron resonance since the driving laser does not interact with the accelerating electrons, and resonant oscillations are induced by the SH ω_1. In terms of the schematic in Fig. 1, the laser corresponding to frequency ω_2 is not present.

In the *two-color case*, the driving laser was as in the previous cases. The SH had slightly shorter pulse duration with $\lambda_1 = 404$ nm, $a_1 = 1.2$, $\tau_1 = 42$ fs, and $d_1 = 10\,\mu$m to compensate for frequency conversion into the TH. The peak-to-peak time delay to the LWFA-driving laser was 92 fs.
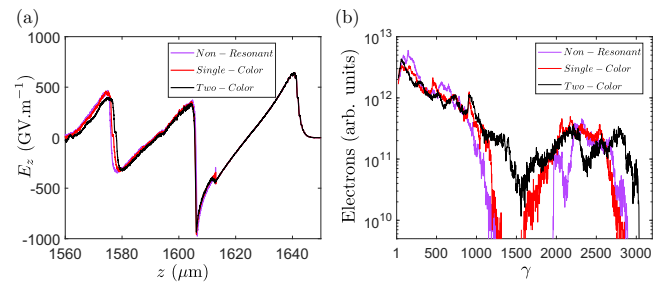

FIG. 4. (a) Longitudinal electrostatic wakefields at 1.6 mm inside the gas target for all three cases. (b) Electron spectra at gas target exit at 5 mm.

The TH was also present with $\lambda_2 = 269$ nm, $a_2 = 0.7$, $\tau_2 = 56$ fs, and $d_2 = 10\,\mu$m, and the peak-to-peak time delay to the fundamental was 100 fs. This case corresponds to single-color betatron resonance since the driving laser does not interact with the accelerating electrons, and resonant oscillations are induced by the SH ω_1. In terms of the schematic in Fig. 1, the laser corresponding to frequency ω_2 is not present. We note that the field of the harmonics interacting with the electrons is kept stable due to the plasma cavity generated by the main driver with ω_d. The high-density electron sheath of the cavity acts as a waveguide for the small amplitude harmonics, which would otherwise diffract in plasma or vacuum over few Rayleigh lengths.

The total number of accelerated electrons is comparable in all three cases. This is understandable since the SH with $a_1 = 1.2$ does not overlap with the electron plasma sheath, and the TH with peak strength $a_2 = 0.7$ overlaps with the sheath only in the region where $a_2 \approx 0.3$, which means that the ponderomotive force $\sim\nabla a^2$ has negligible effect on the evolution of the wake driven by the fundamental harmonic with $a_0 = 5.3$. In Fig. 4(a), we show that the accelerating wakefields for all cases vary $<5\%$ at 1.6 mm inside the target, where the first injected electron bunches are accelerated.

It is also important to consider possible dimensional effects of the wake evolution. It has been shown that, in 2D simulations, the wakefield plasma bubble is elongated, and the focusing fields are stronger than in the case of three-dimensional (3D) simulations of plasma wakefield, while the structure of the accelerating field inside the cavity remains
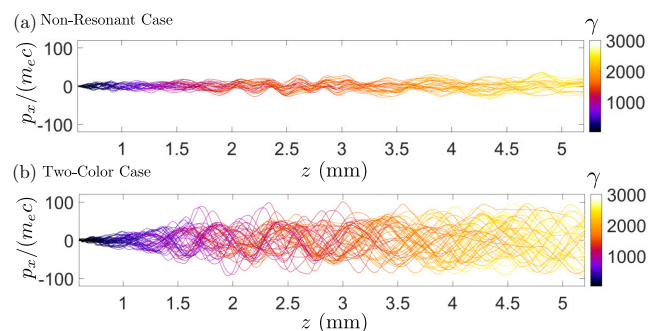

FIG. 5. $\tilde{p}_x$ and γ evolutions for electrons that reach $\gamma > 1800$. (a) Nonresonant case, where no electrons are interacting with a laser. (b) Two-color case.
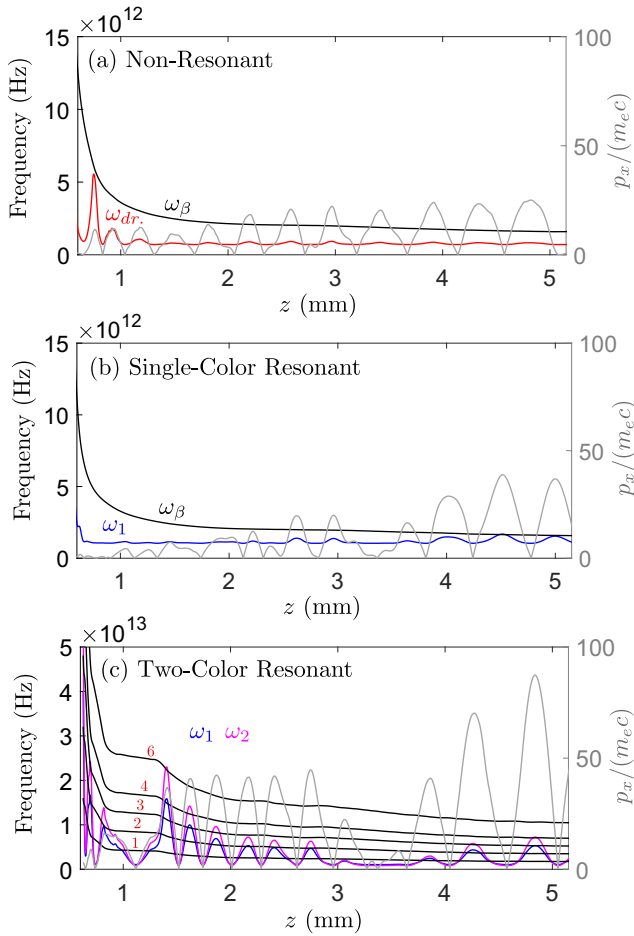
FIG. 6. Shifted laser frequencies $\omega_{1,2}$ seen by a representative electron (left axis, colored), betatron frequency harmonics $n\omega_\beta$ (left axis, black, orders highlighted by red number), and absolute value of normalized transverse momentum $p_x/m_e c$ (right axis, gray).

unchanged in both cases [39]. The reduction of the bubble in the realistic 3D case can be simply compensated by changing group delays of the harmonics with respect to the LWFA driver. Weaker focusing fields in 3D geometry also imply possibly larger efficiency of our scheme since weaker focusing fields reduce the oscillator stiffness of the cavity, and therefore, betatron frequency ω_β is reduced, which for oscillator systems leads to enhancement of resonant amplitude [28]. The effect on the wake by ponderomotive force of the harmonics due to increasing field strength a_0 is analyzed further in Sec. V. Figure 4(b) shows the electron spectra for all three cases at the gas target exit. The total injected charge of electrons accelerated to energy >100 MeV varies by <0.1% when comparing nonresonant and two-color resonant cases, showing negligible effect of the harmonics on the overall electron injection.

In Fig. 5, we show normalized transverse momentum and γ evolution of the most energetic electrons for the nonresonant and two-color cases. For an electron interacting with an electromagnetic wave in a vacuum, the normalized transverse momentum amplitude is limited by the value $\tilde{p}_x < a_0$. The peak amplitudes of harmonics satisfy $a_{1,2} \approx 1$, and we see that

the amplitude of normalized momentum reaches $\tilde{p}_x \approx 100$ in the two-color case, while in the nonresonant case, we see that the natural betatron oscillations are limited to normalized transverse momentum of $\tilde{p}_x \approx 30$. This proves the presence of the resonance phenomenon. A more careful analysis showing the presence of nonlinear resonances is presented in Fig. 6, where we show the evolutions of laser frequencies seen by a representative electron, betatron frequency, and normalized transverse momentum of the electron for all three cases. The nonresonant case shows that Eq. (10) is not satisfied throughout the evolution, and there is no associated growth of transverse momentum amplitude. The single-color resonant case shows primary resonance $\omega_1 \approx \omega_\beta$ and the associated transverse momentum growth between 4 and 5 mm from the entrance of the target. The two-color resonant case shows nonlinear resonances for both shifted frequencies seen by the electron ω_1, ω_2 with harmonic orders $n = 1, 2, 3, 4, 6$. We see that the strongest resonant growth reaching $\tilde{p}_x \approx 90$ corresponds to simultaneous harmonic resonance when $3\omega_\beta \approx \omega_1$ and $4\omega_\beta \approx \omega_2$ around 4.8 mm from the entrance of the target.

V. X-RAY RADIATION ANALYSIS

To see the effect of two-color resonance on x-ray radiation emitted by the accelerated electrons, we have calculated the on-axis photon flux for all three PIC cases according to the radiation integral [18]

$$\frac{\mathbf{d}^2 W}{\mathbf{d}\Omega\mathbf{d}\omega} = \frac{e^2}{16\pi^3\epsilon_0 c} \left| \int_{-\infty}^{\infty} \frac{\mathbf{n} \times ((\mathbf{n} - \boldsymbol{\beta}) \times \dot{\boldsymbol{\beta}})}{(1 - \mathbf{n} \cdot \boldsymbol{\beta})^2} \right.$$
$$\left. \times \exp\left[i\omega\left(1 - \frac{\mathbf{n} \cdot \mathbf{R}}{c}\right)\right] dt \right|^2, \quad (13)$$

where $\mathbf{R}$ is the distance vector between the radiating electron and the observer, $\mathbf{n}$ is the normalized vector pointing from the electron toward the observer, and $\boldsymbol{\beta} = \mathbf{v}/c$ is the normalized velocity. We extracted the electron trajectories from the PIC simulation results to calculate the radiation emitted according to Eq. (13). The knowledge of acceleration of the particle $\dot{\boldsymbol{\beta}}$ is necessary, which was calculated by interpolating the individual particle trajectories with a time step sufficiently small to achieve numerical convergence in Eq. (13). The results are presented in Fig. 7. We observe enhancement in the single-color case. However, a larger enhancement of more than an order of magnitude in peak photon flux and up to two orders of magnitude enhancement in the hard x-ray region is present in the two-color case, when compared with nonresonant betatron x-ray generation. The critical energy for the nonresonant case is calculated as $\hbar\omega_c \approx 25$ keV, while for the two-color resonant case is $\hbar\omega_c \approx 31$ keV. We see that the number of photons is enhanced almost uniformly across the whole energy spectrum, with a stronger boost in the hard x-ray region.

Our results can be compared with previously published works focusing on betatron x-ray enhancement mentioned in Sec. I, for example, by longitudinal and transverse density modulation in Ref. [21], where an order of magnitude enhancement was achieved in the hard x-ray region and a factor of $\sim$2–3 in peak photon flux. In Ref. [20], a shift of critical energy into the millielectronvolt range due to the resonant
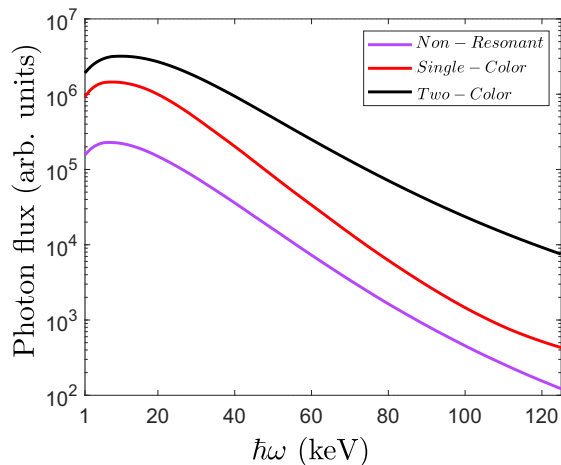
FIG. 7. On-axis photon flux of radiated x rays in log scale. Non-resonant case (purple), single-color case (red), and the two-color case (black).

interaction of LWFA electrons with the laser tail of the driving laser was observed without peak photon flux enhancement. A peak photon flux enhancement due to resonant interaction with the laser tail from ionization injected electrons by a factor ∼3 compared with results in Ref. [20] was reported in Ref. [27]. An order of magnitude enhancement was also achieved within the mildly nonlinear regime by steering the plasma wakefield driven by a laser with $a_0 = 1.6$ by introducing a slanted plasma target [25], where the betatron strength parameter K in the reference betatron case without steering was $K \approx 2.1$. We note that this is more than an order of magnitude less than our reference nonresonant case with giga-electronvolt range electrons reaching $K \approx 30$. We further note that the only requirement of our method is frequency conversion of the LWFA-driving laser into its harmonics, implying its potential compatibility with various plasma targets.

As mentioned in Sec. IV, the interacting laser field strengths a_i cannot be too strong since the ponderomotive force scales as $\sim \nabla a^2$, which adversely affects wake evolution, resulting in poor electron injection and acceleration. To show this in terms of radiated x rays, we performed four different PIC simulations with the same parameters as in the two-color resonant case discussed earlier, except we did not include the SH and only kept the TH overlapping with the plasma sheath. In Fig. 8, we see the radiated energy where the fundamental laser acts as a LWFA driver, and the TH induces betatron resonance in oscillating electrons. We have varied the field strength of the TH for values $a_0 = 0.4, 0.7, 1, 1.5$. The results show that x-ray photon flux starts dropping when a_0 approaches and surpasses the value $a_0 \approx 1$, indicating modified wake dynamics by ponderomotive force and inefficient resonant oscillations. We note, however, that even in this inefficient case where $a_0 = 1.5$, the peak photon flux is still a factor of 2.5 larger than the standard betatron x-ray generation denoted above as the nonresonant case. We see that, for the settings presented above, the value of $a_2 = 0.7$ is optimized for efficient radiation generation.

Lastly, we evaluate the practical energy efficiency of the two-color scheme. Let us consider a 7 J energy laser pulse
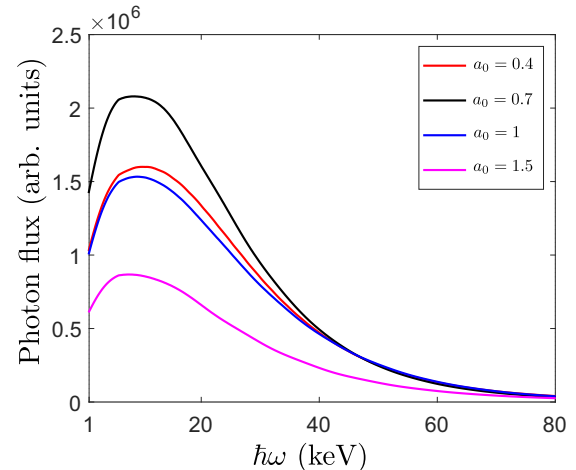

FIG. 8. On-axis photon flux of betatron x rays in linear scale showing decrease in radiated energy due to perturbation of the wake through increasing ponderomotive force of the third harmonic (TH). The laser fields present in the particle-in-cell (PIC) simulation are only the fundamental laser wakefield acceleration (LWFA) driver with wavelength $\lambda_d = 808$ nm and the TH with ω_2.

having the same spatial and temporal parameters as discussed for the LWFA driver with fundamental wavelength $\lambda_d = 808$ nm. This results in the field strength $a_0 \approx 6$. We denote this case *nonresonant, 7 J*. If we consider splitting off 1.9 J laser energy from the main 7 J beam and converting it to the SH and TH with conversion efficiency ∼11%, where we take into consideration both parametric efficiency and other losses as discussed in Sec. VI, we may obtain the SH and TH with respective pulse energies of ∼0.2 J, which corresponds to the spatial and temporal pulse parameters and field strengths of the harmonics as presented in the two-color resonant case. Here, we denote this case *two-color, 5.5 J*. In Fig. 9, we show that the photon flux of the second case with 5.5 J in total laser energy divided among the ω_d (5.1 J), ω_1 (0.2 J), and ω_2 (0.2 J) is still significantly larger than for the case with the whole
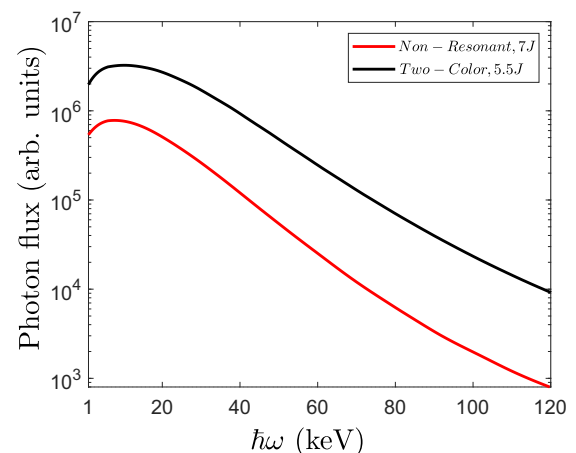

FIG. 9. On-axis photon flux of betatron x rays in log scale showing energy efficiency of the two-color betatron resonant x-ray generation.
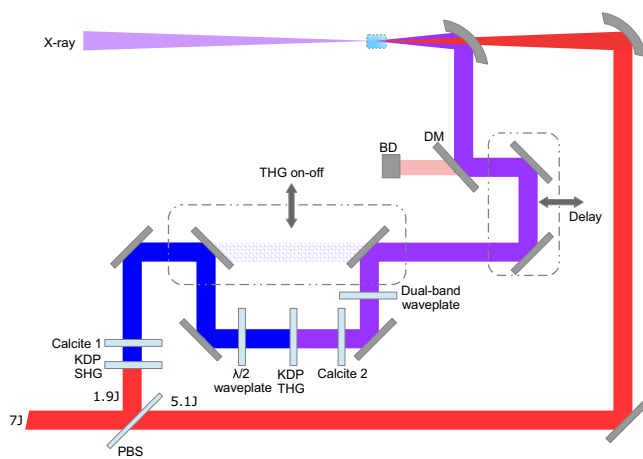
FIG. 10. Experimental setup design for realization of two-color resonant betatron x-ray generation.

7 J of energy in the LWFA driver ω. This result indicates that the enhancement from two-color betatron resonance is highly efficient, and even when considering losses of 1.5 J, we still get almost an order of magnitude enhancement in peak on-axis photon flux and more than an order of magnitude enhancement in the hard x-ray region. This shows that the enhancement from two-color betatron resonance cannot be reasonably replaced by boosting field strength a_0 in standard betatron x-ray generation. Crucially, we also point out that the nonresonant 7 J case results in 21% more injected total charge than the 5.5 J two-color case; however, not even this fact offsets the strong photon flux enhancement due to transverse momentum nonlinear resonances.

VI. EXPERIMENTAL SETUP DESIGN

To complement our theoretical results, we propose the experimental setup, shown in Fig. 10, for realization of two-color resonant betatron x-ray generation. Standard betatron x-ray generation involves a single ultraintense $I \geqslant 10^{18}$ Wcm^{-2} femtosecond laser pulse from a Ti:sapphire laser system centered at 808 nm and either a gas cell or a gas jet, where the gas is usually helium with a small percentage of some noble gas added to trigger ionization injection and achieve greater beam stabilization [40]. The advanced betatron scheme presented here requires the generation of the SH and TH of the fundamental 808 nm wavelength with pulse energy ~200 mJ and pulse duration ~50 fs. Frequency tripling can be achieved directly in materials with strong third-order susceptibility with conversion efficiencies up to 6% [41]. However, due to higher conversion efficiency, a more commonly used method is of sum-frequency generation, which benefits from high values of second-order nonlinearity in crystals [42]. For Ti:sapphire frequency conversion, the widely used crystals for both frequency doubling and tripling are BBO and KDP [43]. For pulse duration of tens of femtoseconds, BBO crystals have the advantage over KDP in an almost six-times-higher effective nonlinear coefficient [44,45], but its spectral acceptance caused by group delay dispersion is roughly three times worse than in KDP crystals. The damage

threshold for BBO crystals is on the order of hundreds of gigawatts per square centimeter for femtosecond pulses [46]. Combined with the difficulties involved in manufacturing of large aperture crystals, it is almost impossible to use BBO for few-joule femtosecond pulses.

To relate to the theoretical results, a 7 J, 28 fs FWHM infrared (IR) laser pulse produced from a Ti:sapphire laser system is considered in the experimental setup; therefore, KDP crystals are considered further. The necessity of delay control between the IR LWFA driver and its harmonics leads to a two-arm experimental setup, where one arm has variable time delay. This requires micrometer-precise spatial synchronization and stability of the two differently focused beams [47]. In the proposed setup, a pellicle beamsplitter extracts a 1.9 J portion of the beam into the harmonic generation arm without any changes in the transmitted beam due to its thinness. The first KDP is a 1-mm-thick type-1 crystal used for efficient SH generation (SHG). The efficiency for hundreds of femtosecond pulses can reach as high as 80%, as discussed in Ref. [48]. However, we consider pulse lengths on the order of ~50 fs in our PIC simulations. Thus, the efficiency will be reduced due to group velocity dispersion. Calcite 1 is negative uniaxial crystal used for compensation of group delay between IR and SH pulses originated in KDP as well as in the half-waveplate. The temporal overlap of IR and SH pulses is crucial in the second KDP crystal used for TH generation (THG). A thin, zero-order half-waveplate for IR wavelength also serves as a λ waveplate for the SH, which assures parallel polarization for both the IR and SH to ensure THG type-1 phase matching in the second KDP crystal. This is to exploit the higher conversion efficiency of type-1 over type-2 THG [42,43]. THG in this configuration can lead to conversion efficiency up to 11%, as discussed in Ref. [43]. Calcite 2 is used (similarly to Calcite 1) for group delay compensation between the residual SH and the generated TH. A dual-band waveplate is optimized as $\lambda/2$ for the SH and λ for the TH to rotate polarizations of the SH and TH to be parallel, it can be easily moved out to switch to a configuration where the TH is perpendicular to the SH. Group delay from the dual-band waveplate is also compensated by Calcite 2.

The proposed setup has the possibility to easily switch off THG (THG on-off) with a motorized linear stage and therefore easily go between single-color, two-color, or two-color with a single harmonic, where resonance is achieved due to a long-pulse LWFA-driving laser and a SH with tunable laser polarizations. A dichroic mirror is optimized for reflectance of the TH and SH and therefore transmits the residual IR pulse into the beam dump. According to discussed efficiencies, this system should be capable of delivering three-color interaction into the target composed of 5.1 J IR, 200 mJ SH, and 200 mJ TH ultrashort pulses. For higher energy laser systems, even greater range of optimization is possible with more energy in the IR beam and possibly the harmonics as well, if crystals of large enough aperture are available. The advantages of this setup are the full control over the laser polarizations and the delays between the IR and SH as well as between the SH and TH and separate focusing for the harmonics through an off-axis parabola with a hole. The conversion efficiency can be tuned with crystal angle tuning.

VII. CONCLUSIONS

In summary, we have presented theory and numerical results exploring two-color nonlinear resonances in betatron oscillations and an experimental setup design for realization of our scheme. We have shown that the dynamics of relativistic electrons reduce to nonlinear oscillations with two-frequency forcing, which causes the emergence of nonlinear resonances in transverse momentum. PIC simulations for experimentally accessible parameters reveal two-color betatron resonance behavior beyond the paraxial approximation, showing strong enhancement of electron transverse momentum. The radiation emitted by electrons undergoing such resonant oscillations is enhanced by more than an order of magnitude in

peak photon flux and up to two orders of magnitude in the hard x-ray region when compared with standard betatron x-ray generation.

[1] T. Tajima and J. M. Dawson, Laser Electron Accelerator, Phys. Rev. Lett. **43**, 267 (1979).

[2] A. J. Gonsalves *et al.*, Petawatt Laser Guiding and Electron Beam Acceleration to 8 Gev in a Laser-Heated Capillary Discharge Waveguide, Phys. Rev. Lett. **122**, 084801 (2019).

[3] A. Pukhov and J. Meyer-ter Vehn, Laser wake field acceleration: the highly non-linear broken-wave regime, Appl. Phys. B **74**, 355 (2002).

[4] W. Lu, C. Huang, M. Zhou, W. B. Mori, and T. Katsouleas, Nonlinear Theory for Relativistic Plasma Wakefields in the Blowout Regime, Phys. Rev. Lett. **96**, 165002 (2006).

[5] S. Kiselev, A. Pukhov, and I. Kostyukov, X-Ray Generation in Strongly Nonlinear Plasma Waves, Phys. Rev. Lett. **93**, 135004 (2004).

[6] A. Rousse, K. T. Phuoc, R. Shah, A. Pukhov, E. Lefebvre, V. Malka, S. Kiselev, F. Burgy, J.-P. Rousseau, D. Umstadter, and D. Hulin, Production of a keV X-Ray Beam from Synchrotron Radiation in Relativistic Laser-Plasma Interaction, Phys. Rev. Lett. **93**, 135005 (2004).

[7] S. Corde, K. Ta Phuoc, G. Lambert, R. Fitour, V. Malka, A. Rousse, A. Beck, and E. Lefebvre, Femtosecond x rays from laser-plasma accelerators, Rev. Mod. Phys. **85**, 1 (2013).

[8] S. Fourmaux, E. Hallin, U. Chaulagain, S. Weber, and J. Kieffer, Laser-based synchrotron x-ray radiation experimental scaling, Opt. Express **28**, 3147 (2020).

[9] F. Albert, A. Thomas, S. Mangles, S. Banerjee, S. Corde, A. Flacco, M. Litos, D. Neely, J. Vieira, Z. Najmudin, R. Bingham, C. Joshi, and T. Katsouleas, Laser wakefield accelerator based light sources: potential applications and requirements, Plasma Phys. Controlled Fusion **56**, 084015 (2014).

[10] J. Wenz, S. Schleede, K. Khrennikov, M. Bech, P. Thibault, M. Heigoldt, F. Pfeiffer, and S. Karsch, Quantitative x-ray phase-contrast microtomography from a compact laser-driven betatron source, Nat. Commun. **6**, 7568 (2015).

[11] U. Chaulagain, K. Bohacek, M. Kozlova, J. Nejdl, M. Krus, V. Horny, B. Mahieu, and K. Ta-Phuoc, X-ray phase contrast imaging of biological samples using a betatron x-ray source generated in a laser wakefield accelerator, in *Laser Acceleration of Electrons, Protons, and Ions IV* (International Society for Opti and Photonics, Bellingham, WA, 2017), Vol. 10240, p. 1024014.

[12] J. C. Wood *et al.*, Ultrafast imaging of laser driven shock waves using betatron x-rays from a laser wakefield accelerator, Sci. Rep. **8**, 11010 (2018).

[13] B. Mahieu, N. Jourdain, K. T. Phuoc, F. Dorchies, J.-P. Goddet, A. Lifschitz, P. Renaudin, and L. Lecherbourg, Probing warm dense matter using femtosecond x-ray absorption spectroscopy with a laser-produced betatron source, Nat. Commun. **9**, 3276 (2018).

[14] J.-N. Gruse *et al.*, Application of compact laser-driven accelerator x-ray sources for industrial imaging, Nucl. Instrum. Methods Phys. Res. Sect. A **983**, 164369 (2020).

[15] B. Kettle *et al.*, Single-Shot Multi-Kev X-Ray Absorption Spectroscopy Using an Ultrashort Laser-Wakefield Accelerator Source, Phys. Rev. Lett. **123**, 254801 (2019).

[16] E. Esarey, B. A. Shadwick, P. Catravas, and W. P. Leemans, Synchrotron radiation from electron beams in plasma-focusing channels, Phys. Rev. E **65**, 056505 (2002).

[17] S. Fourmaux, S. Corde, K. Ta Phuoc, P. M. Leguay, S. Payeur, P. Lassonde, S. Gnedyuk, G. Lebrun, C. Fourment, V. Malka, S. Sebban, A. Rousse, and J. C. Kieffer, Demonstration of the synchrotron-type spectrum of laser-produced betatron radiation, New J. Phys. **13**, 033017 (2011).

[18] J. D. Jackson, *Classical Electrodynamics* (John Wiley & Sons, New York, 1999).

[19] B. Lei, J. Wang, V. Kharin, M. Zepf, and S. Rykovanov, γ-Ray Generation from Plasma Wakefield Resonant Wiggler, Phys. Rev. Lett. **120**, 134801 (2018).

[20] S. Cipiccia *et al.*, Gamma-rays from harmonically resonant betatron oscillations in a plasma wake, Nat. Phys. **7**, 867 (2011).

[21] M. Kozlova, I. Andriyash, J. Gautier, S. Sebban, S. Smartsev, N. Jourdain, U. Chulagain, Y. Azamoum, A. Tafzi, J.-P. Goddet, K. Oubrerie, C. Thaury, A. Rousse, and K. Ta Phuoc, Hard X Rays from Laser-Wakefield Accelerators in Density Tailored Plasmas, Phys. Rev. X **10**, 011061 (2020).

[22] Y. Ma, L. Chen, D. Li, W. Yan, K. Huang, M. Chen, Z. Sheng, K. Nakajima, T. Tajima, and J. Zhang, Generation of femtosecond γ-ray bursts stimulated by laser-driven hosing evolution, Sci. Rep. **6**, 30491 (2016).

[23] S. G. Rykovanov, C. B. Schroeder, E. Esarey, C. G. R. Geddes, and W. P. Leemans, Plasma Undulator Based on Laser Excitation of Wakefields in a Plasma Channel, Phys. Rev. Lett. **114**, 145003 (2015).

[24] X.-L. Zhu, M. Chen, S.-M. Weng, T.-P. Yu, W.-M. Wang, F. He, Z.-M. Sheng, P. McKenna, D. A. Jaroszynski, and J. Zhang, Extremely brilliant geV γ-rays from a two-stage laser-plasma accelerator, Sci. Adv. **6**, eaaz7240 (2020).

[25] C. Yu, J. Liu, W. Wang, W. Li, R. Qi, Z. Zhang, Z. Qin, J. Liu, M. Fang, K. Feng, Y. Wu, L. Ke, Y. Chen, C. Wang, Y. Xu, Y. Leng, C. Xia, R. Li, and Z. Xu, Enhanced betatron radiation by steering a laser-driven plasma wakefield with a tilted shock front, Appl. Phys. Lett. **112**, 133503 (2018).

[26] A. Pukhov, Z.-M. Sheng, and J. Meyer-ter Vehn, Particle acceleration in relativistic laser channels, Phys. Plasmas **6**, 2847 (1999).

[27] K. Huang, Y. F. Li, D. Z. Li, L. M. Chen, M. Z. Tao, Y. Ma, J. R. Zhao, M. H. Li, M. Chen, M. Mirzaie, N. Hafz, T. Sokollik, Z. M. Sheng, and J. Zhang, Resonantly enhanced betatron hard x-rays from ionization injected electrons in a laser plasma accelerator, Sci. Rep. **6**, 27633 (2016).

[28] A. H. Nayfeh and D. T. Mook, *Nonlinear Oscillations* (John Wiley & Sons, New York, 2008).

[29] I. Kostyukov, A. Pukhov, and S. Kiselev, Phenomenological theory of laser-plasma interaction in "bubble" regime, Phys. Plasmas **11**, 5256 (2004).

[30] A. Pukhov, S. Gordienko, S. Kiselev, and I. Kostyukov, The bubble regime of laser-plasma acceleration: monoenergetic electrons and the scalability, Plasma Phys. Controlled Fusion **46**, B179 (2004).

[31] B.-S. Xie, H.-C. Wu, H. Wang, N.-Y. Wang, and M. Yu, Analysis of the electromagnetic fields and electron acceleration in the bubble regime of the laser-plasma interaction, Phys. Plasmas **14**, 073103 (2007).

[32] B. Liu, H. Y. Wang, J. Liu, L. B. Fu, Y. J. Xu, X. Q. Yan, and X. T. He, Generating Overcritical Dense Relativistic Electron Beams via Self-Matching Resonance Acceleration, Phys. Rev. Lett. **110**, 045002 (2013).

[33] L. D. Landau and E. M. Lifshitz, *Mechanics* (Pergamon Press, Oxford, 1976).

[34] T. D. Arber, K. Bennett, C. S. Brady, A. Lawrence-Douglas, M. G. Ramsay, N. J. Sircombe, P. Gillies, R. G. Evans, H. Schmitz, A. R. Bell, and C. P. Ridgers, Contemporary particle-in-cell approach to laser-plasma modelling, Plasma Phys. Controlled Fusion **57**, 113001 (2015).

[35] R. Lehe, C. Thaury, E. Guillaume, A. Lifschitz, and V. Malka, Laser-plasma lens for laser-wakefield accelerators, Phys. Rev. ST Accel. Beams **17**, 121301 (2014).

[36] F. Li, K. G. Miller, X. Xu, F. S. Tsung, V. K. Decyk, W. An, R. A. Fonseca, and W. B. Mori, A new field solver for modeling of relativistic particle-laser interactions using the particle-in-cell algorithm, Comput. Phys. Commun. **258**, 107580 (2021).

[37] L.-L. Yu, E. Esarey, C. B. Schroeder, J.-L. Vay, C. Benedetti, C. G. R. Geddes, M. Chen, and W. P. Leemans, Two-Color Laser-Ionization Injection, Phys. Rev. Lett. **112**, 125001 (2014).

[38] C. McGuffey, A. G. R. Thomas, W. Schumaker, T. Matsuoka, V. Chvykov, F. J. Dollar, G. Kalintchenko, V. Yanovsky, A. Maksimchuk, K. Krushelnick, V. Yu. Bychenkov, I. V. Glazyrin, and A. V. Karpeev, Ionization Induced Trapping in a Laser Wakefield Accelerator, Phys. Rev. Lett. **104**, 025004 (2010).

[39] A. Golovanov and I. Y. Kostyukov, Bubble regime of plasma wakefield in 2*d* and 3*d* geometries, Phys. Plasmas **25**, 103107 (2018).

[40] A. Döpp, B. Mahieu, A. Lifschitz, C. Thaury, A. Doche, E. Guillaume, G. Grittani, O. Lundh, M. Hansson, J. Gautier, M. Kozlova, J. P. Goddet, P. Rousseau, A. Tafzi, V. Malka, A. Rousse, S. Corde, and K. Ta Phuoc, Stable femtosecond x-rays with tunable polarization from a laser-driven accelerator, Light: Sci. Appl. **6**, e17086 (2017).

[41] P. S. Banks, M. D. Feit, and M. D. Perry, High-intensity third-harmonic generation, JOSA B **19**, 102 (2002).

[42] W. Yan-Ling, Z. Xu-Gui, W. Hong, and D. Liang-En, Efficient collinear frequency tripling of femtosecond laser with compensation of group velocity delay, Chin. Phys. B **18**, 4308 (2009).

[43] Y. Nabekawa, K. Kondo, N. Sarukura, K. Sajiki, and S. Watanabe, Terawatt KrF/Ti:sapphire hybrid laser system, Opt. Lett. **18**, 1922 (1993).

[44] R. C. Eckardt and R. L. Byer, Measurement of nonlinear optical coefficients by phase-matched harmonic generation, in *Inorganic Crystals for Optics, Electro-Optics, and Frequency Conversion* (International Society for Optics and Photonics, Bellingham, 1991), Vol. 1561, pp. 119–127.

[45] G. Bhar, A. Chaudhary, P. Kumbhakar, A. Rudra, and S. Sabarwal, A comparative study of laser-induced surface damage thresholds in BBO crystals and effect of impurities, Opt. Mater. (Amsterdam) **27**, 119 (2004).

[46] V. Krylov, J. Gallus, U. Wild, A. Kalintsev, and A. Rebane, Femtosecond noncollinear and collinear parametric generation and amplification in BBO crystal, Appl. Phys. B **70**, 163 (2000).

[47] S. Li, G. Li, Q. Ain, M. S. Hur, A. C. Ting, V. V. Kulagin, C. Kamperidis, and N. A. Hafz, A laser-plasma accelerator driven by two-color relativistic femtosecond laser pulses, Sci. Adv. **5**, eaav7940 (2019).

[48] M. Aoyama, T. Harimoto, J. Ma, Y. Akahane, and K. Yamakawa, Second-harmonic generation of ultra-high intensity femtosecond pulses with a KDP crystal, Opt. Express **9**, 579 (2001).

B.4 Generation of intense magnetic wakes by relativistic laser pulses in plasma

The following article is reproduced from M. Lamač, U. Chaulagain, J. Nejdl and S. V. Bulanov (2023). Generation of intense magnetic wakes by relativistic laser pulses in plasma. *Scientific Reports*, **13**(1), 1701.

scientific reports

OPEN

Generation of intense magnetic wakes by relativistic laser pulses in plasma

Marcel Lamač[1,2]✉, Uddhab Chaulagain[1], Jaroslav Nejdl[1,3] & Sergey V. Bulanov[1,4]

The emergence of petawatt lasers focused to relativistic intensities enables all-optical laboratory generation of intense magnetic fields in plasmas, which are of great interest due to their ubiquity in astrophysical phenomena. In this work, we study generation of spatially extended and long-lived intense magnetic fields. We show that such magnetic fields, scaling up to the gigagauss range, can be generated by interaction of petawatt laser pulses with relativistically underdense plasma. With three-dimensional particle-in-cell simulations we investigate generation of magnetic fields with strengths up to 10^{10} G and perform a large multi-parametric study of magnetic field in dependence on dimensionless laser amplitude a_0 and normalized plasma density n_e/n_c. The numerical results yield scaling laws that closely follow derived analytical result $B \propto \sqrt{a_0 n_e/n_c}$, and further show a close match with previous experimental works. Furthermore, we show in three-dimensional geometry that the decay of the magnetic wake is governed by current filament bending instability, which develops similarly to von Kármán vortex street in its nonlinear stage.

Intense magnetic fields in plasmas are induced by fast charged particles, which can be accelerated by laser-plasma interaction. In the non-relativistic or mildly relativistic regime, magnetic field generation can be due to inverse Faraday effect, which can be understood as the exchange of angular momentum from light to charged particles, which leads to magnetization of plasma[1–5]. In the regime of relativistic intensities, nonlinear plasma response breaks the adiabaticity between plasma electrons and laser, which leads to non-reversible gain of energy and angular momentum and therefore quasistatic magnetic field generation[3,6,7].

Laboratory generation of intense magnetic fields in plasmas attracts a lot of attention due to a broad range of applications[8], such as magnetically enhanced fast-ignition fusion[9], generation of collisionless shocks in magnetized plasma[10], magnetically assisted ion acceleration[11–15] or magnetic field reconnection research[16–19]. Of special interest is also generation of magnetic fields in the gigagauss (GG) range, where the magnetic cyclotron and atomic binding energies compete and atoms can deform into long rod shapes, leading to distinct atomic physics which occur in astrophysical objects like neutron stars and white dwarfs[20–22]. Even stronger magnetic fields are thought to exist in magnetars, where the magnetic fields cross the critical Schwinger field of quantum electrodynamics (QED) $B_{cr} = \frac{m_e^2 c^2}{e\hbar} \approx 4.4 \times 10^{13}$ G, where m_e is the electron mass, c the speed of light, e the elementary charge and $\hbar$ the reduced Planck constant. In such magnetic fields atoms deform into narrow spindles and the vacuum itself becomes strongly polarized, which introduces a slew of additional physics of fundamental interest, such as vacuum birefringence, magnetic pair production, synergic synchrotron-Cherenkov radiation, photon splitting or scattering suppression[22–26].

In recent decades, the process of laser-driven generation of magnetic fields has been investigated, in various schemes, theoretically[1–3,5,6,27–31] and experimentally in underdense plasmas[4,32–34] or solid targets[35] up to relativistic intensities, $a_0 \approx 1$[4,35], where $a_0 = \frac{eE_0}{m_e c\omega}$ is the dimensionless laser amplitude, E_0 the amplitude of the electric field and ω the laser angular frequency. Reaching $a_0 \approx 1$ indicates a shift towards relativistic dynamics, where the electron momentum changes by more than $m_e c$ in a single laser cycle, leading to highly nonlinear plasma response, which can lead to geometrically non-trivial plasma currents. The advent of petawatt (PW) laser systems enables experimental investigation of magnetic field generation in plasma within ultra-relativistic regime $a_0 \gg 1$, where magnetic fields reaching hundreds of megagauss (MG), or more, are expected[1,6,36]. These schemes often

[1]ELI Beamlines Facility, The Extreme Light Infrastructure ERIC, Za Radnicí 835, Dolní Břežany 25241, Czechia. [2]Faculty of Mathematics and Physics, Charles University, Ke Karlovu 3, Prague 2 12116, Czechia. [3]Faculty of Nuclear Science and Physical Engineering, Czech Technical University in Prague, Břehová 7, Prague 1 11519, Czechia. [4]Kansai Photon Science Institute, National Institutes for Quantum and Radiological Science and Technology, 8-1-7 Umemidai, Kizugawa-shi, 619-0215 Kyoto, Japan. ✉email: marcel.lamac@eli-beams.eu
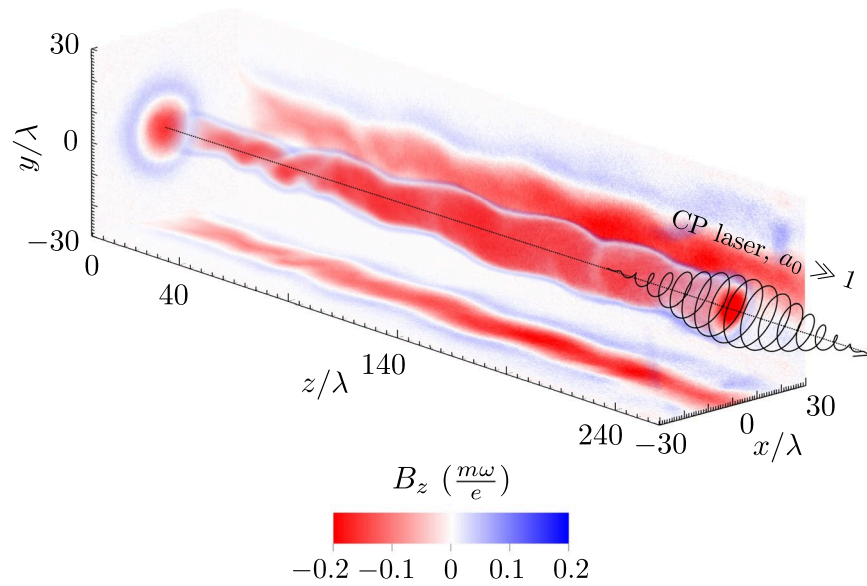
Figure 1. Schematic of intense magnetic wakefield generation by a relativistic laser in plasma. Magnetic fields generated by a relativistic right-hand circularly polarized relativistic laser pulse propagating in plasma. Axial component shown for relativistically underdense plasma where $n_e/n_c = 0.02$, $a_0 = 80$ and pulse duration $\tau_{fwhm} = 11.7\ T$, where T is a laser period. Magnetic field given in units $\frac{m\omega}{e} = 110$ MG for $\lambda = 1\ \mu$m.

require disposable structured overdense targets or multiple laser beams to achieve gigagauss magnetic fields[15,37,38]. Underdense plasmas generated by a laser enable high-repetition rate, allow density tailoring and straightforward implementation of optical diagnostics[39]. While extensive research on magnetic field generation in underdense plasmas up to $a_0 \approx 1$ has already been done, to the best of our knowledge, extended study involving multiparametric numerical simulations focused on generation of long-lived intense magnetic fields is still lacking.

In this work, we study magnetic field generation with ultra-relativistic lasers in plasma over a broad range of parameters, from underdense to overcritical plasmas, through analytic theory and numerical simulations. We give an overview of the process of magnetic field generation in the relativistic $a_0 \gg 1$ regime and specifically, being the experimentally most easily tunable parameters, we study dependency of the magnetic field on dimensionless laser amplitude a_0 and normalized electron density n_e/n_c for relativistically underdense ($n_e/n_c < a_0$) plasmas, where n_e is the electron density, $n_c = \frac{\omega^2 m_e \epsilon_0}{e^2}$ is the critical electron density and ϵ_0 is the vacuum permittivity. We present a large numerical multi-parametric study, which shows magnetic field generation in plasmas with circularly polarized laser pulses up to 10^{10} G, and reveals scaling laws describing magnetic fields which can be also long-lived and macroscopically large, as shown in Fig. 1. We explore the temporal and spatial properties of the magnetic field and show in three-dimensional geometry that its decay is governed by bending instability of the electron current filament[40,41], which leads to von Kármán antisymmetric electron vortex street development in its nonlinear stage. Furthermore, we show a close match of the obtained numerical scaling laws with magnetic fields observed in other experimental and theoretical works. Lastly, we discuss the possibility to use intense magnetic wakes to probe the physics of strong field QED.

Results and discussion

Analytical model for magnetic field strength.
Let us consider a simple model where we assume efficient generation of a plasma channel by a circularly polarized laser pulse. This is valid for relativistically underdense plasmas when the laser waist size is given as $w_0 \approx \sqrt{a_0} \frac{c}{\omega_p}$[14,42–44], where $\omega_p^2 = \frac{n_e e^2}{m_e \epsilon_0}$ is the electron plasma frequency. The magnetic field generated inside the plasma channel is given by Ampère's law as

$$\nabla \times \boldsymbol{B} = \mu_0 \boldsymbol{j}. \qquad (1)$$

where $\boldsymbol{j}$ is the current density inside the plasma channel and μ_0 is the vacuum permeability. As it is shown in the following section, the magnetic field is induced primarily by helical motion of relativistic electrons. For simplicity, let us assume that the longitudinal and transverse velocity components of the electrons are equal and the electron speed approaches speed of light, $v_i \approx \frac{c}{\sqrt{3}}$. The current density components are then $j_i \approx -en_e \frac{c}{\sqrt{3}}$. Since the transverse size of the magnetic field corresponds to the transverse size of the plasma channel l, Eq. (1) becomes $B = \mu_0 jl$. As mentioned above, in the case of a laser propagating in relativistically underdense plasma, a channel is generated with $l \approx \sqrt{a_0} \frac{c}{\omega_p}$, which gives us for the strength of the magnetic field components
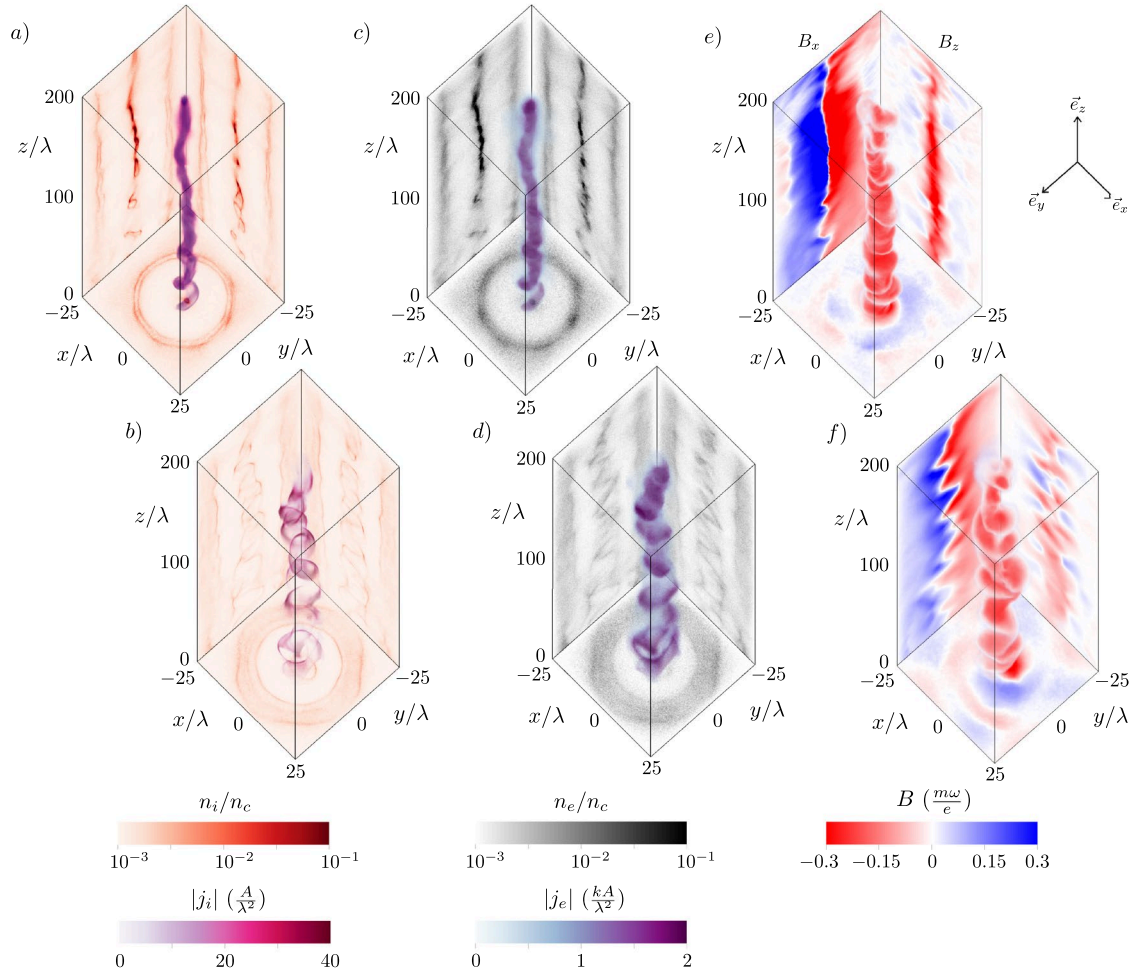
Figure 2. Evolution of quasistatic magnetic fields and plasma currents generated by ultrarelativistic laser. Ion current density magnitude $|j_i|$ (volumetric) and normalized ion density n_i/n_c (central planes) at simulation time 360 T (**a**) and 600 T (**b**). Electron current density magnitude $|j_e|$ (volumetric) with normalized electron density n_e/n_c (central planes) at simulation time 360 T (**c**) and 600 T (**d**). Axial magnetic field B_z (volumetric, x-y and x-z central planes) and transverse magnetic field component B_x (y-z central plane), which corresponds to the azimuthal magnetic field B_ϕ, at simulation time 360 T (**e**) and 600 T (**f**).

$$B = \frac{1}{\sqrt{3}} \frac{m_e \omega}{e} \sqrt{\frac{a_0 n_e}{n_c}}. \tag{2}$$

We note that for efficient magnetic field generation the laser pulse must be short enough to prevent complete plasma cavitation, $\tau < \omega_i^{-1}$, where $\omega_i^2 = \frac{n_i(Ze)^2}{m_i \epsilon_0}$ is the ion plasma frequency, where Z is the ion charge number, n_i is the ion density and m_i is the ion mass, otherwise the ions will be pushed out by the combined electrostatic and ponderomotive forces before any electrons pushed out are able to return and establish strong current inside the plasma channel through Weibel instability. We further note that laser waists with size $w_0 > l$ are less efficient for magnetic field generation. This is due to the onset of laser filamentation instability, which limits the length scale of the plasma channel, and therefore the scale of magnetic field, to $l \approx \sqrt{a_0} \frac{c}{\omega_p}$[14,44]. We can recast Eq. (2) in practical units, such as the laser power P, since from the matching condition we have $a_0 = 2(\frac{P}{P_c})^{1/3}$[43], where $P_c = \frac{8\pi m^2 c^5 \epsilon_0}{e^2} \frac{\omega^2}{\omega_p^2}$ is the self-focusing critical power, and therefore Eq. (2) becomes in practical units

$$B \text{ [GG]} \approx 0.1 \times (\lambda \text{ [}\mu\text{m]})^{1/3} (P \text{ [PW]})^{1/6} (n_e \text{ [}10^{20} \text{ cm}^{-3}\text{]})^{2/3}. \tag{3}$$

Let us now consider a technologically feasible scenario where we focus a laser with power $P = 1$ PW and central wavelength $\lambda = 1$ μm into a spot matched to plasma with density $n_e = 10^{21}$ cm^{-3}, which therefore corresponds to $a_0 \approx 74.4$. According to either Eqs. (2) or (3), this generates quasistatic magnetic field with strength $B \approx 0.5$ GG, indicating the potential for intense magnetic field generation in relativistically underdense plasmas. We proceed towards quantitative investigation of this potential in the next section.
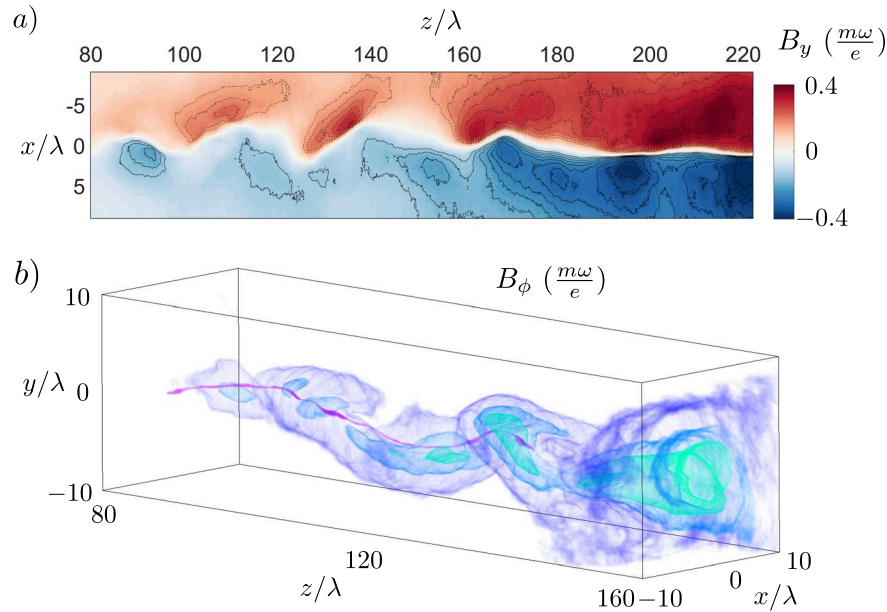
Figure 3. Bending instability of a current filament. (**a**) Magnetic field component B_y (central x-z plane) with solid (dashed) isocontours showing electron fluid velocity streamlines indicating negative (positive) vorticity at $t = 378\ T$. (**b**) Volumetric isocontours of azimuthal magnetic field component for $B_\phi = 0.03, 0.18, 0.23, 0.28\ \frac{m\omega}{e}$ (purple, dark blue, light blue, green) showing the helical topology of the vortices at $t = 378\ T$.

Intense magnetic wake generation in underdense plasma by relativistic laser pulse. To self-consistently study magnetic field generation by ultrarelativistic laser in underdense plasma, we have performed a series of numerical simulations in three-dimensional (3D) Cartesian geometry (see Methods for simulation details). In this section we illustrate the mechanism of magnetic field generation by a relativistic laser pulse.

The laser field is defined as a right-hand circularly polarized laser propagating along the z-axis defined with normalized laser amplitude $a_0 = 80$ and angular frequency $\omega = 2\pi c/\lambda$, where $\lambda = 1$ μm is the wavelength of the laser in vacuum. The circular polarization is chosen because we are interested not only in azimuthal magnetic fields, but also in axial magnetic fields, which are not generated for linear polarization and zero orbital angular momentum of the laser pulse, since in such a case there can be no longitudinal angular momentum transferred to plasma[1,2,7,37,45]. The laser pulse has a Gaussian spatial and temporal envelope with full width at half maximum pulse duration $\tau = 11.7\ T$, where $T = \lambda/c$ is the laser cycle period. Such laser pulse duration is chosen to satisfy conditions $\omega_p^{-1} < \tau < \omega_i^{-1}$, which prevents complete ion cavitation before electrons manage to return inside the channel and establish helical currents. To prevent laser filamentation and enable efficient magnetic field generation, we match the beam waist of the focused laser to the plasma channel transverse size given by $w_0 = \sqrt{a_0}\frac{c}{\omega_p}$. The target is composed of helium atoms with density $n_{He} = n_e/2$, where the normalized electron plasma density is established as $n_e/n_c = 0.07$ after barrier suppression ionization.

The circularly polarized laser pulse enters the gas target at $t = 0$, accelerates electrons and leaves the simulation with highest energy electrons at $t \approx 360\ T$, leaving a plasma channel in its wake. During this time interval, the attraction of laser-accelerated plasma-wake electron currents flowing in the direction of the laser pulse propagation, in combination with the repulsion from the return currents flowing along the channel periphery, leads to on-axis current filament coalescence. This coalescence leads to current density distribution anisotropy, and therefore magnetic field development, according to the Weibel instability with a characteristic transverse scale $\sqrt{a_0}\frac{c}{\omega_p}$ and a maximum growth rate given by $\Gamma_{We} = \omega_p/\sqrt{a_0}$[46,47]. Figure 2 shows at $t \approx 360\ T$ the volumetric plot of the magnitude of the ion (a) and electron (c) current density, $|j_i|$ and $|j_e|$, which are opposite in direction, as well as the central planes of respective normalized particle densities n_i/n_c and n_e/n_c, which also show the coalescent particle filaments as well as plasma channel walls containing the electron return current sheets ensuring plasma charge neutrality. The saturated magnetic fields are shown in Fig. 2e, with a volumetric plot of the axial magnetic field B_z, with central planes of both the axial magnetic field B_z, as well as the B_x component, which represents the magnitude of the azimuthal magnetic field B_ϕ in the y-z central plane. We draw attention to the large aspect ratio of the longitudinal and transverse coordinate axes, which reveals a very long region of intense magnetic wakefield, which is homogeneous over a length of 200 λ, as was shown for different parameters in Fig. 1.

Due to the nonlinearity of the plasma wavebreaking producing fast electron currents, the filament grows spatially inhomogeneous and develops a bending instability even in the case of linear polarization, as discussed in Ref.[40,41,47], showing a transition from the transverse-symmetric current evolution in the case of linear plasma response ($a_0 < 1$) discussed in previous works[28,29]. Figure 2b,d,f show the snapshots of the plasma evolution
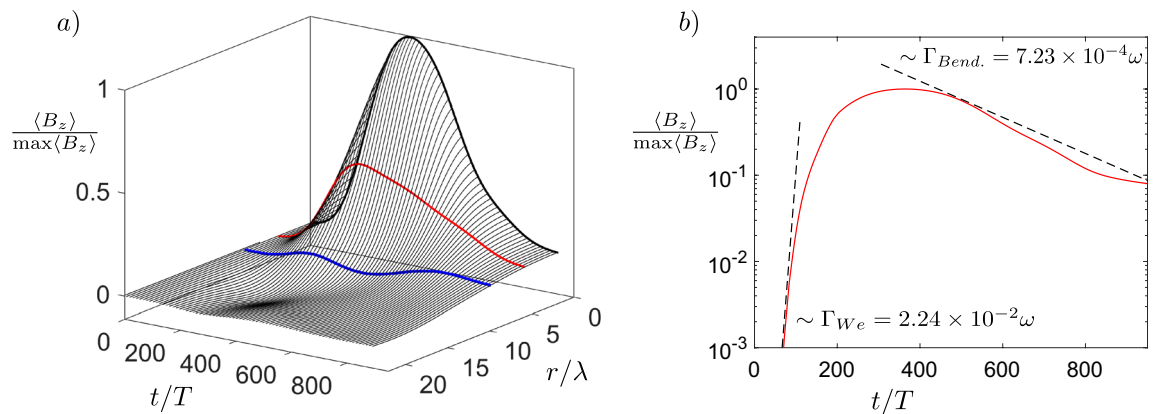
Figure 4. Temporal evolution of generated magnetic field. (**a**) Longitudinally averaged radial lineout of axial magnetic field with slices highlighted at radial distance $r/\lambda = 0$ (black), 4 (red), 8 (blue). (**b**) Axial magnetic field for $r/\lambda = 0$. $\max\langle B_z \rangle = 0.3 \frac{m\omega}{e}$.
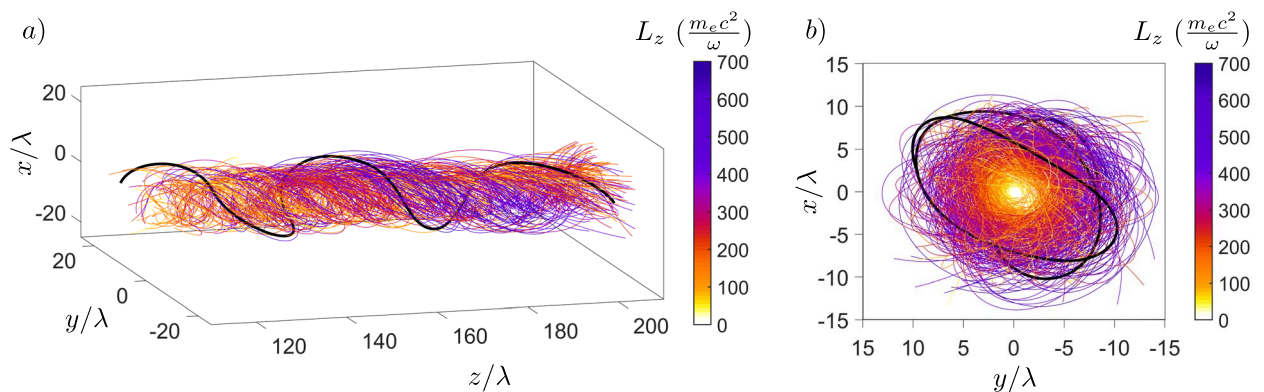

Figure 5. Electron trajectories generating axial and azimuthal magnetic fields. (**a**) Longitudinal angular momentum evolution with a z-direction view (**b**) shown in color, where $\frac{m_e c^2}{\omega} = 263776\ \hbar$ for $\lambda = 1\ \mu m$, which reveals the large absorption of right-handed photon spin angular momentum $S_z = +\hbar$ by electrons. The black curve highlights a single electron trajectory with angular momentum $L_z = 500\ \frac{m_e c^2}{\omega}$.

at $t = 600\ T$, where we see pronounced bending of the current filament in the late stage of the evolution. For initially irrotational plasma, the electron fluid vorticity is frozen into the magnetic field, since $\nabla \times \boldsymbol{p} = e\boldsymbol{B}$, where $\boldsymbol{p}$ is the electron momentum, therefore the bending of the current filament leads to development of isolated electron fluid vortices. In two-dimensional geometry, this instability manifests as the bending instability of a current sheet[40], which initially develops symmetric electron vortex pairs with vortex size of the order of or larger than the collisionless skin depth c/ω_p and with separation distance of the order of the plasma wavelength $\lambda_p = 2\pi c/\omega_p$. The bending instability further separates these vortices into an antisymmetric electron vortex row similar to the von Kármán vortex street[48]. In Fig. 3a, we show a central slice through the transverse component of the magnetic field B_y, which shows the initial development of the bending instability and the emergence of antisymmetric vortex pairs, in agreement with two-dimensional results[40,41]. Fully three-dimensional topology of the vortices is shown in Figs. 3b and 2f, which show them following the helical bending of the current filament. Late stage of the evolution is shown in Fig. 2b,d,f, at which point the growth rate of the instability is slower and the antisymmetric von Kármán vortex row is well established. It can be seen in the B_x component of the magnetic field in Fig. 2f corresponding to electron vorticity in the same direction.

To quantify the temporal evolution of the quasistatic magnetic field, as well as the instability, over the whole region of interest, we define the longitudinally averaged radial lineout of the axial magnetic field as $\langle B_z \rangle(r) = \frac{1}{2\pi L} \int_0^{2\pi} \int_0^L B_z(r, \phi, z)\ dz d\phi$. Temporal evolution of $\langle B_z \rangle(r)$ with $L = 200\ \lambda$ is shown in Fig. 4, where we see the growth of the electron Weibel instability between $t = 0$ and $t = 360\ T$ with maximum growth rate $\Gamma_{We} = \omega_p/\sqrt{a_0} \approx 2.24 \times 10^{-2}\omega$, at the end of which it saturates as the magnetic energy density becomes comparable to the energy density in the electron flow $B_{sat.} \approx \frac{m\omega}{e} \sqrt{\frac{a_0 n_e}{n_c}}$ [46,47] in accordance with Eq. (2). As the bending instability takes over the evolution at $t = 360\ T$, it leads to decay of the longitudinally averaged magnetic field. At the initial stage of the instability, the distances between the vortices are estimated as 5 μm and 2.5 μm in the
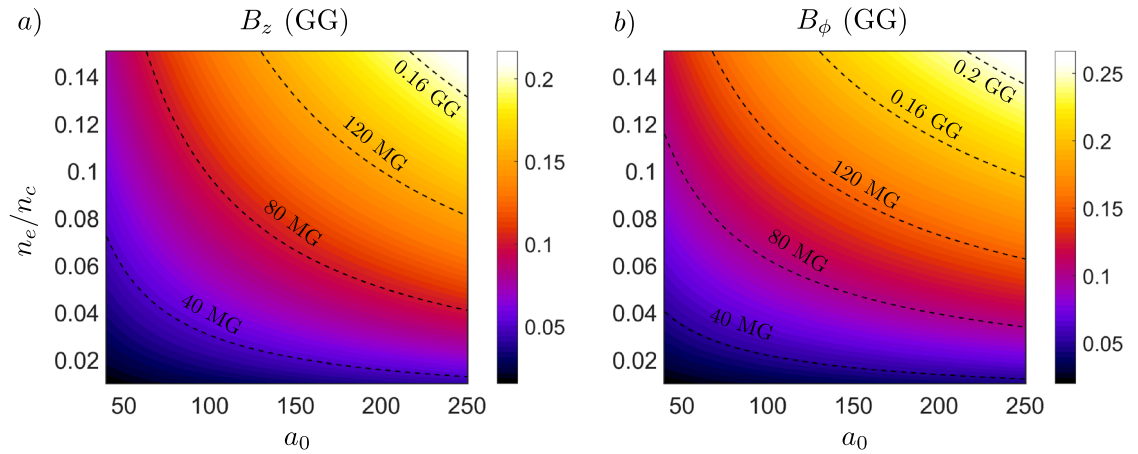
Figure 6. Numerical scaling laws for magnetic field components. Dependence of magnetic field components B_z (**a**) and B_ϕ (**b**) on normalized electron density n_e/n_c and normalized laser amplitude $a_0 \gg 1$. For laser wavelength $\lambda = 1$ μm.

horizontal and vertical direction respectively, with perturbation wavelength estimated as 20 μm. Calculating the growth rate of the instability for the antisymmetrical vortex row from Eq. (5) in Ref.[40], we get $\Gamma_{Bend.} \approx 7.27 \times 10^{-4}\omega$, which matches the observed decay rate of the magnetic field. The bending instability starts to slow at the late nonlinear stage $t = 600\ T$, in accordance with results of Refs.[40,41]. The topology of the bending instability is similar to the drift-kink instability of the ion current filament discussed in Ref.[49], however, the growth rate of the ion kink instability is at least an order of magnitude smaller. It is the faster electrons which are responsible for the topology and evolution of the magnetic field in our case, which validates the assumptions of the bending instability discussed in Refs.[40,41]. The full width at half maximum duration of the magnetic field is found to be $\tau_B \approx 390\ T$, which is in the picosecond range. This is up to two orders of magnitude longer than the duration of magnetic fields reported in other works[30,38]. Samples of helical trajectories of electrons carrying the longitudinal and transverse currents generating transverse and longitudinal magnetic fields respectively and evolution of their longitudinal angular momentum L_z are shown in Fig. 5.

Multi-parametric study in underdense plasma. To study the magnetic field strength dependence on normalized laser amplitude a_0 and normalized electron density n_e/n_c, we have carried out series of 3D PIC simulations. The parameter range of the PIC simulations (see Methods for details) corresponds to currently available laser systems and f-numbers of focusing optics capable of reaching the relativistic regime with $a_0 \gg 1$. For $\lambda = 1$ μm, the range of underdense plasma densities corresponds to $10^{18} - 10^{20}$ cm^{-3}.

We measure the maximum cycle-averaged magnetic field strength of the longitudinal B_z and azimuthal B_ϕ field component after the laser leaves the simulation. Performing nonlinear regression on the obtained data set yields the following numerical scaling laws for the strength of magnetic field components

$$\frac{eB_z}{m_e\omega} = 0.22\left(\frac{n_e}{n_c}\right)^{0.59} a_0^{0.56}, \tag{4a}$$

$$\frac{eB_\phi}{m_e\omega} = 0.61\left(\frac{n_e}{n_c}\right)^{0.65} a_0^{0.44}. \tag{4b}$$

We see a good correspondence between Eqs. (4) and Eq. (2), which validates the assumptions of the simple analytical model (2). We plot the magnetic fields given by Eq. (4) within the scanned parameter range in Fig. 6.

More interestingly, Eq. (4) fit well with magnetic fields measured in other works outside the studied parameter range. Picosecond-long axial magnetic field with magnetic field $B_z \approx 3.9$ MG generated in underdense plasma was experimentally measured in Ref.[4] for $\lambda = 1.054$ μm, $a_0 = 2.5$ and $n_e/n_c = 0.02$. Plugging these values into Eq. (4a) gives axial field strength of $B_z \approx 3.8$ MG, showing a close correspondence, which is not present with analytical models presented therein that heavily underestimate the magnetic field strength, as discussed by the authors. Another experimental work[33] observed axial magnetic field due to nonlinear inverse Faraday effect with $B_z \approx 1.5$ MG for $\lambda = 1.06$ μm, $a_0 = 9 \times 10^{-3}$, $n_e/n_c \approx 1$ and for such values, Eq. (4a) gives $B_z \approx 1.6$ MG. Similarly, in the numerical work[15], long-lived azimuthal magnetic fields of $B_\phi \approx 1$ GG can be seen generated in the wake of the main magnetic vortex trailing behind a laser propagating in dense plasma for $\lambda = 0.8$ μm, $a_0 = 80$ and $n_e/n_c = 3.32$. Plugging these values into the scaling law for the azimuthal field component Eq. (4b) gives $B_\phi \approx 1$ GG. This correspondence holds for all the other cases discussed there as well. These agreements show the applicability of the scaling laws (4), in order of magnitude, to a broader range of parameters in the underdense regime due to the dense data set of the multi-parametric study, which strenghtens their predictive potential.
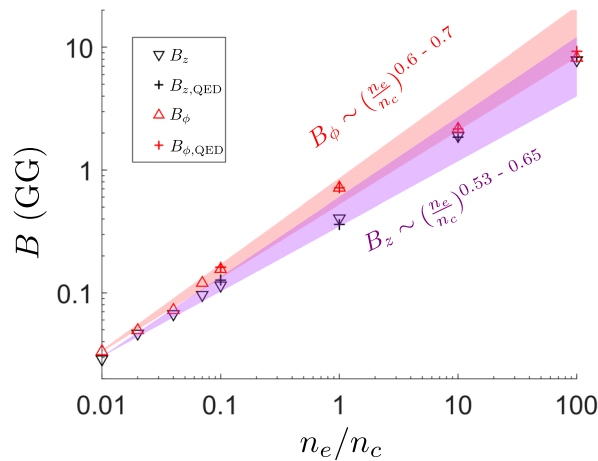
Figure 7. Magnetic field strength dependence on normalized electron density for $a_0 = 200$. Magnetic field strength of components B_z and B_ϕ measured from simulations with numerical scaling laws plotted within 95% confidence bounds of electron density dependence power index obtained through nonlinear regression. Simulations were performed both with (crosses) and without (triangles) quantum electrodynamics effects for $n_e/n_c \geq 0.1$.
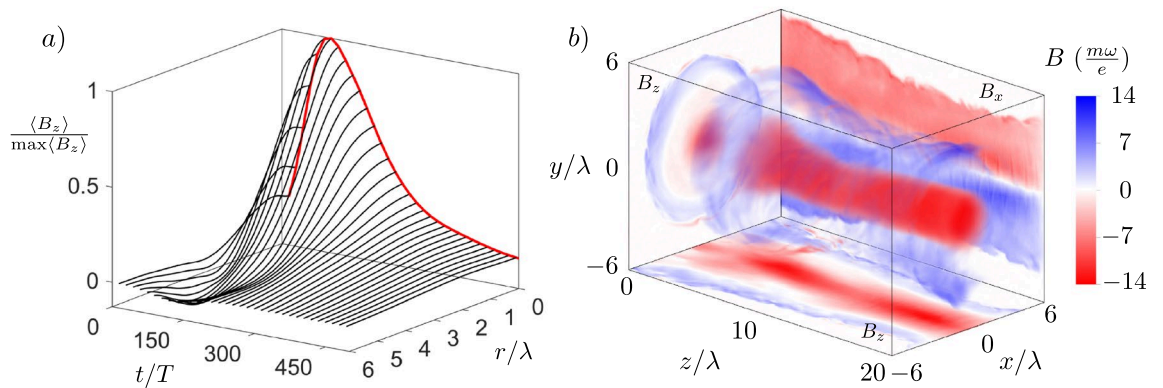
Figure 8. Extremely intense magnetic field generated for $a_0 = 200$, $n_e/n_c = 10$. (**a**) Time evolution of longitudinally averaged ($L = 20\ \lambda$) radial lineout of axial magnetic field. (**b**) Longitudinal (volumetric, x–y and x–z central planes) and transverse (y–z central plane) field components at magnetic field saturation time $t = 120\ T$.

Extremely intense magnetic wake generation in dense plasma.   To further evaluate the predictive potential of Eqs. (2) and (4) for higher plasma densities, we conduct additional simulations of magnetic field generation in dense targets for $a_0 = 200$ (see Methods for details). Figure 7 shows the strength of the obtained magnetic fields corresponding to gas, liquid or solid, but relativistcally underdense ($n_e/n_c < a_0$) targets. Intense magnetic fields reaching up to $\approx 10^{10}$ G are found in accordance with Eqs. (2, 4). The temporal and spatial properties of the magnetic field with $B_z \approx 1.8$ GG and $B_\phi \approx 2$ GG generated for the case of $n_e/n_c = 10$ are shown in Fig. 8a,b, from which we see that the temporal duration of the magnetic field equals $\tau_B \approx 165\ T$, which is 0.5 picosecond for $\lambda = 1\ \mu$m, and the magnetic field extends homogeneously over a length of 20 λ at the time of Weibel instability saturation $t = 120\ T$.

Additionally, we have performed simulations both with and without the inclusion of effects of QED as described in Ref.[50]. We have found that these processes, notably radiation friction, have negligible effect on magnetic field generation in the scanned parameter range, which is shown in Fig. 7. This is in accordance with the results of Ref.[36], where it was discussed that energy dissipation through radiation friction is of the order of energy lost due to numerical error for $a_0 \leq 200$ for $n_e/n_c = 90$, which we now confirm for plasma densities in the range $n_e/n_c = 0.1 - 100$.

We proceed to consider the use of intense long-lived magnetic wakes generated by relativistic lasers for laboratory probing of strong field QED effects in magnetized plasma[23,24]. QED processes are essential in magnetized plasmas surrounding pulsars and especially magnetars[21,22,24,26], and their transition probabilities generally

increase with the Lorentz invariant parameter $\chi = \gamma(B/B_{cr})$, where γ is the Lorentz factor of the electron interacting with magnetic field. The value of $\chi \approx 1$ indicates the quantum regime threshold, beyond which quantum effects cannot be neglected[23]. Sending relativistic electrons with $\gamma \approx 10^{3-4}$, which could be produced in the same optically synchronized setup through laser wakefield acceleration[51], to a magnetic wake with 10^{10} G gives magnetic field in the electron rest frame as $B \approx B_{cr}$ and therefore the Lorentz invariant quantum parameter becomes $\chi \approx 1$. Recent experimental work with relativistic electrons accelerated up to $\gamma \approx 10^5$ verified the necessity for the use of quantum models of synchrotron radiation for $\chi \approx 1$ using a crystal as a target, which is limited to a field corresponding to 10^8 G[52]. Electrons with $\gamma \approx 10^5$ would generate synergic synchrotron-Cherenkov radiation in tenuous plasma even with magnetic field $\approx 10^3$ G, as discussed in Ref.[24]. Interacting with extremely intense magnetic wakes reaching 10^{10} G, such electrons would experience $\chi \geq 10^2$, which would enable probing of strong field QED in magnetized plasmas close to the conjectured non-perturbative regime threshold $\alpha\chi^{2/3} \approx 1$[53–55], where α is the fine-structure constant. These considerations indicate the potential of laser generated intense magnetic wakes to serve as a test bench for strong field QED in magnetized plasmas over a broad range of quantum parameters χ, which is possible due to the tunability of magnetic field strength through a_0 and n_e/n_c, as given by Eq. (2).

Conclusion

We have investigated analytically and numerically generation of spatially extended, long-lived and intense magnetic fields by circularly polarized relativistic laser pulses in plasmas for the parameter range $a_0 = 40 - 200$, $n_e/n_c = 0.01 - 100$. We show that circularly polarized relativistic laser pulse transfers angular momentum to plasma electrons, leading to development of strong helical currents through Weibel instability that sustain the longitudinal, as well as the transverse, component of the magnetic field. These currents can sustain long-lasting intense magnetic fields with strengths up to 10^{10} G inside the plasma channel. We have identified the magnetic field decay due to bending instability, which develops similarly to von Kármán vortex street in its nonlinear stage. Furthermore, we have performed a multi-parametric study of magnetic field strength dependence on a_0 and n_e/n_c in relativistically underdense plasmas ($n_e/n_c < a_0$), which revealed numerical scaling laws (4) that follow the analytical result (2). We have found agreement between the scaling laws (4) and magnetic fields produced in other experimental and theoretical works, which further supports their predictive power over a broad range of parameters in the relativistically underdense regime. Finally, we envision interactions of relativistic electrons with studied intense magnetic wakes for probing of strong field quantum electrodynamics in magnetized plasmas.

Our results pave way towards generation of intense, tunable and long-lived magnetic fields in plasmas at various laboratory conditions, which lead to innumerable applications in plasma physics, fundamental physics or laboratory astrophysics.

Methods

Particle-in-cell simulations. We have performed numerical simulations in the full 3D Cartesian geometry with the relativistic, massively parallelized PIC code EPOCH[56]. Second order Yee scheme Maxwell solver and Higuera-Cary algorithm are used for the field and particle evolutions respectively. To reduce numerical dispersion in the second order scheme, Courant-Friedrichs-Lewy number was set to $c\Delta t/\Delta z = 0.99$. Third-order interpolation is employed to reduce grid heating. The size of the simulation box corresponding to the benchmark simulation results presented in Figs. 2, 3, 4 and 5 was set as $320\,\lambda \times 50\,\lambda \times 50\,\lambda$ with grid size $4000 \times 360 \times 360$. The number of macro-particles per cell is 4, giving a total of 2×10^9 macro-particles for helium ions and 4×10^9 macro-particles for electrons. We use absorbing boundary conditions for both particles and fields. The simulation is evolved up to simulation time $t_{end} = 1500\,T$, which is long enough to see the full temporal evolution and decay of the magnetic field. Finally, as we are interested in the slow quasistatic evolution of the magnetic fields, all field variables were averaged every laser cycle as $\bar{A} = \frac{1}{T}\int_0^T A(t)\,dt$, where T is the laser cycle period. With this remark, we do not use the bar notation in the article.

For the multi-parametric study in underdense plasmas (Fig. 6), due to large computational demands of 3D simulations, we have reduced the number of macro-particles per cell to 2 and considered the ionised helium atoms as immobile. We have found that this approximation leads to negligible differences in generated magnetic field strengths, since the electron and ion current densities differ by two orders of magnitude (Fig. 2) and the Weibel instability of the electron current filaments is the main source of the magnetic field, as discussed in the article. We note that other properties of the magnetic field not investigated with the multi-parametric study, such as spatial and temporal homogeneity, are affected by ion immobility, as discussed elsewhere[31]. Since the laser spot size is changing for each data point according to $w_0 = \sqrt{a_0}\frac{c}{\omega_p}$, the dimensions of the simulation box are decreased with decreasing w_0. The resolution of the grid is set for each case to resolve $\lambda = \min(\lambda_p, \lambda_L)$ with at least 10 samples, which assures sufficient resolution of the important wavelengths according to the Nyquist-Shannon sampling theorem. The study is performed over the span of following parameter values: $a_0 = 40, 80, 120, 160, 200$ and $n_e/n_c = 0.01, 0.02, 0.04, 0.07, 0.1$.

Simulations of dense targets presented in Figs. 7 and 8 with mobile ions and also with and without QED effects were further performed for $a_0 = 200$. The number of electron and ion particles per cell was chosen as 4 and 2 respectively. The plasma density range was selected as $n_e/n_c = 0.01, 0.04, 0.07, 0.1, 1, 10, 100$. In addition to third-order interpolation, current smoothing is turned on for $n_e/n_c \geq 1$ to ensure suppression of grid heating[56]. The resolution and size of the simulation box was selected according to the same criteria as in the multi-parametric study, e.g. for the lowest density $n_e/n_c = 0.01$, we set $\frac{\lambda_p}{\Delta x,y} = 67$, $\frac{\lambda_p}{\Delta z} = 125$, $\frac{\lambda_L}{\Delta x,y} = 13$ and for the highest density

$n_e/n_c = 100$, we set $\frac{\lambda_L}{\Delta x,y,z} = 100$, $\frac{\lambda_p}{\Delta x,y,z} = 10$. For $n_e/n_c \geq 10$, the waist of the laser is fixed to $1 \ \mu$m as the relativistic skin depth is smaller than laser wavelength and we do not consider tight focusing of the laser. This leads to energetically less efficient plasma channel and magnetic field generation due to laser filamentation, however, the Weibel saturated magnetic field is fixed by a choice of a_0 and n_e/n_c[44,46,47].

We have performed convergence tests that involved doubling the number of particles and increasing transverse resolution which produced minimal differences in peak magnetic fields.

Data availibility

The data that support the findings of this study are available from the corresponding author upon reasonable request.

Code availability

Numerical PIC simulations were performed with the open source massively parallelized PIC code EPOCH, available at https://github.com/Warwick-Plasma/epoch. Data analysis and visualization was done with commercial software Matlab, Wolfram Mathematica and the open source visualization tool Visit, available at https://www.visitusers.org/index.php?title=Main_Page. All other relevant code used in this study is available from the corresponding author upon reasonable request.

References

1. Haines, M. Generation of an axial magnetic field from photon spin. *Phys. Rev. Lett.* **87**(13), 135005 (2001).
2. Ali, S., Davies, J. & Mendonca, J. Inverse faraday effect with linearly polarized laser pulses. *Phys. Rev. Lett.* **105**(3), 035001 (2010).
3. Nuter, R., Korneev, P., Dmitriev, E., Thiele, I. & Tikhonchuk, V. Gain of electron orbital angular momentum in a direct laser acceleration process. *Phys. Rev. E* **101**(5), 053202 (2020).
4. Najmudin, Z. *et al.* Measurements of the inverse faraday effect from relativistic laser interactions with an underdense plasma. *Phys. Rev. Lett.* **87**(21), 215004 (2001).
5. Sheng, Z. & Meyer-ter-Vehn, J. Inverse faraday effect and propagation of circularly polarized intense laser beams in plasmas. *Phys. Rev. E* **54**(2), 1833 (1996).
6. Berezhiani, V., Mahajan, S. & Shatashvili, N. Theory of magnetic field generation by relativistically strong laser radiation. *Phys. Rev. E* **55**(1), 995 (1997).
7. Lehner, T. Intense magnetic field generation by relativistic ponderomotive force in an underdense plasma. *Phys. Scr.* **49**(6), 704 (1994).
8. Herlach, F. & Miura, N. *High Magnetic Fields. Techniques and Experiments.* (World Scientific, Singapore, 2003).
9. Strozzi, D. *et al.* Fast-ignition transport studies: Realistic electron source, integrated particle-in-cell and hydrodynamic modeling, imposed magnetic fields. *Phys. Plasmas* **19**(7), 072711 (2012).
10. Sagdeev, R. Cooperative phenomena and shock waves in collisionless plasmas. *Rev. Plasma Phys.* **4**, 23 (1966).
11. Kuznetsov, A., Esirkepov, T. Z., Kamenets, F. & Bulanov, S. Efficiency of ion acceleration by a relativistically strong laser pulse in an underdense plasma. *Plasma Phys. Rep.* **27**(3), 211–220 (2001).
12. Fukuda, Y. *et al.* Energy increase in multi-mev ion acceleration in the interaction of a short pulse laser with a cluster-gas target. *Phys. Rev. Lett.* **103**(16), 165002 (2009).
13. Nakamura, T., Bulanov, S. V., Esirkepov, T. Z. & Kando, M. High-energy ions from near-critical density plasmas via magnetic vortex acceleration. *Phys. Rev. Lett.* **105**(13), 135002 (2010).
14. Bulanov, S. *et al.* Helium-3 and helium-4 acceleration by high power laser pulses for hadron therapy. *Phys. Rev. Spec. Top. Accel. Beams* **18**(6), 061302 (2015).
15. Park, J. *et al.* Ion acceleration in laser generated megatesla magnetic vortex. *Phys. Plasmas* **26**(10), 103108 (2019).
16. Kopp, R. & Pneuman, G. Magnetic reconnection in the corona and the loop prominence phenomenon. *Sol. Phys.* **50**(1), 85–98 (1976).
17. Masuda, S., Kosugi, T., Hara, H., Tsuneta, S. & Ogawara, Y. A loop-top hard x-ray source in a compact solar flare as evidence for magnetic reconnection. *Nature* **371**(6497), 495–497 (1994).
18. Kuramitsu, Y. *et al.* Magnetic reconnection driven by electron dynamics. *Nat. Commun.* **9**(1), 1–6 (2018).
19. Gu, Y.-J., Bulanov, S.V.: Magnetic field annihilation and charged particle acceleration in ultra-relativistic laser plasmas. High Power Laser Sci. Eng. **9** (2021)
20. Lai, D. Matter in strong magnetic fields. *Rev. Mod. Phys.* **73**, 629–662. https://doi.org/10.1103/RevModPhys.73.629 (2001).
21. Vanlandingham, K. M. *et al.* Magnetic white dwarfs from the SDSS. II. the second and third data releases. *Astron. J.* **130**(2), 734–741. https://doi.org/10.1086/431580 (2005).
22. Duncan, R.C.: Physics in ultra-strong magnetic fields. In: AIP Conference Proceedings, vol. 526, pp. 830–841 (2000). American Institute of Physics
23. Erber, T. High-energy electromagnetic conversion processes in intense magnetic fields. *Rev. Mod. Phys.* **38**(4), 626 (1966).
24. Schwinger, J., Tsai, W.-Y. & Erber, T. Classical and quantum theory of synergic synchrotron-čerenkov radiation. *Ann. Phys.* **96**(2), 303–332 (1976).
25. Mourou, G. A., Tajima, T. & Bulanov, S. V. Optics in the relativistic regime. *Rev. Mod. Phys.* **78**(2), 309 (2006).
26. Bulanov, S. *et al.* On the problems of relativistic laboratory astrophysics and fundamental physics with super powerful lasers. *Plasma Phys. Rep.* **41**(1), 1–51 (2015).
27. Gradov, O. & Stenflo, L. Magnetic-field generation by a finite-radius electromagnetic beam. *Phys. Lett. A* **95**(5), 233–234 (1983).
28. Gorbunov, L., Mora, P. & Antonsen, T. Jr. Magnetic field of a plasma wake driven by a laser pulse. *Phys. Rev. Lett.* **76**(14), 2495 (1996).
29. Sheng, Z., Meyer-ter-Vehn, J. & Pukhov, A. Analytic and numerical study of magnetic fields in the plasma wake of an intense laser pulse. *Phys. Plasmas* **5**(10), 3764–3773 (1998).
30. Nuter, R., Korneev, P., Thiele, I. & Tikhonchuk, V. Plasma solenoid driven by a laser beam carrying an orbital angular momentum. *Phys. Rev. E* **98**(3), 033211 (2018).
31. Wilson, T., Sheng, Z., Eliasson, B. & McKenna, P. Magnetic field amplification by high power lasers in underdense plasma. *Plasma Phys. Controlled Fusion* **63**(8), 084001 (2021).
32. Horovitz, Y. *et al.* Measurements of inverse faraday effect and absorption of circularly polarized laser light in plasmas. *Phys. Rev. Lett.* **78**(9), 1707 (1997).

33. Horovitz, Y. *et al.* The inverse faraday effect in plasma produced by circularly polarized laser light in the range of intensities 109–1014 w/cm2. *Phys. Lett. A* **246**(3–4), 329–334 (1998).
34. Deschamps, J., Fitaire, M. & Lagoutte, M. Inverse faraday effect in a plasma. *Phys. Rev. Lett.* **25**(19), 1330 (1970).
35. Tatarakis, M. *et al.* Measuring huge magnetic fields. *Nature* **415**(6869), 280–280 (2002).
36. Liseykina, T., Popruzhenko, S. & Macchi, A. Inverse faraday effect driven by radiation friction. *New J. Phys.* **18**(7), 072001 (2016).
37. Jiang, K., Pukhov, A. & Zhou, C. Magnetic field amplification to gigagauss scale via hydrodynamic flows and dynamos driven by femtosecond lasers. *New J. Phys.* **23**(6), 063054 (2021).
38. Murakami, M., Honrubia, J., Weichman, K., Arefiev, A. & Bulanov, S. Generation of megatesla magnetic fields by intense-laser-driven microtube implosions. *Sci. Rep.* **10**(1), 1–11 (2020).
39. Harilal, S., Phillips, M., Froula, D., Anoop, K., Issac, R., Beg, F.: Optical diagnostics of laser-produced plasmas. arXiv preprint arXiv:2201.08783 (2022)
40. Bulanov, S., Lontano, M., Esirkepov, T. Z., Pegoraro, F. & Pukhov, A. Electron vortices produced by ultraintense laser pulses. *Phys. Rev. Lett.* **76**(19), 3562 (1996).
41. Bulanov, S., Esirkepov, T. Z., Lontano, M. & Pegoraro, F. The stability of single and double vortex films in the framework of the hasegawa-mima equation. *Plasma Phys. Rep.* **23**(8), 660–669 (1997).
42. Kostyukov, I., Pukhov, A. & Kiselev, S. Phenomenological theory of laser-plasma interaction in "bubble" regime. *Phys. Plasmas* **11**(11), 5256–5264 (2004).
43. Lu, W. *et al.* Generating multi-gev electron bunches using single stage laser wakefield acceleration in a 3d nonlinear regime. *Phys. Rev. Spec. Topics Accel. Beams* **10**(6), 061301 (2007).
44. Mourou, G. *et al.* On the design of experiments for the study of relativistic nonlinear optics in the limit of single-cycle pulse duration and single-wavelength spot size. *Plasma Phys. Rep.* **28**(1), 12–27 (2002).
45. Qiao, B., He, X. & Zhu, Sp. Fluid theory for quasistatic magnetic field generation in intense laser plasma interaction. *Phys. Plasmas* **13**(5), 053106 (2006).
46. Fiúza, F., Fonseca, R., Tonge, J., Mori, W. B. & Silva, L. Weibel-instability-mediated collisionless shocks in the laboratory with ultraintense lasers. *Phys. Rev. Lett.* **108**(23), 235004 (2012).
47. Askar'yan, G., Bulanov, S., Pegoraro, F. & Pukhov, A. Magnetic interaction of self-focusing channels and fluxes of electromagnetic radiation: their coalescence, the accumulation of energy, and the effect of external magnetic fields on them. *Soviet J. Exp. Theor. Phys. Lett.* **60**, 251 (1994).
48. Lamb, H. *Hydrodynamics, 585/587* (Cambridge Univ, Press, 1975).
49. Ruyer, C. & Fiuza, F. Disruption of current filaments and isotropization of the magnetic field in counterstreaming plasmas. *Phys. Rev. Lett.* **120**(24), 245002 (2018).
50. Ridgers, C. P. *et al.* Modelling gamma-ray photon emission and pair production in high-intensity laser-matter interactions. *J. Comput. Phys.* **260**, 273–285 (2014).
51. Gonsalves, A. *et al.* Petawatt laser guiding and electron beam acceleration to 8 gev in a laser-heated capillary discharge waveguide. *Phys. Rev. Lett.* **122**(8), 084801 (2019).
52. Andersen, K. K. *et al.* Experimental investigations of synchrotron radiation at the onset of the quantum regime. *Phys. Rev. D* **86**(7), 072001 (2012).
53. Ritus, V. Radiative corrections in quantum electrodynamics with intense field and their analytical properties. *Ann. Phys.* **69**(2), 555–582 (1972).
54. Narozhny, N. Expansion parameter of perturbation theory in intense-field quantum electrodynamics. *Phys. Rev. D* **21**(4), 1176 (1980).
55. Di Piazza, A., Wistisen, T., Tamburini, M. & Uggerhøj, U. Testing strong field qed close to the fully nonperturbative regime using aligned crystals. *Phys. Rev. Lett.* **124**(4), 044801 (2020).
56. Arber, T. *et al.* Contemporary particle-in-cell approach to laser-plasma modelling. *Plasma Phys. Controlled Fusion* **57**(11), 113001 (2015).

Acknowledgements

Author contributions

M.L. concieved the research, performed the analysis and processed the data and wrote the manuscript. M.L and S.V.B conceived the idea to use magnetic wakes for probing QED. U.C., J.N. and S.V.B. provided critical feedback and helped to shape the research, analysis, data visualization, and the manuscript. All authors reviewed the final manuscript.

Competing interests

The authors declare no competing interests.

Additional information

Correspondence and requests for materials should be addressed to M.L.

Reprints and permissions information is available at www.nature.com/reprints.

Publisher's note Springer Nature remains neutral with regard to jurisdictional claims in published maps and institutional affiliations.